Preparation, characterization, and evaluation of Mg-Al mixed oxide supported nickel catalysts for the steam reforming of ethanol

by

Luke James Ivor Coleman

A thesis
presented to the University of Waterloo
in fulfillment of the
thesis requirement for the degree of
Doctor of Philosophy
in
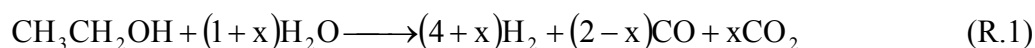Chemical Engineering

Waterloo, Ontario, Canada, 2008

Author's Declaration

I hereby declare that I am the sole author of this thesis. This is a true copy of the thesis, including any required final revisions, as accepted by my examiners.

I understand that my thesis may be made electronically available to the public.

Abstract

The conversion of ethanol to hydrogen or syngas can be achieved by reacting ethanol with water via steam reforming,

$$CH_3CH_2OH + (1+x)H_2O \longrightarrow (4+x)H_2 + (2-x)CO + xCO_2 \qquad \text{(R.1)}$$

$$CH_3CH_2OH + H_2O \longrightarrow 4H_2 + 2CO \qquad \Delta H^\circ_{298K} = 255.72\,\frac{kJ}{mol} \qquad \text{(R.2)}$$

$$CO + H_2O \longrightarrow H_2 + CO_2 \qquad \Delta H^\circ_{298K} = -41.19\,\frac{kJ}{mol} \qquad \text{(R.3)}$$

Ideally, the ethanol steam reforming reaction can achieve a hydrogen yield of 6 moles of hydrogen per mole of ethanol when the value of x in (R.1) equals 2. High theoretical H_2 yield makes ethanol steam reforming a very attractive route for H_2 production. Thermodynamic equilibrium studies have shown that ethanol steam reforming produces mixtures of H_2, CO, CO_2, and CH_4 below 950 K, while above 950 K the ethanol steam reforming reaction (R.1) adequately describes the product composition

In this study a series of 10wt% Ni loaded Mg-Al mixed oxide supported catalysts were evaluated for the production of hydrogen via the steam reforming of ethanol. Mg-Al mixed oxide supported nickel catalysts were found to give superior activity, steam reforming product selectivity (H_2 and CO_x), and improved catalyst stability than the pure oxide supported nickel catalyst at both temperatures investigated. Activity, product selectivity, and catalyst stability were dependent upon the Al and Mg content of the support. At 923 K, the Mg-Al mixed oxide supported nickel catalysts were the best performing catalysts exhibiting the highest steam reforming product yield and were highly stable, showing no signs of deactivation after 20 h of operation. The improved performance of the Mg-Al mixed oxide supported catalysts was related to the incorporation of the pure oxides, MgO and Al_2O_3, into $MgAl_2O_4$. The formation of $MgAl_2O_4$ reduced nickel incorporation with the support material

since $MgAl_2O_4$ does not react with Ni; therefore, nickel was retained in its active form. In addition, incorporation of Mg and Al in to $MgAl_2O_4$, a slight basic material, modified the acid-base properties resulting in a catalyst that exhibited moderate acidic and basic site strength and density compared to the pure oxide supported catalysts. Moderation of the acid-base properties improved the activity, selectivity, and stability of the catalysts by reducing activity for by-product reactions producing ethylene and acetaldehyde.

At lower reaction temperatures, below 823 K, Mg-Al mixed oxide supported nickel catalysts experienced substantial deactivation resulting in reduced ethanol conversion but interestingly, the H_2 and CO_2 yields increased, exceeding equilibrium expectations with time on stream while CH_4 yield decreased far below equilibrium expectations, suggesting a direct ethanol steam reforming reaction pathway. Over stabilized Mg-Al mixed oxide supported nickel catalysts, direct ethanol steam reforming was activated by a reduction in the catalyst's activity for the production and desorption of CH_4 from the surface.

The effect of pressure on the direct ethanol steam reforming reaction pathway over stabilized Mg-Al mixed oxide supported nickel catalysts was investigated at 673 and 823 K. At 823 K, increasing the total pressure resulted in a product distribution that closely matched the thermodynamic expectations. However, at 673 K, the product distribution deviated from thermodynamic expectations, giving substantially greater yields for the steam reforming products, H_2, CO, and CO_2, while CH_4 yield was consistently less than equilibrium expectations.

The identification of an alternative direct ethanol steam reforming reaction pathway at relatively low temperatures (below 823 K) that could be operated at elevated pressures will result in an energy efficient process for the production of hydrogen from bio-ethanol.

Acknowledgements

To start, I would like to thank my supervisors, Dr. Eric Croiset and Dr. Bob Hudgins, who showed great confidence in me, provided me with a great deal of support, and sent me to many conferences. To this group, Dr. Peter L. Silveston, should be added. Although he was not a member of the final defense committee, he contributed throughout this project. I would like to extend thanks to my review committee for trudging through this gargantuan document. They were:

Dr. Brant Peppley (Queens' University, Kingston ON)

Dr. Roydon Fraser (Department of Mechanical Engineering)

Dr. Flora Ng (Department of Chemical Engineering)

Dr. Michael Fowler (Department of Chemical Engineering)

The Department of Chemical Engineering staff, in particular Pat Anderson, Liz Bevan, and Ingrid Sherrer, were all very helpful and understanding of my tendency to do everything at the last possible moment. Thank you for you time and patience. I would also like to thank Ralph Dickhout, the Department's Analytical Technician, for helping me with many technical issues and trusting me with HF in his lab.

Throughout the thesis I used several characterization devices external to the Chemical Engineering Department. I would like to thank Mark Sobon of the Department of Civil Enegineering, Waste Water Treatment group, for training me on the ICP-AES for elemental analysis. I spent many hours using Dr. Linda Nazar's XRD unit. Thanks to Brian Ellis, Dr. Nazar's PhD student, I was able to generate useful data and interpret it meaningfully. I would also like to thank Brian for his assistance with the SEM

Two very good friends and colleagues, Dr. Bill Epling and, the recent Dr., Petr Chladek, were essential to the successful completion of this thesis. Petr, we made a great team in the lab, in the Grad House, and at many conferences. Bill, thank you so much for your time and

effort as my Interim PhD Advisor. Also, thanks for taking it upon yourself to take care of me at many conferences. It was much appreciated. Every time I am in Waterloo we must go for chicken wings. To you both, I hope our paths cross again.

Throughout my PhD studies I made many good friends at the University of Waterloo that have not already been mentioned: Mathew Scorah, Julie Scorah (Smythe), Will Ripmeester, Deb Sarzotti, Luigi D'Agnillo, Spencer Miniely, Nik Krpan, and Brian Barclay. As we have all learned, graduate school is only temporary, but the friends we make are not. We had many great times together and I am sure that they will continue in the future.

I would also like to thank my soccer team for helping with the stress … Go Lions!!!

Finally, I would like to acknowledge my best friend and wife, the recently dissertated, Dr. Julie Gauley. Julie, we met during our PhDs, we flourished through the ups and downs of grad school, and now I am excited to begin the rest of our lives together. Thank you for believing in me.

Table of Contents

List of Figures

List of Tables

Chapter 1
Introduction and Motivation

With unstable and rising petroleum and natural gas prices and the need for reduced greenhouse gas emissions, considerable attention has been focused on the development of clean, renewable fuels. Recently, biologically-derived feedstocks such as bio-diesel and bio-ethanol have received much attention because they can lessen the demand for and reliance upon non-renewable fuels and reduce total CO_2 emissions [Wu et al.(2006)]. In addition, bio-fuels can be produced from a wide variety of carbohydrate sources that can be obtained from dedicated agricultural products or agricultural and forestry by-products leading to raw material flexibility. The socio-economical effects of agriculture-based fuel raw materials are currently being explored. A major point of contention is the use of food based materials for fuels which would promote competitive pricing between foods and fuels resulting in substantially higher food, mainly cereals, costs. In addition, the ecological damage caused by increased erosion, and use of fertilizers and pesticides, and a potential loss of biodiversity due to monoculture raw materials are cited as concerns [Hill (2007)]. However, if a responsible approach is taken, such as only using agricultural and forestry waste streams, these adverse effects can be minimized.

A recent life cycle assessment for the production of ethanol from a lignocellulosic material, switch grass, [Cardona Alzate and Sanchez Toro (2004)] revealed that the resulting bio-ethanol had a positive net energy value of 17.65 - 18.93 MJ per L of ethanol, representing 55-59% of the lower heating value (LHV) of gasoline, and the process was essentially CO_2-neutral. Studies such as this highlight the future role of ethanol as an energy carrier and with worldwide ethanol production doubling from 2000 to 2005 and expected to increase by 6.5% in 2006 [Rass-Hansen et al. (2007)], its role as an energy carrier is being quickly defined.

1

Currently, ethanol is being used as a fuel additive to improve octane number and reduce the non-renewable content of vehicle fuels such as gasoline. To further the integration of renewable and non-renewable fuels, the use of hybrid fuels with renewable content is being supported by government agencies. For example, in 2005, the Province of Ontario mandated that all gasoline sold in the province contain a minimum of 5 vol% ethanol [http://www.e-laws.gov.on.ca/html/regs/english/elaws_regs_050535_e.htm]. Higher ethanol content fuels such as E85, which typically contains 70-85 vol% ethanol with the balance being gasoline, have been shown to reduce the use of non-renewable fuels by 66-93%, and reduce CO_2 and SO_x emissions by 82-87% and 39-43%, respectively [Wu et al. (2006)]. However, substantial quantities of water must be removed from bio-ethanol prior to blending with gasoline. Bio-ethanol contains approximately 12 vol% ethanol with the balance being mostly water [Akande et al. (2006)], but for use in blended fuels it must be near- or nearly anhydrous, < 1% water. This purification is typically achieved via distillation and adsorption which requires substantial energy investment.

The use of ethanol as a combustion fuel in an internal combustion engine, which converts chemical to thermal to mechanical energy, is limited by the Carnot cycle efficiency, which typically achieves overall efficiencies of approximately 25% [Schlapbach and Zuttel (2001)]. Fuel cells which convert chemical energy directly to electrical energy have substantially higher overall efficiencies, which is limited by the Nernst efficiency, of typically ranging between 50-60% [Schlapbach and Zuttel (2001), Song (2002), Rostrup-Nielsen (2001)], and therefore represent an alternative approach for the conversion of ethanol to energy. Fuel cells operate on high hydrogen content feeds usually in the form of highly-purified hydrogen for proton-exchange membrane fuel cells (PEM) or syngas for solid oxide fuel cells (SOFCs) and therefore the conversion of ethanol to hydrogen or syngas must also be considered in addition to the fuel cell efficiency.

Bio-ethanol is considered a prime candidate as a hydrogen carrier for fuel cell applications [Rostrup-Nielsen (2001)]. It is an easily transportable liquid at ambient

conditions, it is non-poisonous, and has a high hydrogen content (H/C = 3). The conversion of ethanol to hydrogen or syngas can be achieved by reacting ethanol with water via steam reforming,

$$CH_3CH_2OH + (1+x)H_2O \longrightarrow (4+x)H_2 + (2-x)CO + xCO_2 \qquad \text{(R.1)}$$

$$CH_3CH_2OH + H_2O \longrightarrow 4H_2 + 2CO \qquad \Delta H^{\circ}_{298\,K} = 255.72\,\frac{kJ}{mol} \qquad \text{(R.2)}$$

$$CO + H_2O \longrightarrow H_2 + CO_2 \qquad \Delta H^{\circ}_{298\,K} = -41.19\,\frac{kJ}{mol} \qquad \text{(R.3)}$$
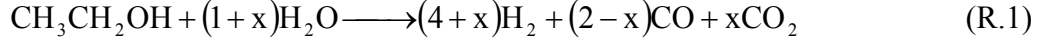
Ethanol steam reforming, described by (R.1), is a combination of reactions (R.2) and (R.3), which represents the contribution of the equilibrium limited water-gas shift reaction. The value of x in (R.1) is dependent upon temperature and water concentration in the feed and describes the extent of the water-gas shift reaction. Ideally, the ethanol steam reforming reaction can achieve a hydrogen yield of 6 moles of hydrogen per mole of ethanol when the value of x in (R.1) equals 2. The high theoretical H_2 yield makes ethanol steam reforming a very attractive route for H_2 production [Klouz et al. (2002); Fierro et al. (2002)]. The steam reforming of ethanol is an endothermic process ($\Delta H^{\circ}_{298\,K} = 173.33\,{kJ}/{mol}$ when x = 2) and coupled with the need to vaporize the high water content feed stream represents a major limitation of the steam reforming of bio-ethanol (Agrell et al. 2002). However, the energy required to vaporize the steam reforming feed would be the same as that required for the distillation of bio-ethanol. Therefore, only the endothermic heat of reaction should be considered a negative aspect of the steam reforming process.

Thermodynamic equilibrium studies have shown that ethanol steam reforming produces mixtures of H_2, CO, CO_2, and CH_4 below 950 K, while above 950 K the ethanol steam reforming reaction (R.1) adequately describes the product composition [Garcia and Laborde (1991); Vasudeva et al. (1996); Fishtik et al. (2000)]. Pressure has been shown to negatively affect hydrogen yield, favoring the formation of CH_4 but can be offset by

increasing the temperature [Garcia and Laborde (1991)]. The results of these studies indicated that the steam reforming of ethanol was a viable H_2 production method and have thus sparked interest in the development of catalytic processes which efficiently and effectively produce hydrogen.

Steam reforming of ethanol has been investigated over a wide variety of supported metal catalysts and several reviews on the subject have recently been published [Haryanto et al. (2005); Vaidya and Rodrigues (2006)]. Supported nickel catalysts have shown good ethanol steam reforming activity and high steam reforming product selectivity (H_2 and CO_x), but have been found to deactivate by coking, sintering, and phase transformations [Sun et al. (2005)]. The physical and chemical properties of the catalyst support material have been found to significantly contribute to the activity, selectivity, and stability of the supported nickel catalysts [Fatsikostas et al. (2002)]. γ-Al_2O_3, an acidic support, catalyzes the dehydration of ethanol producing ethylene, a known coking precursor [Fatsikostas et al. (2002); Freni et al. (2002, 2003)]. MgO supported nickel catalysts, MgO being a basic support, have shown reduced deactivation by coking compared to γ-Al_2O_3 supported catalysts [Fatsikostas et al. (2002)], however, were found to have enhanced rates of deactivation by nickel crystallite sintering [Freni et al. (2002); Frusteri et al. (2004)] and suffer from sintering-like effects such as loss of surface area [Schaper et al. (1989)] and significant shrinkage of the pore diameter [Stobbe et al. (1991)].

As an extension, the combination of Mg and Al into a mixed oxide phase derived from hydrotalcite–like precursors has been found to result in a high surface area and exhibits both acidic and basic properties that are of moderate density and strength compared to the pure oxides, MgO and γ-Al_2O_3. In addition, the mixed oxide phase-supported samples demonstrated improved stability in the presence of steam compared to MgO [Schaper et al. (1989)]. As a support for transition metal catalysts, Mg-Al mixed oxides have been studied for methane steam reforming [Djaidja et al. (2006)], methane partial oxidation [Basile et al. (1998,2003) ; Lee and Lee (2002); Villa et al. (2003)], methane dry reforming [Guo et al.

(2004)], and propane oxidative dehydrogenation [Sloczynski et al. (1999)]. Mg-Al mixed oxide supports were found to outperform pure oxide supported catalysts in terms of activity and stability due to improved nickel crystallite stability, reduced Ni phase transformation to $NiAl_2O_4$, and reduced carbon formation.

Research Objectives

The overall objective of this thesis was the identification of a supported nickel catalyst that delivered stable performance for the steam reforming of ethanol. It is proposed that the stabilizing effects of Mg-Al mixed oxide supports will improve the stability and lifetime of supported nickel catalysts compared to the pure oxide supports, MgO and γ-Al_2O_3. In addition, it is proposed that H_2 yield can be substantially improved at low temperatures by reducing the nickel catalysts activity for the CH_4 producing reactions. As a result, the steam reforming of ethanol could be performed at elevated pressures without the adverse effect of increased CH_4 yield and considerable energy saving could be realized.

The specific, key objectives of this thesis were:

1) To evaluate the performance of Mg-Al mixed oxide supported nickel catalysts for the production of hydrogen via ethanol steam reforming and to relate performance to physical and chemical properties of the catalyst.

2) To examine the effect of reaction variables on catalyst activity, selectivity, and stability.

3) To further the understanding of the ethanol steam reforming reaction network over supported nickel catalysts.

4) To investigate the effect of pressure on the ethanol steam reforming reaction.

Chapter 2

Background Material and Literature Review

This chapter provides standard background material and a survey of the pertinent research literature for the development of ethanol steam reforming catalysts.

2.1 Thermodynamic studies of the ethanol-water system

Thermodynamic analysis of reaction systems is performed to improve the understanding of the viability of reaction-product model systems and develop relationships between process variables (i.e., temperature, pressure, and feed composition) and the product distribution. Two analytical techniques are typically applied: Gibbs' free energy minimization and equilibrium constant. Both techniques have their pros and cons. For example, the Gibbs' free energy minimization technique determines the equilibrium composition based on a defined set of product species and is therefore independent of reaction pathways. This technique essentially assumes that an infinite number of reaction pathways are viable at all conditions, which in many cases does not adequately describe the reaction system being investigated. The equilibrium constant technique differs in that it requires prior knowledge of the complete reaction network and therefore intimate knowledge of the reaction system is necessary, which is typically not known when a project is being started. In this study, the Gibbs' free energy minimization technique was used to estimate product compositions.

Thermodynamic studies using both techniques have been performed for the ethanol-water chemical system [Garcia and Laborde (1991); Vasudeva et al. (1996); Fishtik et al. (2000); Ioannides (2001)] to determine the effect of process variables, specifically temperature, pressure, and water-to-ethanol feed ratio on product yield and distribution and likelihood of carbon formation [Garcia and Laborde (1991); Vasudeva et al. (1996)]. In all studies, H_2, CO, CO_2, CH_4, and H_2O were the only thermodynamically viable species even

though reaction products such as acetaldehyde, ethylene, acetic acid, and diethyl ether have been found in experimental studies. In fact, in all studies ethanol was predicted to be completely consumed even at temperatures as low as 300 K.

2.1.1 Effect of temperature

The effect of temperature on the composition of the ethanol-water chemical system at atmospheric pressure and a H_2O:EtOH feed ratio of 8.4:1 is given graphically in Figure 2.1. The results presented in Figure 2.1 to Figure 2.3 were generated using the Gibbs' equilibrium reactor utility in Aspen 12.1. At low reaction temperatures, below 650 K, the product composition is dominated by CH_4 and CO_2, while at high temperatures, above 850 K, the product gas is comprised of H_2, CO, and CO_2. The predicted equilibrium composition at low temperatures suggests that ethanol is consumed via (R.4)

$$CH_3CH_2OH \longrightarrow \frac{3}{2}CH_4 + \frac{1}{2}CO_2 \qquad \text{(R.4)}$$
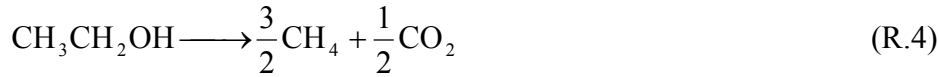
whereas at high temperatures the ethanol steam reforming reaction as defined in (R.1), adequately describes the reaction network

$$CH_3CH_2OH + (1+x)H_2O \longrightarrow (4+x)H_2 + (2-x)CO + xCO_2 \qquad \text{(R.1)}$$
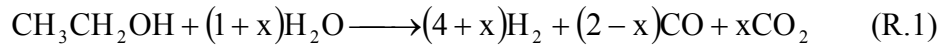
where x represents the contribution of the water gas-shift reaction (R.3). The transition in product gas composition from low temperatures (R.4) to high temperature (R.1) is explained by the author as an increase in the steam reforming of CH_4 via (R.5),

$$CH_4 + (1+y)H_2O \longrightarrow (3+y)H_2 + (1-y)CO + yCO_2 \qquad \text{(R.5)}$$

8
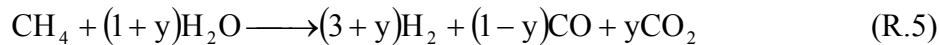
where y corresponds to the contribution of the water-gas shift reaction (R.3). The similarity between the right hand side of (R.5) and (R.1) should be noted. H_2 yield increases with increasing temperature and is matched with a decrease in CH_4 yield. The contribution of the water-gas shift reaction (R.3) to the product composition is noted by an increase in CO_2 yield for temperatures below 800 K, while the role of the reverse water gas shift reaction is exhibited by an increase in CO yield for temperatures above 950 K with equimolar reduction in H_2 and CO_2.

$$CO + H_2O \longrightarrow H_2 + CO_2 \qquad\qquad (R.3)$$

The temperature dependence of the thermodynamically predicted equilibrium compositions for the ethanol-water system suggests that ethanol steam reforming can be simply regarded as a methane steam reforming/water-gas shift reaction system.
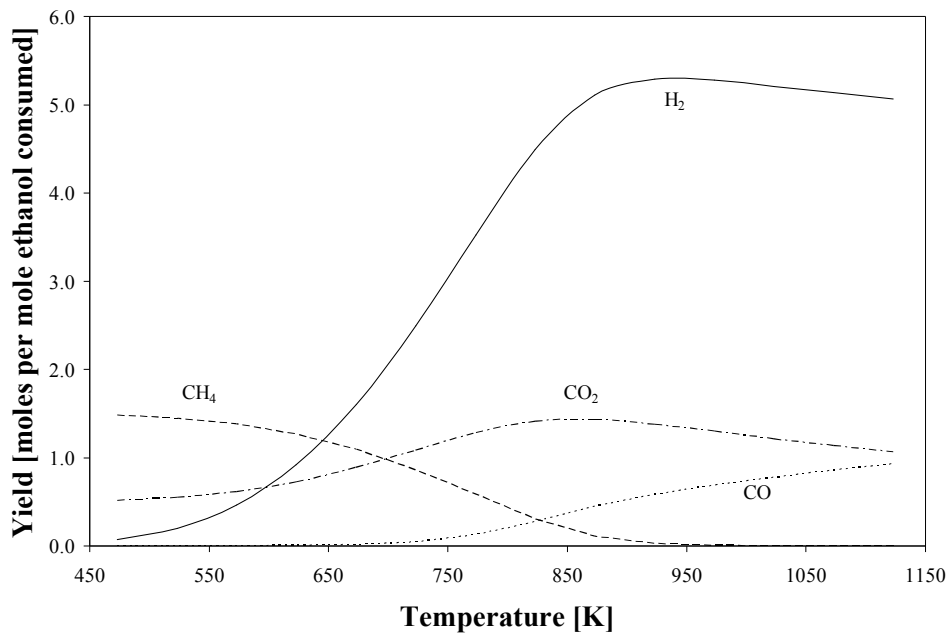
Figure 2.1: Effect of temperature on the equilibrium composition of the ethanol-water system. Atmospheric pressure and H_2O:EtOH = 8.4:1, obtained by the minimization of Gibbs' free energy method. Plot was generated using Aspen 12.1.

2.1.2 Effect of pressure

Increasing the total pressure of the ethanol-water system has been found to decrease selectivity for the steam reforming products, H_2, CO, and CO_2 favoring CH_4 [Garcia and Laborde (1991)]. The effect of pressure as a function of temperature on H_2 and CH_4 yields is presented in Figure 2.2. The ethanol steam reforming reaction (R.1) having a positive change in molar yield is thermodynamically favored at low pressures. The direct relationship between H_2 and CH_4 yields with increasing pressure and temperature suggest that the reduction in H_2 yield that the author related to reduced thermodynamic favorability for the methane steam reforming reaction (R.5). The detrimental effects of increasing pressure are most prominent at low pressures (1 to 5 atm) and increases above 5 atm affect H_2 yield less significantly. One option for offsetting the negative effects of pressure on H_2 yield would be to increase the temperature. For example, at atmospheric pressure a H_2 yield of 5.0 can be achieved at approximately 860 K while to maintain the same H_2 yield at 10 atm the corresponding temperature would be approximately 1123 K.
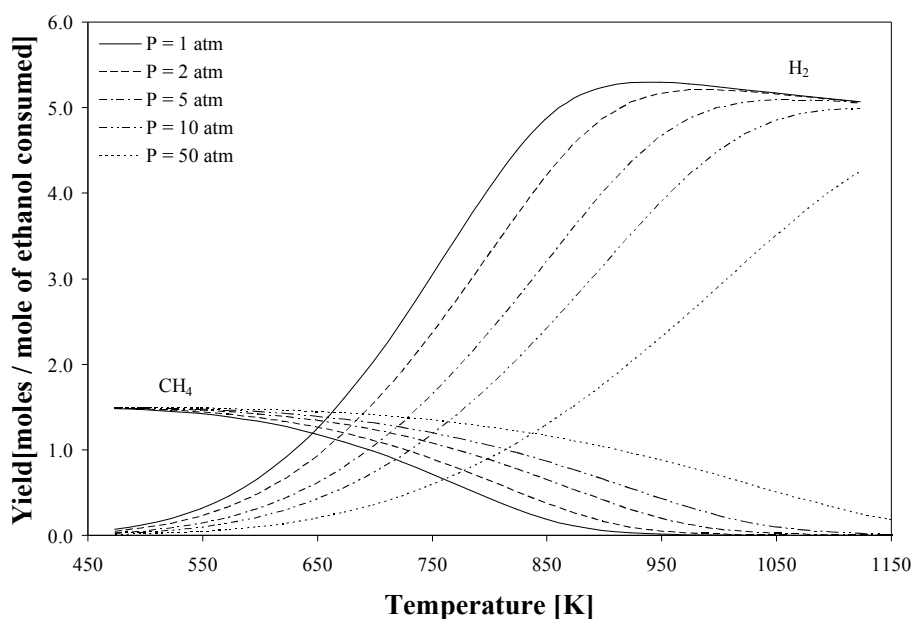
Figure 2.2:   Effect of pressure on H_2 and CH_4 product yields as a function temperature for a H_2O:EtOH molar feed ratio of 8.4:1, obtained by the minimization of Gibbs' free energy method. Plot was generated using Aspen 12.1.

2.1.3 Effect of H₂O:ethanol molar feed ratio

Increasing the amount of water in the ethanol-water feed mixture was found to have a significant, positive effect on H_2 production [Garcia and Laborde (1991); Vasudeva et al. (1996); Fishtik et al. (2000)]. The effect of the H_2O:EtOH molar feed ratio on the product distribution is presented in Figure 2.3 for H_2O:EtOH molar feed ratios of 8.4:1 and 3:1 (stoichiometric).
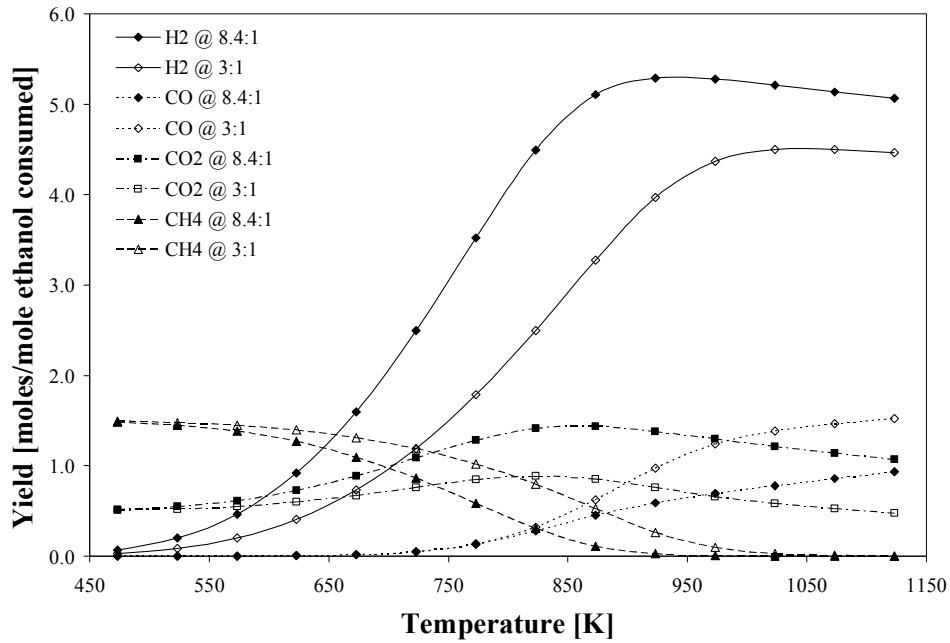
Figure 2.3:   Effect of H_2O:EtOH molar feed ratio on product yield and distribution as a function of temperature at atmospheric pressure for H_2O:EtOH = 8.4:1 (filled data points) and H_2O:EtOH = 3:1 (hollow data points), obtained by the Gibbs' free energy minimization method. Plot was generated using Aspen 12.1.

H_2 yield improves significantly with greater than stoichiometric amounts of water. Fishtik et al. (2000) stated that an increase in the H_2O:EtOH ratio can only lead to an increase in the production of H_2. As the water content increased, the equilibrium was forced in the direction of the steam reforming products, H_2, CO, and CO_2 at the expense of reduced CH_4 yield. The contribution of the water-gas shift reaction to the product composition is again

realized by noting an increase in CO_2 yield at high temperatures for the 8.4:1 feed ratio. The H_2O:EtOH feed ratio had a similar but opposite effect on the H_2 yield as pressure, suggesting that increasing the water composition of the ethanol-water feed mixture can counteract the detrimental effects of pressure.

2.1.4 Carbon formation

Garcia and Laborde (1991) and Vasudeva et al. (1996) identified regions of operation (temperature, pressure, and H_2O:EtOH feed ratio) that were favorable for the formation of elemental carbon. In both cases the CO disproportionation reaction (R.6), also known as the Boudouard reaction, was the most likely reaction pathway leading to the formation of carbon, since it had the lowest Gibbs' free energy of the carbon forming reactions considered.

$$2CO \longrightarrow CO_2 + C \qquad\qquad\qquad (R.6)$$

The formation of elemental carbon via (R.6) was favorable at low temperatures, low pressures, and low H_2O:EtOH feed ratios. A minimum H_2O:EtOH molar feed ratio of 2:1 [Garcia and Laborde (1991)] was suggested to avoid carbon formation at essentially all conditions; however, substantially higher feed ratios were recommended. Increasing the water content reduces the likelihood of carbon deposition and, as discussed above, also improves steam reforming product yield, but at the cost of reduced energy efficiency. Ioannides (2001) found that implementing a H_2O:EtOH feed ratio greater than the stoichiometric requirement of 3:1 was not beneficial in terms of energy efficiency due to the additional energy required to vaporize the excess water. Increasing the H_2O:EtOH feed ratio above 3:1 led to improved H_2 yields but the additional energy required to vaporize the excess water outweighed the gains in H_2 generation. However, the detrimental effect of carbon deposition on catalyst performance and lifetime were not accounted for in the energy efficiency analysis.

2.1.5 General comments on the thermodynamics for the steam reforming of ethanol

The results of the thermodynamic studies indicate that the steam reforming of ethanol is a viable H_2 production method and have thus sparked interest in the development of catalytic processes that efficiently and effectively produce H_2. Applying the knowledge obtained from these studies, two approaches to catalyst development can be taken. The first approach would be the development of a catalyst that performs well at high temperatures and is capable of achieving equilibrium-predicted product yields, which would result in high H_2 productivity. The second approach would be the development of a catalyst that is not active for the production of CH_4. At low temperatures, CH_4 is the most thermodynamically favorable species. The development a catalyst that was not active for the formation of CH_4 would result in improved H_2 yields at lower temperatures and eliminate or moderate the adverse effects of increasing pressure on H_2 yield.

2.2 Ethanol steam reforming catalysts

The steam reforming of ethanol has been investigated over a wide variety of supported metal catalysts and several reviews on the subject have recently been published [Haryanto et al. (2005); Vaidya and Rodrigues (2006)]. The activity, product distribution, and catalyst stability have been found to be dependent upon the catalyst composition, support material, catalyst preparation and pretreatment technique, and reaction conditions such as reaction temperature, H_2O:EtOH ratio, and residence time. The following discussion will focus on these parameters.

2.2.1 Catalyst composition

2.2.1.1 Copper

Copper catalysts have been studied under ethanol steam reforming conditions and have displayed activity at temperatures as low as 573 K, producing mainly H_2 and acetaldehyde [Mariño et al. (1998, 2001); Velu et al. (2002)]. By-products such as acetic

acid, diethyl ether, and ethylene were reported, but generally make up only a small portion of the products. Over copper catalysts, ethanol has been found to dehydrogenate to H_2 and acetaldehyde via the ethanol dehydration reaction (R.7).

$$CH_3CH_2OH \longrightarrow CH_3CHO + H_2 \qquad\qquad (R.7)$$

The dehydrogenation of ethanol is endothermic and thermodynamically favorable at temperatures above 600 K. Copper and/or copper-zinc catalysts have been thoroughly investigated for methanol steam reforming [Agrell et al. (2002)], but are not widely used for ethanol steam reforming due to copper's inability to catalyze the cleavage of the C-C bond and thus the reduction of C_2- to C_1-species [Mariño et al. (1998, 2001)]. However, copper catalysts are able to produce very high-purity H_2 since acetaldehyde can be condensed (b.p.21°C) yielding a pure H_2 gas product. A major disadvantage of this process is the low H_2 yield of one compared to six for the steam reforming reaction.

To improve the steam reforming activity of copper-containing catalysts, copper-nickel (Cu-Ni) bimetallic catalysts were investigated. Nickel was selected due to its ability to promote C-C bond scission decomposing C_2- to C_1-species [Mariño et al. (1998, 2001); Velu et al. (2002)]. The rationale for developing Cu-Ni catalysts was that the bimetallic catalyst would achieve higher H_2 yields since nickel could decompose acetaldehyde produced on copper sites. The addition of nickel was found to increase ethanol conversion and improve the total molar yield. Acetaldehyde was found to decompose via reaction (R.8).

$$CH_3CHO \longrightarrow CH_4 + CO \qquad\qquad (R.8)$$

Mariño et al. (1998, 2001) using a Cu-Ni/K-Al$_2$O$_3$ catalyst found that the concentrations of CH_4 and CO in the product stream were approximately equal suggesting that they were formed by the acetaldehyde decomposition (R.8). This fact coupled with the

14

absence of CO_2 signified that the water-gas shift reaction (R.3) contributed very little to the overall reaction. Therefore, no additional H_2 was produced.
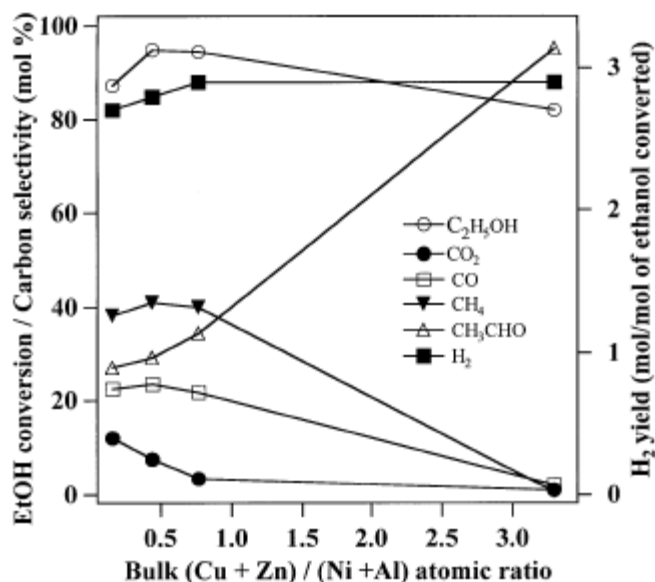
Figure 2.4: Effect of (Cu+Zn)/(Ni+Al) atomic ratio on the catalytic performance of CuNiZnAl mixed oxide catalysts at 573 K. The ratio (Cu+Zn)/(Ni+Al) can be interpreted as Cu/Ni for this study since the atomic ratio of Zn/Al remained relatively constant for all experiments at 0.8/1. Velu et al. (2002).

Using a Cu-Ni/Zn-Al catalyst, Velu et al. (2002) found that the addition of nickel to copper-zinc catalysts did not influence the conversion of ethanol, but had a significant effect on the product distribution, as shown in Figure 2.4. At low nickel contents (high values on the x-axis), the selectivity towards acetaldehyde was very high. As the nickel content increased (moving from right to left), acetaldehyde selectivity decreased and selectivity for the decomposition products, CH_4 and CO, increased. Unlike the findings of Mariño et al. (1998, 2001), activity for the water-gas shift reaction (R.3) was noted by the presence of CO_2 which increased with the Ni content of the catalyst. They proposed that copper was

responsible for the adsorption and subsequent dehydrogenation of ethanol to acetaldehyde and H_2 via (R.7) and nickel, being capable of C-C bond scission, decomposed the C_2-species, ethanol and acetaldehyde, to C_1 species.

One observation that should be brought to the reader's attention is that both studies were performed at a relatively low temperature of 573 K. Considering the equilibrium product yield at 573 K (see Figure 2.1), the experimentally obtained H_2 yield of one closely matched the equilibrium predicted value. The product distribution for the Cu-Ni catalyst system deviated from equilibrium as exhibited by a high acetaldehyde yield even with high ethanol conversion and the CH_4 yield, which ws affected by the acetaldehyde yield, was less than one. Cu-Ni bimetallic catalysts, especially at 573 K, although highly active for converting ethanol to acetaldehyde, were not active for the ethanol steam reforming reaction (R.1). The conversion of acetaldehyde proceeds via the decomposition reaction (R.8) producing CH_4 and CO. Discrepancy between the research groups over the activity of the water-gas shift reaction on Cu-Ni bimetallic catalysts might indicate the role that the support material, the difference between the two catalysts was that the Velu et al. (2002) study incorporated ZnO, can have on viable reaction pathways and product selectivity of the catalysts. The conversion of acetaldehyde to steam reforming products was hindered by the inability of the catalysts to convert CH_4 into steam reforming products.

2.2.1.2 Cobalt

Supported cobalt catalysts have been studied for the ethanol steam reforming reaction by several research groups [Haga et al. (1997b); Cavallaro et al. (2001); Llorca et al. (2002, 2003); Batista et al. (2003); Freni et al. (2003); Sahoo et al. (2007)]. Cobalt was originally evaluated for the ethanol steam reforming reaction by Haga et al. (1997a). In that original study, the activity and product selectivity of many transition metals (Ti, Zr, Cr, Mn, Fe, Co, Ni, Cu, Zn, Cd, Sb, Ru, Pt, and Rh) supported on γ-Al_2O_3 were evaluated for the steam reforming of ethanol at 673 K. Co/γ-Al_2O_3 was identified as the most active catalyst achieving complete ethanol conversion and a H_2 yield of 3.75, which is significantly above

16

the equilibrium expectation. In addition, the γ-Al_2O_3 supported cobalt catalyst was found to have the highest CO_x/C-product yield ratio suggesting that cobalt preferentially catalyzes the ethanol steam reforming reaction (R.1). CH_4 was the only by-product of the reaction and its yield was 0.4, which is substantially less than equilibrium predictions. They concluded that the selectivity for the steam reforming reaction followed Co>>Ni>Rh>Pt, Ru, Cu. Haga et al. (1997b) continued the survey by investigating the steam reforming of ethanol over cobalt catalysts with different supports. The effect of γ-Al_2O_3, SiO_2, ZrO_2, MgO, and activated carbon (C) on the performance of cobalt as a catalyst was evaluated. They found that the product composition for each catalyst varied suggesting that the support material played a significant role in the reaction. A more detailed discussion of the effect of the support on the ethanol steam reforming reaction can be found in section 2.2.2.

To elucidate the contributing reaction pathways that occurred during ethanol steam reforming on cobalt, Haga et al. (1997b) conducted reaction product co-feed experiments. Co-feed experiments were performed by mixing the reaction product CO with the water-ethanol feed mixture before entering the reactor. Over Co/γ-Al_2O_3, co-feeding CO with the water-ethanol feed mixture resulted in a significant increase in CO_2 yield, while only a marginal increase in CH_4 yield was detected. CO_2 and CH_4 yields returned to their initial steady-state values upon removal of CO from the feed mixture. The authors concluded that these results indicated the presence of the water-gas shift reaction (R.3), and a small contribution from the reverse CH_4 steam reforming (CO methanation) reaction (R.5). The effect of CO co-feed on ethanol conversion was not reported.

$$CO + H_2O \longrightarrow H_2 + CO_2 \qquad\qquad\qquad (R.3)$$

$$CO + 3H_2 \longrightarrow CH_4 + H_2O \qquad\qquad\qquad (R.5)$$

In a very similar study, Batista et al. (2003) investigated the contribution of the CO methanation reaction (R.5) to the production of CH_4 in the ethanol steam reforming reaction network and concluded that over Co/γ-Al_2O_3 the CO methanation reaction contributed

17

insignificantly to the formation of CH_4. They attributed CH_4 yield solely to the ethanol/acetaldehyde decomposition reaction (R.8).

The Freni group [Frusetri et al. (2004); Freni et al. (2003)] conducted a comparative study on the activity, product selectivity, and stability of MgO-supported nickel and cobalt catalysts for the ethanol steam reforming reaction at 923 K for use in molten carbonate fuel cell applications. Cobalt catalysts generally exhibited lower ethanol conversion and H_2 yields than the nickel catalysts and the rate of catalyst deactivation experienced by the cobalt catalysts was much higher. Acetaldehyde was produced by both catalysts, but as time on stream progressed, the acetaldehyde selectivity for the cobalt catalysts increased and reached 100% after only a few hours of operation. The rate of carbon formation was measured using a CHONS (Carbon, Hydrogen, Oxygen, Nitrogen, Sulfur)-elemental analyzer and it was found that both catalysts experienced approximately the same amount of carbon deposition, therefore the greater rate of deactivation experienced by the Co catalyst could not be attributed to the formation of carbon on the catalyst surface. The Co/MgO catalyst was found to be active only for the ethanol dehydrogenation reaction. The deactivation of the cobalt-supported catalyst was attributed to the oxidation of the Co metal in the presence of large quantities of water to CoO (Co^{2+}). The metallic form, Co^0, catalyzes the steam reforming reaction (R.1) while the oxide form, Co^{2+}, catalyzes the dehydrogenation reaction (R.7).

Studies reporting on the activity of cobalt catalysts for the steam reforming of ethanol revealed that it was possible to substantially reduce CH_4 yields at low temperatures by reducing or eliminating the CH_4 forming reactions, for example the CO methanation reaction (R.5). In addition, they found that Co catalysts were easily oxidized under steam reforming conditions which adversely affected activity for the steam reforming reaction, resulting in the formation of a catalyst that was highly active and selective for the dehydrogenation of ethanol (R.7).

2.2.1.3 Precious metals

Haga at al. (1997a) reported that rhodium (Rh) was the most active and selective of the precious metals for the ethanol steam reforming reaction under relatively mild reaction conditions (673 K, 1 atm, H_2O:EtOH = 8.4). Breen et al. (2002) and Liguras et al. (2003) investigated the performance of platinum (Pt), palladium (Pd), and Rh supported on γ-Al_2O_3 for the steam reforming of ethanol at more extreme reaction temperatures (700 – 1123 K). On γ-Al_2O_3, Rh was found to be the only precious metal capable of converting ethanol. Pt and Pd gave ethanol conversions similar to the γ-Al_2O_3 support alone suggesting that they were completely inactive for ethanol-water reactions.

The Freni group [Cavallaro et al. (2003a,b); Freni et al. (2001)] explored the use of a 5%Rh/γ-Al_2O_3 catalyst for the steam reforming of ethanol. For temperatures below 734 K, ethanol conversion was low and the dominant reaction was the ethanol decomposition reaction (R.9) producing CH_4, CO, and H_2.

$$CH_3CH_2OH \longrightarrow CH_4 + CO + H_2 \qquad\qquad (R.9)$$
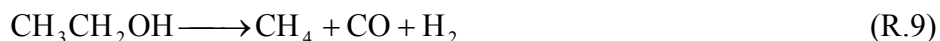
The authors suggested that the dehydrogenation of ethanol to a surface ethoxide group, which rapidly decomposed to form CO and CH_4 without subsequent desorption of acetaldehyde, adequately described the reaction mechanism since only very small amounts of acetaldehyde were detected in the product gas stream. Unlike the non-precious metals which have been shown to be active for the production/desorption of acetaldehyde, Rh was found to be highly active for this the decomposition of the ethoxide surface intermediate. For temperatures between 734 and 923 K, the selectivity of CO and CH_4 decreased and CO_2 increased as well as the H_2 yield and water consumption. These observations indicated that steam reforming became the dominant reaction pathway in this temperature range. However, it was not ascertained whether ethanol, acetaldehyde, or CH_4 was the predominantly steam reformed species. Above 850 K, it was proposed that CH_4 was consumed via the methane steam reforming reaction (R.5), which coupled with the ethanol steam reforming and water-

gas shift reactions aided in the production of H_2. At 923 K, the product gas consisted of 69.2% H_2, 17.25% CO_2, 9.64% CO, and 3.88% CH_4, which closely approached the equilibrium composition. To investigate the ethanol steam reforming reaction pathway over a Rh/γ-Al_2O_3, Cavallaro et al. (2003b) adjusted the gas hourly space velocity (GHSV) by changing the amount of catalyst loaded. At low GHSVs (large amount of catalyst), ethanol conversion was complete and as the GHSV increased (lower amounts of catalyst) the conversion decreased. The selectivity for by-products, CO, CH_4, and acetaldehyde, increased with increasing GHSV. As expected, CO_2 selectivity and H_2 yield decreased with increasing selectivity for by-product formation. This study identified that H_2 and CO_2 were secondary reaction products produced from reactions between water and the primary reaction products CH_4, CO, and acetaldehyde, not directly from ethanol.

Rh/γ-Al_2O_3 catalysts, although highly active and selective for the production of H_2 via the steam reforming of ethanol, especially at 923 K, have not shown adequate stability. Precious metals supported on γ-Al_2O_3 suffer from rapid deactivation due to carbon deposition on the catalyst surface, which is related to the support catalyzed formation of ethylene, a known carbon deposition precursor. Rh was determined to be the most active of the precious metals, but only at high temperatures. Recently, interest in precious metals has been renewed by the utilization of unconventional support materials such as CeO_2 (ceria) and ZrO_2 (zirconia).

The benefits of CeO_2-ZrO_2 as a support material for the steam reforming of ethanol was realized by Breen et al. (2002) who found that in addition to Rh, Pt and Pd catalysts also were highly active for the conversion of ethanol and gave high selectivity to the steam reforming products H_2, CO, and CO_2. Similar results were obtained by Diagne et al. (2002). CeO_2-ZrO_2 supported precious metal catalysts were found to be highly active for the ethanol steam reforming reaction (R.1) at relatively low reaction temperatures of 673 and 723 K giving H_2 and CO_2 yields of 5 to 5.7 and 1.5 to 1.8 respectively. These are very close to the stoichiometric values of the global ethanol steam reforming reaction (R.1), but are

substantially greater than equilibrium predicted values suggesting that a direct ethanol steam reforming reaction pathway exists.

Recent studies on a Rh/CeO_2-ZrO_2 catalyst for the steam reforming of ethanol performed at Pacific Northwest National Laboratory [Roh et al. (2006a, b)] revealed that the ethanol steam reforming reaction (R.1) was active at very low reaction temperatures producing H_2 and CO_2 yields substantially above equilibrium predictions. They proposed that the Rh/CeO_2-ZrO_2 catalyst favored H_2 over CH_4 formation at low reaction temperatures. However, the performance was not stable and small amounts of carbon deposits were found on the catalyst surface. Increasing ethylene yield was found to coincide with the loss in activity suggesting it was responsible for carbon deposition and catalyst deactivation.

2.2.1.4 Nickel

Nickel-based catalysts have received much attention for the production of H_2 by the steam reforming of ethanol due to their use in many hydrocarbon steam reforming applications [Rostrup-Nielsen (2001)]. In addition, compared to precious metals, nickel is very abundant and relatively inexpensive. The performance of supported nickel catalysts for the production of H_2 from the steam reforming of ethanol has been the focus of many investigations with mixed results being reported [Haryanto et al. (2005); Vaidya and Rodrigues (2006)]. Supported nickel catalysts are not active for ethanol-water reactions at low temperatures. The conversion of ethanol at 573 K has been found to be less than 5% over several supported nickel catalysts [Mariño et al. (1998, 2001); Fatsikostas et al. (2002); Fatsikostas and Verykios (2004)]. However, at temperatures of 923 K and above, supported nickel catalysts have been found to be very efficient for the conversion of ethanol to the steam reforming products (H_2, CO, and CO_2) [Freni et al. (2002, 2003); Frusetri et al. (2004); Fatsikostas and Verykios (2004); Benito et al. (2005); Yang et al. (2006)] with product yields achieving near equilibrium values.

Using a temperature programmed reaction technique, the ethanol steam reforming reaction pathways over Ni/La$_2$O$_3$ [Fatsikostas et al. (2002)] and Ni/La$_2$O$_3$-Al$_2$O$_3$ [Fatsikostas and Verykios (2004)] were investigated as a function of temperature. At 573 K, ethanol conversion was very low (<5%) and the primary products were acetaldehyde, H$_2$, and trace amounts of CH$_4$ indicating that at this temperature, supported nickel catalysts have activity for the ethanol dehydrogenation reaction (R.7) and little activity for the ethanol and acetaldehyde decomposition reactions (R.9 and R.8 respectively). As the temperature was increased, acetaldehyde yield decreased until it was no longer present in the product gas, which occurred at approximately 823 K. The H$_2$ yield increased from approximately one at 573 K to approximately 5.7 at 973 K and above.

A proposed ethanol steam reforming reaction pathway over supported nickel catalysts [Mariño et al. (1998, 2001); Freni et al (2002, 2003); Fatsikostas et al. (2002); Fatsikostas and Verykios (2004)] proceeds through the dehydrogenation of ethanol to acetaldehyde via (R.7). Acetaldehyde is subsequently decomposed (R.8) or steam reformed (R.10) producing a mixture of CH$_4$, CO, and H$_2$.

$$CH_3CH_2OH \longrightarrow CH_3CHO + H_2 \qquad\qquad (R.7)$$

$$CH_3CHO \longrightarrow CH_4 + CO \qquad\qquad (R.8)$$

$$CH_3CHO + H_2O \longrightarrow 3H_2 + 2CO \qquad\qquad (R.10)$$
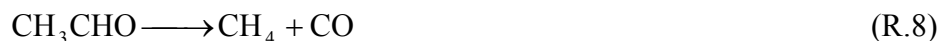
H$_2$ and CO$_2$ are then formed as secondary reaction products by CH$_4$ steam reforming via (R.5) and CO by the water-gas shift reaction (R.3), which is a highly equilibrium limited reaction. The effect of the water-gas shift reaction equilibrium limitation on the H$_2$, CO, CO$_2$ product distribution is exhibited by the rise in CO with a concomitant CO$_2$ decrease in the absence of other carbonaceous species such as CH$_4$ (see temperatures above 850 K in Figure 2.1).

$$CH_4 + H_2O \longrightarrow 3H_2 + CO \qquad\qquad (R.5)$$

$$CO + H_2O \longrightarrow H_2 + CO_2 \qquad\qquad (R.3)$$

2.2.1.4.1 Deactivation of supported nickel catalysts

Supported nickel catalysts have shown good activity and product selectivity (H_2, CO, and CO_2) for the steam reforming of ethanol, but have been found to deactivate by coking, sintering, and phase transformations [Sun et al. (2005)]. Several informative reviews on catalyst deactivation have been written addressing the topics of poisoning, sintering, carbon deposition, phase transformation, and pore blocking [Forzatti and Lietti (1999); Bartholomew (2001)]. Sulfur poisoning of Ni-based steam reforming catalysts is of significant industrial relevance since many of the hydrocarbon-based feedstocks contain H_2S or other organosulfur compounds. However, sulfur poisoning is of very little importance for the steam reforming of biologically derived ethanol [Akande et al. (2006)].

Supported nickel catalysts typically experience crystallite sintering under steam reforming conditions; high temperatures and highly reducing environments [Sehested et al. (2006)]. Sintering generally refers to the loss of surface area due to the agglomeration of small particles into larger particles resulting in lower surface-to-volume ratios and therefore a reduction in the active surface area of the catalyst [Sehested et al. (2004)]. Freni et al. (2003) and Frusteri et al. (2004) found that under ethanol steam reforming conditions at 923 K, Ni/MgO catalysts experienced significant nickel crystallite sintering. Frusteri et al. (2004) reported that the nickel crystallite size increased from 72.2 to 197 Å over a 20 h period and resulted in a decline in ethanol conversion from approximately 80% to 45%, but with no affect on product distribution. Alkaline doping of the MgO support with potassium (K), sodium (Na), and lithium (Li) were found to reduce the rates of nickel sintering and improve the stability of the Ni/MgO catalyst.

The most significant and destructive deactivation mechanism that supported nickel catalysts experience under ethanol steam reforming conditions is coking, also known as carbon deposition. Carbon deposition on catalyst surfaces can take several forms: (1) encapsulating films comprised of polymer-like, highly unsaturated hydrocarbons of the form C_mH_n, (2) filamentous carbon also known as carbon nanotubes, and (3) pyrolytic carbon [Forzatti and Lietti (1999); Bartholomew (2001)]. Encapsulating films form a mono- or multi-layer of highly unsaturated hydrocarbon species (C_mH_n) over the entire surface of the metal crystallite blocking the gaseous reactants from the catalyst sites. The formation of encapsulating films occurs at relatively low temperatures, below 773 K, and generally results in the slow but progressive loss of catalytic activity [Forzatti and Lietti (1999); Bartholomew (2001)]. Filamentous carbon deposits are commonly formed on catalysts where the active metal has appreciable carbon solubility (i.e., nickel and iron). The growth of filamentous carbon structures occurs by a highly complex mechanism and is beyond the scope of this review; however, their effects on catalyst activity will be discussed. The formation of filamentous carbon deposits occurs at temperatures above 723 K and does not affect the activity of the catalyst until a critical point is surpassed [Forzatti and Lietti (1999); Bartholomew (2001)]. During the formation of filamentous carbon, catalyst activity is maintained since the carbon growth occurs only at the crystallite-support interface, which would not be utilized for the desired catalytic reaction. Filamentous carbon growth in the internal pore structure of the catalyst would eventually result in pore blockage, reducing reactant accessibility to active sites and ultimately lead to the disintegration of the catalyst particle. On the external surface of the catalyst particle, filamentous carbon growth results in substantial reduction of the interstitial spacing between catalyst particles, ultimately resulting in the intertwining of individual particles into large agglomerations and effectively reducing the porosity of the catalyst bed and increasing the pressure drop through the catalyst bed [Forzatti and Lietti (1999); Bartholomew (2001)]. The formation of pyrolytic carbon deposits is only significant for reactions were the H_2O-to-hydrocarbon ratio is very low and at temperatures above 873 K. These conditions are not commonly used in the steam reforming

of ethanol and therefore this type of carbon deposition will not be addressed; however, for more information please see Forzatti and Lietti (1999) or Bartholomew (2001).

Both encapsulating film and filamentous carbon deposits have been identified in catalysts studies of ethanol steam reforming. The rates of carbon deposition were found to be highest for acidic catalyst support materials. Nickel supported on γ-Al_2O_3 rapidly deactivated by carbon deposition because γ-Al_2O_3, an acidic support, catalyzes the dehydration of ethanol (R.11) producing ethylene, a known coking precursor [Fatsikostas et al. (2002), Freni et al. (2002, 2003)].

$$CH_3CH_2OH \longrightarrow C_2H_4 + H_2O \qquad \text{(R.11)}$$

Dybkjaer (1995) proposed that carbonaceous deposits were formed by the acidic site catalyzed polymeric dehydrogenation of ethylene via (R.12).

$$C_2H_4 \longrightarrow olefins \longrightarrow polymers \longrightarrow coke \qquad \text{(R.12)}$$

However, ethylene is not the only route to carbon deposition. Nickel supported on basic support materials such as MgO and La_2O_3, which essentially have no activity for the formation of ethylene, experienced carbon deposition, but at severely reduced rates compared to γ-Al_2O_3 [Freni et al. (2002, 2003); Fatsikostas et al. (2002); Fatsikostas and Verykios (2004); Frusteri et al. (2004)]. In addition to the polymeric dehydrogenation of ethylene, carbon deposits can be formed via the Boudouard reaction (R.6) and the CH_4 decomposition reaction (R.13).

$$2CO \longrightarrow CO_2 + C \qquad \text{(R.6)}$$
$$CH_4 \longrightarrow C + 2H_2 \qquad \text{(R.13)}$$

To identify the types of carbon deposits on the spent catalysts, transmission electron microscopy (TEM), scanning electron microscopy (SEM), and temperature programmed oxidation techniques have been employed. Fatsikostas and Verykios (2004) identified both encapsulating film and filamentous deposits on a spent Ni/La_2O_3-Al_2O_3 catalyst which was evaluated for the steam reforming of ethanol at 923 K. Similarly, Frusteri et al. (2004) identified both encapsulating film and filamentous deposits on a spent Ni/MgO catalyst evaluated for the steam reforming of ethanol at 923 K.

Ni supported catalysts can also experience deactivation by phase transformation. Under steam reforming reaction conditions, nickel has been found to be incorporated into the crystal structure of the support material. For example, nickel forms highly stable nickel aluminates ($NiAl_2O_4$) with γ-Al_2O_3 [Aupretre et al (2005); Djaidja et al. (2006)] and solid-solutions of NiO-MgO [Djaidja et al. (2006)] with MgO. These phase transformations can substantially reduce the activity of the supported nickel catalysts by converting active metallic nickel to a non-active nickel oxide. However, these phase transformations have also been found to improve resistance to carbon deposition [Lee and Lee (2002); Guo et al. (2004); Djaidja et al. (2006)] and reduce the rate of sintering due to enhanced metal-support interaction [Hou and Yashima (2004);Villa et al. (2003)].

Supported nickel catalysts can experience severe deactivation under ethanol steam reforming conditions with the deposition of filamentous carbon being the most destructive. If one recalls that the use of nickel is desirable due to its abundant availability and relative low cost, the most significant contribution to the development of an ethanol steam reforming process would be the identification of a stable supported nickel catalyst. The most common approach to stabilize the performance of supported nickel catalysts has been to identify suitable supports that reduce/eliminate carbon deposition, specifically filamentous carbon. The following section discusses the current state of the search for an adequate nickel support material for the steam reforming of ethanol.

2.2.2 Catalyst supports materials

The physical and chemical properties of support materials have been found to significantly contribute to the activity, selectivity, and stability of supported nickel catalysts for the steam reforming of ethanol. An ideal support material should have high surface area, high thermal and chemical stability, not negatively interact with the active metal, and not promote by-product reactions. γ-Al_2O_3 is a commonly used support material for steam reforming and oxidation catalysts due to its intrinsically high surface area, and high thermal and steaming stability. However, γ-Al_2O_3 is acidic in nature, having both Lewis and Brønsted acidity [Di Cosimo et al. (1998, 2000)]. In the presence of ethanol, γ-Al_2O_3 has been shown to be active for the dehydration reaction (R.11) producing ethylene. Ethylene is a known precursor for carbon deposition [Dybkjaer (1995)] leading to deactivation of the catalyst. Under ethanol steam reforming reaction conditions, nickel supported on γ-Al_2O_3 has been to found rapidly deactivate by carbon deposition [Fatsikostas et al. (2002); Freni et al. (2002, 2003)].

To increase catalyst stability, basic or neutral support materials such as MgO, ZrO_2, La_2O_3, and CeO_2 have been used successfully to eliminate or significantly reduce deactivation due to carbon formation. Basic or neutral support materials are not active in the ethanol dehydration reaction (R.11) and therefore generally deactivate via a carbon deposition mechanism at a much reduced rate. To minimize ethylene production and potentially coking, basic supports have been investigated. Marino et al. (1998, 2000) impregnated γ-Al_2O_3 with potassium to neutralize the acidic sites associated with γ-Al_2O_3, while others have focused on basic metal oxides such as MgO [Freni et al. (2000, 2002, 2003); Fatsikostas et al. (2002); Frusteri et al. (2004)] and La_2O_3 [Fatsikostas et al. (2002); Fatsikostas and Verykios (2004); Sun et al. (2005)]. In addition, CeO_2 and CeO_2-ZrO_2 have been investigated due to their high redox capacity or oxygen storage capacity [Breen et al. (2002); Diagne et al. (2002); Srinivas et al. (2003); Deluga et al. (2004)], which have been shown to reduce carbon deposition via a carbon oxidation mechanism.

The catalyst support material not only affects the physical characteristics of the catalyst but also contributes to the product distribution. Haga et al. (1997a) investigated the steam reforming of ethanol over supported cobalt catalysts. The effects of γ-Al_2O_3, SiO_2, ZrO_2, MgO, and activated carbon (C) as potential supports were evaluated. They found that the product distribution for each catalyst varied, suggesting that the support material played a significant role in the reaction. No comment was made on the degree of ethanol conversion; however, the H_2 yield decreased in the order γ-Al_2O_3>ZrO_2>MgO>SiO_2>C. Mean crystallite size and the support surface area were measured and no correlation was found between cobalt dispersion, metal surface area, or support surface area on the activity of the catalyst for the steam reforming reaction.

The Freni group [Freni et al (2000, 2002, 2003); Frusteri et al. (2004)] has thoroughly investigated the use of MgO-supported nickel catalysts for the steam reforming of ethanol at 923 K specifically for molten carbonate fuel cell applications. They found that compared to a γ-Al_2O_3-supported nickel catalyst, the MgO-supported catalysts exhibited superior stability and substantially reduced rates of carbon deposition, on the order of one order of magnitude less.

Fatsikostas et al. (2002) and Fatsikostas and Verykios (2004) showed that nickel supported on La_2O_3 was more active and stable for the steam reforming reaction than a Ni/γ-Al_2O_3 catalyst. Figure 2.5 graphically illustrates the beneficial effects that La_2O_3 as a nickel support material has on the activity, product selectivity, and most importantly stability for the steam reforming of ethanol. The reduced stability of the γ-Al_2O_3-supported catalyst was attributed to the formation of coke on the surface of the catalyst, which resulted in the gradual decay in its activity. La_2O_3 was also reported to possess a self-regenerating mechanism that removes deposited carbon from the support and metal-support surface in the form of CO via a lanthanum oxycarbonate mechanism.
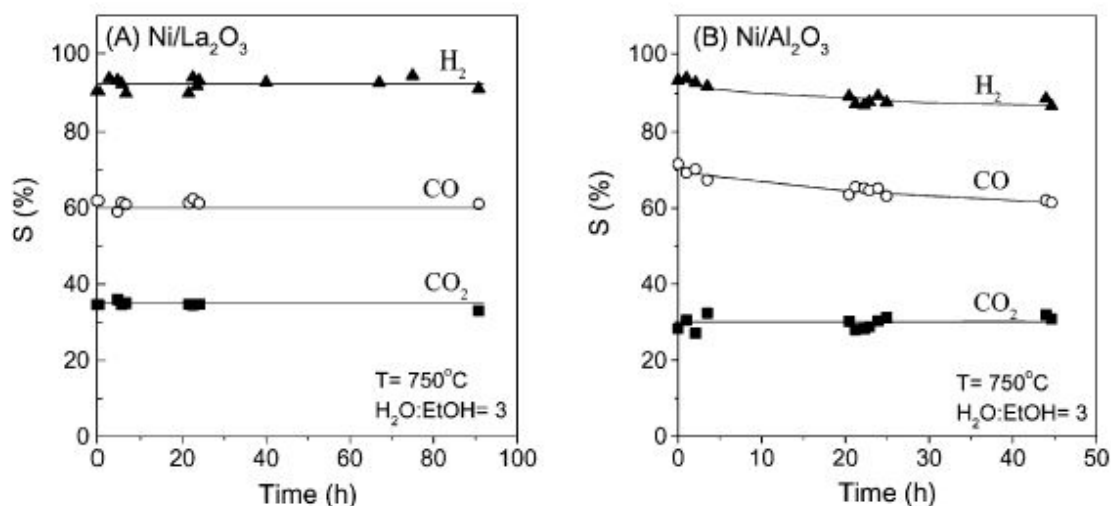
Figure 2.5: Support effects on the activity, selectivity, and stability as a function of time-on-stream for 17wt% Ni supported on A) La_2O_3 and B) Al_2O_3 for the ESR reaction {T=1023 K, H_2O:EtOH =3:1, GHSV ~ 96,000h^{-1}} under complete ethanol conversion conditions. Fatsikostas et al. (2002).

CeO_2, ZrO_2, and mixed CeO_2-ZrO_2 have recently received a lot of interest as support materials. These supports are of great interest because they have been shown to actively participate and influence the catalytic reaction either by interacting with the reactant(s), interacting with the electron configuration of the supported active phase, and/or enhancing the morphology of the supported metal particles capacity [Breen et al. (2002); Diagne et al. (2002); Srinivas et al. (2003); Deluga et al. (2004)].

For ZrO_2, the OH groups associated with the superlattice structure have been found to interact with methanol, in the methanol steam reforming reaction on Cu/ZnO-ZrO_2 catalysts to form adsorbed methoxide species [Velu et al. (2000,2001)]. These methoxide species are dehydrogenated to produce formaldehyde, which subsequently decompose to CO_2 and H_2. The metal-support system is synergistic in that copper accepts the hydrogen released from the species adsorbed on the zirconia and desorbs the hydrogen in its molecular form (H_2). Velu et al. (2002) found that zirconia increased metal dispersion, metal surface area, and

reduced the mean metal crystallite size and reduction temperature and thus enhanced the catalyst's activity.

CeO$_2$ has been found to have an oxygen storage capacity that is capable of incorporating atomic oxygen into the crystal structure under oxidizing conditions and release atomic oxygen under reducing conditions [Roh et al. (2006a)]. The high mobility of oxygen is beneficial in many reactions. For example, CeO$_2$ has shown activity for the direct CO oxidation (R.14) and water gas shift reactions (R.3) [Diagne et al. (2002)]. CeO$_2$ is the most basic of the oxides and preferentially adsorbs CO to form CO$_2$, which easily desorbs from the surface.

$$CO + \frac{1}{2}O_2 \longrightarrow CO_2 \qquad\qquad\qquad (R.14)$$

$$CO + H_2O \longrightarrow H_2 + CO_2 \qquad\qquad\qquad (R.3)$$

However, most attention is being paid to the CeO$_2$-ZrO$_2$ mixed oxide support. CeO$_2$-ZrO$_2$ has shown better selectivity for CO oxidation (R.14) and water-gas shift (R.3) reactions than ceria alone and more readily desorbs CO$_2$ from the surface [Diagne et al. (2002)]. In addition, the addition of ZrO$_2$ to CeO$_2$ has been shown to improve metal dispersion and thermal stability [Roh et al. (2006a,b)].

2.2.2.1 Magnesium-Aluminum mixed oxide support materials

The combination of magnesium and aluminum into a mixed oxide phase derived from hydrotalcite-like precursors has been the focus of many recent research publications. Mg-Al mixed oxides have been investigated for their properties as acid-base catalysts [Di Cosimo et al. (1998, 2000); Diez et al.(2003); Prescott et al. (2005)] and as catalyst support materials due to their high surface area, high thermal and chemical stability, and moderate and modifiable acid-base characteristics. See Table 2.1 for a list of studies where Mg-Al mixed oxide supported nickel catalysts were investigated.

Table 2.1: Compilation of Mg-Al mixed oxide supported nickel catalysts

Reaction System	Authors
Propane oxidative dehydrogenation	Sloczynski et al. (1999)
Methane partial oxidation	Lee and Lee (2002)
	Villa et al. (2003)
Methane dry reforming	Hou and Yashima (2004)
	Gou et al. (2004)
	Djaidja et al. (2006)
Methane steam reforming	Comas et al. (2006)
	Ohi et al. (2006)
Methane oxidative steam reforming	Takehira et al. (2004)

This section does not attempt to summarize the vast literature concerning the preparation, characterization, and evaluation of hydrotalcites, but to inform the reader on the application of thermally decomposed hydrotalcite-like precursors as catalyst support materials. For more information on hydrotalcites, several comprehensive reviews have been written [Rajamathi et al. (2001); Vaccari (1998,1999)].

Hydrotalcite-like precursors are generally prepared by co-precipitation of magnesium and aluminum salts, typically nitrates, in an alkaline media, typically a combination of carbonates and hydroxides, which results in the formation of a layered double hydroxide material [Di Cosimo et al. (1998, 2000); Diez et al. (2003)], shown graphically in Figure 2.6. This preparation technique results in the intimate incorporation of magnesium (M^{2+}) and aluminum (M^{3+}) molecules into a single well-dispersed crystal structure [Di Cosimo et al. (1998, 2000); Prinetto et al. (2000)].
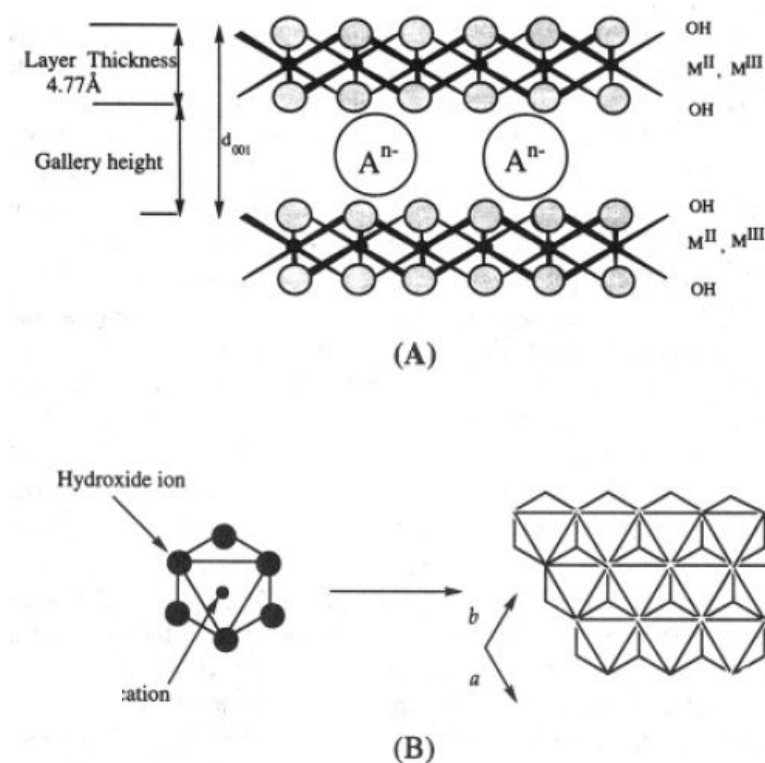
Figure 2.6: Schematic representation of a hypothetical hydrotalcite. (a) a layered double hydroxide structure containing brucite-like layers intercalated by hydrated anions and (b) the AB packing of hydroxide ions giving rise to the octahedral interstices occupied by M^{2+} and M^{3+} metal cations. Constantino and Pinnavaia (1995).

Thermal decomposition of the hydrotalcite above 773 K results in the irreversible destruction of the layered double hydroxide crystal structure favoring the formation of a highly dispersed $MgAl_2O_4$ spinel crystal structure [Ohi et al. (2006); Takehira et al. (2004); Comas et al. (2006)]. The transition from hydrotalcite to mixed oxide is accompanied by loss in surface area for decomposition temperatures above 873 K and a significant rise in basicity occurs due to the removal of the intercalating anion which blocks basic sites [Shen, et al. (1998); Kustowski et al. (2004)]. Thermal decomposition of hydrotalcite-like compounds, unlike hydroxides, yields materials with highly dispersed and near homogeneous $MgAl_2O_4$ spinel with very little phase separation, which produces regions of pure Al_2O_3 or MgO.

Acid-base titrations have revealed that Mg-Al mixed oxides exhibit both acidic and basic properties that are of moderate density and strength compared to the pure oxides, MgO and γ-Al$_2$O$_3$ [Rossi et al. (1991); Shen et al. (1994) Fishel and Davis (1994)]. In addition, Mg-Al mixed oxides demonstrate improved thermal stability [Shen et al. (1998)] and chemical stability in the presence of steam compared to MgO [Schaper et al. (1989)]. As a support for transition metal catalysts, Mg-Al mixed oxides have been found to outperform pure oxide supported catalysts in terms of activity and stability due to improved nickel crystallite stability [Villa et al. (2003); Guo et al. (2004); Comas et al. (2006)], reduced rates of Ni phase transformation to NiAl$_2$O$_4$ and NiO-MgO [Guo et al. (2004); Hou and Yashima. (2004); Ohi et al. (2006)], and reduced carbon formation [Lee and Lee (2002); Djaidja et al (2006)].

2.2.3 Reaction parameters

2.2.3.1 Reaction temperature

The effect of reaction temperature on the ethanol steam reforming reaction has been thoroughly studied over numerous catalyst systems. Essentially, all investigations examined the effect of the reaction temperature on the ethanol conversion and product distribution to determine the activity, selectivity, and stability of the catalyst for the ethanol steam reforming reaction.

Figure 2.7 shows the dependence of ethanol conversion and product distribution on the reaction temperature for two different catalysts (a: 17% Ni/La$_2$O$_3$ and b: 1%Rh/γ-Al$_2$O$_3$). Increasing temperature results in increased ethanol conversion and total product yield. Fatsikostas et al. (2002) (see Figure 2.7a), reported a marked decrease in the selectivity for the formation of C$_2$-species (acetaldehyde and ethylene) and an increase in H$_2$ and C$_1$-species (CO, CO$_2$, and CH$_4$) selectivities. Liguras et al. (2003), Figure 2.7b, found a very different temperature effect on product selectivity. This point highlights the role of the active catalyst

33

metal (i.e., Ni or Rh) in determining the dominant reaction pathways. The temperature dependence of the product distribution also emphasizes the role of temperature in determining the dominant reaction pathway.
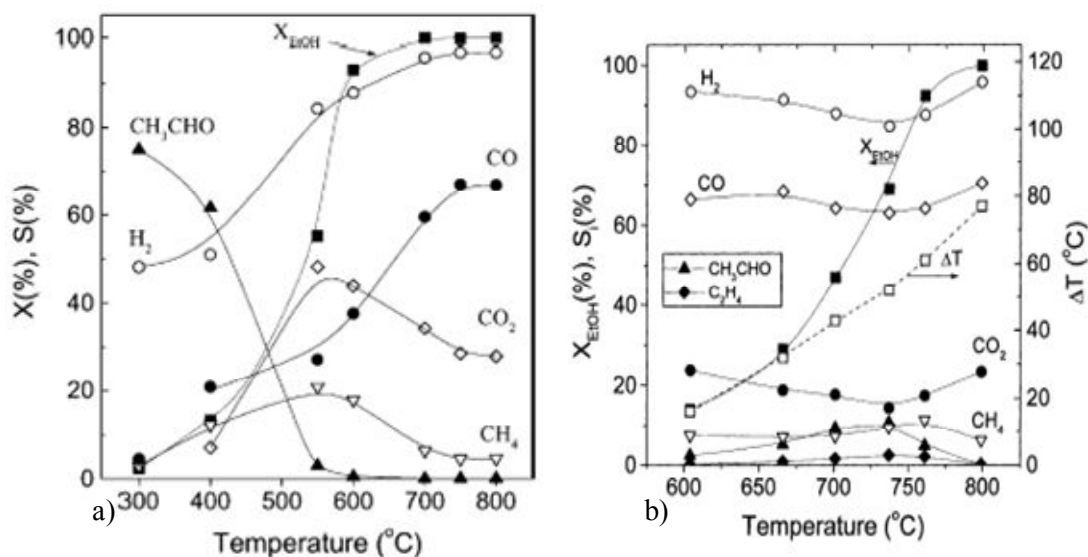
Figure 2.7: Effect of reaction temperature on ethanol conversion and product selectivity for the ESR reaction on a) 17wt% Ni/La_2O_3 (Fatsikostas et al. 2002) and b) 1%Rh/γ-Al_2O_3 (Liguras et al. 2003). All curves indicate percent selectivity [S(%)] unless otherwise labeled.

2.2.3.2 H_2O:EtOH feed ratio

The H_2O:EtOH molar feed ratio is an important parameter for the steam reforming of ethanol because it describes the number of moles of water to the number of moles of carbon fed to the system. Consider the overall ethanol steam reforming reaction (R.1), 3 moles of water are required to fully oxidize the 2 moles of carbon from the ethanol molecule to CO_2. Fierro et al. (2002), Klouz et al. (2002), and Cavallaro et al. (2003a,b) studied the effect of the H_2O:EtOH feed ratio on the ESR reaction. Figure 2.8 shows the influence of the H_2O:EtOH ratio on ethanol conversion and product distribution.

34

Increasing the H_2O:EtOH ratio resulted in a decrease in the selectivities for the undesirable by-products (CH_4, CO, and coke) and an increase in the selectivity for the desirable products H_2 and CO_2. Increasing the H_2O:EtOH molar feed ratio above the stoichiometric value of 3, had little effect on the H_2 selectivity; however, a decrease in the CH_4 and CO selectivities was noticed most likely because of the increasing contributions of the CH_4 steam reforming and the water gas shift reactions. The formation of coke on the catalyst surface was proposed by Dybkjaer (1995) to follow an ethylene polymerization/dehydrogenation mechanism. Ethylene is produced via the ethanol dehydration reaction, therefore as the H_2O:EtOH ratio increases, the dehydration reaction equilibrium will tend to favor the reverse reaction, which would reduce selectivity for ethylene and therefore, the selectivity for coke formation. In addition to this, coke can be removed from the catalyst surface through the carbon steam reforming reaction. The conversion of water decreases with increasing water content.
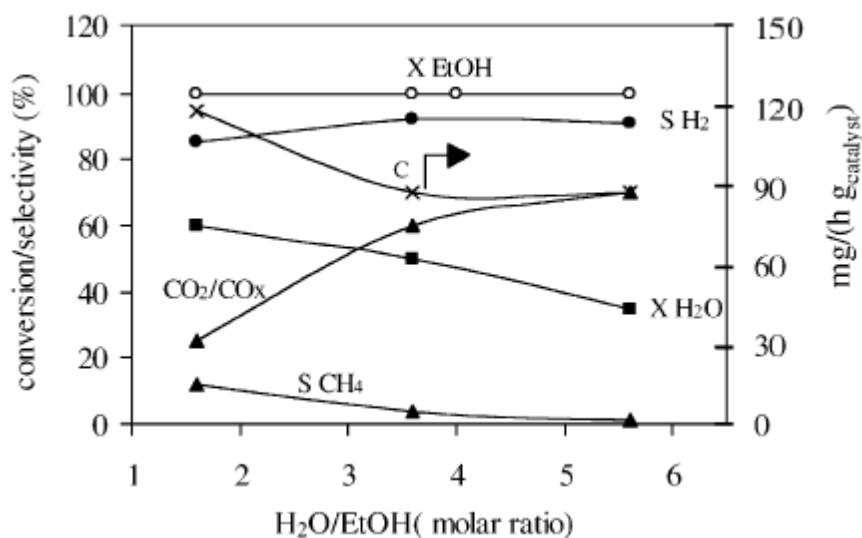
Figure 2.8: Effect of H_2O:EtOH (molar ratio) on the ethanol conversion and product selectivities for the ethanol steam reforming reaction over a 2wt%Cu-16.4wt%Ni/SiO_2 catalyst {T=873 K, GHSV~60,000h^{-1}}. Fierro et al. (2002). Selectivities are indicated unless otherwise labeled.

2.2.3.3 Contact time

Haga et al. (1997b), Cavallaro (2000), Cavallaro et al. (2001), Fatsikostas et al. (2002), Velu et al. (2002), and Cavallaro et al. (2003b) reported on the effect of contact time (GHSV, Space Time (Wcat/Fin)) on the steam reforming of ethanol. Figure 2.9 show the effect of the contact time on the ESR reaction. As expected, all researchers found that ethanol conversion increased with increasing contact time.
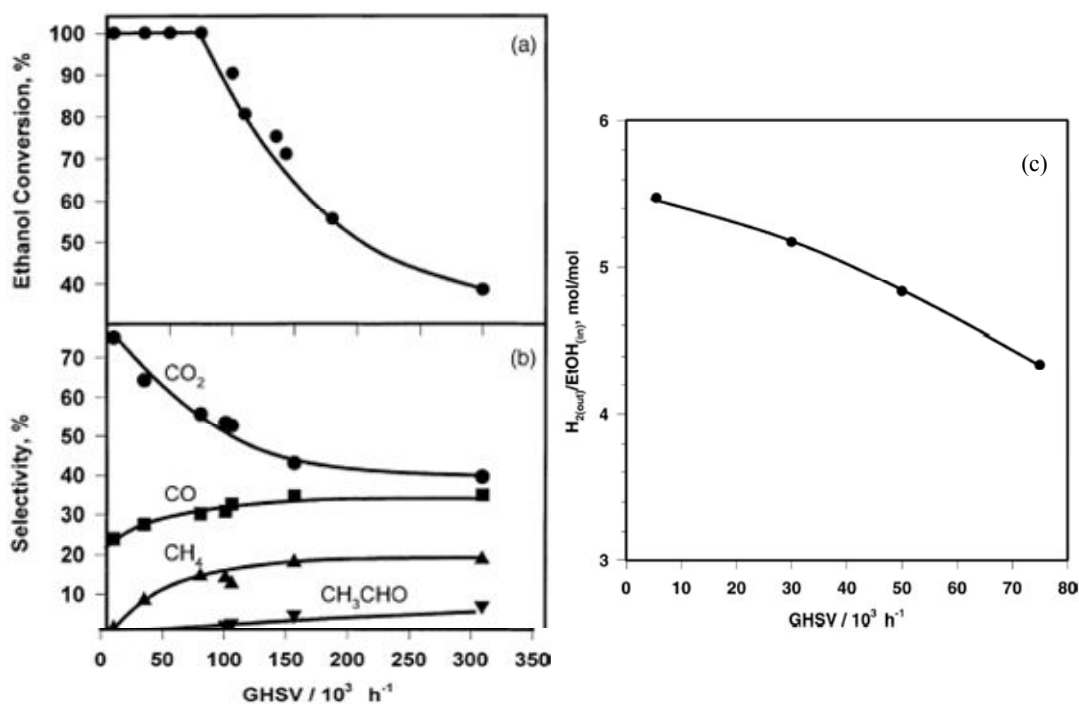
Figure 2.9: Effect of contact time (inverse of GHSV) on a) ethanol conversion, b) carbon product selectivity and c) H_2 yield for the ESR reaction on 5% Rh/Al$_2$O$_3$ {T=973 K, H$_2$O:EtOH=8.4:1}. Cavallaro et al. (2003b).

Figure 2.9 shows the typical effect that contact time has on ethanol conversion, and product distribution. The steam reforming products, H_2, and CO_2, increase with increasing contact time, and by-product selectivities (CO, CH_4 and acetaldehyde) decrease. This result suggests that the steam reforming products are formed through sequential reactions involving

36

the by-products, as discussed in section 2.2.1.4. With increasing contact time, by-product reactions, such as ethanol dehydrogenation (R.7), acetaldehyde decomposition (R.8) or steam reforming (R.10), CH_4 steam reforming (R.5), water-gas shift (R.3), and acetaldehyde decomposition (R.8) or steam reforming (R.10), contribute to the formation of the steam reforming products, H_2 and CO_2.

$$CH_3CH_2OH \longrightarrow CH_3CHO + H_2 \qquad\qquad\qquad\qquad (R.7)$$

$$CH_3CHO \longrightarrow CH_4 + CO \qquad\qquad\qquad\qquad\qquad (R.8)$$

$$CH_3CHO + H_2O \longrightarrow 3H_2 + 2CO \qquad\qquad\qquad (R.10)$$

$$CH_4 + H2O \longrightarrow 3H_2 + CO \qquad\qquad\qquad\qquad (R.5)$$

$$CO + H_2O \longrightarrow H_2 + CO_2 \qquad\qquad\qquad\qquad\qquad (R.3)$$

Chapter 3

Experimental

This section addresses the experimental techniques used in this study for the preparation, characterization, and evaluation of Ni/Mg-Al mixed oxide catalysts for the ethanol steam reforming reaction. Thorough characterization of Ni/Mg-Al mixed oxide catalysts was performed to relate specific physical and chemical properties to activity and product selectivity.

3.1 Catalyst Preparation

Mg-Al mixed oxide precursors, metal hydroxides, metal carbonates, and possibly hydrotalcites, were prepared by the co-precipitation of an aqueous solution containing $Mg(NO_3)_2 \cdot 6H_2O$ (ACS grade, Sigma-Aldrich) and $Al(NO_3)_3 \cdot 9H_2O$ (ACS grade, Sigma-Aldrich) at 298 K and a constant pH of 10. 750 mL of the Mg-Al nitrate solution having a total metal ion concentration of 1.00 M was added drop-wise into 750 mL of 0.5 M Na_2CO_3 over a period of 2 h with vigorous stirring. The pH was maintained at 10.0 ± 0.1 by the addition of 3.0 M NaOH. The resulting precipitate was aged in the mother liquor at 338 K for 12 h. The precipitate was filtered and washed in 2 L of hot distilled deionized water and this process was repeated four times to remove residual Na^+. The filter cake was then dried at 373 K for 24 hours. The Mg-Al mixed oxide precursors were calcined at 1123 K in air for 5 h to irreversibly decompose the precursor yielding a mixed oxide. The Mg-Al mixed oxides were then crushed and sieved to collect smaller than 80 mesh particles. This procedure was modified from the works of Schaper et al. (1989), Di Cosimo et al. (1998, 2000), and Diez et al. (2003).

Commercial γ-Al_2O_3 (3 micron powder, 80-120 m^2 g^{-1}, 99.97% metal basis) [Alfa-Aesar, Ward Hill, MA, USA] and MgO (magnesium oxide light, min. assay 98.0%) [BDH,

VWR, Laval, QC, Canada] were also used in this study. K-doped γ-Al$_2$O$_3$ was prepared by impregnating commercial γ-Al$_2$O$_3$ with a KOH solution [527 μmol K/g γ-Al$_2$O$_3$] as suggested by Shen et al. (1994) to neutralize the acidic nature of γ-Al$_2$O$_3$ without the formation of strong basic sites associated with K$_2$O. The K-doped γ-Al$_2$O$_3$ sample was dried at 373 K overnight, crushed into smaller than 80 mesh particles, and calcined at 1123 K in air for 5 h. All supports were wet impregnated with a Ni(NO$_3$)$_2$·6H$_2$O solution to give a 10 wt% Ni loading. Powdered supports (smaller than 80 mesh) were added to an aqueous nickel nitrate solution, prepared by dissolving Ni(NO$_3$)$_2$·6H$_2$O into distilled deionized water, which was heated to 333 K and stirred to evaporate excess water. The resulting paste was dried overnight at 373 K, calcined at 1023 K for 5 h, then crushed and sieved to collect the 35-45 mesh particles.

3.2 Catalyst Characterization

Ni/Mg-Al mixed oxide catalysts were characterized using the following techniques, which will be discussed in more detail in the following sections:

Property	Technique
Surface Area Analysis	BET N$_2$ physisorption
Chemical Compositional Analysis	Inductively coupled plasma - atomic emission spectroscopy (ICP-AES)
Crystalline Phase Identification	Powder X-ray diffraction, PXRD
Nickel Crystallite Size	Powder X-ray diffraction, PXRD
Nickel Reducibility	Temperature-programmed reduction (TPR) with H$_2$
Acid site strength and density	Temperature programmed desorption (TPD) of NH$_3$
Base site strength and density	Temperature programmed desorption (TPD) of CO$_2$
Spent Catalyst Analysis:	
Carbonaceous Deposits	Temperature programmed oxidation (TPO) and Scanning electron microscopy (SEM)

3.2.1 Surface Area Analysis

The most common surface area analysis technique used in catalyst characterization is the Brunauer, Emmet, and Teller (BET) method. The BET method for surface area analysis was developed as an extension to the Langmuir isotherm, which in addition to monolayer adsorption, accounts for multilayer adsorption. The BET multilayer adsorption model was derived based on of the following assumptions:

1) the heat of adsorption for the first layer, the monolayer, is constant
2) all other layers have the same heat of adsorption, the value is less than the first layer, and approaches the value of the heat of condensation
3) an infinite number of layers can be adsorbed

The resulting BET model relates the monolayer capacity of a material to the total concentration of gas adsorbed.

$$\frac{p}{(p_0 - p)V} = \frac{1}{cV_m} + \frac{(c-1)}{cV_m}\frac{p}{p_0}$$

where,

V: volume of gas adsorbed evaluated at STP

V_m: volume of gas adsorbed evaluated at STP in the monolayer

p: gas pressure

p_0:   vapor pressure of the condensed pure liquid on the surface

c: constant specific to the adsorbate

A plot of $p/(p_0 - p)V$ versus p/p_0, if linear gives an intercept of $1/cV_m$ and a slope of $(c-1)/cV_m$. From these parameters, the values of V_m and c can be determined. The BET surface area per gram of test material is determined by,

$$BET\ S.A. = \frac{V_m \rho N_{AV} a_{CS}}{MW_{N_2} M_{sample}}$$

where,

        ρ: density of liquid nitrogen at boiling point

        N_{AV}:   Avogadro's number

        a_{CS}:   cross-section surface area of nitrogen molecule

        MW_{N2}:   molecular weight of nitrogen

        M_{sample}:   mass of test material tested

The most commonly used adsorbate is nitrogen. For determination of very small surface areas, krypton and argon have been used. Adsorption occurs at the boiling point of the adsorbate, hence for nitrogen, adsorption occurs at a temperature of 77 K. It should be noted that the linear region for the application of the BET equation exists for partial pressures (p/p_0) of 0.05 to 0.3. When the BET model is applied to this limited range of partial pressures the surface area is calculated to be within 5% of the true value. For materials composed of micro- or meso-pores, erroneous results can arise when using the BET method because the assumption of multilayer adsorption does not adequately describe the condensed layers and the concept of a stack of infinite adsorbed molecules fails to describe the adsorption in very small pores.

BET surface area was determined for all catalysts prepared in this study using an 11-point (spanning (p/p_0) of 0.05 to 0.3) BET method on a Micromeretics Gemini 3 2375 using N_2 as the adsorbate. Prior to measurement of the BET surface area, catalyst samples were degassed to remove adsorbed atmospheric gases (CO_2 and H_2O), at 573 K for 1 h in N_2.

3.2.2 Chemical Composition

Compositional analysis of prepared catalysts was performed by dissolving (digesting) the catalyst sample into liquid form and determining the concentration of the metal ions in solution. Catalyst samples were digested in accordance with ASTM D1977-03: Standard Test Method for Nickel and Vanadium in FCC Equilibrium Catalysts by Hydrofluoric/Sulfuric

Acid Decomposition and Atomic Spectroscopic Analysis. The prepared catalysts were crushed and sieved and 200 mg of the fraction passing through a 100-mesh sieve was retained for analysis. Prior to acid digestion, the catalyst samples were oxidized at 1023 K in air for 1 hour to ensure that the catalyst material was completely oxidized and the sample was degassed removing adsorbed CO_2 and H_2O. The degassed samples were then acid digested using the procedure outline in ASTM D1977-03. The resulting solutions were diluted with 5% HNO_3, prepared using ultra-high purity, Milli-Q, deionized water, to a final total metal ion concentration of approximately 10 ppm (mass/volume).

The concentrations of nickel, magnesium, and aluminum in the digested samples were determined using inductively coupled plasma atomic emission spectroscopy (ICP-AES). The mass of nickel, magnesium, and aluminum ions in the dissolved solutions were calculated by multiplying the concentration data obtained from the ICP-AES analysis by the dilution factor used in the sample preparation. Since the metals were present in the catalyst sample as metal oxides the summation of the metal ion masses was less than the mass of the catalyst sample digested. The catalysts were pretreated at 1023 K in air to ensure that the metals in the samples were in the oxide phase, specifically NiO, MgO, and Al_2O_3. In this solid state system, the spinels, $NiAl_2O_4$ and $MgAl_2O_4$, can be formed, however they have the same chemical formula, or molecular weight, as the parent oxide forms ($NiAl_2O_4$ = NiO + Al_2O_3). Using this procedure, the theoretical weight of the digested sample was calculated assuming all metals were in oxide form. The average mass balance, defined as the theoretical sample mass to the actual mass of catalyst sample digested, for greater than 20-plus measurements was 97.3 ± 3.1%. The catalyst nickel loading was defined as,

$$\text{Nickel Loading wt\%} = \frac{\text{mass of nickel}}{\text{mass of sup port} + \text{mass of nickel}} \cdot 100\%$$

where the support was defined as the summation of the masses of MgO and Al_2O_3.

3.2.3 Phase identification and crystallite size: Powder X-ray Diffraction

A powder X-ray diffraction technique was used for crystalline phase identification and crystallite size analysis. Crystalline phases were identified by application of Bragg's Law,

$$n\lambda = 2d_{hkl}\sin\theta \qquad \text{or} \qquad \theta = \sin^{-1}\left(\frac{n\lambda}{2d}\right)$$

where

n : integer, order of diffraction

λ : wavelength of incident x-ray (Cu- Kα = 1.5425 Å)

d : interplanar spacing of the crystal planes of indices (hkl)

θ : angle between the incident ray and the diffracting place

Bragg's law relates the angular position of the reinforced diffracted x-rays to the interplanar spacing, d_{hkl}, of the crystal planes allowing for identification of crystalline species and phase.

The volume-average nickel crystallite size using the (200) plane was determined by application of the Debye-Scherrer equation for XRD line broadening,

$$d_p = \frac{k\lambda}{\sqrt{B_S^2 - B_R^2}\cos\theta}$$

where

k : shape factor, typically 0.89

λ : wavelength of incident x-ray (Cu- Kα = 1.5425 Å)

B_S : full width half maximum (FWHM) of the Ni (200) peak

B_R : FWHM for silicon standard, line broadening due to instrument

θ : 2θ location of the Ni(200) peak

Powder X-ray diffraction (XRD) patterns were measured on a Bruker AXS D8 Advance using standard Bragg-Brentano geometry with Ni-filtered Cu Kα radiation

(λ_1=1.5406 Å, λ_2=1.5444 Å). Spectra were collected for a 2θ range of 15 to 70° using a step size of 0.05° and a count time of 1 s.

3.2.4 Temperature programmed characterization techniques

Temperature-programmed reduction (TPR) and desorption (TPD) experiments were performed using an in-house built chemisorption unit shown schematically in Figure 3.1. The chemisorption unit was constructed to be a versatile apparatus capable of performing several temperature-programmed characterization experiments such as metal oxide reducibility, metal oxide surface area, and quantification and characterization of acidic and basic properties of catalyst materials. The chemisorption unit consists of a gas metering system, a low-volume quartz tube reactor located in a tubular furnace, a thermal conductivity detector, a set of three-way decision valves for directing gas flow, and a LabView data acquisition and control program for collecting temperature and TCD signal data and finely controlling the temperature and rate of temperature change of the furnace. The chemisorption unit was constructed to be a simple flow system capable of near continuous operation.

As in all chemisorption experiments, two gas types were used, probe gases (i.e., 5% CO_2/He, 5% H_2/N_2, and 2000 ppm NH_3/He) and purge gases (i.e., N_2 and He). All gases used were of ultra-high purity grade and were purchased from Praxair Inc., Kitchener, ON. During operation of the chemisorption unit it is absolutely necessary that the purge gas match the probe balance gas (i.e., Probe Gas: 5% H_2/N_2, Purge Gas: N_2). The probe gases were prepared such that the balance gas, N_2 or He, were selected to maximize the sensitivity and response of the thermal conductivity detector (TCD). TCD response is improved by increasing the difference between the thermal conductivity of the reference (purge gas) and sample (probe gas) gases. A simple rule-of-thumb is that thermal conductivity of a gas is inversely proportional to its molecular weight. Therefore, increasing the difference in molecular weight between the probe and purge gas would increase the TCD response. The gases were passed through indicating oxygen scavenger beds to remove trace amounts of oxygen that would adversely affect the characterization of the catalyst and the life-time of the

thermal conductivity detector. A bank of gas flow meters were used to measure and control the flow rates of the probe and purge gases. Four three-way valves, positioned on the periphery of the chemisorption reactor/furnace, allow for gas selection:

1) to the reactor for pretreatment (purge or probe loading) then to the vent
2) to by-pass the reactor to the vent while valves are in arrangement 3
3) through the TCD to the reactor and back to the TCD and to the vent
4) through the TCD by-pass the reactor and back to the TCD and to the vent, while valves are in arrangement 1
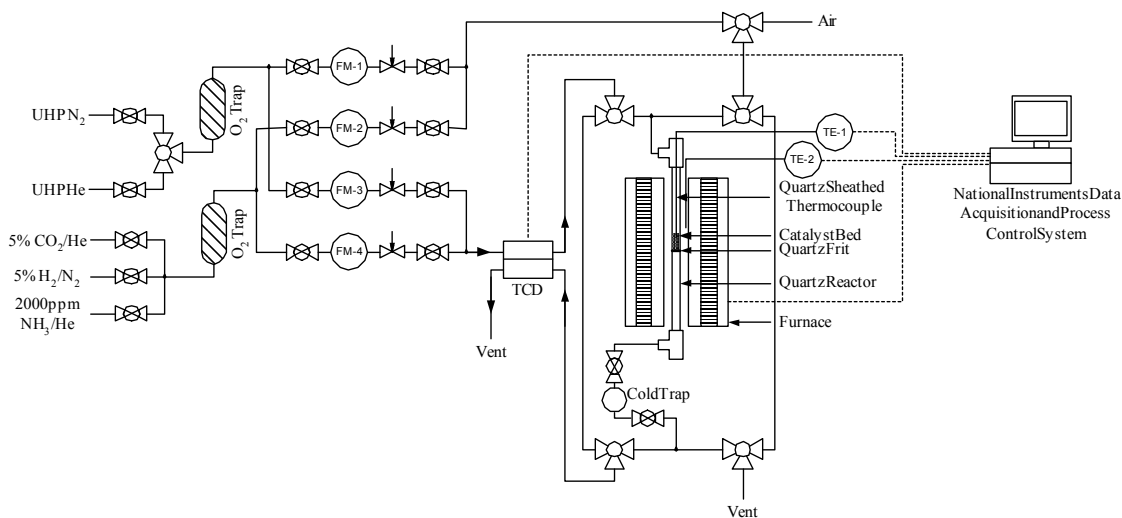
Figure 3.1:   In-house built chemisorption unit for temperature-programmed reduction and desorption experiments.

This arrangement of decision valves allowed for catalyst pretreatment, doping with probe gases, and desorption and measurement without exposure of the catalyst sample or the TCD to atmospheric conditions, most importantly oxygen and moisture. Two chemisorption quartz tube reactors were constructed for this apparatus, one for TPR and one for TPD (Figure 3.2). Due to the high sensitivity of the TCD to changes in hydrogen concentration,

only very small catalyst quantities were required, typically 50 mg for TPR experiments. The TPR reactor was designed to reduce total volume. Larger catalyst samples, 500 – 1000 mg, were typically required for the TPD experiments because of the lower sensitivity of the TCD to NH_3 and CO_2 (acidic and basic site probes) and the low concentration of these probes adsorbed on the catalyst sample and therefore in the effluent gas when released.

The internal diameter of the outlet side of the quartz tube reactors was maintained at 4 mm to reduce the volume of the measurement system (dead volume) between the outlet of the catalyst bed and the TCD. All stainless steel tubing from the outlet of the reactor to the TCD unit was 1/8" and whenever possible 1/16" was used. The total measurement system volume for the TPD reactor, defined as the volume of tubing separating the catalyst bed (top of quartz frit) and the detector, was found to be 13.6 mL using a tracer technique. For a typical purge gas flow rate of 30 mL min^{-1}, the dead volume represented a delay of approximately 27.2 s, or 4.5 K for a temperature ramp rate of 10 K min^{-1}. Since the delay between the desorption of a probe gas molecule and its measurement in the detector was very small, no deconvolution of the raw data was necessary.
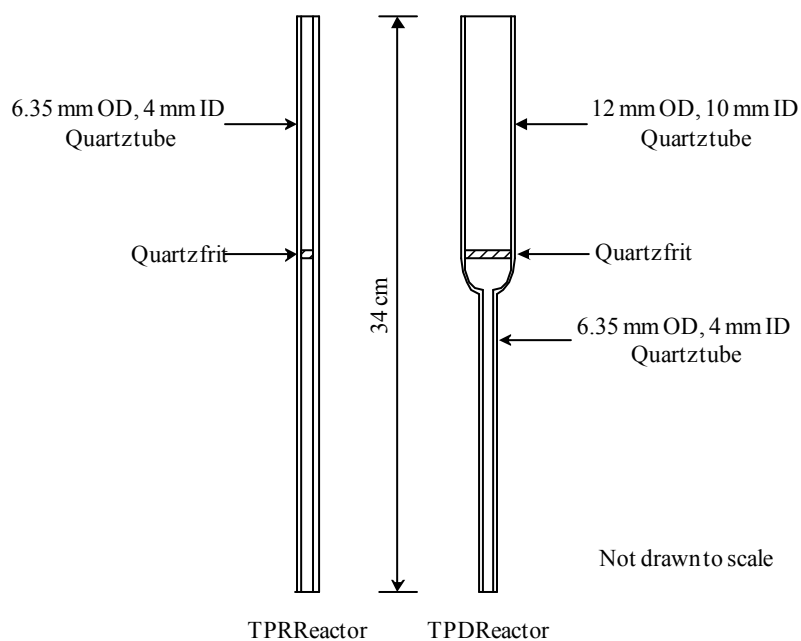
Figure 3.2:   Quartz tube reactors for the chemisorption unit.

46

3.2.5 Temperature programmed reduction (TPR-H$_2$)

Temperature programmed reduction (TPR) is used to characterize metal oxidation states, metal-support interactions, and quantify the amount of reducible metal oxide. The reduction of the metal oxide by hydrogen is given by

$$\text{MeO}_{(s)} + \text{H}_{2(g)} \rightarrow \text{Me}_{(s)} + \text{H}_2\text{O}_{(g)}$$
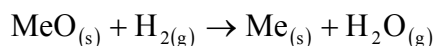
yielding a reduced metal site and gaseous water. In a typical TPR experiment, the temperature of the sample is increased at a constant rate and the rate of H$_2$ consumption is measured. A plot of the rate of H$_2$ consumption versus temperature provides information on the total amount of reducible metal oxide and the strength of the Me-O bond. The effect of metal-support interaction can be inferred by comparing the TPR for a pure metal oxide to the TPR for a supported metal oxide.

For TPR-H$_2$ experiments, a 50 mg sample of catalyst was pretreated in flowing air at 1023 K for 1 hr. Upon cooling to 298 K, the sample was purged with N$_2$. The temperature was ramped at 10 K min^{-1} from 298 to 1223 K in a 5% H$_2$/N$_2$ reduction gas flowing at 30 mL min^{-1}. The gas leaving the reactor passed through an ethanol-dry ice chilled low-volume condenser (cold trap) to remove water from the gas stream exiting the TPR reactor prior to entering the TCD. The amount of hydrogen consumed was determined by the difference in the thermal conductivities of the gases entering and exiting the reactor by the TCD as a function of temperature of the catalyst.

3.2.6 Temperature programmed desorption (TPD)

The acidity and basicity of catalyst materials can be characterized in terms of site binding strength and site density using temperature programmed desorption of probe molecules. Basic molecules, such as NH$_3$ and pyridine, are used as probes for acidic sites and acidic probes, typically CO$_2$, are used to probe basic sites. Unlike surface area analysis where

N_2 adsorption occurs by physisorption (physical adsorption), the acidic and basic probe molecules chemically adsorb (chemisorb) on the surface producing much stronger probe-surface interactions (bonds) than observed with N_2 adsorption. The strength of the probe-surface interaction can be determined by identifying the temperature at which the bond is broken. When the bond is broken the probe molecule is released from the surface and the amount of the probe molecule desorbing from the surface is associated with the site density. After adsorption of the probe molecule and purging to remove physisorbed probe molecules from catalyst material, the temperature of the sample is increased at a constant rate and the concentration of the probe molecule exiting the TPD reactor is measured. Typically, TPD results are reported as concentration of probe molecule desorbed versus sample temperature.

Idealized probe-surface interactions for CO_2-basic sites and NH_3-acidic sites are given in Table 3.1 and Table 3.2 respectively. The strength of the acidic and basic sites was categorized into weak, moderate, and strong site types, which were related published probe-surface interaction complexes.

Table 3.1: Idealized CO$_2$-base site interactions. Adapted from Di Cosimo et al. (1998).
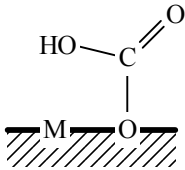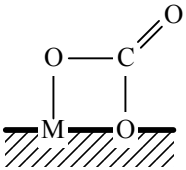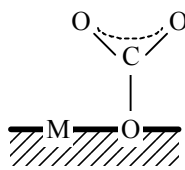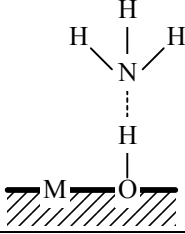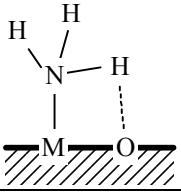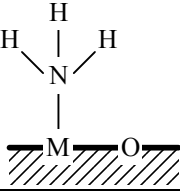
Representation of surfaced adsorbed CO_2 species			
Basic Site Strength	Weak	Moderate	Strong
Adsorbed Species	Bicarbonate	Bidentate Carbonate	Unidentate Carbonate
Adsorption Site	Surface hydroxyl, **Brønsted**	Acid-base pairing (i.e., Mg^{2+}-O^{2-}), **Lewis**	Low coordination O^{2-}, **Lewis**

Table 3.2: Idealized NH₃-acid site interactions. Adapted from Prinetto et al. (2000) and Auroux and Gervasini et al. (1990).

Representation of surfaced adsorbed NH₃ species			
Basic Site Strength	Weak	Moderate	Strong
Adsorbed Species	Coordinated NH$_3$	Coordinated NH$_3$, with H-O interaction	Coordinated NH$_3$
Adsorption Site	Surface hydroxyl, **Brønsted**	Acid-base pairing (i.e., Al^{3+}-O^{2-}), **Lewis**	Electron deficient Al^{3+}, **Lewis**

Temperature programmed desorption curves were deconvoluted by accounting for the contribution of each site type, weak, moderate, and strong, to the overall desorption curve. An exponential-Gaussian hybrid model [Lan and Jorgenson (2001)], a commonly used model for deconvolution of asymmetric chromatography peaks, was used to describe the desorption of the probe molecule from each site type.

$$f_i(T) = \begin{cases} H_i \exp\left(-\dfrac{\left(T-\overline{T}_i\right)^2}{2\sigma_i^2 + \tau_i\left(T-\overline{T}_i\right)}\right) & 2\sigma_i^2 + \tau_i\left(T-\overline{T}_i\right) > 0 \\ 0 & 2\sigma_i^2 + \tau_i\left(T-\overline{T}_i\right) \le 0 \end{cases}$$

where,

    i: Peak type: weak, moderate, strong

    H_i: Weighting factor

    T: Temperature

    $\overline{T}_i$:   Temperature of the peak i maximum

    σ_i: Standard deviation of peak i

    τ_i: Decay time constant for peak i

The fitting parameters ($\bar{T}_i$, σ_i, τ_i) were estimated using a standard non-linear least squares technique by minimizing the difference between the experimental TPD curve and the model predicted by

$$f(T) = f_{Weak}(T) + f_{Moderate}(T) + f_{Strong}(T)$$

Basic properties of the Ni/Mg-Al mixed oxide catalysts were characterized by TPD using a 500 mg sample that had been pretreated in flowing air at 1023 K for 1 h. The sample was then reduced at 1023 K for 1 h in $5\%H_2/N_2$ and purged at 1023 K for 1 h in He and cooled to room temperature. The reduction step was necessary to reduce NiO to Ni which would more closely represent the state of the catalyst during ethanol steam reforming. The samples were exposed to a flowing stream of 5% CO_2/He for 2 h. Physisorbed CO_2 was removed by flushing with 100 mL min^{-1} of He for 1 h. The He purge flow rate was reduced to 30 mL min^{-1} and the temperature was ramped from 298 to 1023 K at 15 K min^{-1}. The rate of CO_2 desorption from the catalyst was measured by a TCD as a function of the catalyst temperature. Using a similar experimental routine, the acidic site density and binding strength were determined by TPD of room temperature adsorbed NH_3.

3.3 Fixed bed reactor system for catalyst performance experiments

A fixed-bed reactor catalyst test station was designed for catalyst performance evaluation experiments. The test system was developed to handle both liquid and gaseous feeds, have on-line analysis of the product stream exiting the reactor, and operate in a near continuous state. A schematic drawing of the fixed-bed reactor catalyst test station used in this study is given in **Figure 3.3**. The fixed-bed reactor catalyst test station consisted of:

1) gas manifold and liquid delivery system
2) pre- and post-reactor heated sections
3) high temperature furnace
4) quartz tube fixed bed reactor
5) data acquisition and process control
6) product gas analysis system

Each section will be described separately.

3.3.1 Gas and liquid reactant feed delivery system

The gas feed delivery system was designed to adapt to the changing requirements of the reactor's gaseous environment: calcination (oxidative), reduction (reductive), and reaction conditions (tracer, reactant feed). The feed gases were supplied from gas cylinders and their flow rates were metered and controlled by UNIT 1100 mass-flow controllers (MFCs). To ensure consistent flow from the MFCs, the MFC backpressure, the gas pressure supplied from the high-pressure gas cylinders, was regulated at 50 psig by dual-stage regulators (Praxair). The gas feed system was constructed entirely of 1/4" stainless steel tubing and compression fittings (Swagelok®). After each MFC, a check valve was installed to ensure that backflow did not occur. All compression fittings were leak-tested at a pressure of 50 psig to confirm that the feed system had no leaks. The MFCs were calibrated with their respective gases using a bubble-film flowmeter. Calibration curves relating the gas volumetric flow rate to the %signal were generated and found to be linearly related with high coefficients of determination ($r^2 > 0.99$).

Ethanol-water feed mixtures, prepared from Milli-Q, sonicated, de-ionized water and anhydrous ethanol (Commercial Alcohols, anhydrous, >99.5%) were stored in an inverted HPLC media storage bottle (Chromatographic Specialties). The feed mixture was metered and delivered to the vaporizer by a high-pressure reciprocating piston liquid metering pump (Model VS, Eldex Inc.). To minimize flow pulsation, typically associated with reciprocating piston pumps, an in-line micro-volume pulse dampener (Chromatographic Specialties) was installed. The Eldex Model VS metering pump was calibrated over the entire operating range of 0.05 to 3.0 mL min^{-1}.

Figure 3.3: Fixed-bed reactor catalyst test station
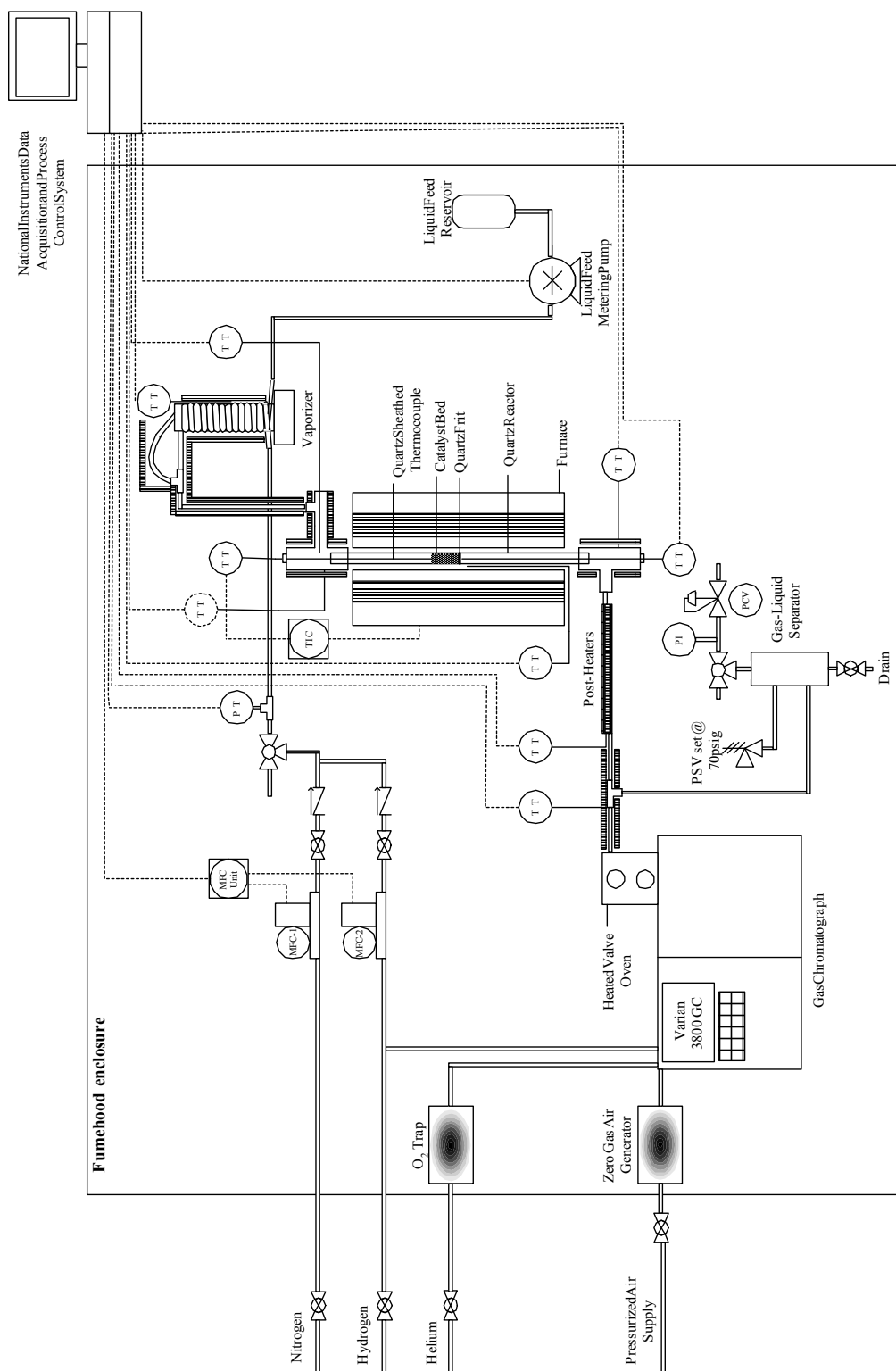
3.3.2 Heated sections: Vaporizer, pre-, and post-reactor heated sections

Six heated sections (vaporizer, pre-reactor heater, three post-reactor heaters, and a GC sample line heater) were maintained at approximately 473 K to ensure that the vaporized reactant feed mixture entering the reactor and the product stream exiting the reactor remained gaseous. Each section of tubing was wrapped in STH101 heating tape (500 W, OMEGA Engineering Inc.) and controlled at 473 K by a LabView control program. The maximum temperature of the pre-reactor and first post-reactor heating sections was constrained by the maximum operating temperature of the Viton O-ring used in the Ultra-Torr fittings, which was approximately 200°C, to connect the quartz reactor to the metal tubing attached at the inlet and outlet of the reactor. Omega FGH051 heavy insulating tape was wrapped around the heating tapes to reduce heat loss to the surrounding air.

3.3.3 Furnace

The temperature of the Lindberg Blue 2000 W furnace was controlled by the LabView control program using a quartz-sheathed micro K-type thermocouple located in the middle of the catalyst bed as the process control parameter. In addition to the control thermocouple, a thermocouple located in the middle of the furnace was constantly monitored to ensure that the furnace temperature did not exceed 1073 K. As a back up to this, a third thermocouple located in the furnace was monitored by a stand-alone high temperature limit switch, set at 1123 K, that would automatically shut off all electrical power to the entire fixed-bed reactor test station.

3.3.4 Quartz tube reactor

Ethanol steam reforming reactions were performed in a standard down-flow fixed-bed quartz tube reactor. Quartz was selected as the material of construction because of its inert chemical structure and inactivity towards the reforming reactions. Metals such as stainless steel, Hastalloy, and Incoloy contain nickel, cobalt, and iron, which have exhibited catalytic activity for the reforming reactions.

53
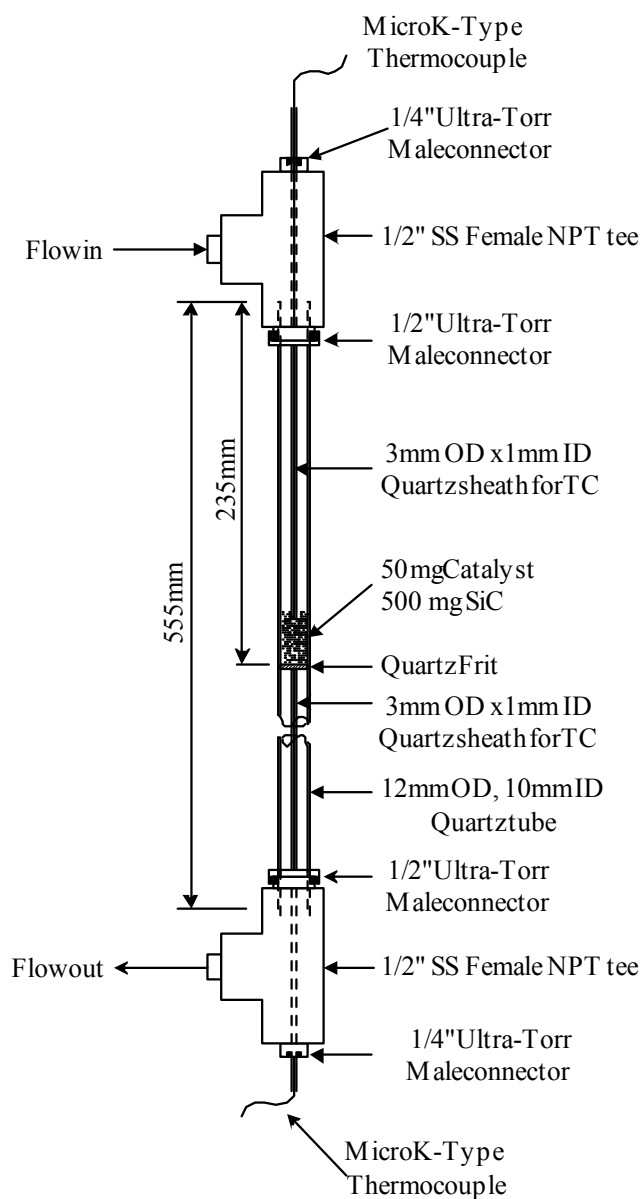
Figure 3.4:   Quartz tube reactor

The quartz reactor, shown schematically in Figure 3.4, was attached to stainless steel tubing at the reactor inlet and outlet by bored-through style 1/2"NPT x 1/2" Swagelok Ultra-Torr® vacuum fittings. The Ultra-Torr® fitting assembly included a finger-tightened knurled

nut and a metal ferrule to compress a Viton O-ring. Upon compression, the Viton O-ring created a tight seal around the quartz tube. The seal was sufficient to maintain a reactor pressure of 70 psig at a reactor temperature 973 K for 24 h. The fitting was bored-through to allow for greater penetration of the quartz tube into the metal tees, which resulted in greater mechanical stability and strength. Approximately 3 cm of the quartz reactor entered the metal tees. The Ultra-Torr® fitting assembly allowed for the easy removal of the reactor, increased mechanical strength (compared to graded quartz-stainless steel seals), and provided a seal sufficiently tight to ensure that the feed and product streams did not leak.

Two 3-mm OD x 1-mm ID quartz sheathed subminiature K-type thermocouple (Omega Engineering Inc.), one located in the catalyst bed and one below the catalyst bed were used to measure the mean temperature of the catalyst bed and the temperature of the product gas exiting the catalyst bed. The sheathed thermocouples were inserted into the reactor from the top and bottom via bored-through style 1/2" NPT x 1/16" Swagelok Ultra-Torr vacuum fittings, similar to that used to connect the quartz reactor.

3.3.5 Data acquisition and process control

A National Instruments FieldPoint measurement, data logging, and process control system in conjunction with an in-house developed LabView process control program was used to collect and store critical process information (i.e., reactant flowrates, total reactor pressure, catalyst bed temperature, and temperature of each controlled section) and control the process. In addition to software safety shutdown procedures, all heated sections were equipped with either high temperature limit switches or thermal fuses to ensure safe shutdown in case an emergency.

3.3.6 Process description

An ethanol-water mixture was fed by a liquid pump (Eldex) at a constant rate of 0.2 mL min^{-1} to the vaporizer, which was maintained at 435 K, to ensure vaporization of the feed mixture without thermally decomposing ethanol. A N_2 trace gas, metered by a Unit 1100 mass flow controller at a constant flow rate of 15 mL min^{-1} was mixed with the vaporized reactant feed as an internal standard to aid in analysis of the product stream and determination of the total product flow rate. The feed mixture (ethanol/steam/N_2) passed through a pre-reactor heater section that was maintained at 473 K to prevent condensation and was delivered to the reactor. The reactor consisted of a 10 mm I.D. quartz tube with a highly porous quartz frit which supported 50 mg (35-45 mesh) of catalyst dispersed in 500 mg (35-50 mesh) of SiC (inert). The temperature of the catalyst bed was measured by a quartz sheathed micro thermocouple located in the middle of the catalyst bed which was used to control the furnace temperature. This arrangement ensured that the average temperature of the bed was maintained at the desired reaction temperature. The product stream exiting the reactor passed through a series of heated sections (post-heaters) maintained at 473 K to ensure the product remained gaseous and continued to a Varian CP3800 GC for compositional analysis. The composition of the product stream was determined in its entirety using a single GC, multi-column, multi-detector approach described by Chladek et al. (2007), see Appendix B.

3.3.7 Evaluation of catalytic performance

The activity and selectivity of the Ni/Mg-Al mixed oxide catalysts for the ethanol steam reforming reaction were evaluated and compared using the parameters defined in Table 3.3.

Table 3.3: Ethanol steam reforming evaluation parameters

Parameter	Formula	Definitions
Ethanol Conversion	$X_{EtOH} = \dfrac{n_{EtOH}^{in} - n_{EtOH}^{out}}{n_{EtOH}^{in}} \cdot 100$	n_{EtOH}^{in}, n_{EtOH}^{out} : molar flow rates of ethanol entering and exiting the reactor
Water utilization	$\eta_{H_2O} = \dfrac{n_{H_2O}^{in} X_{H_2O}}{n_{EtOH}^{in} X_{EtOH}}$	X_{H_2O} :water conversion defined similarly to ethanol conversion
Product yield	$Y_i = \dfrac{n_i^{out}}{n_{EtOH}^{in} X_{EtOH}}$	n_i^{out} : molar flow rate of species i exiting reactor
Carbon balance	$CBal = \dfrac{\sum \chi_i n_i^{out}}{2 n_{EtOH}^{in}} \cdot 100$	χ_i : represents the number of carbon atoms in molecule i ($\chi_{Ethanol} = 2$) Note: Includes all carbonaceous species exiting the reactor, including unconverted ethanol, are included in the numerator term

For comparison of the experimental data with thermodynamic equilibrium expectations, the Gibbs' equilibrium reactor utility in Aspen Plus™ 12.1 (Aspen Technology, Inc.) was used for generation of thermodynamically predicted equilibrium values. The thermodynamic results are typically plotted as continuous dashed or dotted lines in the plots.

3.4 Spent catalyst characterization

Spent catalyst samples were characterized by XRD for crystalline phase and nickel crystallite size changes due to exposure to reaction conditions and by temperature programmed oxidation (TPO) and SEM to quantify and characterize carbonaceous deposits. SEM images were collected on a LEO 1530 FE-SEM.

3.4.1 Thermogravimetric Analysis (TGA)

Thermogravimetric analysis refers to any analytical technique that relates changes in sample weight to temperature. In this study, TGA was used for temperature programmed oxidation (TPO) of spent catalyst materials to quantify and characterize coke (carbonaceous) deposits. Carbonaceous deposits, having a chemical formula of C_mH_n, can be oxidized in the presence of O_2 to produce CO, CO_2, and H_2O.

$$C_mH_n + \frac{2m+n}{4}O_2 \longrightarrow mCO + \frac{n}{2}H_2O$$

$$C_mH_n + \frac{4m+n}{4}O_2 \longrightarrow mCO_2 + \frac{n}{2}H_2O$$
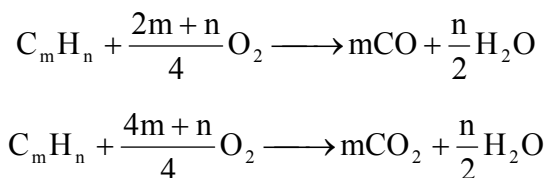
CO, CO_2, and H_2O, leave the sample resulting in a reduction in the samples weight. The amount of carbonaceous deposits on the spent catalyst sample was defined as the wt% change in the sample weight. The amount of carbonaceous deposits on the spent catalyst materials was determined by temperature programmed oxidation (TPO) using a Texas Instruments SDT-2960 with simultaneous TGA-DTA analysis. Approximately 10 mg of spent catalyst was pretreated in flowing N_2 at 393 K for 1 h to remove physisorbed H_2O and CO_2. After pretreatment, the treatment gas was switched to zero-gas air (contains no hydrocarbons) to be used as the oxidant and the temperature of the sample was ramped from 298 to 1123 K at 10 K min^{-1}.

Chapter 4
Preliminary Experimental Work

4.1 Blank Catalyst Experiments: Evaluation of the inertness of the SiC catalyst diluent and the reactor system

The fixed-bed reactor catalyst test station was constructed to perform catalyst evaluation experiments over a wide range of reaction conditions. To ensure that performance measurements (i.e., reactant conversion, product yield, etc.) were solely related to the catalyst and not the test station, the reactor tube was constructed from quartz and ultra-low surface area silicon carbide (SiC) was used as the catalyst diluent. To determine the degree of inertness of the catalyst test system for the conversion of ethanol, ethanol steam reforming reactions were conducted in the test station in the absence of catalyst. Experiments were performed at 723, 773, and 923 K, with a H_2O:EtOH molar feed ratio of 8.4:1, a liquid feed flow rate of 0.2 mL min^{-1}, 500 mg SiC, all at atmospheric pressure for a minimum of at least 4 hours.

Time-average ethanol conversion and product yields for blank reactor experiments are reported in Table 4.1. Ethanol conversion increases with increasing temperature from 0% at 723 K to approximately 17% at 923 K. The level of ethanol conversion at 923 K is more substantial than desired but considering that the addition of 50 mg of catalyst (1/10th the loading of SiC) results in 100% ethanol conversion at these reaction conditions, this low level conversion is reasonable and will not hinder the comparison of catalyst performance.

In addition, it is not unreasonable to consider the conversion of ethanol to the decomposition products, H_2, CO, CH_4, CH_3CHO, and C_2H_4 as homogeneous gas-phase reactions instead of catalyzed surface reactions. In this light, homogeneous gas-phase ethanol decomposition would occur regardless of the material of construction.

Table 4.1: Ethanol conversion and product yield for blank reactor experiments

Temperature (K)	EtOH conversion (%)	Yield						
		H_2	CO	CH_4	CO_2	C_2H_4	AcHO	DEE
723	0.00	0.00	0.00	0.00	0.00	0.00	0.00	0.00
773	0.31	0.00	0.00	0.00	0.00	0.71	0.27	0.00
923	16.87	0.71	0.16	0.18	0.00	0.21	0.61	0.00

Although ethanol conversion was very low at 773 K, the distribution of products indicated that ethanol was being consumed via the ethanol dehydrogenation (R.7) and dehydration reactions (R.11).

$$CH_3CH_2OH \longrightarrow CH_3CHO + H_2 \tag{R.7}$$

$$CH_3CH_2OH \longrightarrow C_2H_4 + H_2O \tag{R.11}$$

At 723 K, the dehydration reaction appeared to be the dominant reaction pathway. Increasing the temperature to 923 K, the dominant reaction pathway changed to the dehydration pathway followed by acetaldehyde decomposition (R.8) to produce CO and CH_4.

$$CH_3CHO \longrightarrow CH_4 + CO \tag{R.8}$$
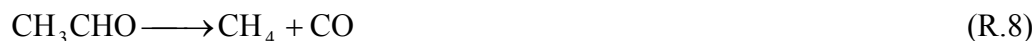
The absence of CO_2 at all temperatures indicates that the water-gas shift reaction (R.3) was not active in the absence of a catalyst.

$$CO + H_2O \longrightarrow H_2 + CO_2 \tag{R.3}$$

Taking into consideration the low levels of ethanol conversion, especially at temperatures below 773 K, the inertness of the quartz tube reactor and the catalyst diluent, SiC, were verified.

4.2 Evaluation of transport limitations

Heterogeneously catalyzed reactions can be described by a series of transport and reaction processes. Fogler (1999) laid out a detailed sequence of steps to describe a solid-phase heterogeneously catalyzed reaction:

1. Mass transfer of the reacting species from the bulk fluid to the external surface of the catalyst
2. Diffusion of the reacting species from the pore mouth through the internal pore structure to the active catalyst site
3. Adsorption of the reacting species onto the active site
4. Surface reaction of the adsorbed species
5. Desorption of the product from the active site to the internal pore structure
6. Diffusion of the product species from the internal pore structure to the pore mouth
7. Mass transfer of the product species from the external surface to the bulk fluid

This series of transport/reaction steps can also be extended to the transfer of heat. The observed reaction rate is affected by the rates of the individual steps and is controlled by the slowest. For example, if steps 3, 4, or 5 are relatively slow in comparison to steps 1, 2, 6, and 7, then the reaction is kinetically controlled, and if the reverse is true, the reaction is transport controlled. To determine the true surface kinetics it is desirable to perform experiments in the absence of transport limitations. Typically, three transport processes describe the transfer of heat and mass in a chemical reactor:

1. Interphase: transport between fluid and external surface of catalyst particle
2. Intraparticle: transport within the catalyst particle
3. Interparticle: transport between fluid and catalyst particles

Interphase transport describes the transfer of heat and mass between the flowing fluid and the external surface of the catalyst particle, through the boundary layer film. If the rate of

transport is sufficiently greater than the rate of reaction, than the surface concentration or temperature will be the same as the bulk fluid phase, resulting in no gradient through the film. However, if the rate of transport is not sufficiently high (or the reaction rate is very high), the surface concentration or temperature can significantly deviate from the bulk fluid. Hudgins (1972) proposed a criterion (Eqn. 4.1) to determine the onset of external mass transfer limitations. The Hudgins (1972) criterion compares the observed rate of reaction to the rate of reaction if the system was entirely mass transfer limited and allowed for a deviation in the surface and bulk concentrations of 5%.

$$\frac{(-r_A)_{obs} d_P}{k_C C_A^0} < 0.3 \qquad \text{Eqn. 4.1}$$

Mears (1971) proposed a similar criterion (Eqn 4.2) for evaluating the onset of external heat transfer limitations by comparing the observed rate of heat generation due to the surface reaction to the rate of heat transfer through the boundary layer film and allowing for a deviation of 5% between the surface and bulk fluid temperatures.

$$\left| \frac{(-\Delta H)(-r_A)_{obs} d_P E_a}{h R T_B^2} \right| < 0.3 \qquad \text{Eqn. 4.2}$$

Intraparticle transport describes the transfer of heat and mass between the external surface of the catalyst and the center of the particle. Hudgins (1968) developed a criterion (Eqn 4.3) for predicting the absence of diffusion control (occurrence of kinetic control) by comparing the observed rate of reaction to the rate of reaction if the entire catalyst particle was exposed to the surface concentration.

$$\frac{(-r_A)_{obs} r_P^2}{D_e} \cdot \frac{-r_A'(C_A^0)}{-r_A(C_A^0)} < 1 \ (0.75)$$

Eqn. 4.3

The value of 0.75 was replaced by 1 by Hudgins to simplify/generalize the analysis. For a 1st order reaction,

$$\frac{-r_A'(C_A^0)}{-r_A(C_A^0)} = \frac{1}{C_A^0}$$

Eqn. 4.4

The Hudgins kinetic control criterion for intraparticle transport for a 1st order reaction, is obtained by combining Eqn 4.3 and Eqn. 4.4.

$$\frac{-r_A r_P^2}{D_e C_A^0} < 1$$

Eqn. 4.5

Similarly, Mears (1971) proposed a criterion (Eqn. 4.6) for determining the onset of internal heat transfer limitations.

$$\left| \frac{(-\Delta H)(-r_A) r_P^2 E_a}{\lambda R T_S^2} \right| < 1$$

Eqn. 4.6

Interparticle transport describes the transport of heat and mass in the radial and axial directions of the bulk fluid and catalyst phase. Of particular importance is radial heat transfer between the catalyst particles, the fluid, and the wall, resulting in the formation of "hot" or "cold" spots in the catalyst bed and axial dispersion, or back mixing. Mears (1971) developed a relationship (Eqn. 4.7) comparing the relative importance of interphase and interparticle transport.

$$\frac{1-\varepsilon}{1+b}\frac{hd_P}{\lambda}\frac{r_R}{r_P} < 5.3 \qquad\qquad \text{Eqn. 4.7}$$

For the case where Eqn. 4.7 is true, interphase transport becomes the dominant resistance to heat transfer and generally interparticle heat transfer can be ignored. Radial mass transfer is negligible in comparison to radial heat transfer and therefore, if the radial heat transfer is negligible it can be assumed that the role of radial mass transfer is also negligible.

Mears (1971) developed a criterion (Eqn. 4.8) for predicting when axial dispersion (back mixing) effects significantly affect the observable reaction rate.

$$\frac{d_P}{L}\frac{20}{Pe_a}\ln\frac{1}{1-X} < 1 \qquad\qquad \text{Eqn. 4.8}$$

The role of axial heat conduction is generally less significant than the axial dispersion and therefore if Eqn. 3.8 is satisfied then axial conduction can also be neglected.

In experimental lab-scale reactors the relative importance of the transport limitations generally follows:

interparticle heat > interphase heat > intraparticle mass >
interphase mass > interparticle mass > intraphase heat
[Mears (1971, 1973)]

The observed reaction rate was evaluated at the start of the experiment (initial) and at steady state and accounts for the deactivation of the catalyst. Initially, all experiments at reaction temperatures above 723 K achieved complete ethanol conversion and therefore

transport limitation evaluation is not informative; the reaction system was certainly heat and mass transfer limited. The calculation procedure is given in Appendix G.

Reaction Conditions:

Reaction Temperature:	673, 723, 773, 823, 873, 923 K
H_2O:EtOH:	8.4:1 molar
Catalyst Weight:	0.05 g
Catalyst Diameter:	4.27×10^{-4} m (35-45 mesh)
Liquid Feed Rate:	0.2 mL min^{-1}

4.2.1 Evaluation of interphase transport limitation criteria

Results for the evaluation of the interphase criteria are given in Table 4.2. For all reaction conditions the Hudgins (1972) criterion is met indicating that all experiments were free of external mass transfer limitations. Therefore, the surface concentration of ethanol was essentially the same as the concentration of ethanol in the bulk gas phase. On the contrary, essentially all experiments exhibited significant deviation from thermal kinetic control, suggesting substantial heat transfer resistance across the boundary layer film. The temperature of the catalyst surface would be substantially less than the bulk gas phase since the ethanol steam reforming reaction is highly endothermic. The maximum temperature difference across the film can be estimated by (Eqn 4.9) [Levenspiel (1999)].

$$\Delta T_{film} = T_B - T_S = \frac{\left(-\Delta H_{rxn}\right)\left(-r_A\right)_{obs} d_P}{6\,h} \qquad \text{Eqn. 4.9}$$

Initially, the temperature of the catalyst surface was greater than 20 K cooler than the bulk gas phase. However, as the catalyst deactivated, the temperature difference between the bulk gas phase and the surface was reduced significantly. The estimation of the transport of heat across the boundary layer film presents a worst case scenario. It is assumed that ethanol

is being converted directly to the steam reforming products, H_2 and CO_x, which would result in an over estimation of the true heat of reaction. In addition, the catalyst bed was diluted 10 times with an inert (SiC), which would aid in supplying heat to the catalyst particles via conduction.

Table 4.2: Interphase transport limitation

Temperature (K)	673	723	773	823	873	923
Conversion						
Initial	79.40	100.00	100.00	100.00	100.00	100.00
Steady State	7.20	21.30	37.00	60.00	75.90	100.00
$-r_{A,obs}$ [mol m_{cat}^{-3} s^{-1}]						
Initial	302.11	>380.50	>380.50	>380.50	>380.50	>380.50
Steady State	27.40	81.05	140.78	228.30	288.80	>380.50
Mass Transfer < 0.3						
Initial	0.038	>0.046	>0.044	>0.043	>0.041	>0.040
Steady State	0.003	0.010	0.016	0.026	0.031	>0.040
Heat Transfer < 0.3						
Initial	2.78	>2.89	>2.41	>2.03	>1.73	>1.49
Steady State	0.25	0.61	0.89	1.22	1.32	1.49
Film ΔT						
Initial	21.10	>26.14	>24.93	>23.87	>22.90	>22.03
Steady State	1.91	5.57	9.22	14.32	17.38	>22.03

Shaded areas: Failing the criterion for absence of transport limitations

4.2.2 Evaluation of intraparticle transport limitation criteria

Results for the evaluation of the intraparticle transport limitation criteria are presented in Table 4.3. During the initial operation of the reactor, all reaction experiments failed the Hudgins internal diffusion criterion meaning that a significant concentration gradient existed within the catalyst particle radius. Therefore, active catalytic sites within the pore structure are not exposed to the same concentration of ethanol as the catalytic sites at the external surface of the catalyst particle as is expected with reaction systems achieving complete conversion. However, as the catalyst deactivated, the rate of reaction and ethanol conversion

decreased resulting in the Hudgins internal diffusion criterion being met for experiments below 923 K, which maintained complete ethanol conversion. The Mears internal heat transfer limitation criterion was satisfied for reaction temperatures indicating that the catalyst particle is isothermal owing to its relatively high thermal conductivity.

Table 4.3: Intraparticle transport limitations

Temperature (K)	673	723	773	823	873	923
Mass Transfer < 1						
Initial	1.35	1.57	1.47	1.38	1.28	1.18
Steady State	0.12	0.33	0.54	0.83	0.97	1.18
Heat Transfer < 1						
Initial	0.098	0.098	0.079	0.065	0.054	0.045
Steady State	0.009	0.021	0.029	0.039	0.041	0.045

Shaded areas: Failing the criterion for absence of transport limitations

4.2.3 Evaluation of interparticle transport limitation criteria

Table 4.4 gives the results of the evaluation of the interparticle limitation criteria. Evaluation of Eqn 4.7 reveals that interphase heat transport is substantially more significant for all reaction temperatures than the transfer of heat on the interparticle scale because of high catalyst dilution with inert SiC and a relatively low d_R/d_P of 23.4. Applying Mears (1971) axial dispersion criterion, it is apparent that L/d_P used in this study was sufficiently large to ensure minimal contribution of back mixing for reaction temperatures below 873 K.

Table 4.4: Interparticle transport limitations

Temperature (K)	673	723	773	823	873	923
Eqn. 4.7 < 5.3						
	0.285	0.266	0.258	0.251	0.244	0.239
Axial Dispersion < 1						
Initial	1.35	---	---	---	---	---
Steady State	0.064	0.205	0.395	0.783	1.215	---

Shaded areas: Failing the criterion for absence of transport limitations

4.2.4 Summary

Analysis of the transport limitations has revealed that for this reaction system, the relative importance of the transport effects follow the order:

$$\text{interphase heat} > \text{intraparticle mass}$$

The remaining transport processes were found to contribute insignificantly to the observed reaction rate. All experiments were found to be external heat transfer and internal mass transfer limited initially. As the catalysts deactivated with time on stream and stabilized at a steady state activity, the reaction rate had decreased such that the rate of diffusion through the internal pore structure of the catalyst no longer affected the reaction rate, except at the highest reaction temperature (923 K), which gave complete ethanol conversion.

At the beginning of the experiment, external heat transfer limitations were very significant, resulting in a temperature gradient greater than 20 K across the boundary layer film and could be substantially higher when complete ethanol conversion was achieved, as would be expected. As the catalyst deactivated, the temperature deviation across the boundary layer became considerably smaller. The low temperature experiment (673 K), which gave less than 10% conversion at steady state, met the external heat transfer limitation criterion. The higher temperature experiments continued to exhibit significant external heat transfer limitations even at steady state. As discussed previously, the external heat transfer limitation is overemphasized because of overestimation of the heat of reaction and neglecting the role of the diluent as a heat source/sink. Therefore, the temperature gradient across the film is expected to be smaller, but most likely still significant, especially for experiments above 823 K where high conversions are achieved.

The presence of transport limitations complicates the realization of the true kinetic parameters (i.e., activation energies). However, the high degree of deactivation that the catalysts experience during the experiment, especially at low reaction temperatures, ensures

that extracting kinetic parameters is essentially impossible (or at least very difficult) owing to the uncertainty in the number and type of active catalyst sites. The experimental data, although not useful for the extraction of kinetic data, can be used to evaluate the performance of catalysts (i.e., screening study), aid in the development of a reaction mechanism, determine the modes of deactivation, and the effect of deactivation on the reaction mechanism.

Chapter 5

Preparation, characterization, and evaluation of Ni/Mg-Al mixed oxide catalyst for the steam reforming of ethanol

This study focuses on the evaluation of the catalytic activity, selectivity, and stability of a series of 10wt% Ni loaded Mg-Al mixed oxide supported catalysts for the production of hydrogen via ethanol steam reforming at 773 and 923 K at atmospheric pressure. Several characterization techniques are employed to determine the effect of the Mg-Al content of the support on the nickel crystal structure and crystallite size, nickel reducibility, and acidic and basic properties. These properties are then related to the activity, selectivity, and deactivation mechanisms experienced by the nickel supported Mg-Al mixed oxide supported catalysts. In addition, post mortem characterization of the spent catalyst by temperature-programmed oxidation (TPO), X-ray diffraction (XRD), and scanning electron microscopy (SEM) were performed.

5.1 Physical and chemical characterization of the prepared catalysts

Two Mg-Al mixed oxide support materials were prepared using the procedure detailed in section 3.1, having desired Mg:Al ratios of 1:2 (Mg1Al2) and 2:1 (Mg2Al1). The Mg-Al mixed oxides, Al_2O_3, $K-Al_2O_3$, and MgO were impregnated with a nickel precursor to obtain as nickel loading of 10 wt% as described in section 3.1. The BET surface area and the chemical composition of the prepared catalysts are reported in Table 5.1. The Mg-Al mixed oxide supports, Mg1Al2 and Mg2Al1, gave the highest surface areas compared to the commercial supports especially after nickel impregnation. In all cases, the surface area was reduced upon nickel impregnation and subsequent calcination at 1023 K. Nickel loading determined by ICP, data also listed in Table 5.1, showed that the catalysts had approximately the same nickel content and confirmed that the desired Ni loading of 10 wt % was achieved. Mg-Al mixed oxide support materials were prepared to have Al/(Al+Mg) molar ratios of 0.66

(Mg1Al2) and 0.33 (Mg2Al1) and ICP confirmed that the desired molar ratios were achieved.

Table 5.1: BET surface area and chemical composition of prepared catalysts

Sample ID	BET S.A. $[m^2\ g^{-1}]$ [a]	% Ni Loading [b]	Al/ $(Al+Mg)$ [b]
Ni/Al	56.34 (80.98)	9.85	1
Ni/KAl	63.19 (80.49)	10.08	1
Ni/Mg1Al2	90.44 (114.37)	9.41	0.693
Ni/Mg2Al1	91.92 (102.80)	9.51	0.351
Ni/Mg	74.41 (112.86)	10.50	0

[a] Values in parentheses refer to the surface area of the calcined support material
[b] Determined by ICP

X-ray diffraction patterns for calcined and reduced catalysts are shown in Figure 5.1 and Figure 5.2 respectively. Calcined catalyst samples were reduced at 1023 K in 200 mL min^{-1} of 5% H_2/N_2 for 1h. The samples were cooled to room temperature in the reducing gas and stored in sample bags. XRD patterns were collected over a 72 h period for the Ni/Mg1Al2 sample and it was found to be free of NiO and the Ni (200) peak did not change in intensity or breadth indicating that reduced nickel catalysts were stable at atmospheric conditions. The XRD patterns for the Al_2O_3 supported catalysts, Ni/Al and Ni/KAl, show the presence of defect Al_2O_3, NiO, and possibly $NiAl_2O_4$ spinel. The diffraction pattern for the K-doped Al_2O_3 catalyst closely matched that of the Al_2O_3 catalyst indicating that potassium doping did not alter the crystalline structure of the support or the nickel oxide. Nickel impregnation and calcination at 1023 K for 5 h of the commercial Al_2O_3 samples led to a shift in the defect Al_2O_3 spinel peaks to lower than expected 2θ angles. The expected location of the (440) defect Al_2O_3 spinel peak is 67.3° [Li et al. (2006)], whereas for the nickel-impregnated samples the (440) peak was located at 66.8°. Several authors [Li et al. (2006); Kim et al. (2004); Cai et al. (2001); Lif et al. (2004)] have proposed that nickel is incorporated into the defect Al_2O_3 spinel structure forming $NiAl_2O_4$. Nickel incorporation

71

into the defect spinel structure increases the lattice parameters since the ionic radius of Ni^{2+} is greater than Al^{3+} resulting in a lowering of the Bragg angle. The small shift in the (440) peak suggests the formation of an incomplete $NiAl_2O_4$ spinel phase in addition to NiO and therefore Ni exists in two distinct crystalline phases. The incorporation of Ni in the defect spinel was verified by a shift in the (440) peak to higher 2θ angles after reduction of the catalysts.

The XRD diffraction pattern for the Ni/Mg sample is consistent with the formation of a crystalline $Ni_xMg_{1-x}O$ solid solution [Arena et al. (1991); Lee and Lee (2002); Djaidja et al. (2006); Parmaliana et al. (1990)]. After reduction, Ni in the Ni/Mg catalyst remained in the $Ni_xMg_{1-x}O$ crystal structure, showing no separate reduced Ni phase. Visually, the Ni/Mg sample changed color from green-brown (calcined) to dark brown-black (post reduction) suggesting that the oxidation state of Ni in the solid solution had been reduced from $Ni_xMg_{1-x}O$ to $Ni_xMg_{1-x}O_{1-y}$, where y<<x, while maintaining the cubic oxide (NaCl-type) crystal structure.

The calcined nickel impregnated Mg-Al mixed oxide supported catalysts gave more complicated diffraction patterns than the pure oxide supported catalysts. The diffraction pattern for Ni/Mg1Al2 and Ni/Mg2Al1 indicate the presence of MgO, NiO, $MgAl_2O_4$ and possibly $NiAl_2O_4$. The complete absence of a defect Al_2O_3 spinel phase should be noted (no peak at 67.3°). The calcined Ni/Mg1Al2 sample, having an Al/(Al+Mg) molar ratio of 0.693 shows a well-developed $MgAl_2O_4$/$NiAl_2O_4$ spinel crystal structure and very little MgO/NiO. Reduction of Ni/Mg1Al2 led to the appearance of a reduced Ni phase and the disappearance of the NiO/MgO peaks, most noticeable at approximately 43.3° and 62.7°, indicating that Mg had been completely incorporated into the $MgAl_2O_4$ spinel phase and therefore this catalyst is MgO free, or at least free of large crystalline MgO regions. The calcined Ni/Mg2Al1 sample, having an Al/(Al+Mg) molar ratio of 0.351, shows a reduction in the intensity of the spinel peaks and a rise in MgO/NiO peak intensity compared to Ni/Mg1Al2. After reduction, the peaks associated with MgO/NiO remained, although their relative intensity compared to

the spinel peaks decreased and a separate reduced Ni phase appeared suggesting the support for Ni/Mg2Al consists of MgO-MgAl$_2$O$_4$. Therefore, reduction of the supported nickel catalyst clarifies that the support material of Ni/Mg1Al2 consisted primarily of the spinel MgAl$_2$O$_4$ and Ni/Mg2Al1 of a mixture of MgO-MgAl$_2$O$_4$.

Volume-average nickel crystallite sizes were determined for the Al-containing catalysts by the Scherrer XRD line broadening technique and are reported in Table 5.2. The crystallite size was not reported for the Ni/Mg catalyst since no separate reduced Ni phase was detected. Ni/Mg1Al2, the Mg-Al spinel supported catalyst had the smallest nickel crystallite particle size. Increasing the Mg content (Ni/Mg2Al1) above the stoichiometric requirement for the formation of the MgAl$_2$O$_4$ spinel resulted in the formation of excess MgO and an increase in the nickel crystallite size by a factor of approximately 1.5 times compared to Ni/Mg1Al2. In comparison, the γ-Al$_2$O$_3$ supported catalyst, Ni/Al, had a slightly larger nickel crystallite size than Ni/Mg1Al2. An interesting finding was the substantial effect the basic dopant, potassium, had on sintering. Ni/KAl, the K doped γ-Al$_2$O$_3$ supported catalyst, had the largest nickel crystallite size, nearly twice the diameter of the Ni/Mg1Al2 sample. Although it titrates the strong acid sites resulting in improved performance, K-doping has been found to promote nickel sintering by reducing the interaction between nickel and the support [Sehested et al. (2006)] resulting in a substantial increase in the nickel crystallite size.
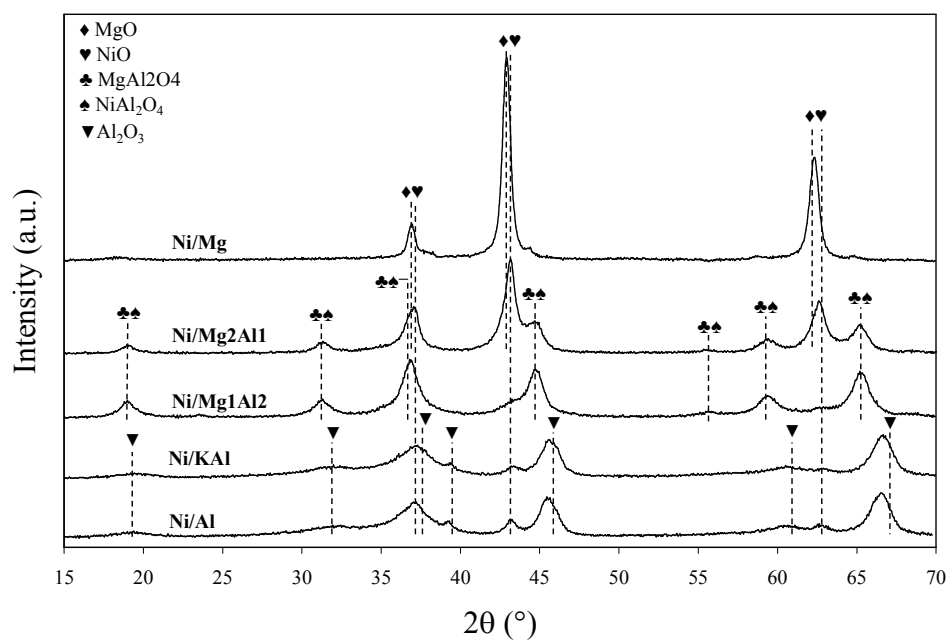
Figure 5.1: XRD patterns of pure and Mg-Al mixed oxide supported nickel catalyst calcined at 1023 K.
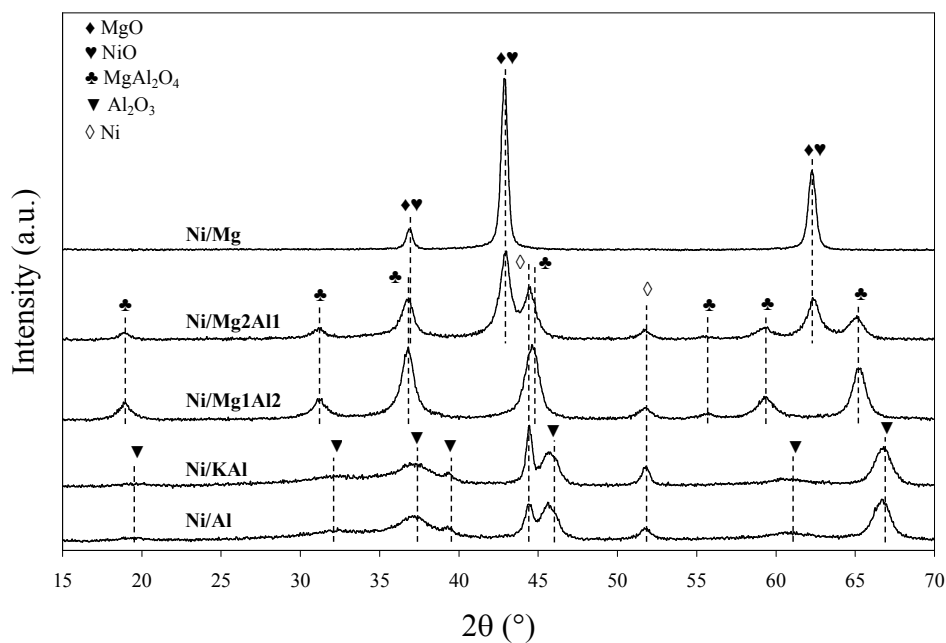

Figure 5.2: XRD patterns of the reduced pure and Mg-Al mixed oxide supported nickel catalyst calcined at 1023 K.

Table 5.2: XRD characterization of reduced and unreduced supported nickel catalysts

Sample ID	Unreduced	Reduced	Nickel Crystallite Size (nm)[a]
Ni/Al	Al_2O_3 defect spinel $NiAl_2O_4$ spinel NiO	Al_2O_3 defect spinel Ni	9.06
Ni/KAl	Al_2O_3 defect spinel $NiAl_2O_4$ spinel NiO	Al_2O_3 defect spinel Ni	15.25
Ni/Mg1Al2	$MgAl_2O_4$ and $NiAl_2O_4$ spinel MgO and NiO	$MgAl_2O_4$ spinel Ni	8.34
Ni/Mg2Al1	$MgAl_2O_4$ and $NiAl_2O_4$ spinel MgO and NiO	$MgAl_2O_4$ spinel MgO Ni	12.31
Ni/Mg	MgO and NiO	MgO and NiO	---

[a] Determined by XR line broadening of the reduced sample using the Ni (200) peak

Temperature-programmed reduction by H_2 (TPR-H_2) results for the calcined nickel catalysts are presented in Figure 5.3 as the rate of H_2 consumption with respect to temperature. The H_2 consumption curves reveal that nickel exists in several phases with differing degrees of interaction with the support. It is evident that the composition of the support has a significant effect on the reducibility of the supported nickel. The reduction of unsupported NiO typically shows a single broad maximum located at approximately 640 K [Parmaliana et al. (1990)] spanning 523 to 700 K [Parmaliana et al. (1990), Chang et al. (2004)]. From our results, it is apparent that free NiO does not exist as a separate phase and therefore must be stabilized either through incorporation in or interaction with the support. The TPR profile for Ni/Mg shows a small broad peak at 735 K followed by a slow rise in the rate of H_2 consumption from 800 to 1200 K. The low temperature peak is ascribed to the

reduction of NiO that is interacting with the surface of the support, while the slow rise in H_2 consumption starting at approximately 800 K is indicative of the incorporation of NiO into the MgO matrix by the formation of a $Ni_xMg_{1-x}O$ solid solution. $Ni_xMg_{1-x}O$ solid solutions are very difficult to reduce, typically requiring reduction temperatures greater than 1173 K [Parmaliana et al. (1990)]. As seen in the XRD for the reduced catalysts in Figure 5.2, Ni was not extracted from the $Ni_xMg_{1-x}O$ solid solution producing a separate Ni^0 phase even after reduction at 1123 K for 1h. Addition of Al to the support composition drastically improved NiO reduction as seen by the appearance of a peak in H_2 consumption at 1153 K for Ni/Mg2Al1 (Figure 5.3). Increasing the Al content in the Mg-Al mixed oxide support material continued the improvement in NiO reducibility resulting in a lowering of the peak temperature from 1153 K (Ni/Mg2Al1) to 1064 K (Ni/Mg1Al2). This coincides with the incorporation of MgO into $MgAl_2O_4$ suggesting that the interaction of Ni with MgO ($Ni_xMg_{1-x}O$ solid solution) is much stronger than Ni interaction with $MgAl_2O_4$ in the form of $Ni_xMg_{1-x}Al_2O_4$.

TPR-H_2 profiles for the γ-Al_2O_3 supported nickel catalysts, Ni/Al and Ni/KAl, indicate that NiO interaction with γ-Al_2O_3 takes several forms: NiO interacting with surface γ-Al_2O_3, NiO interacting with K modified γ-Al_2O_3, and $NiAl_2O_4$. From our XRD results of the Al and KAl supported samples only NiO and $NiAl_2O_4$ are found and no apparent effect of K doping on the crystal structure was observed. Two distinct peaks in the rate of H_2 consumption are identified for the Ni/Al sample corresponding to NiO interacting with surface γ-Al_2O_3 (888 K) and $NiAl_2O_4$ (1129 K), which is in good agreement with reported values [Juan-Juan et al. (2006); Hou et al. (2003)]. Ni/KAl gave three maxima in H_2 consumption, located at 822, 991, and 1096 K, which are associated with the intimate interaction of NiO with surface γ-Al_2O_3, NiO interacting with K modified surface γ-Al_2O_3 [Juan-Juan et al. (2006)], and $NiAl_2O_4$ respectively.
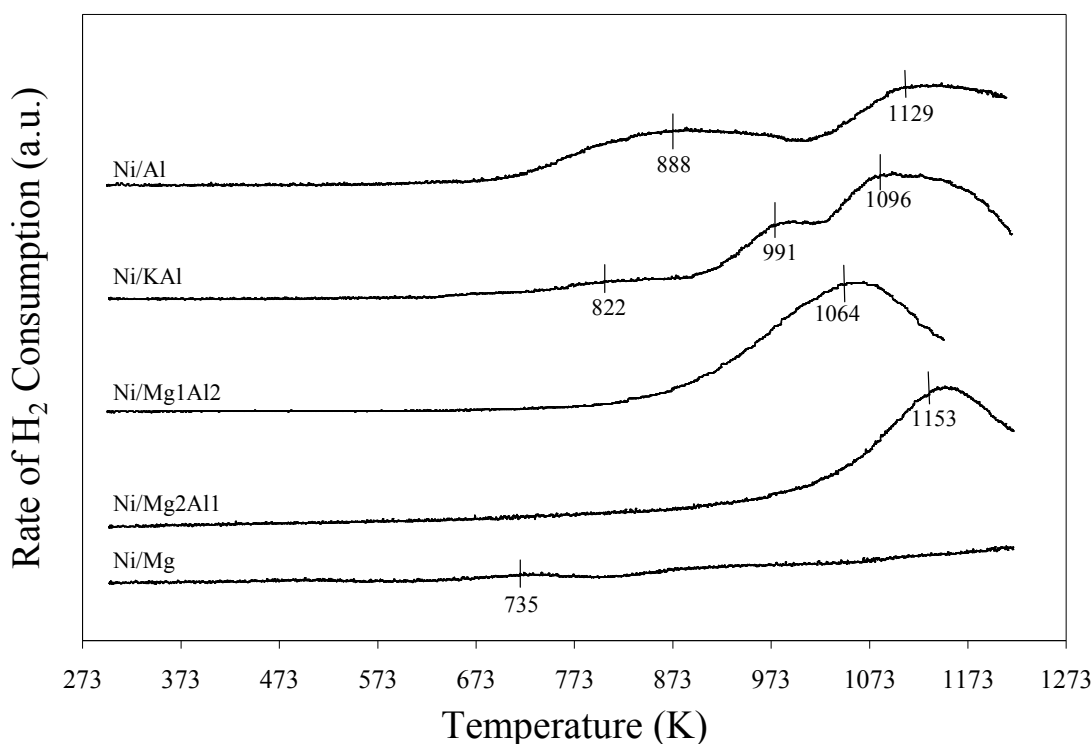
Figure 5.3: TPR-H_2 profiles for pure and mixed oxide supported nickel catalysts calcined at 1023 K.

The relative degree of reduction, defined as the total H_2 consumed for a sample divided by the total H_2 consumed for the Ni/Al sample, is shown in Table 5.3. Integration of the area under the H_2 consumption curve up to 1023 K shows a direct relationship between the relative degree of reduction and the Al content of the support. Increasing the integration temperature to 1123 K, instead of 1023 K, the degree of reduction passed through a maximum at a Al/(Al+Mg) ratio of 0.693 (Ni/Mg1Al2). The XRD results for Ni/Mg1Al2 in both calcined and reduced forms (Figure 5.1 and Figure 5.2) show a fully formed $MgAl_2O_4$ spinel structure whereas the Al_2O_3 supported catalyst had a defect Al_2O_3 spinel structure showing Ni^{2+} inclusion. This suggests that the strength of the interaction of Ni^{2+} with $MgAl_2O_4$ is less than with the Al_2O_3 structure, which is supported by the TPR data, and could be due to the presence of the Mg^{2+} ions.

Table 5.3: Relative degree of reduction

Sample ID	Degree of Reduction Relative to Ni/Al[a]	
	1023 K	1123 K
Ni/Al	1.00	1.00
Ni/KAl	0.75	0.98
Ni/Mg1Al2	0.92	1.17
Ni/Mg2Al1	0.60	0.78
Ni/Mg	0.36	0.33

[a] Defined as total H_2 consumed per gram of Ni up to 1023 and 1123 K respectively for each catalyst divided by the total H_2 consumed per gram of Ni for the same temperature span by the Ni/Al catalyst

The acidic and basic properties of the Mg-Al mixed oxide and pure oxide supported nickel catalysts were characterized by temperature programmed desorption (TPD) of room temperature adsorbed NH_3 (basic molecule, acidic probe) and CO_2 (acidic molecule, basic probe). The basic site strength and density data of the nickel-supported catalysts investigated by CO_2-TPD are presented in Figure 5.4. The shape and breadth of the CO_2 desorption curves reveal considerable heterogeneity in the base site strength distributions and densities for the pure and mixed oxide catalysts. IR analysis of CO_2 adsorbed on Mg-Al mixed oxide materials has shown that CO_2 forms three distinct chemisorbed species on basic sites and are characterized as low (bicarbonate), medium (bidentate carbonate), and high (unidentate carbonate) strength [Shen et al. (1994,1998); Di Cosimo et al. (1998,2000); Prinetto et al. (2000); Diez et al. (2003); Prescott et al. (2005)] and are shown pictorial in Table 5.4. Bicarbonates are formed on Brønsted base sites and are the result of the interaction of CO_2 with surface hydroxyl groups. Surface Lewis acid-base site pairings, such as Al^{3+}-O^{2-} and Mg^{2+}-O^{2-}, adsorb CO_2 in the bidentate carbonate coordination, while the unidentate carbonate species are formed by the interaction of CO_2 with strong Lewis base sites (low-coordination surface O^{2-}). Deconvolution of the desorption curves was achieved by accounting for the contribution of each site type, weak, moderate, and strong, to the overall desorption curve using an exponential-Gaussian hybrid model as described in section 3.2.6. Base site strength distribution and density are given in Table 5.6.

Table 5.4: Idealized CO₂-base site interactions. Adapted from Di Cosimo et al. (1998).

Representation of surfaced adsorbed CO_2 species			
Basic Site Strength	Weak	Moderate	Strong
Adsorbed Species	Bicarbonate	Bidentate Carbonate	Unidentate Carbonate
Adsorption Site	Surface hydroxyl, **Brønsted**	Acid-base pairing (i.e., Mg^{2+}-O^{2-}), **Lewis**	Low coordination O^{2-}, **Lewis**

Table 5.5: Idealized NH₃-acid site interactions. Adapted from Prinetto et al. (2000) and Auroux and Gervasini et al. (1990).

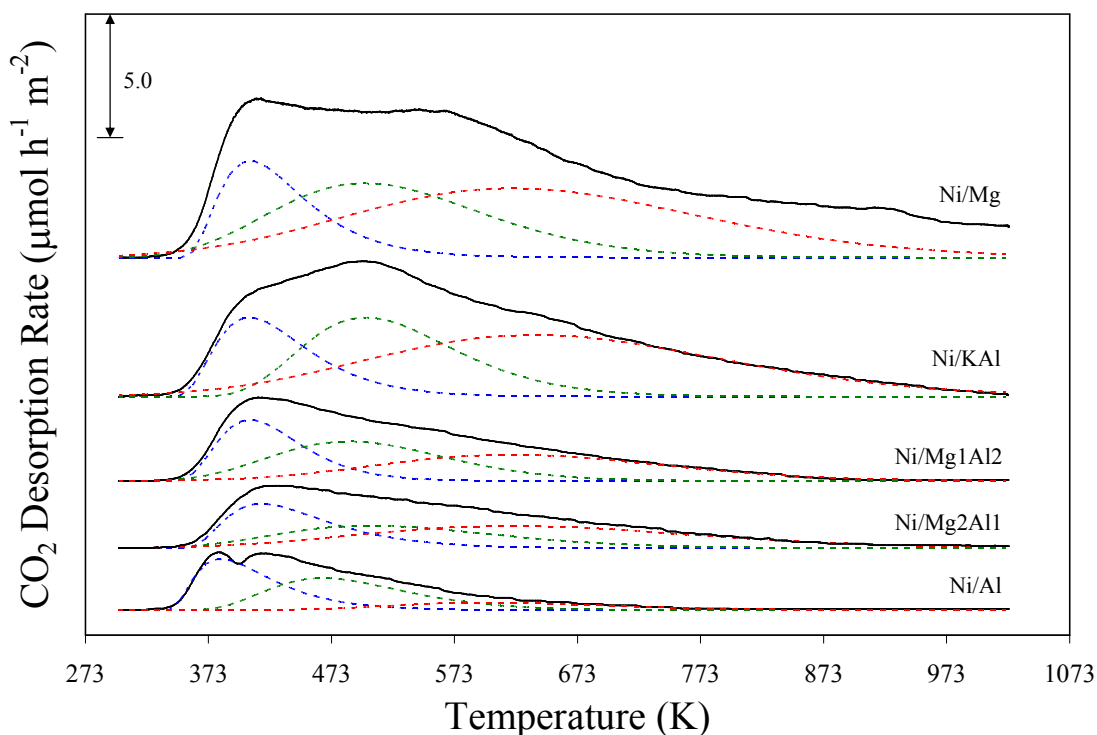| Representation of surfaced adsorbed NH_3 species			
Basic Site Strength	Weak	Moderate	Strong
Adsorbed Species	Coordinated NH_3	Coordinated NH_3, with H-O interaction	Coordinated NH_3
Adsorption Site	Surface hydroxyl, **Brønsted**	Acid-base pairing (i.e., Al^{3+}-O^{2-}), **Lewis**	Electron deficient Al^{3+}, **Lewis**

Figure 5.4: TPD-CO_2 profiles for pure and Mg-Al mixed oxide supported nickel catalysts. Weak site type contribution (Blue dashed line). Moderate strength site type contribution (Green dashed line). Strong site type contribution (Red dashed line).

Deconvolution revealed three distinct desorption peaks with maxima in the rate of CO_2 desorption occurring at 406-416, 486-505, and 620-630 K for the Mg-containing and Ni/KAl catalysts, while for Ni/Al the maxima in the rate of CO_2 desorption appeared at 383, 466, and 600 K. This shift to lower CO_2 desorption temperatures for the Ni/Al sample indicates that the bond strength between CO_2 and the surface is less than with the Mg- or K-containing samples and is attributed to the reduced electronegativity of the γ-Al_2O_3 surface [Shen et al. (1994)]. The Ni/Al catalyst possessed the lowest base site density, 0.466 μmol m^{-2}, a result comparable to reported values [Di Cosimo et al. (1998, 2000); McKenzie et al. (1992)(]. Low and medium strength base sites corresponding to surface HO^- and Al^{3+}-O^{2-} Lewis acid-base pairings dominate the Ni/Al surface, while the contribution of the high-strength base site type, related to low-coordination surface O^{2-}, is very small. Alkaline

impregnation of γ-Al$_2$O$_3$ with K, performed to neutralize the acidic nature of γ-Al$_2$O$_3$, considerably increased the number of basic sites (approximately a 5-fold increase) and the strength of the CO$_2$ bond with the surface. The absolute density of all site types was greater for the alkaline treated support but most important was the increase in the relative contribution of the high-strength base site type. Such an increase in the density of the strong base site type indicates that potassium (K) was added in excess of the amount required for neutralization of the acidic sites associated with γ-Al$_2$O$_3$ and led to the formation of highly basic K$_2$O-rich regions on the surface. The MgO-supported catalyst, Ni/Mg, exhibited the highest base site density, 2.64 μmol m^{-2}, and favored the medium- and high-strength base site types, a result that compares well to reported values [Di Cosimo et al. (1998, 2000); McKenzie et al. (1992)].

Table 5.6: Acidic and Basic Site Density for the prepared catalysts

Sample	Base Site Distribution and Density					Acid Site Distribution and Density					Ratio
	L^a	M^a	H^a	μmol m^{-2}	μmol g^{-1}	L^a	M^a	H^a	μmol m^{-2}	μmol g^{-1}	Acidic/Basic
Ni/Al	41.6	42.5	15.9	0.466	26.25	26.4	23.1	50.5	0.494	27.83	1.06
Ni/KAl	18.4	29.1	52.5	1.826	115.4	71.5	28.5	0.0	0.089	5.624	0.0484
Ni/Mg1Al2	26.5	35.0	38.4	0.854	77.27	45.0	24.1	30.9	0.200	18.08	0.234
Ni/Mg2Al1	28.1	28.8	43.1	0.750	68.94	39.9	22.0	38.1	0.136	12.50	0.181
Ni/Mg	18.2	32.1	49.7	2.643	196.7	0	0	0	0	0	0

^{a} (L)ow, (M)edium, and (H)igh temperature peaks determined by deconvolution of the TPD curves.

The Mg-Al mixed oxide supported nickel catalysts, NiMg1Al2 and Ni/Mg2Al1, exhibited moderate base site strength and density compared to the pure oxide supported nickel catalysts. A comparison of the Mg-Al mixed oxide supported catalysts with the MgO-supported catalyst, Ni/Mg, reveals the substantial effect that Al has on reducing the base site strength and density. Increasing the Al content of the support material from 0 (Ni/Mg) to 0.351 (Ni/Mg2Al1) (Table 5.6) decreased the base site density (μmol m^{-2}) by a factor of 3.5 and reduced the contribution of the medium- and high-strength site types. From our XRD

results, the Ni/Mg2Al1 support consisted of a mixture of MgO and $MgAl_2O_4$ with no γ-Al_2O_3 present. Assuming that Al was completely incorporated into the $MgAl_2O_4$ spinel phase, 73 mol% of the Mg in the sample would be present as MgO. The substantial decrease in the base site density is inconsistent with the fractional reduction in the support composition of MgO. McKenzie et al. (1992) using ^{27}Al MAS NMR and Di Cosimo et al. (1998) using a combined XPS and bulk elemental analysis method found enrichment of Al on the surface of calcined Mg-Al mixed oxides having an Al/(Al+Mg) ratio < 0.5, while their XRD results showed only the presence of a crystalline MgO phase. They proposed that an amorphous AlO_y species formed on the surface of the MgO crystallites reducing the strength and density of the basic sites by blocking the Mg^{2+}-O^{2-} (medium strength) or low-coordination O^{2-} (high strength) sites from CO_2 adsorption. Our CO_2-TPD results suggest that Al incorporation into the $MgAl_2O_4$ spinel for the Ni/Mg2Al1 sample was not complete and that an amorphous AlO_y surface species, which would not be observed in the XRD patterns, was created resulting in a substantial decrease in basic site strength. Further increasing the Al content from 0.351 (Ni/Mg2Al1) to 0.693 (Ni/Mg1Al2) slightly increased the total base site density of the sample, while the base site strength distribution shifted from high- to medium-strength sites. Di Cosimo et al. (1998, 2000) found similar results for their Mg-Al mixed oxides having a similar Al/(Al+Mg) ratio. They suggested that the increase in Al content stabilized the formation of an Al-rich phase resulting in the depletion of the amorphous surface AlO_y species and the exposure of the MgO phase at the surface. In our case, the increase in Al content resulted in the complete incorporation of Mg into an $MgAl_2O_4$ spinel phase, as indicated by the disappearance of the $Ni_xMg_{1-x}O$ (cubic oxide) peak in our XRD results for reduced Ni/Mg1Al2. $MgAl_2O_4$, unlike MgO, does not possess strong basic sites [Rossi et al. (1991)] since the surface O^{2-} anions of the spinel are bound to at least one Al^{3+} cation resulting in the reduction or elimination of the low-coordination O^{2-}, high-strength, sites. Incorporation of Mg and Al into the spinel phase increased the acid-base site pairings (Mg^{2+}-O^{2-}-Al^{3+}) and thus increased the contribution of the medium strength site.

NH$_3$-TPD was performed to characterize the acidic site strength and density of the supported nickel catalysts. The rate of NH$_3$ desorption as a function of temperature is given in Figure 5.5. Similar to the CO$_2$-TPD results, the broad desorption curves of the Al-containing catalysts are indicative of an inhomogeneous surface containing different acidic site types and densities. Deconvolution of the NH$_3$ desorption curves, using the technique described above, revealed three distinct maxima in the rate of NH$_3$ desorption occurring at 410-421, 514-527, and 622-634 K for the Ni/Mg1Al2, Ni/Mg2Al1, and Ni/Al catalysts, while the high-temperature peak was absent for Ni/KAl. On Mg-Al mixed oxide catalysts, Di Cosimo et al. (2000) and Diez et al. (2003) attributed NH$_3$ chemisorption on Mg-Al mixed oxides to two site types: low (Brønsted acid) and high temperature (Lewis acid). Brønsted acidity was described as the interaction of NH$_3$ with surface hydroxyl groups and Lewis acidity on the Mg-Al mixed oxides was attributed to nitrogen interaction with an Al^{3+}-O^{2-}-Mg^{2+} acid-base pairing having an acidic nature. On γ-Al$_2$O$_3$, Lewis acidity was attributed to nitrogen interaction with an electron-deficient Al^{3+}. In deconvoluting our NH$_3$-TPD curves, we accounted for the contribution of Brønsted and both Lewis acid site types. The interaction of NH$_3$ with these three site types is shown pictorially in Table 5.5. We propose that the strong Lewis acid sites associated with an electron-deficient Al^{3+} are present in the mixed oxide samples as an amorphous AlO$_y$ species, as discussed above, and must be accounted for in the explanation of the acidic properties of the mixed oxides. The contribution of the individual site types, Brønsted acid and weak and strong Lewis acid sites, to the overall desorption curves are presented in Table 5.6.
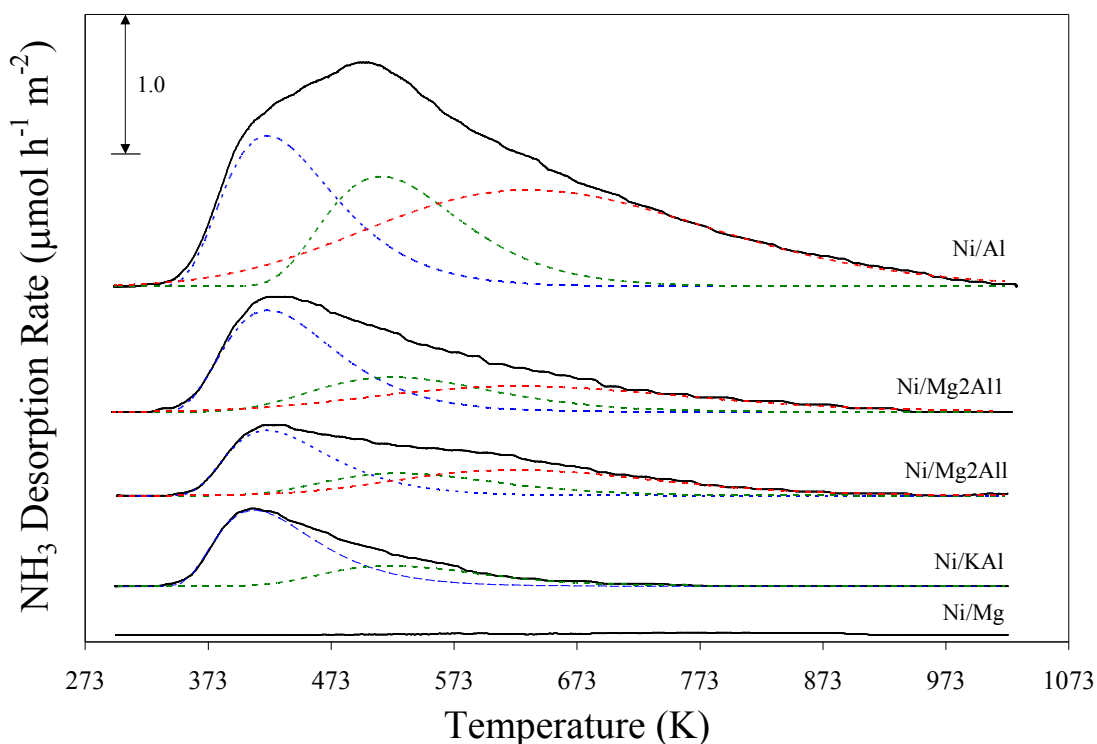
Figure 5.5: TPD-NH₃ profiles for pure and Mg-Al mixed oxide supported nickel catalysts. Weak site type contribution (Blue dashed line). Moderate strength site type contribution (Green dashed line). Strong site type contribution (Red dashed line).

Very little to no NH_3 desorbed from Ni/Mg indicating that the catalyst does not possess acidic sites. This finding is in agreement with previous work [Wang et al. (1997), Aberuagba et al. (2002), and Prescott et al. (2005)]. For example, Wang et al. (1997) found that increasing the calcination temperature of MgO from 873 to 1073 K completely eliminated acidic sites, resulting in no NH_3 desorption. They proposed that acidic sites were present in the MgO sample calcined at 873 K as a result of oxygen vacancies in the structure and subsequent presence of unpaired Mg^{2+} cations, giving rise to a local positive charge. Increasing the calcination temperature to 1073 K eliminated the oxygen deficiency and hence the acidic sites. In this study, the catalysts were calcined at 1023 K for 5 h, which was sufficient to eliminate the acidic sites in the Ni/Mg sample.

The γ-Al$_2$O$_3$ supported catalyst, Ni/Al, was the most acidic catalyst having the highest acidic site density and strong Lewis acid site contribution. Strong Lewis acid sites accounted for approximately 50% of the acid sites, in good agreement with the findings of Di Cosimo et al. (1998) and Diez et al. (2003). The abundance of strong Lewis acid sites on the Ni/Al sample are related to electron-deficient Al^{3+} cations that occupy tetrahedral positions [Abbattista et al. (1989)], while the Al^{3+}-O^{2-} cation-anion pairing, having an acidic nature, account for the weak Lewis acid sites. K-doping γ-Al$_2$O$_3$ significantly decreased the acid site density and the strength of the bond between NH$_3$ and the surface. The strong Lewis acid sites were completely eliminated resulting in the Ni/KAl having only weak and moderate strength acid sites and the absolute density of the weak Lewis acid site was decreased.

Similar to the CO$_2$-TPD results presented above, the Mg-Al mixed oxide supported catalysts exhibited moderate acid site strength and density compared to the pure oxide supported catalysts. A comparison of the Mg-Al mixed oxide supported catalysts with Ni/Mg reveals the substantial effect that Al has on the acid site strength and density. Increasing the Al content of the support from 0 (Ni/Mg) to 0.351 (Ni/Mg2Al1) substantially increased the acid site density and strength. Al addition led to the formation of a MgAl$_2$O$_4$ spinel phase dispersed in MgO (Figure 5.1, Figure 5.2, and Table 5.2), which was responsible for the increase in acidity. The spinel phase accounts for the presence of the Brønsted acid and weak Lewis acid sites (Al^{3+}-O^{2-}-Mg^{2+}), however, it lacks strong Lewis acid sites [Rossi et al. (1991)]. Strong Lewis acid sites in Ni/Mg2Al1 are attributed to the surface enrichment of Al^{3+} in the form of amorphous AlO$_y$ species as discussed in the CO$_2$-TPD section. Increasing the Al content from 0.351 (Mg2Al1) to 0.693 (Mg1Al2) resulted in the complete incorporation of Al and Mg into the spinel phase as seen from the XRD results. As a result, the total acid site density of the Ni/Mg1Al2 sample increased but the contribution of the strong Lewis acid sites decreased due to the incorporation of the amorphous AlO$_y$ species found in the Ni/Mg2Al1 sample into the bulk spinel phase.

In comparison with the parent pure oxide supported catalysts, Ni/Mg and NiAl, the acid-base properties of Mg-Al mixed oxide supported catalysts were moderated in terms of site strength distribution and density. Most important among these modifications was the significant decrease in the density of the strong Lewis acid and strong Lewis base sites associated with γ-Al_2O_3 and MgO, respectively. The effect of the Al/(Al+Mg) ratio on the acidic/basic site density ratio is presented in Table 5.6. The ratio of acidic to basic sites increased as Al content increased from 0 for Ni/Mg to 1.06 for Ni/Al. However, the acidic/basic site density ratio was not proportional to the composition of the mixed oxide supports, which were found to be predominantly basic (i.e. acidic/basic site ratios < 0.5) even when the support was composed primarily of Al.

5.2 Catalytic performance

The activity, selectivity, and stability of pure and Mg-Al mixed oxide supported nickel catalysts were evaluated at 773 and 923 K, H_2O:EtOH = 8.4:1, GHSV = 260 000 mL_{Feed} h^{-1} g_{cat}^{-1} (corresponding to 50 mg of catalyst sample), and atmospheric pressure for the production of H_2 via the steam reforming of ethanol. Prior to the reaction, catalysts were reduced in-situ at 1023 K for 1 h in 200 mL min^{-1} of 10% H_2/N_2 and cooled to the desired reaction temperature in flowing N_2. After each reaction, the spent catalyst was cooled in flowing N_2 to room temperature and stored for post reaction characterization.

5.2.1 Evaluation at 773 K

As seen in Figure 5.6, the initial ethanol conversion for all supported-Ni catalysts was high; however, as time on stream progressed, the effect of the support composition on catalyst stability becomes apparent. Table 5.7 presents ethanol conversion, H_2O utilization, and product yield results for the prepared catalysts evaluated at 773 K after 10 h on stream as well as the equilibrium expectations and the contribution of the catalyst diluent and reactor system. The contribution of the catalyst diluent (SiC), the reactor wall (quartz), and homogeneous gas phase reactions to the conversion of ethanol were found to be minimal at

773 K, giving an ethanol conversion of 0.3% with the detectable products being acetaldehyde and ethylene. H_2, produced via ethanol dehydrogenation (R.11), was not detected because its concentration in the product stream was below the TC detector sensitivity of the gas chromatograph.

Table 5.7: Ethanol conversion and product selectivity at 10 h time on stream (T = 773K, H_2O:EtOH = 8.4:1, GHSV = 260000 mL_{Feed} h^{-1} g_{cat}^{-1})

	X_{EtOH} (%)	η_{H_2O}	Yield					
			H_2	CO_2	CO	CH_4	CH_3CHO	C_2H_4
Equilibrium	100	1.70	3.52	1.28	0.13	0.59	0.00	0.00
SiC	0.30	---	0.00	0.00	0.00	0.00	0.28	0.72
Ni/Al	98.70	-0.35	0.73	0.22	0.02	<0.01	0.008	0.87
Ni/KAl	51.53	2.35	4.52	0.16	0.16	0.20	0.07	0.0013
Ni/Mg1Al2	39.96	2.31	4.34	1.30	0.22	0.17	0.07	0.08
Ni/Mg2Al1	27.10	1.49	3.41	1.11	0.21	0.18	0.195	0.009
Ni/Mg	6.52	1.29	1.41	0.14	0.14	<0.01	0.85	0.004

Ni/Al was the best performing catalyst in terms of ethanol conversion, but as seen in Figure 5.7, was highly selective for ethylene, a coke precursor. Ethylene is produced by ethanol dehydration (R.11) following an E_2-elimination mechanism, which is catalyzed by an acid-base site pairing where the acidic site is stronger than the base site [Di Cosimo et al. (1998)]. Acid-base site characterization of the Ni/Al catalyst by NH_3- and CO_2-TPD revealed that this catalyst had an acid/base site ratio of 1.06 (Table 5.6) and the highest concentration of moderate and strong acidic sites indicating that the catalyst, and more specifically the support (γ-Al_2O_3), was ideal for ethylene production.

$$CH_3CH_2OH \longrightarrow C_2H_4 + H_2O \qquad\qquad (R.11)$$

Initially, Ni/Al was active for reactions producing steam-reforming products (H_2 and CO_x) giving a H_2 yield of 3.90 (Figure 5.8), CO_x yield of 1.04 (Figure 5.9), and consuming 2.4 moles of H_2O per mole of ethanol converted (Figure 5.10).

As time on stream progressed, ethylene yield increased considerably (Figure 5.7) and the ability of the catalyst to produce steam-reforming products (H_2 and CO_x) decreased as seen by a decline in the H_2 yield, CO_x yield, and H_2O utilization. The H_2O utilization plot (Figure 5.10) reveals the change in the dominant reaction pathway. After 1 h of operation, H_2O utilization changed from positive to negative indicating a change from H_2O-consuming to H_2O-producing reactions, thus confirming that the dominant reaction pathway on Ni/Al switched from steam reforming to dehydration (R.11). Several groups [Haga et al., 1997; Aupretre et al. (2004, 2005); Fatsikostas and Verykios (2004); Coleman et al. (2007) given in Appendix D] have shown that γ-Al_2O_3, although active for ethanol dehydration, is not capable of steam reforming ethanol to produce H_2 and CO_x and that an active metal phase is required. The rapid decline in the steam-reforming products (H_2 and CO_x) indicate that nickel deactivated in the presence of high ethylene concentrations, most likely via carbon encapsulation of the nickel crystallite. As will be discussed in a subsequent section, XRD and TPO analysis of the carbonaceous deposits on the Ni/Al catalyst revealed a significant amount of accumulated graphitic (filamentous) carbon. Carbon balance calculations showed that after 0.15 h on stream (first GC injection) only 89.4% of the carbon entering the reactor was accounted for in the product gas stream, while for the remaining injections, the carbon balance was nearly 100% (99.45% ± 0.27). Carbon accumulation during the first 0.66 h on stream (by the second injection) led to rapid deactivation of the nickel active sites and subsequent loss in selectivity for the steam-reforming products (H_2 and CO_x); however, had no effect on the conversion of ethanol.
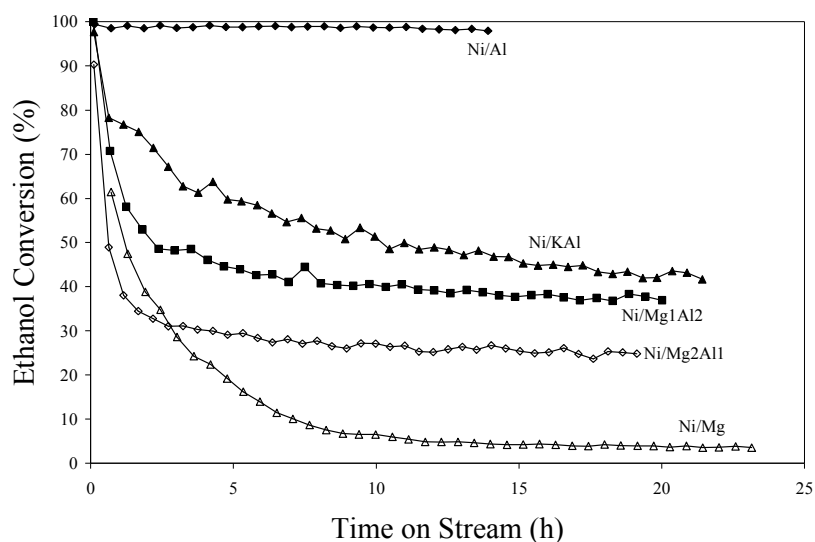
Figure 5.6: Ethanol conversion and catalyst stability as a function of time on stream for pure and Mg-Al mixed oxide supported nickel catalysts evaluated at 773 K, H_2O:EtOH = 8.4:1, GHSV = 260000 mL_{Feed} h^{-1} g_{cat}^{-1}.
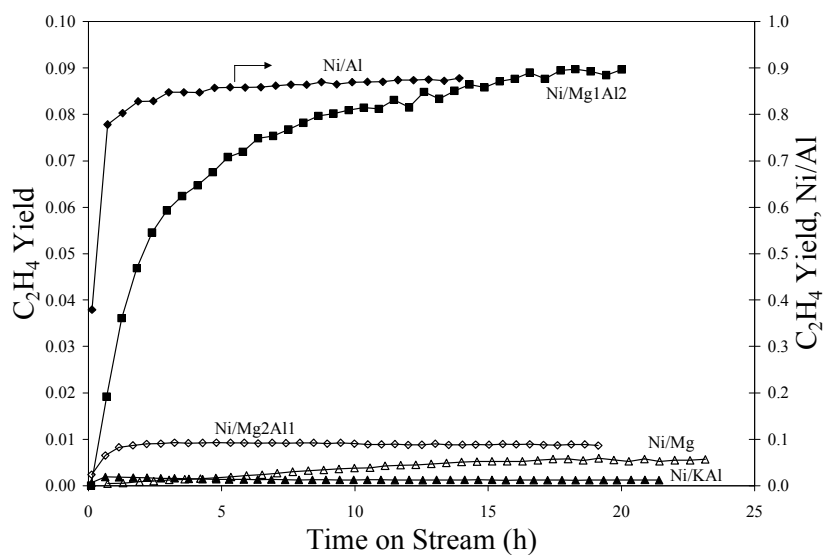

Figure 5.7: Ethylene yield as a function of time on stream for pure and Mg-Al mixed oxide supported nickel catalysts evaluated at 773 K, H_2O:EtOH = 8.4:1, GHSV = 260000 mL_{Feed} h^{-1} g_{cat}^{-1}.
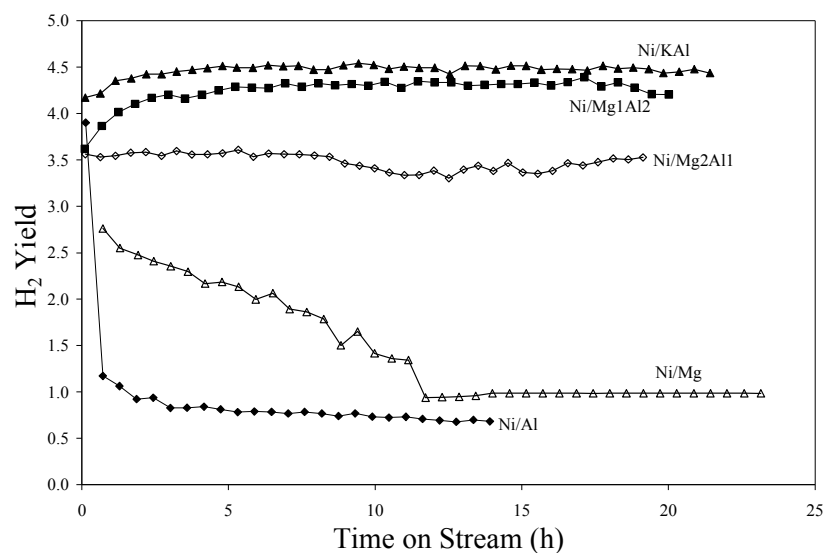
Figure 5.8: H$_2$ yield as a function of time on stream for pure and Mg-Al mixed oxide supported nickel catalysts evaluated at 773 K, H$_2$O:EtOH = 8.4:1, GHSV = 260000 mL$_{Feed}$ h^{-1} g$_{cat}^{-1}$.
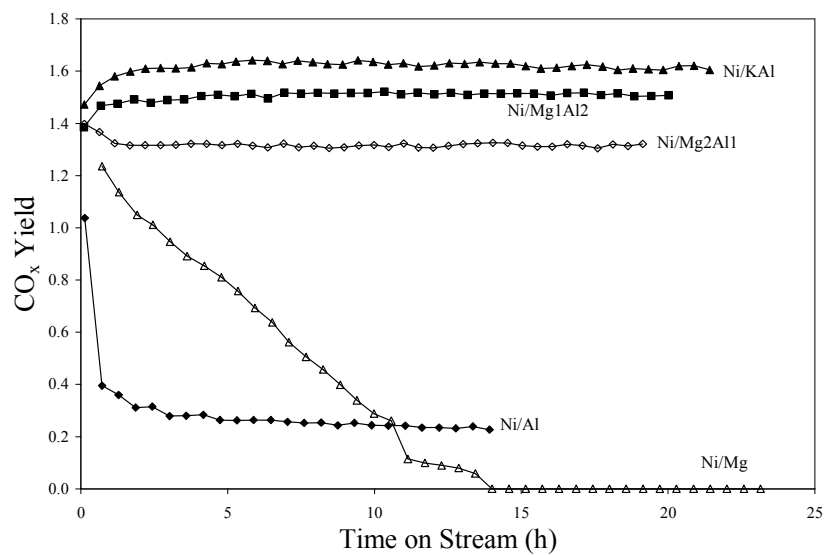

Figure 5.9: CO$_x$ yield as a function of time on stream for pure and Mg-Al mixed oxide supported nickel catalysts evaluated at 773 K, H$_2$O:EtOH = 8.4:1, GHSV = 260,000 mL$_{Feed}$ h^{-1} g$_{cat}^{-1}$.
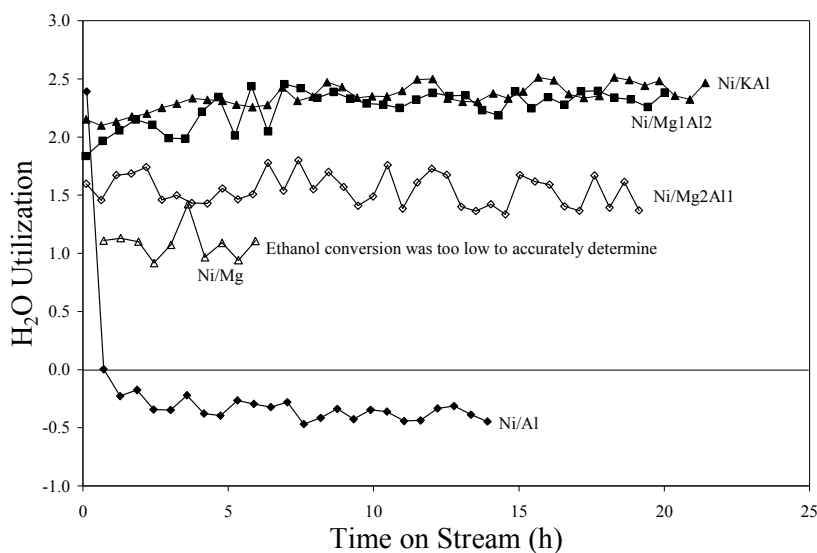
90

Figure 5.10: H_2O utilization as a function of time on stream for pure and Mg-Al mixed oxide supported nickel catalysts evaluated at 773 K, H_2O:EtOH = 8.4:1, GHSV = 260000 mL_{Feed} h^{-1} g_{cat}^{-1}.

K-doping the γ-Al_2O_3 support (Ni/KAl) improved selectivity for the steam reforming products, greatly reduced ethylene selectivity (Figure 5.7), but adversely affected ethanol conversion (Figure 5.6). Ni/Al and Ni/KAl gave similar performances in the first hour of operation, however, as time on stream progressed, Ni/KAl experienced deactivation in ethanol conversion, while maintaining activity for the ethanol steam reforming reaction. H_2 and CO_x yield and H_2O utilization remained relatively constant over the entire length of the experiment (20 h) even though Ni/KAl experienced significant deactivation. In fact, H_2 and CO_2 yields (Table 5.7) for Ni/KAl exceeded equilibrium expectations. The improved performance (H_2 and CO_2 yield and H_2O utilization) of Ni/KAl compared to Ni/Al is associated with the modified acid-base characteristics of the K-treated catalyst. Potassium treatment eliminated the strong Lewis acid sites associated with γ-Al_2O_3 and reduced the overall acidity of the catalyst resulting in a predominantly basic catalyst (Table 5.6). As a result, activity for the acid-catalyzed ethanol dehydration reaction (R.11) was reduced and this is verified by Ni/KAl giving the lowest ethylene yield (<0.002) of the catalysts studied at

773 K. However, unexpectedly, it also experienced the highest rate of carbon accumulation (Table 5.9). These observations suggest that carbon accumulation on supported-nickel catalysts in ethanol steam reforming reaction environments is caused by multiple reactant species, not exclusively ethylene. In fact, acetaldehyde steam reforming experiments performed in our lab have verified that carbon accumulation can occur on supported nickel catalysts without the presence of ethylene. The addition of a small amount of potassium (K) to Ni/γ-Al$_2$O$_3$ has been shown to increase the rate of carbon deposition favoring filamentous carbon growth at 733 K [Dimicheli et al. (1994)]. Dimicheli et al. (1994) proposed that potassium (K) weakened the Ni-support interaction making it easier for Ni to detach from the surface: a mechanism required for the production of filamentous carbon. This is consistent with our findings that the product selectivity was not affected by the loss in activity suggesting that deactivation was associated with the loss of active sites and not modification of the site or the reaction mechanism.

Ni/Mg exhibited rapid loss in activity (Figure 5.6) approaching complete deactivation in approximately 10 h on stream. Initially, Ni/Mg performed well giving high ethanol conversion and selectivity for the steam reforming products (H$_2$ and CO$_x$) but as the catalyst deactivated, the product selectivity changed favoring acetaldehyde formation. In fact, after approximately 10 h on stream, no C$_1$ species were detected in the product gas (Table 5.7). The lack of C$_1$ species in the product gas is consistent with deactivation of the nickel sites since MgO is not capable of gasifying ethanol. Acetaldehyde is generally considered a reaction intermediate of the ethanol steam reforming reaction scheme on transition metal catalysts [Fatsikostas and Verykios (2004); Benito et al. (2005); Fierro et al. (2005); Haryanto et al. (2005); Rasko et al. (2006); Roh et al. (2006a,b); Vaidya and Rodrigues (2006)], but can also be produced on metal oxides. On MgO, acetaldehyde is produced via ethanol dehydrogenation (R.7) catalyzed by a strong Brønsted base - weak Lewis acid - strong Brønsted base (O^{2-}-Mg^{2+}- O^{2-}) site arrangement [Di Cosimo et al. (2000)].

$$CH_3CH_2OH \longrightarrow CH_3CHO + H_2 \qquad\qquad (R.7)$$

The low activity of the Ni/Mg catalyst for the ethanol dehydrogenation reaction can be explained by the absence or very low density of Lewis acid sites (Table 5.6) due to the preferential exposure of unpaired O^{2-} anions (strong Brønsted base) and not the Mg^{2+} cation on the MgO surface [Di Cosimo et al. (1998, 2000), Fishel et al. (1994)]. Crystal structure analysis by XRD of calcined and reduced Ni/Mg revealed that Ni was retained in the $Ni_xMg_{1-x}O$ solid solution (cubic oxide) crystal structure even after reduction. Loss in activity and selectivity for the nickel catalyzed steam reforming reactions suggest oxidation of nickel in the $Ni_xMg_{1-x}O$ solid solution during the reaction by water.

Mg-Al mixed oxide supported nickel catalysts, Ni/Mg2Al1 and Ni/Mg1Al2, gave superior performance in terms of steam reforming product yield (H_2 and CO_x) compared to the pure oxide supported nickel catalysts. Ethanol conversion, stability, and product yield were dependent upon the Al and Mg content of the support. Increasing the Al content of the support from 0 (Ni/Mg) to 0.351 (Ni/Mg2Al1) improved ethanol conversion and catalyst stability (Figure 5.6). After 10 h, Ni/Mg completely deactivated, while Ni/Mg2Al, although it experienced considerable deactivation, stabilized in terms of ethanol conversion and product selectivity. Incorporation of Al into the MgO structure improved the stability of MgO in the presence of steam [Schaper et al. (1989), Ohi et al. (2006)], in our case by the formation of an $MgAl_2O_4$ spinel phase, but also enabled the formation of a separate reducible Ni^0 species (Figure 5.2). However, Ni inclusion in a $Ni_xMg_{1-x}O$ solid solution cannot be ruled out for the Ni/Mg2Al1 catalyst even though a reduced Ni phase was identified by XRD. Ni inclusion in $Ni_xMg_{1-x}O$, as discussed above concerning the performance of Ni/Mg, experiences rapid loss in activity and selectivity for the nickel catalyzed steam reforming reactions. Increasing the Al content of the support from 0.351 (Ni/Mg2Al1) to 0.693 (Ni/Mg1Al2), led to improved ethanol conversion, catalyst stability, and steam reforming product selectivity by completely incorporating MgO into $MgAl_2O_4$ and therefore eliminating Ni inclusion in $Ni_xMg_{1-x}O$.

The Mg-Al mixed oxide supported nickel catalysts were highly selective for steam reforming products (H_2 and CO_x) initially, and unlike the pure oxide supported nickel catalysts, deactivation had little effect on the product selectivity. The Mg-Al composition of the catalyst support affected the product selectivity (Table 5.7). The pure-oxide supported nickel catalysts were almost exclusively selective for C_2 products and not the steam reforming products after approximately 10 h on stream. In contrast, Mg-Al mixed oxide supported nickel catalysts had good selectivity for the steam reforming products, while still exhibiting selectivity for both C_2-products. C_2-product yield depended upon the composition of the support. Increasing the Al content of the support increased selectivity for ethylene because of an increase in the acid/base site ratio (Table 5.6) favoring the dehydration of ethanol (R.11), and an increase in the Mg content of the support increased selectivity for acetaldehyde production (R.7). Increasing the Al content of the mixed oxide support from 0.351 (Ni/Mg2Al1) to 0.693 (Ni/Mg1Al2) reduced selectivity for C_2 products and improved H_2 and CO_x yield, and H_2O utilization, indicating an improvement in the catalysts activity for the steam reforming reactions. Aside from differences in the acid-base properties, the Mg-Al content of the mixed oxide support affected the degree of nickel reduction and hence the interaction of Ni with the support. As discussed above, increasing the Al content of the support improved nickel reducibility (Table 5.3) and resulted in smaller nickel crystallites (Table 5.2). The presence of both Mg and Al in the support significantly improved the ability of nickel to produce the steam reforming products, compared to the pure oxide supported catalysts, Ni/Al and Ni/Mg. H_2 yield at least doubled and the conversion of ethanol to CO_x was greatly increased, as was the H_2O utilization.

After 10 hours on stream, the H_2 and CO_x yields for Ni/Mg1Al2 and Ni/KAl exceeded equilibrium expectations, while exhibiting selectivity for C_2 products, which are not thermodynamically favorable at 773 K (Table 5.7). Exceeding equilibrium expectations cannot, in this case, be attributed to carbon accumulation, which would artificially increase the H_2 and CO_x yield. The carbon balance for both catalysts exceeded 99.5% ± 0.2 and TPO of the spent catalysts revealed that less than 1% of the ethanol converted resulted in

deposited carbon. Therefore, these findings present evidence that the reaction is kinetically controlled and suggest a direct steam-reforming pathway for these catalysts. The direct steam-reforming pathway is described by an overall reaction (R.1) that produces H_2 and CO_x directly from a C_2 species (i.e., ethanol, acetaldehyde, or ethylene) while avoiding a methane reaction intermediate that is associated with decomposition reactions (R.8 and R.9).

$$CH_3CH_2OH \longrightarrow CH_4 + CO + H_2 \qquad\qquad (R.9)$$

$$CH_3CHO \longrightarrow CH_4 + CO \qquad\qquad (R.8)$$

Methane production and more specifically methane desorption from the catalyst surface is highly undesirable because it represents a redundancy in the reaction pathway. To elaborate, methane is produced from ethanol decomposition reactions (R.8 and R.9) by the hydrogenation of a surface methyl group (CH_3^*) followed by CH_4 desorption into the gas phase. For H_2 and CO_x to be produced from CH_4, it must be re-adsorbed and sequentially dehydrogenated. Therefore, the presence of CH_4 in the product gas presents redundancy and inefficiency in the utilization of the active sites. If, however, the adsorbed methyl group (CH_3^*) remains on the surface due to either insufficient surface hydrogen (H^*), rapid dehydrogenation, or reaction with surface –OH groups, H_2 and CO_x are produced in the absence of gas phase CH_4. It is proposed that it is the inability of the adsorbed methyl group (CH_3^*) to desorb from the surface as CH_4, especially at low temperatures, that enables these catalysts to deviate from equilibrium expectations, favoring the direct steam reforming reaction pathway and giving high H_2 and CO_2 yields.

5.2.2 Evaluation at 923K

At 923 K, all supported-nickel catalysts initially gave complete ethanol conversion (Figure 5.11), high H_2 and CO_x yield Figure 5.12 and Figure 5.13), and no selectivity for C_2 products (Figure 5.14). As time on stream progressed, the effect of the support composition on product selectivity and catalyst stability become apparent. The pure oxide supported nickel catalysts (Ni/Al, Ni/KAl, and Ni/Mg) experienced deactivation during the 20 h on

stream experiments. Table 5.8 presents ethanol conversion and product yields for the prepared catalysts at 923 K after 10 h on stream as well as the equilibrium expectations and the contribution of the reactor system. The reactor system (quartz wall, SiC diluent, gas phase reactions) gave an ethanol conversion of 16.87% and high selectivity for the C_2 products, acetaldehyde and ethylene, and no selectivity for the steam reforming products. Yields reported in Table 5.8 for SiC suggests that H_2 was produced via ethanol dehydrogenation (R.7), producing acetaldehyde. The later then being thermally decomposed (R.8) producing CH_4 and CO, which is in agreement with the similar yields of CO and CH_4 (Table 5.8). The absence of CO_2 in the product stream indicates that the water-gas shift and steam reforming reactions are not active without a catalyst.

Ni/Al rapidly deactivated and stabilized at approximately 50% ethanol conversion after 10 h on stream. The onset of deactivation was accompanied by a rapid rise in ethylene yield (Figure 5.14) and a corresponding decline in H_2 and CO_x yields (Figure 5.12 and Figure 5.13). Ethylene yield rapidly increased in the first 2 h of operation and then decreased to eventually stabilize after 10 h. The H_2 and CO_x yields followed the opposite trend, passing through a minimum. The relationship between the yield of the steam-reforming products, ethylene, and the loss in ethanol conversion in the first 2 h of operation is consistent with deactivation of the catalyst by an ethylene-assisted coking mechanism. The rise in ethylene yield in the first 2 h on stream coupled with the decline in the steam reforming products and ethanol conversion indicate a loss in active nickel metal sites, most likely by carbon deposition/nickel encapsulation. As will be discussed in a following section, Ni/Al experienced the greatest amount of carbon accumulation of the catalysts evaluated at 923 K (Table 5.8). After 2 h, the rise in the yield of the steam reforming products, decline in ethylene yield, and stabilization of the ethanol conversion suggest deactivation of the ethylene producing sites. During this period acetaldehyde selectivity slowly increased, an observation consistent with a reduction in the nickel sites. The complexity of the loss in activity and change in product selectivity suggests that multiple deactivation mechanisms and multiple catalytic site types are contributing to the overall reaction pathway and that the

dominant mechanism changes after approximately 2 h on stream. Even though the dominant mechanism changes to predominantly H_2 and CO_x producing, Ni/Al continues to be the worst performing catalyst at 923 K.
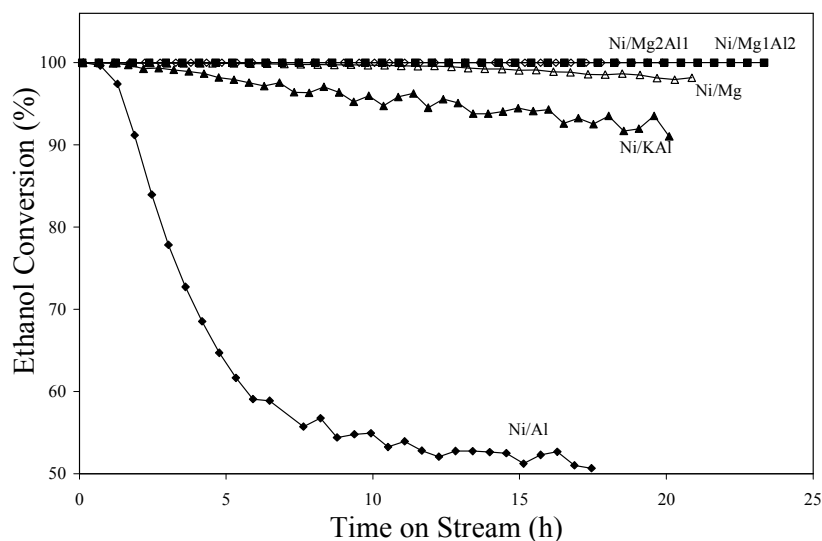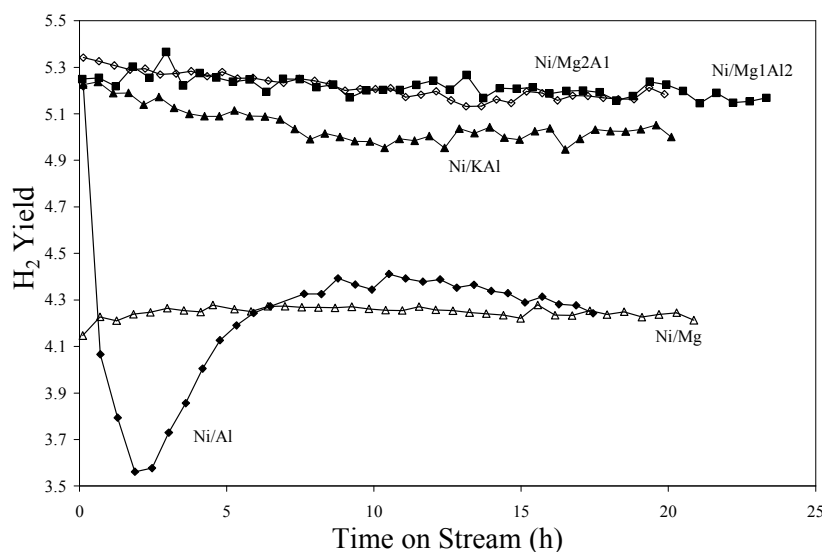

Figure 5.11: Ethanol conversion and catalyst stability as a function of time on stream for pure and Mg-Al mixed oxide supported nickel catalysts evaluated at 923 K, H_2O:EtOH = 8.4:1, GHSV = 260000 mL_{Feed} h^{-1} g_{cat}^{-1}.
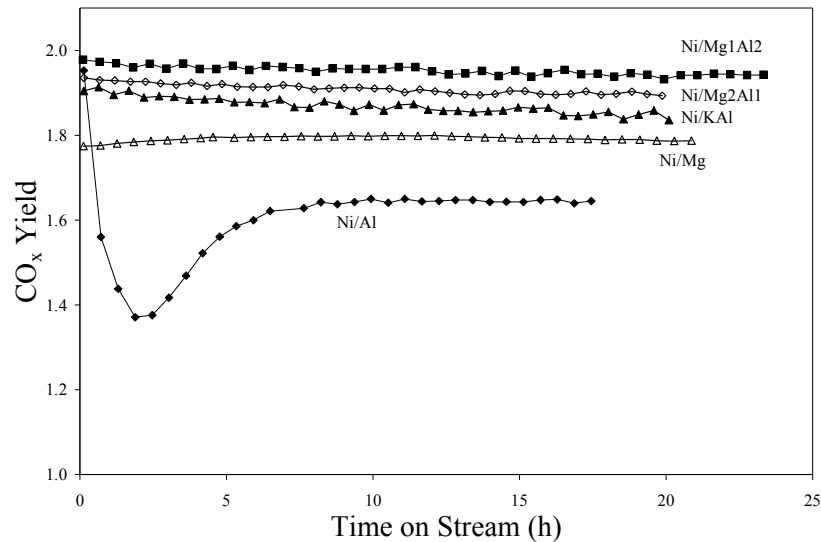

Figure 5.12: H_2 yield as a function of time on stream for pure and Mg-Al mixed oxide supported nickel catalysts evaluated at 923 K, H_2O:EtOH = 8.4:1, GHSV = 260000 mL_{Feed} h^{-1} g_{cat}^{-1}.

Figure 5.13: CO_x yield as a function of time on stream for pure and Mg-Al mixed oxide supported nickel catalysts evaluated at 923 K, H_2O:EtOH = 8.4:1, GHSV = 260000 mL$_{Feed}$ h^{-1} g$_{cat}$$^{-1}$.
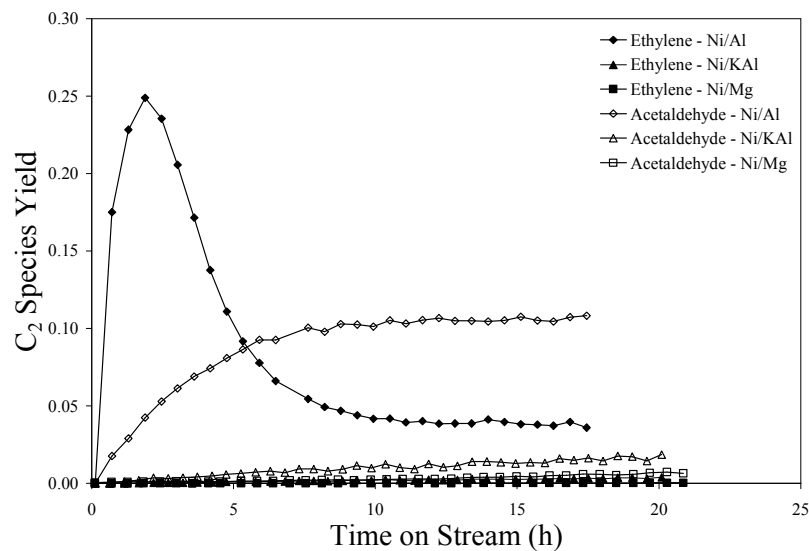

Figure 5.14: C_2-product yield as a function of time on stream for pure oxide supported nickel catalysts evaluated at 923 K, H_2O:EtOH = 8.4:1, GHSV = 260000 mL$_{Feed}$ h^{-1} g$_{cat}$$^{-1}$. Product gas for Mg-Al mixed oxide support catalysts had no C_2 products over the length of the experiment.

98

Table 5.8: Ethanol conversion and product selectivity at 10 h time on stream (T = 923K, H_2O:EtOH = 8.4:1, GHSV = 260000 mL_{Feed} h^{-1} g_{cat}^{-1}).

	X_{EtOH} (%)	η_{H_2O}	Yield					
			H_2	CO_2	CO	CH_4	CH_3CHO	C_2H_4
Equilibrium	100	2.35	5.29	1.38	0.59	0.03	0.00	0.00
SiC	16.87	---	0.69	0	0.16	0.17	0.60	0.20
Ni/Al	54.90	1.80	4.34	1.18	0.46	0.06	0.10	0.04
Ni/KAl	96.00	2.32	4.98	1.35	0.52	0.10	0.01	0.002
Ni/Mg1Al2	100	2.23	5.20	1.29	0.66	0.05	0	0
Ni/Mg2Al1	100	2.30	5.21	1.38	0.53	0.09	0	0
Ni/Mg	99.70	2.03	4.26	1.04	0.76	0.20	0.002	<0.001

Potassium doping of the γ-Al_2O_3 support (Ni/KAl) improved H_2 and CO_x yields and retarded deactivation compared to the untreated, Ni/Al, catalyst. Ni/KAl gave near-equilibrium H_2 and CO_x yields and substantially less selectivity for C_2 products than Ni/Al. Similar to the findings at 773 K, the improved performance of Ni/KAl compared to Ni/Al is related to neutralization of the acidic sites associated γ-Al_2O_3. Potassium doping transformed acidic γ-Al_2O_3 into a predominantly basic support (Table 5.6). Reduction in the acid site strength and density by potassium (K) treatment reduced selectivity for ethylene and therefore improved nickel stability and selectivity for the steam reforming reaction. In addition to reduced activity for the acid-catalyzed dehydration reaction producing ethylene (R.11), significant improvement in catalyst stability and improved coking resistance, which will be discussed in a subsequent section, is related to the catalytic activity of potassium (K) for the steam reforming of carbon above 873 K [Pechimuthu et al. (2006), Juan-Juan et al. (2004, 2006)]. Potassium treatment promoted two beneficial properties, elimination of strong acidic sites and promotion of carbon gasification, leading to improved nickel stability and resulted in near-equilibrium yields for the steam reforming products.

Ni/Mg performed much better at 923 K than at 773 K giving nearly complete ethanol conversion and good steam reforming product yield (H_2 and CO_x yield (Figure 5.12 and Figure 5.13)). The catalyst experienced only slight deactivation in the first 10 h and, as time

on stream progressed, so did the rate of deactivation. In the first 10 h, deactivation resulted in a 0.3% reduction in conversion, while the next 10 h gave a decline of 1.8%. However, results given in Table 5.8 indicate that, of the catalysts evaluated at 923 K, Ni/Mg gave the lowest yield for the steam reforming products (H_2 and CO_2) and the highest selectivity for CO and CH_4. Ni/Mg was found to be less active than the Al-containing catalysts for the CH_4 steam reforming (R.5) or water-gas shift (R.3) reactions.

$$CH_4 + H_2O \longrightarrow 3H_2 + CO \qquad\qquad\qquad (R.5)$$

$$CO + H_2O \longrightarrow H_2 + CO_2 \qquad\qquad\qquad (R.3)$$

An alternative interpretation would be that the rate of CO and CH_4 desorption from the Ni/Mg surface is greater than for the Al-containing catalysts. Regardless of the mechanism, the end result is that even though Ni/Mg converts more ethanol than the Al-containing catalysts it is less active for the reactions producing H_2 and CO_2. The reduced selectivity for H_2 and CO_2 is most likely related to the absence of a separate nickel phase (Figure 5.2) suggesting that $Ni_xMg_{1-x}O_y$ is not a good catalyst for water-gas shift (R.3) or methane steam reforming (R.5) reactions.

At 923 K, Ni/Mg1Al2 and Ni/Mg2Al1 were the best-performing catalysts in terms of activity, selectivity, and stability. Increasing the temperature from 773 to 923 K substantially improved the performance of both Mg-Al mixed oxide supported catalysts, especially when compared to the pure-oxide supported catalysts. Both Mg-Al mixed oxide supported nickel catalysts maintained 100% ethanol conversion (Figure 5.11), near-equilibrium steam reforming product yield (H_2 and CO_x yield (Figure 5.12 and Figure 5.13)), and no C_2 product selectivity (Figure 5.14) for over 20 h. The onset of deactivation (incomplete ethanol conversion) for the pure-oxide supported catalysts was accompanied by the appearance of C_2 products (i.e. ethylene, acetaldehyde) in the product gas, and thus the absence of C_2 products in the product gas, even after 20 h operation, signifies not only the enhanced stability of the Mg-Al mixed oxide catalysts at 923 K, but also that the onset of deactivation is not expected

for a much longer period of time on stream. Improved performance of the Mg-Al mixed oxide supported nickel catalysts may be related to the presence of $MgAl_2O_4$. The formation of $MgAl_2O_4$ upon calcination of the precipitated hydrotalcites resulted in the incorporation of the pure oxides, MgO and Al_2O_3, into a highly stable, slightly basic support, which stabilizes the Ni crystallite size [Villa et al. (2003)] and does not react with Ni to form less reactive $Ni_xMg_{1-x}O$ or $NiAl_2O_4$. Stabilization of the Ni crystallite by reducing sintering maintains catalytic activity and selectivity of the active site. For the mixed-oxide supported catalysts, this is verified by the catalyst's ability to maintain 100% ethanol conversion and the products yields for over 20 h on steam, which is much longer than the pure oxide supported catalysts. In addition to reducing Ni sintering, incorporation of MgO and Al_2O_3 into $MgAl_2O_4$ reduced the contribution of the strong acidic and basic sites (Table 5.6) compared to the pure oxide support nickel catalysts. As discussed above, reducing the strong acidic and basic site types reduces activity for by-product reactions producing ethylene (R.11) and acetaldehyde (R.7). Both byproducts adversely affect the activity, stability, and steam reforming product yields.

Another important observation is the improvement in performance of Ni/Mg2Al1 with increasing reaction temperature. At 773 K, Ni/Mg1Al2 gave better stability and steam reforming product yield than Ni/Mg2Al1, but increasing the temperature to 923 K resulted in the two mixed oxide supported catalysts performing very similarly. This improvement is consistent with the results obtained for Ni/Mg, the MgO-supported catalyst. The support material for Ni/Mg2Al1 is primarily MgO with $MgAl_2O_4$. Although a separate reducible nickel phase is present, the presence of a $Ni_xMg_{1-x}O_y$ phase cannot be ignored. It is highly likely that the inclusion of Ni in a $Ni_xMg_{1-x}O_y$ phase was responsible for the poor performance of Ni/Mg2Al1 at 773 K and similar to Ni/Mg, the significant improvement in performance at 923 K.

5.3 Characterization of spent catalysts

Upon removal of the spent catalyst from the reactor, it was apparent that carbonaceous deposits were present on all catalysts at both 773 and 923 K. Temperature-programmed oxidation of the spent catalysts (Table 5.9) revealed that the rate of accumulation of the carbonaceous deposits, either time averaged or with respect to the amount of ethanol converted, was higher for the experiments conducted at the lower temperature. This was verified by collecting XRD patterns of the spent catalyst (Figure 5.15). Graphitic carbon is present on the surface of all Al-containing catalysts while the MgO-supported catalyst, Ni/Mg, is free of graphitic carbon after the reaction at 773 K. Increasing the reaction temperature to 923 K substantially reduced the amount of graphitic carbon for all Al-containing catalysts. The diffraction pattern for graphitic carbon is still present for Ni/Al, while Ni/KAl and Ni/Mg2Al1 show very small deviations in the baseline suggesting the presence of minute amounts of graphitic carbon. Thermodynamic calculations predict [Garcia and Laborde (1991); Vasudeva et al. (1996)] a reduction in the amount of carbonaceous deposits at higher temperatures because of a reduction in the Gibbs' free energy of the reforming reactions that gasify ethanol and its products (C_2H_4, CH_3CHO, CH_4, and C).

Table 5.9: Temperature programmed oxidation of spent catalysts

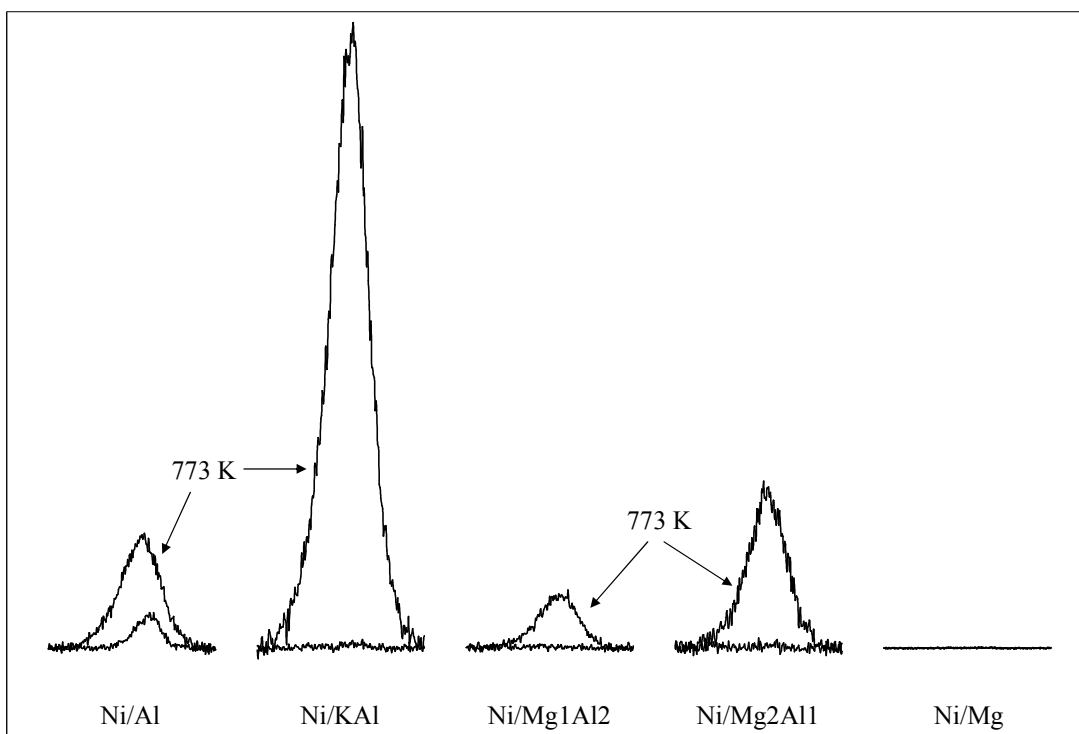| Catalyst | Rate of Carbon Deposition | | | | Peaks (K) | |
| | $(mg_{Coke}\ hr^{-1})$ | | $(mg_{Coke}\ g_{EtOH,Converted}^{-1})$ | | | |
	773 K	923 K	773 K	923 K	773 K	923 K
Ni/Al	5.82	1.74	2.18	1.03	773	948
Ni/KAl	11.57	0.40	7.97	0.15	868	568, 926
Ni/Mg1Al2	3.80	0.13	3.20	0.048	857	562, 939
Ni/Mg2Al1	4.61	0.47	5.73	0.17	863	644, 931
Ni/Mg	0.76	0.52	2.44	0.19	673, 834	606, 671, 927

Figure 5.15: XRD of spent catalysts for experiments performed at 773 and 923 K. Focusing on the 2θ range of 20 to 30° to identify the presence of graphitic carbon.

Under steam reforming conditions, the rate of carbon accumulation on supported-Ni catalysts depends upon the relative rates of the carbon-forming and gasification reactions [Bartholomew (2001)]. Evidently, the rate of the carbon forming reactions at 773 K exceeded that of the gasification reactions resulting in deposition of carbon. At 923 K, the rate of the gasification reaction increased faster than the rate of the carbon depositing reaction and thus the rate of carbon accumulation decreased. Increasing the reaction temperature by 150 K reduced the rate of carbon deposition by more than an order of magnitude for all catalysts except for Ni/Al. Increasing the reaction temperature shifted the maxima in the rate of oxidation to higher temperatures, from approximately 863 to 923 K, indicating that the carbon deposits for the higher temperature experiments, even though significantly less in

absolute amount, were more ordered and less reactive (more graphitic) [Bartholomew (2001)].

XRD of the spent Ni/Mg catalysts for both reaction temperatures revealed a surface that was free of filamentous carbon (Figure 5.15). SEM images of the spent Ni/Mg catalyst for experiments performed at 773 K (Figure 5.16a,b) showed that the Ni/Mg surface was free of filamentous carbon but was covered by an amorphous layer of carbon. Compared to the reduced catalyst (Figure 5.16a), the crystallites are larger, and form a more uniform, continuous surface. The volume-average crystallite size (XRD line broadening) did not change between the reduced or spent samples suggesting that carbon formed on the surface of the $Ni_xMg_{1-x}O$ crystallites enlarged their apparent diameter and therefore produced a more continuous surface because the crystallites grew together. The absence of filamentous carbon suggests that nickel was tightly bound in the $Ni_xMg_{1-x}O$ solid-solution structure and was not being extracted. At 923 K (Figure 5.16d), unlike at 773 K (Figure 5.16c), the crystallites retained their original size and the crystallites did not grown together, supporting the TPO results that less carbon was deposited on the catalyst at 923 K than at 773 K. A few filamentous features (Figure 5.16d, white arrows) were observed; however, they were significantly smaller than what has been observed on the other catalysts (See Figure 5.16-Figure 5.20), suggesting that they might not be carbon based, but a filamentous (whisker) Mg species which has previously been observed on steamed MgO [Stobbe et al. (1991)].
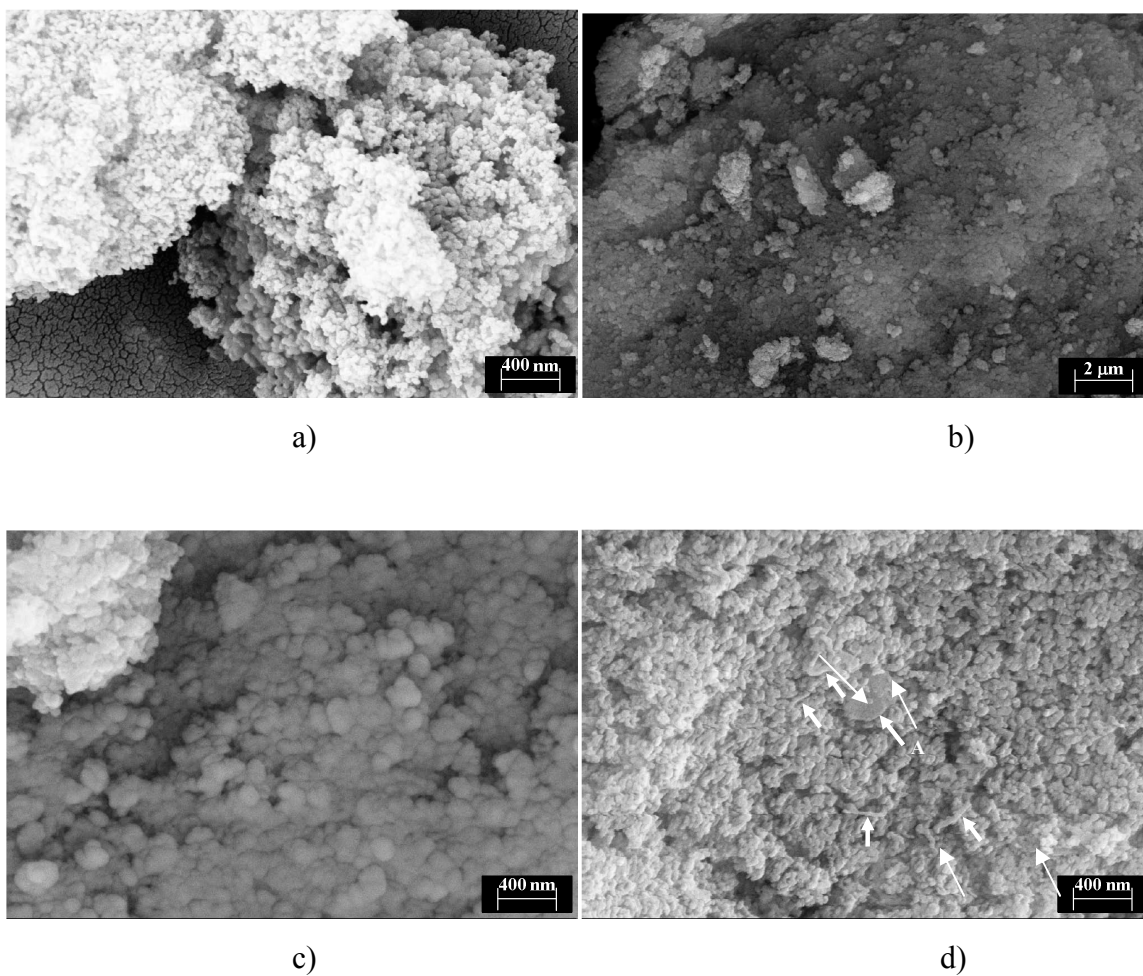
a)

b)

c)

d)

Figure 5.16: SEM images of Ni/Mg. For a) after reduction (prior to reaction), b) and c) spent catalyst after reaction for approximately 20 h at 773 K, and d) spent catalyst after reaction for approximately 20 h at 923 K.
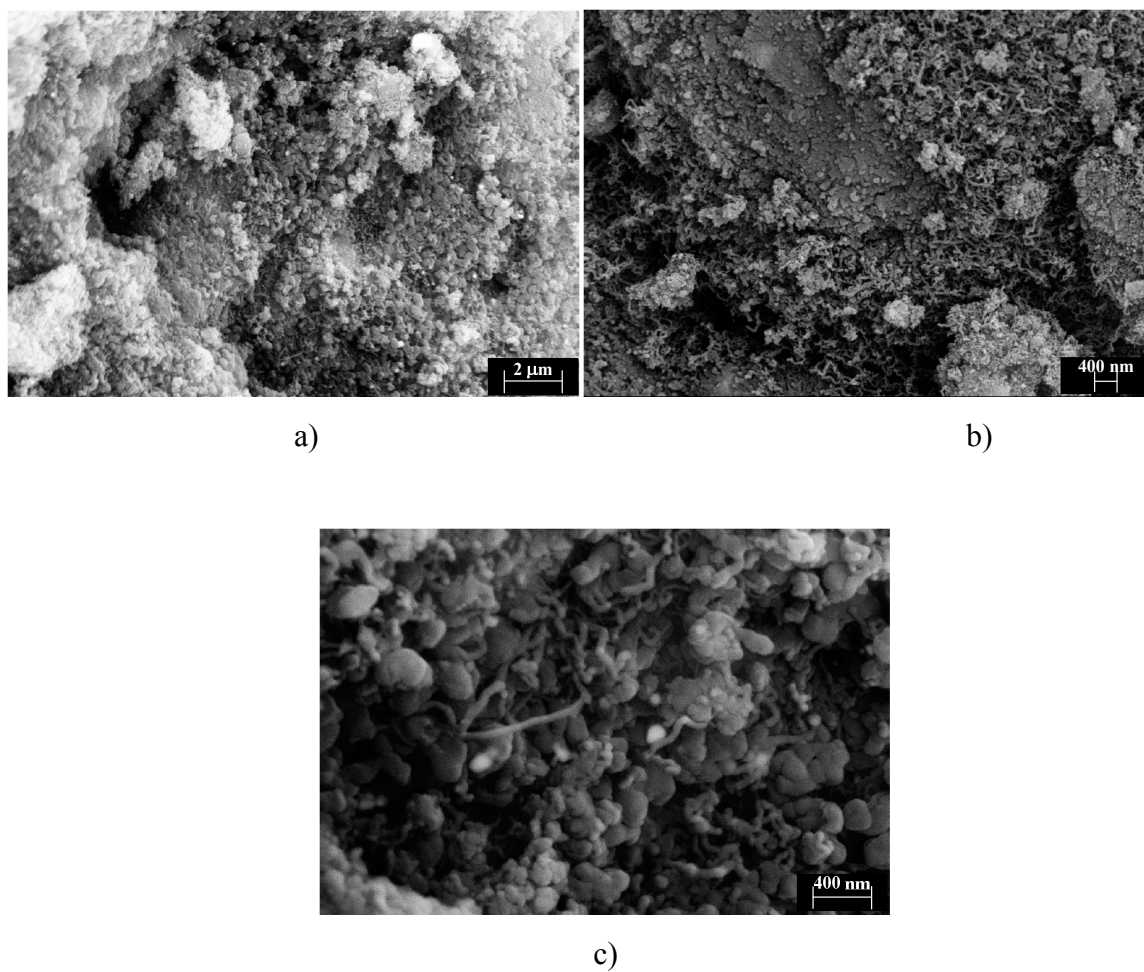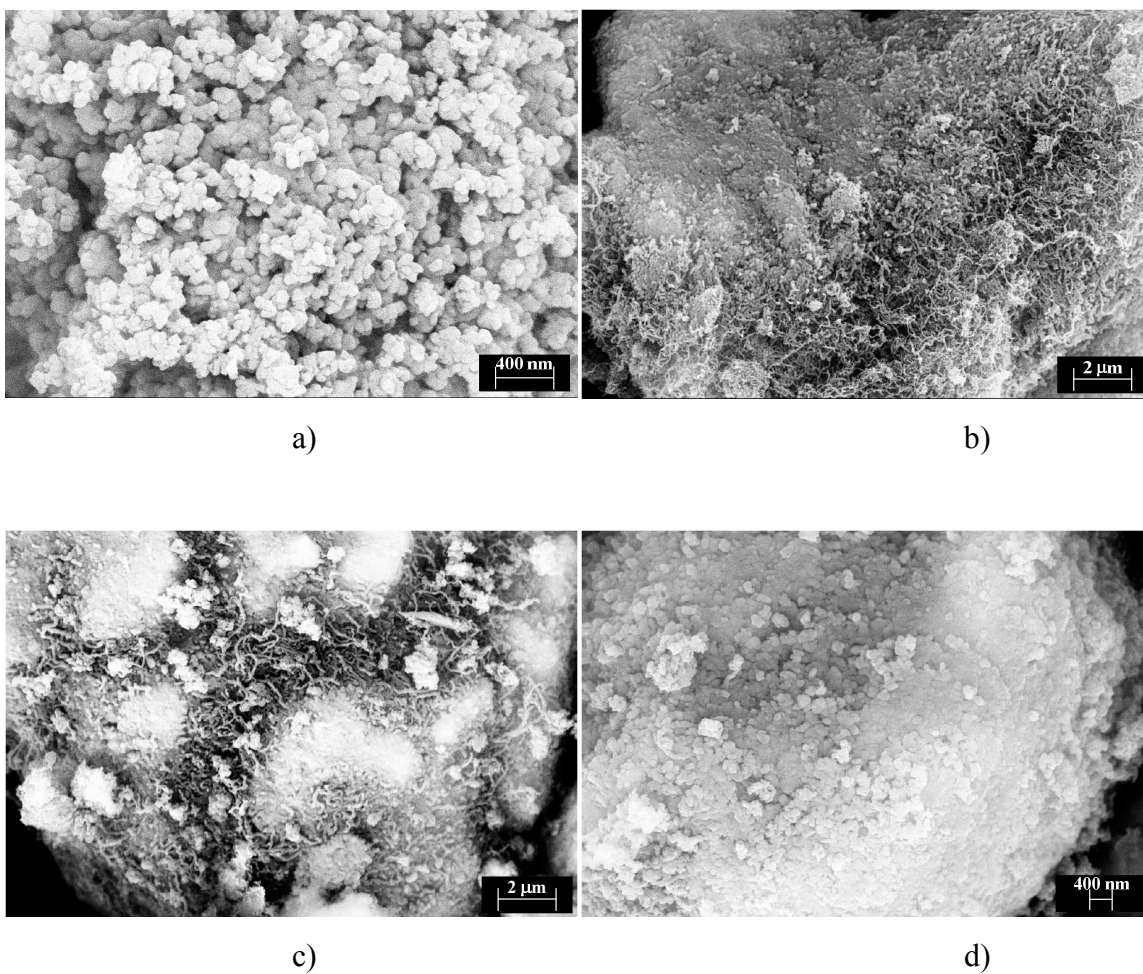
a)

b)

c)

Figure 5.17: SEM images of Ni/Al. For a) after reduction (prior to reaction), b) spent catalyst after reaction for approximately 20 h at 773 K, and c) spent catalyst after reaction for approximately 20 h at 923 K.
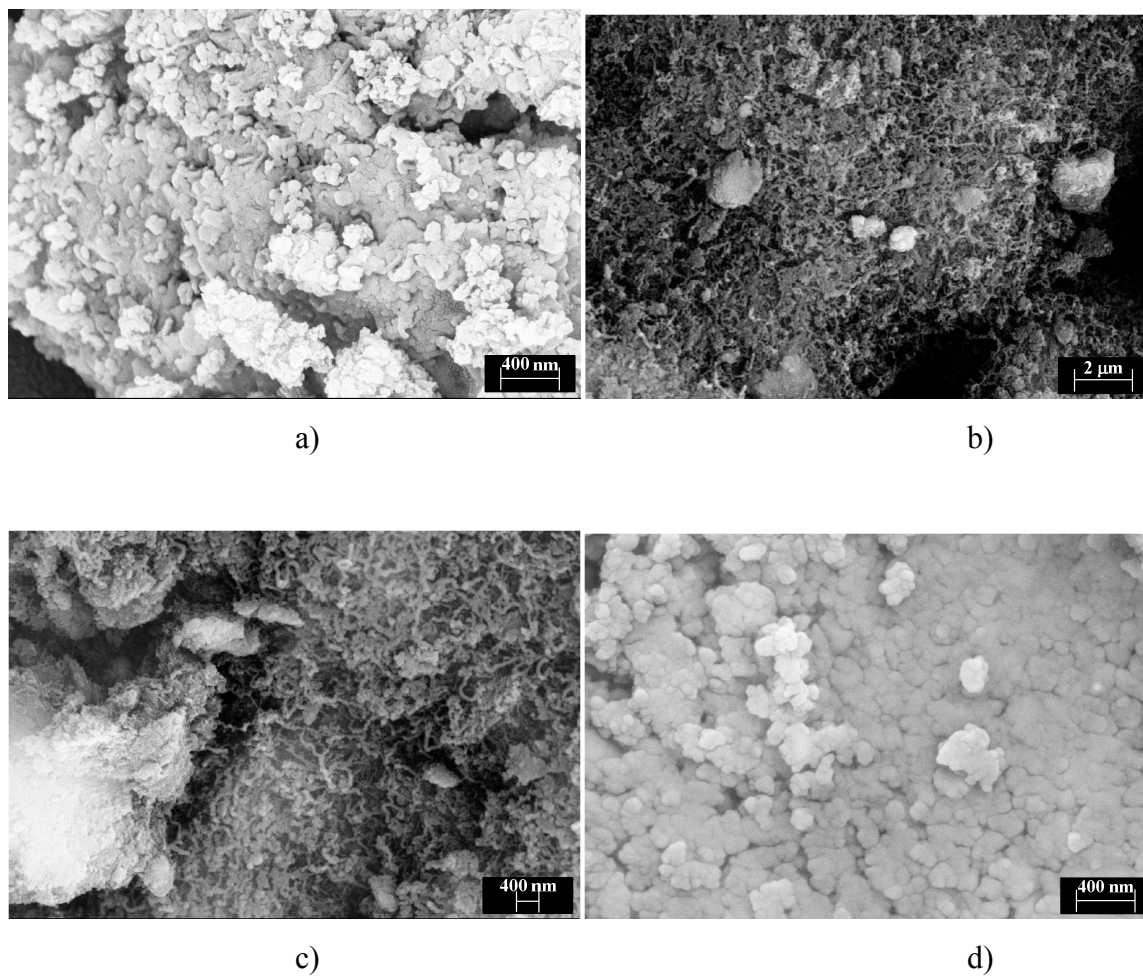
a)

b)

c)

d)

Figure 5.18: SEM images of Ni/KAl. For a) after reduction (prior to reaction), b) spent catalyst after reaction for approximately 20 h at 773 K, and c) and d) spent catalyst after reaction for approximately 20 h at 923 K.

Figure 5.19: SEM images of Ni/Mg1Al2. For a) after reduction (prior to reaction), b) and c) spent catalyst after reaction for approximately 20 h at 773 K, and d) spent catalyst after reaction for approximately 20 h at 923 K.
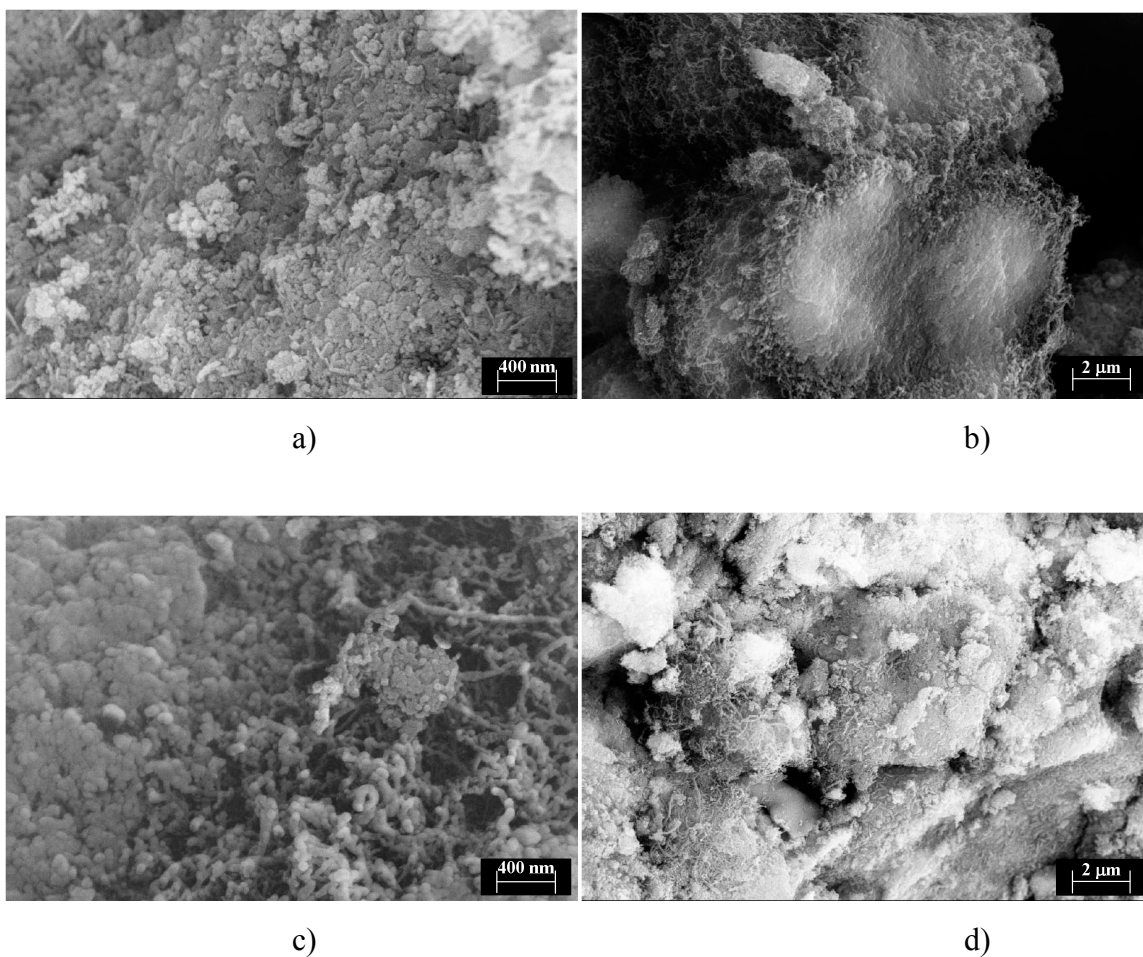
Figure 5.20: SEM images of Ni/Mg2Al1. For a) after reduction (prior to reaction), b) and c) spent catalyst after reaction for approximately 20 h at 773 K, and d) spent catalyst after reaction for approximately 20 h at 923 K.

XRD of the spent Ni/Al catalysts revealed the presence of filamentous carbon at both temperatures investigated, 773 and 923 K. Similarly, SEM images (Figure 5.17) showed that the catalyst surfaces were entirely covered with encapsulating and filamentous carbon. XRD results suggested that Ni/Al was the only catalyst to have filamentous carbon on the spent catalyst surface for reactions at 923 K; however, SEM images revealed small regions containing filamentous carbon on both spent Ni/KAl (Figure 5.18c) and Ni/Mg2Al1 (Figure 5.20d). The surface of the Ni/Al catalyst spent at 773 K was heterogeneously covered with encapsulating and filamentous carbon (Figure 5.17b). Increasing the reaction temperature to 923 K reduced the total amount of carbon (Table 5.9) and most importantly, the amount of filamentous carbon was drastically reduced. At 923 K, encapsulating carbon dominated the surface as exhibited by a substantial reduction in the density of filamentous carbon and an increase in the size of the individual particulates compared to the reduced catalyst. Filamentous carbon was still present but much less than observed at 773 K. The bright "dots" are most likely exposed nickel crystallites.

XRD of Ni/KAl spent at 773 K (Figure 5.15) agreed with the TPO results (Table 5.9) that it was the most coked catalyst in this study. SEM images revealed that the surface is dominated by filamentous carbon, however, regions (Figure 5.18b, upper left hand corner) are encapsulated by layered, most likely graphitic carbon. Increasing the reaction temperature to 923 K substantially changed the coking characteristics of the catalyst. The catalyst changed from the most coked catalyst of the study to the second least coked, experiencing a 53-times reduction in the rate of carbon accumulation. SEM revealed that the Ni/KAl surface after the 923 K experiment was substantially different than that observed for the spent catalyst at 773 K. Filamentous carbon is still found in small regions; however, its density is much reduced (Figure 5.18d is more representative of the entire surface of the spent catalyst) and the micrographs show exposed catalyst surface (bright regions in Figure 5.18c), suggesting that the catalyst surface is no longer completely carbon covered.

TPO of the spent Mg-Al mixed oxide supported nickel catalysts, Ni/Mg1Al2 and Ni/Mg2Al1, revealed carbon deposits at both reaction temperatures, 773 and 923 K (Table 5.9). At 773 K, the mixed-oxide supported catalyst gave moderate rates of carbon accumulation, performing better than the γ-Al$_2$O$_3$-supported catalysts but having higher carbon accumulation rates than the MgO-supported catalyst. XRD of the spent Mg-Al mixed oxide supported catalysts, Ni/Mg1Al2 and Ni/Mg2Al1, (Figure 5.15) agreed with the TPO findings that Ni/Mg1Al2 experienced a lower coking rate than Ni/Mg2Al1 even though Ni/Mg1Al2 was more selective for ethylene (Table 5.7), a known coking precursor. SEM images show the surface of the mixed oxide supported nickel catalysts spent at 773 K (Figure 5.19b,c and Figure 5.20b,c) to be completely covered with carbon. Carbonaceous deposits on Ni/Mg1Al2 were predominantly filamentous, as can be seen in Figure 5.19b,c, while the surface of Ni/Mg2Al1 was covered by both filamentous and encapsulating carbon (Figure 5.20c, left hand side). Similar to Ni/Mg (Figure 5.16c) the particles in the encapsulating region have grown together making a near continuous, smooth surface, which appears different from the surface of the reduced catalyst. This finding supports the earlier made claim that Ni in the reduced Ni/Mg2Al1 catalyst had been incorporated into a Ni$_x$Mg$_{1-x}$O solid solution. SEM images of Ni/Mg1Al2 spent at 923 K (Figure 5.19d) revealed that the surface was free of filamentous carbon, showing only layered encapsulating carbon deposits, while the surface of Ni/Mg2Al1 spent at 923K was decorated with small regions of filamentous and encapsulating carbon deposits and exposed surface. Increasing the reaction temperature to 923 K drastically reduced the amount of carbon deposited on all catalysts, but most substantially on Ni/Mg1Al2, which experienced the lowest rate of carbon accumulation at 923 K. In fact, the rate of carbon accumulation on Ni/Mg1Al2 was approximately 3-times less than that on the potassium-doped catalyst (Ni/KAl), which is a significant finding considering potassium is catalytically active for carbon gasification above 873 K [Dimicheli et al. (1994)].

Inspection of the catalysts spent at 773 K after TPO revealed that the carbonaceous deposits caused the disintegration of all Al-containing catalysts, which could have occurred

111

during the steam reforming experiment or the oxidation step. The Ni/Mg catalyst at 773 K and all catalysts spent at 923 K retained their original particulate form after oxidation. The integrity of the catalyst particle was compromised by filamentous carbon [Bartholomew (2001)].

Although significant amounts of deposited carbon were detected on the catalysts evaluated at 773 K and oxidization of the spent catalysts revealed that the deposited carbon destroyed the catalyst structure, analysis of the reaction data sheds much light on the effect of the support composition on activity, product selectivity, and stability of the nickel sites.

5.4 Summary

Calcination of co-precipitated mixtures of Mg and Al having Al/(Al+Mg) ratios of 0.693 and 0.357 resulted in the formation of support materials having relatively high surface area and a chemical composition of $MgAl_2O_4$ and $MgO-MgAl_2O_4$ respectively. Nickel impregnation and subsequent reduction led to the formation of nickel supported on $MgAl_2O_4$ (Ni/Mg1Al2) and $MgO-MgAl_2O_4$ (Ni/Mg2Al1) giving nickel crystallite sizes of approximately 8.34 and 12.31 nm. Temperature programmed reduction revealed that increasing the Al content of the mixed oxide support improved nickel reducibility. Compared to the pure oxide supported catalysts, the mixed oxide supported catalysts exhibited moderate acidic and basic site strength and density, specifically a reduction in the strong site types were noted.

The activity, selectivity, and stability of Mg-Al mixed oxide supported nickel catalysts for the steam reforming of ethanol was evaluated and compared to Ni/MgO, Ni/K-Al_2O_3, and Ni/Al_2O_3. At 773 K, the Mg-Al mixed oxide supported nickel catalysts gave superior performance in terms of steam reforming activity and product selectivity compared to the pure oxide supported nickel catalysts. Activity, stability, and product selectivity were dependent upon the Al and Mg content of the support. At 923 K, the Mg-Al mixed oxide supported nickel catalysts were the best performing catalysts exhibiting the highest steam

112

reforming product yield (H_2 and CO_x) and were highly stable, showing no signs of deactivation after 20 h operation. The improved performance of the Mg-Al mixed oxide supported catalysts was related to the incorporation of the pure oxides, MgO and Al_2O_3, into $MgAl_2O_4$. The formation of $MgAl_2O_4$ reduced nickel incorporation with the support material since $MgAl_2O_4$ does not react with Ni; therefore, nickel was retained in its active form. In addition, incorporation of Mg and Al in to $MgAl_2O_4$, a slight basic material, modified the acid-base properties resulting in a catalyst that exhibited moderate acidic and basic site strength and density compared to the pure oxide supported catalysts. Moderation of the acid-base properties improved the activity, selectivity, and stability of the catalysts by reducing activity for by-product reactions producing ethylene and acetaldehyde.

Chapter 6

Ethanol steam reforming over Ni/Mg1Al2: An in-depth analysis

6.1 Temperature Programmed Reaction Experiments

Transient, temperature programmed reaction experiments were performed in the fixed-bed reactor catalyst test station described in the section 3.3. The reactor was loaded with 50 mg (35-45 mesh) of Ni/Mg1Al2 dispersed in 500 mg (35-50 mesh) of SiC (inert). Prior to reaction initiation, the catalyst (Ni/Mg1Al2) was reduced in-situ at 1023 K for 1 h in 200 mL min^{-1} of 5% H_2/N_2 and cooled to 523 K, the starting reaction temperature. The liquid feed mixture was delivered to the vaporizer at a specific rate to ensure that the gas hourly space velocity (GHSV) was maintained at approximately 260000 mL$_{Feed}$ h^{-1} g$_{cat}$$^{-1}$. Upon introduction of the ethanol-water feed mixture to the reactor, the temperature program was initiated. The reaction temperature was ramped at a rate of 1 K min^{-1} from 523 K (250°C) to 923 K (650°C). The GC method, described in Appendix B, took approximately 32 minutes to determine the composition of the injected sample and prepare for the subsequent sample injection. Therefore compositional analysis of the product gas was obtained at approximately 32 K intervals, resulting in approximately 13 product gas sample analyses over the temperature range. In addition, the slow temperature ramp rate allowed for pseudo steady state reaction kinetics.

6.1.1 H_2O:EtOH feed ratio

The effect of the H_2O:EtOH feed ratio on the activity of the catalyst (Ni/Mg1Al2) and reaction pathways was investigated as a function of the reaction temperature. Three H_2O:EtOH feed ratios were investigated (H_2O:EtOH = 8.4:1, 3:1, and 1:1). The liquid feed flow rate was adjusted to maintain the total GHSV by accounting for changes in the average molecular weight of the feed mixture, thereby ensuring a constant total residence time. The

actual GHSVs used for the three feed ratios in descending order were 276000, 256900, and 262100 mL_{Feed} h^{-1} g_{cat}^{-1} respectively.

The effect of the H_2O:EtOH feed ratio on ethanol conversion is shown in Figure 6.1a. Generally, increasing the water content of the feed mixture improved ethanol conversion. Ethanol conversion was essentially of the same for the lower feed ratios; the stoichiometric, 3:1 and sub-stoichiometric, 1:1. Exceeding the stoichiometric feed ratio of 3 drastically improved ethanol conversion, being the only feed ratio to achieve and maintain 100% ethanol conversion at temperatures above 800 K. For all feed ratios, the ethanol conversion did not monotonically increase when the temperature was ramped from approximately 675 to 750 K. Within this temperature range, ethanol conversion rapidly increased and then decreased with increasing temperature until 750 K. To simplify the interpretation of the experimental results, the discussion of the results will be separated into three temperature regions (< 675 K, 675-750 K, and >750 K). The thick dashed lines presented in the product yield figures represent the equilibrium yield expectations determined using the Gibbs' equilibrium reactor utility in Aspen Plus™ 12.1 (Aspen Technology, Inc.).
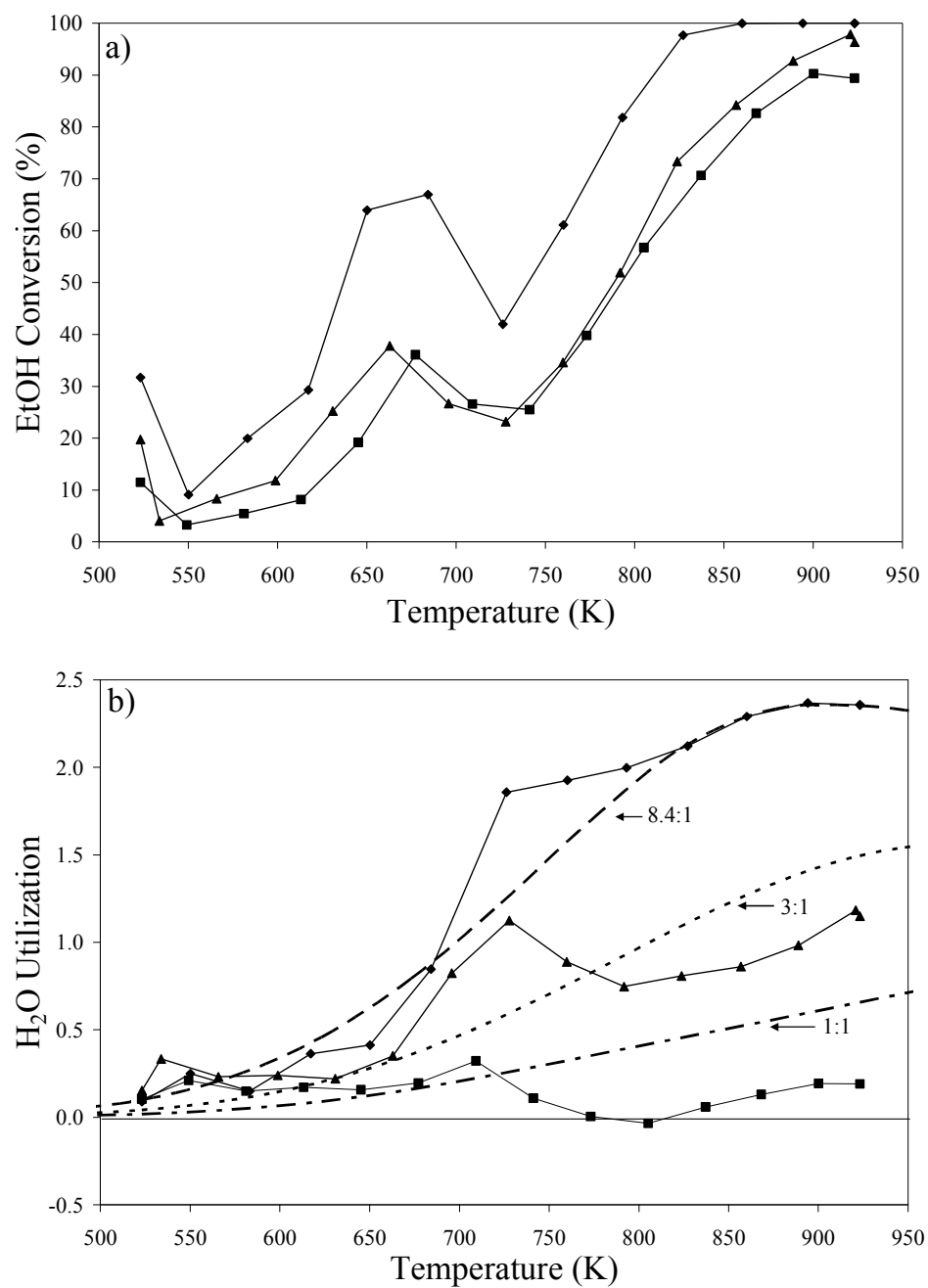
Figure 6.1 (a-b): Temperature programmed reaction over Ni/Mg1Al2 for various H_2O:EtOH ratios. (—◆—) 8.4:1 (—▲—) 3:1 (—■—) 1:1. Equilibrium expectations are represented by dashed lines.
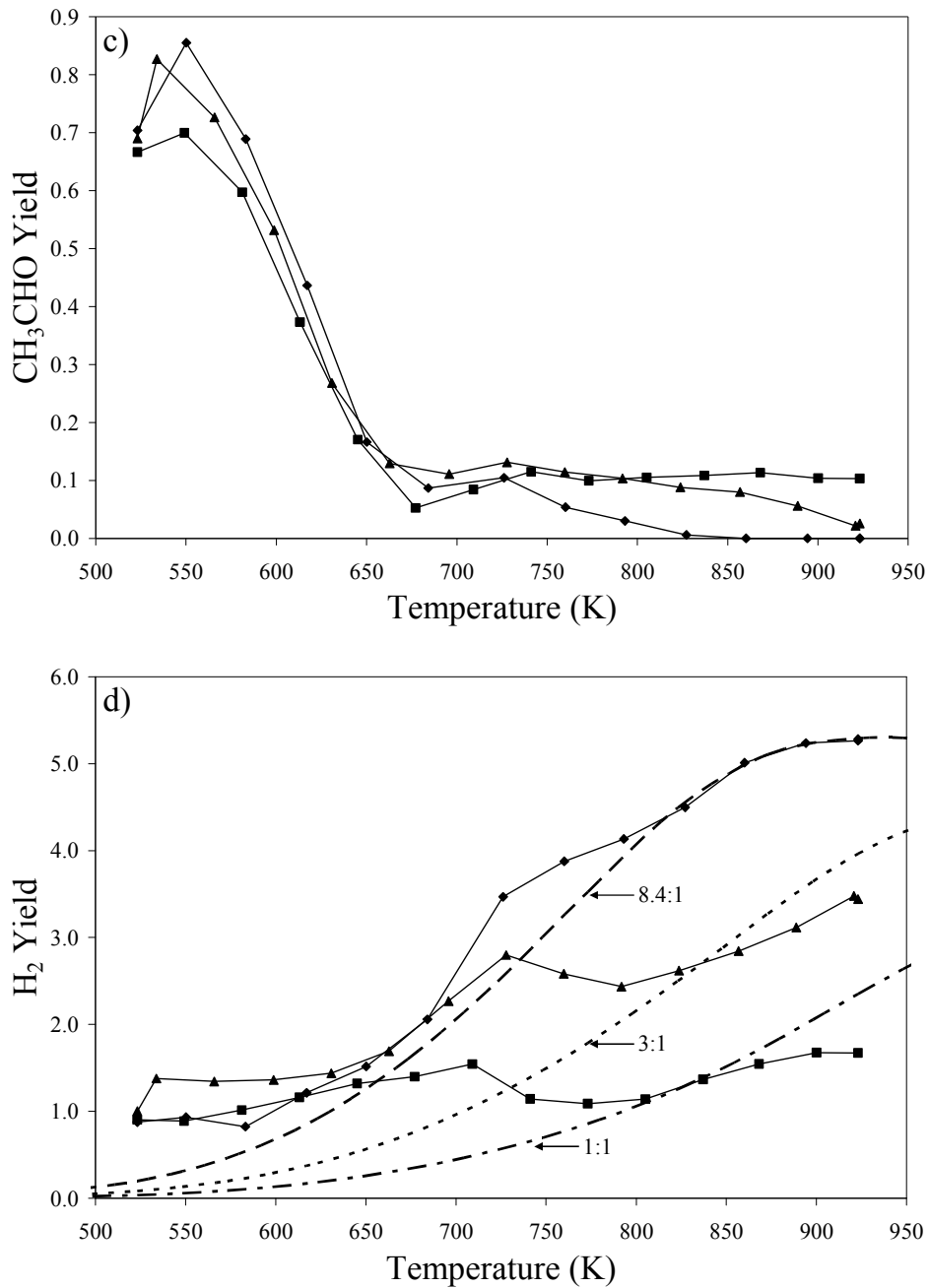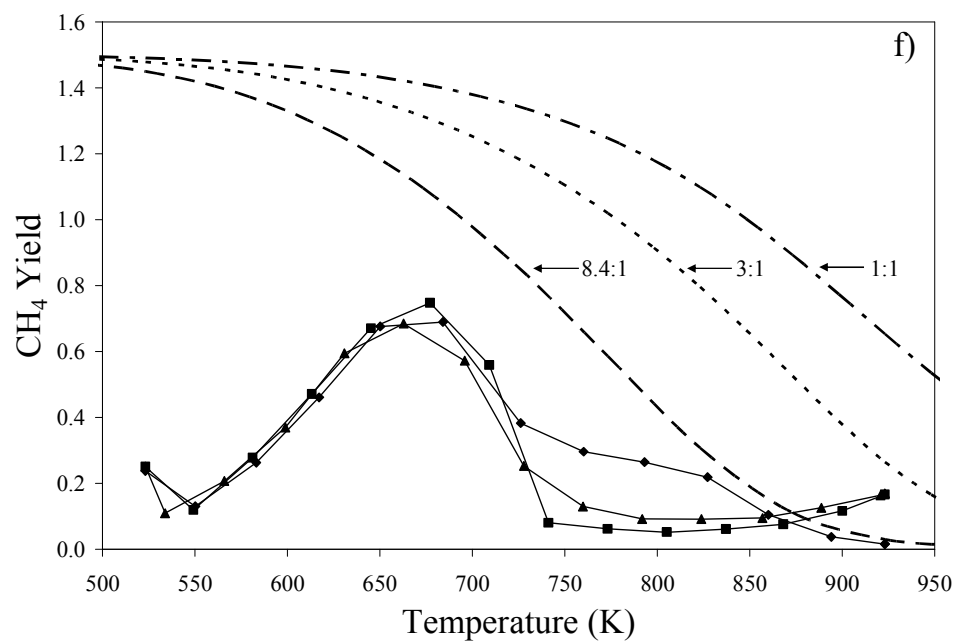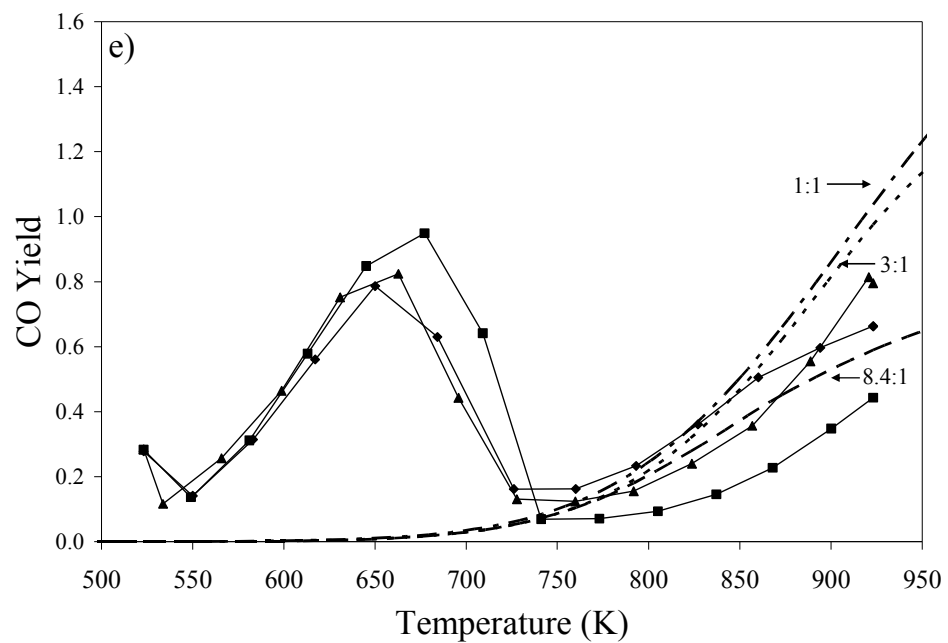
Figure 6.1 (c-d): Temperature programmed reaction over Ni/Mg1Al2 for various H_2O:EtOH ratios. ($\blacklozenge$) 8.4:1 ($\blacktriangle$) 3:1 ($\blacksquare$) 1:1. Equilibrium expectations are represented by dashed lines.

Figure 6.1 (e-f): Temperature programmed reaction over Ni/Mg1Al2 for various H_2O:EtOH ratios. (—◆—) 8.4:1 (—▲—) 3:1 (—■—) 1:1. Equilibrium expectations are represented by dashed lines.
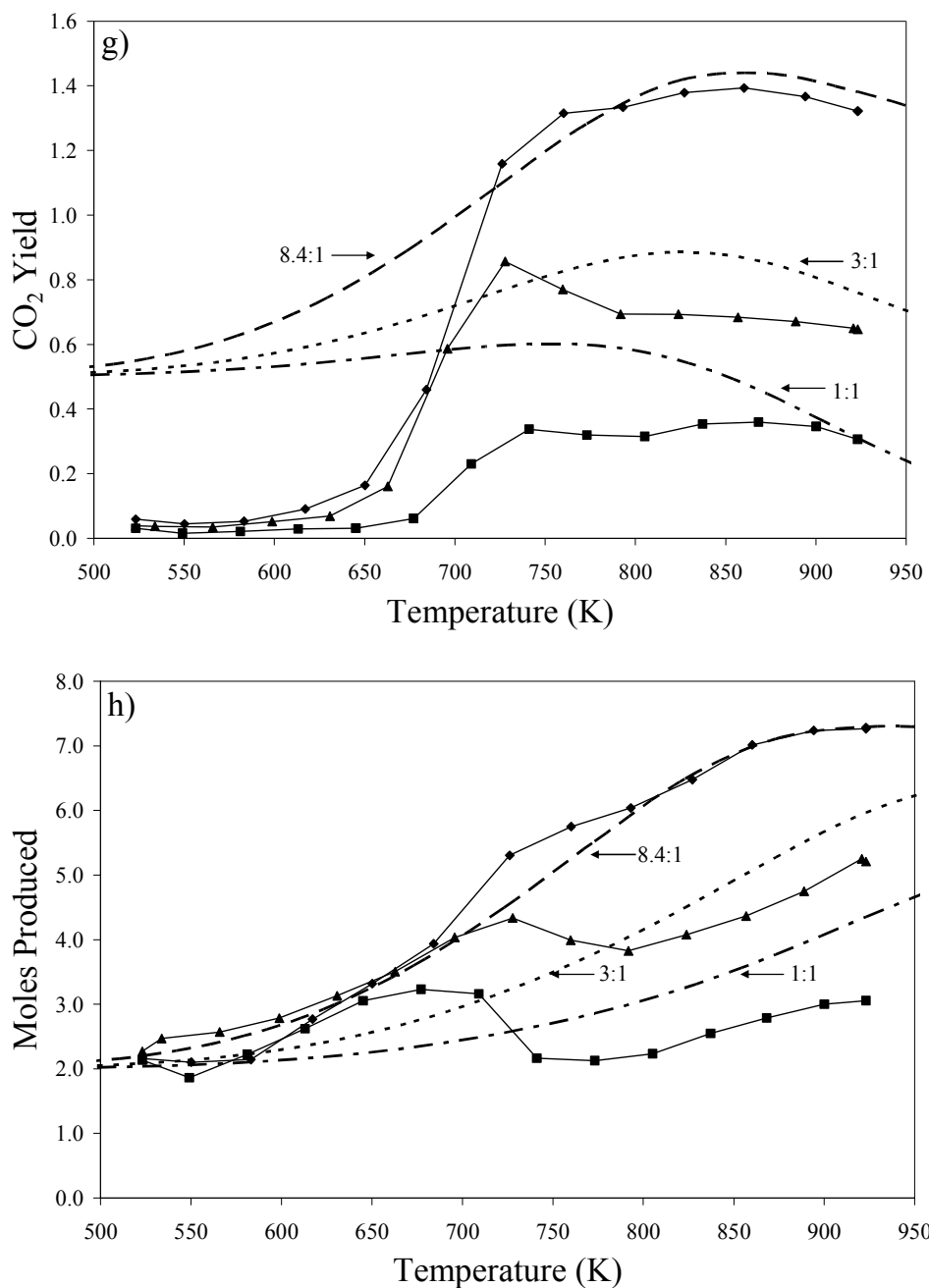
118

Figure 6.1 (g-h): Temperature programmed reaction over Ni/Mg1Al2 for various H_2O:EtOH ratios. (—♦—) 8.4:1 (—▲—) 3:1 (—■—) 1:1. Equilibrium expectations are represented by dashed lines.
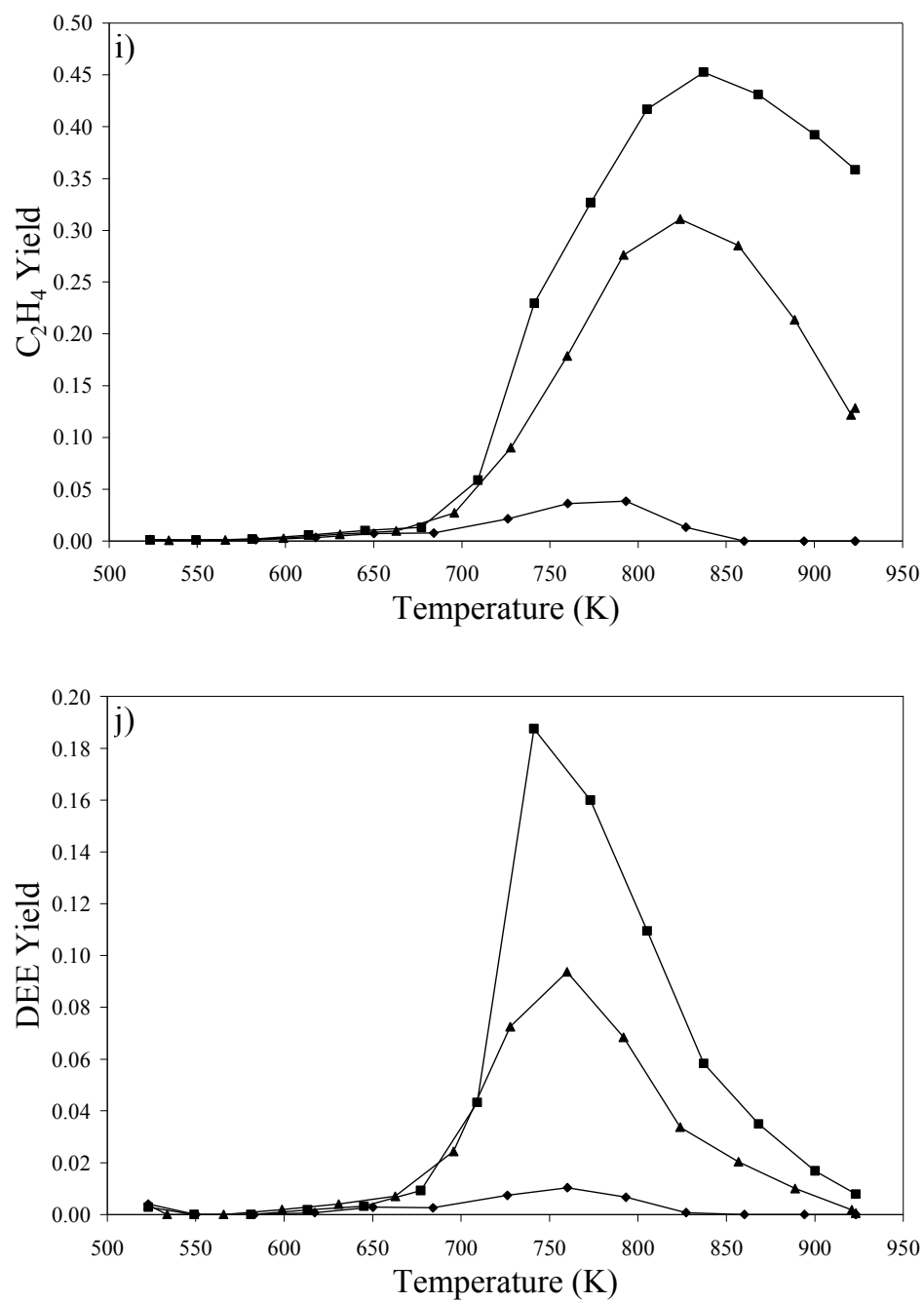
Figure 6.1 (i-j): Temperature programmed reaction over Ni/Mg1Al2 for various H$_2$O:EtOH ratios. ($\text{---}\blacklozenge\text{---}$) 8.4:1 ($\text{---}\blacktriangle\text{---}$) 3:1 ($\text{---}\blacksquare\text{---}$) 1:1. Equilibrium expectations are represented by dashed lines.

6.1.1.1 Low temperature region, < 675 K

At low reaction temperatures, below 675 K, ethanol was primarily converted to acetaldehyde (Figure 6.1c), hydrogen (Figure 6.1d), carbon monoxide (Figure 6.1e), and methane (Figure 6.1f), with very little contribution to the product gas composition by any of the other products and, in addition, very little water was consumed (Figure 6.1b). For temperatures below 600 K, the acetaldehyde and hydrogen yields were near equimolar, one mole of acetaldehyde to one mole of hydrogen, suggesting that the dominant reaction in this low temperature region is ethanol dehydrogenation (R.7). This reaction is generally considered the primary intermediate reaction pathway in the nickel catalyzed ethanol steam reforming reaction network [Akande et al. (2006); Fatsikostas and Verykios (2004); Marino et al. (2004)].

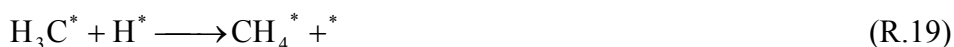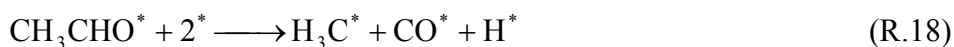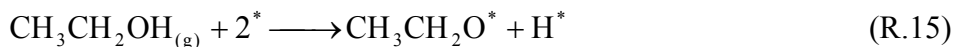$$CH_3CH_2OH \longrightarrow CH_3CHO + H_2 \qquad \qquad (R.7)$$

Acetaldehyde yields fall below the expected value of one and decrease with increasing temperature. For temperatures below 675 K, decreasing acetaldehyde yield was matched with an increase in the acetaldehyde decomposition (R.8) products, CO (Figure 6.1e) and CH_4 (Figure 6.1f), in near-equimolar proportions.

$$CH_3CHO \longrightarrow CH_4 + CO \qquad \qquad (R.8)$$

An alternative interpretation of the relationship between declining acetaldehyde yield with simultaneously increasing CO and CH_4 yields would be a change in the dominant ethanol decomposition reaction. The decomposition pathway could change from indirect (acetaldehyde intermediate) via (R.8) to direct from ethanol via reaction (R.9), a pathway commonly reported for noble metal catalysts [Erdohelyi et al. (2006), Jacobs et al. (2007), Rasko et al. (2006)].

$$CH_3CH_2OH \longrightarrow CH_4 + CO + H_2 \qquad\qquad (R.9)$$

Using a kinetic isotope exchange technique, Gates et al. (1986) proposed that on pure nickel (Ni (111)), ethanol decomposition proceeds through an ethoxy intermediate, $CH_3CH_2O^*$ in (R.15), followed by dehydrogenation (R.16) to form a surface adsorbed acetaldehyde. Adsorbed acetaldehyde can either desorb from the surface forming gas-phase acetaldehyde (R.17) or decompose to surface adsorbed CH_3^*, CO^*, and H^* via (R.18). Regardless of the decomposition pathway, direct from ethanol (R.9) or indirect from acetaldehyde (R.8), this literature evidence shows that both reactions proceed though the same surface intermediate. Recently, a more sophisticated surface study using *in-situ* diffuse reflectance infra-red Fourier transform spectroscopy (DRIFTS) [Resini et al. (2007)] validated the mechanism proposed by Gates et al. (1986) and demonstrated that it can be extended to ethanol adsorption and surface reaction for supported nickel catalysts, for example on Ni/MgO.

$$CH_3CH_2OH_{(g)} + 2^* \longrightarrow CH_3CH_2O^* + H^* \qquad\qquad (R.15)$$

$$CH_3CH_2O^* + ^* \longrightarrow CH_3CHO^* + H^* \qquad\qquad (R.16)$$

$$CH_3CHO^* \longrightarrow CH_3CHO_{(g)} + ^* \qquad\qquad (R.17)$$

$$CH_3CHO^* + 2^* \longrightarrow H_3C^* + CO^* + H^* \qquad\qquad (R.18)$$

$$H_3C^* + H^* \longrightarrow CH_4^* + ^* \qquad\qquad (R.19)$$

$$CH_4^* \longrightarrow CH_{4(g)} + ^* \qquad\qquad (R.20)$$

$$CO^* \longrightarrow CO_{(g)} + ^* \qquad\qquad (R.21)$$

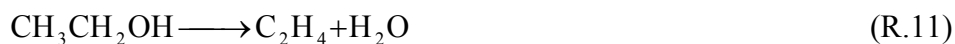$$2H^* \longrightarrow H_{2(g)} + 2^* \qquad\qquad (R.22)$$

The composition of the product gas then depends on the relative rates of acetaldehyde desorption (R.17) and the combined rates of reactions (R.18-22), accounting for ethanol/acetaldehyde decomposition and decomposition product desorption. The number of

moles produced per mol of ethanol converted (Figure 6.1h) increases from approximately 2 at 523 K to approximately 3 at 675 K verifying that the product composition changed from the dehydrogenation (total product yield = 2) to the decomposition (total product yield = 3) products. The dehydrogenation and decomposition reaction mechanisms sufficiently describe the experimental results for temperatures below 675 K and the reaction network is essentially independent of the H_2O:EtOH feed ratio. The CO_2 yield for all H_2O:EtOH feed ratios falls below the equilibrium expectations even though CO yields exceed equilibrium expectations suggesting that the water-gas shift and CO disproportionation reactions (R.3 and R.6) are not kinetically active on this catalyst in this low temperature range.

$$CO + H_2O \longrightarrow H_2 + CO_2 \qquad\qquad (R.3)$$

$$2CO \longrightarrow C + CO_2 \qquad\qquad (R.6)$$

6.1.1.2 Moderate temperature range, 675 – 750 K

A significant change in the catalyst activity and the distribution of products occurred as the reaction temperature increased from 675 to 750 K. For all H_2O:EtOH feed ratios, the catalyst activity passed through a maximum and ethanol conversion then decreased with increasing temperature. The reduction in conversion was highly unexpected because the consumption of ethanol is not equilibrium limited. The thermodynamically expected value is 100%, and according to Arrhenius kinetics (increasing rate with temperature), the rate of reaction should increase with temperature. The onset of the loss in catalytic activity is accompanied by the appearance of known carbon deposition precursors, ethylene (Figure 6.1i) and diethyl ether (Figure 6.1j). Ethanol dehydration reactions (R.11 and R.23) are catalyzed by the acidic sites [Di Cosimo et al. (1998)] present on the support material ($MgAl_2O_4$), see NH_3-TPD results in the previous chapter.

$$CH_3CH_2OH \longrightarrow C_2H_4 + H_2O \qquad\qquad (R.11)$$

$$2CH_3CH_2OH \longrightarrow CH_3CH_2OCH_2CH_3 + H_2O \qquad\qquad (R.23)$$

From Figure 6.1i and Figure 6.1j, it can be seen that increasing the water content of the feed mixture significantly reduced selectivity for the dehydration reaction products, ethylene and diethyl ether, which is to be expected since water is obviously a product of the dehydration reactions. However, increasing the water content of the feed did not similarly affect the loss in ethanol conversion. In fact, the experiment with the highest amount of H_2O in the feed experienced the greatest relative reduction in conversion.

Gates et al. (1986) found that for temperatures between 670 and 750 K, surface carbon (C^*) produced from the dehydrogenation of CH_3^* (R.24) can:

1. dissolve into the nickel crystallite producing non-catalytically active nickel carbide,
2. deposit carbon (C^*) on the nickel crystallite surface blocking ethanol adsorption sites,
3. and promote ethanol desorption from the surface.

Studying ethylene adsorption and decomposition on Ni (111), Zuhr and Hudson (1977) found that ethylene completely dehydrogenated at temperatures above 423 K and graphitic carbon deposits were detected above 623 K. In addition to these hydrocarbon sources, CO^* can disproportionate via the Boudouard reaction (R.6) to form surface carbon (C^*) and CO_2.

$$H_3C^* + 3^* \longrightarrow C^* + 3H^* \quad\quad\quad\quad (R.24)$$

Therefore, in this study, CH_3^*, CO^*, and ethylene are expected to have led to carbon formation on the catalyst surface resulting in a reduction in catalysts activity. For the ethanol steam reforming reaction system, carbon formation is thermodynamically favored at low temperatures and low H_2O:EtOH feed ratio mixtures [Garcia and Laborde (1991); Vasudeva et al. (1996)]. However, the rate of carbon deposition is dependent upon the relative rates of

124

the carbon-depositing and carbon-consuming reactions. Furthermore, the relative rates of the decomposition/disproportionation reactions and product desorption dictate the formation of carbon on the catalyst surface. For this temperature range, carbon deposits would form encapsulating films, blocking reactants from the nickel crystallites [Bartholomew (2001)]. Therefore, the loss in catalytic activity as displayed by a reduction in ethanol conversion is related to the formation of carbonaceous encapsulating films on the catalyst surface and in the absence of carbon-consuming reactions, such as carbon gasification, the loss in activity would continue.

For temperatures below 675 K, only trace amounts of ethylene and diethyl ether were detected in the product gas and ethanol conversion increased as expected. Selectivity for the dehydration reactions increased significantly in the moderate temperature range accounting for approximately 60% of the ethanol converted at 750 K for the 1:1 H_2O:EtOH feed ratio experiment. Increasing the water content of the feed mixture was found to significantly reduce selectivity for the dehydration products. Equilibrium analysis of the ethanol dehydration reaction (R.11) [results not shown] indicated that above 523 K ethanol conversion was complete and independent of the amount of water in the feed mixture. Therefore, the negative effect that increasing water content of the feed mixture has on ethylene yield is not related to the equilibrium limitations of the dehydration reaction (R.11 and R.23). Instead, it must be related to the increased importance of other reaction pathways or surface kinetics due to the presence of water. Fatsikostas and Verykios (2004) reported that ethanol and water compete for the same catalytic site type on the surface of the support. The dehydration reactions are catalyzed by the acidic sites on the catalyst support and therefore, increasing the water content should result in a decrease in the concentration of ethanol on the support surface and thus a reduction in the rate of the dehydration reactions.

Even though ethanol conversion decreased with increasing temperature in this intermediate temperature range, water utilization (Figure 6.1b) rose with increasing water content in the feed mixture, indicating an increase in the steam reforming of the converted

ethanol. For the 1:1 feed ratio, the high selectivity for the ethanol dehydration reactions (R.11 and R.23) led to a reduction in H_2O utilization due to the production of 1 mol of water for every mol of ethanol converted to ethylene and 0.5 moles of water for every mole of ethanol converted to diethyl ether, which resulted in a reduction in the total product yield (Figure 6.1h) and H_2O utilization (Figure 6.1b) with increasing temperature. Acetaldehyde yield remained relatively constant and independent of the water content of the feed. However, unlike the low temperature region (< 675 K), hydrogen yield increased above 1.0 indicating that it was produced from reactions other than ethanol dehydrogenation (R.7). The increase in H_2 yield coincided with a rise in CO_2 yield and H_2O utilization and a decline in the CO and CH_4 yields indicating that the steam reforming (R.5) and water-gas shift (R.3) reactions are active in this temperature range. Instead of desorbing from the catalyst surface via (R.20) and (R.21), CH_3^* and CO^* apparently react with water to produce H_2 and CO_2.

$$CH_4 + H_2O \longrightarrow 3H_2 + CO \hspace{5cm} (R.5)$$

CO and CH_4 yields passed though maxima, located at approximately 675 K, suggesting that the water-gas shift (R.3) and methane steam reforming (R.5) reactions were very slow compared to the ethanol and acetaldehyde decomposition reactions (R.7-R.9) below approximately 650 K. Above 650 K, the rate for the water-gas shift and reforming reactions increase and the CO_2 and hydrogen yields rapidly increase and exceed equilibrium expectations between 675 and 775 K. Methane yield is below equilibrium expectations, while CO, CO_2, and hydrogen yields exceed equilibrium expectations indicating that the reverse steam reforming reaction, also known as CO methanation, is not occurring or is very slow.

6.1.1.3 High temperature region (>750 K)

The high temperature region is characterized by monotonically increasing ethanol conversion and a product distribution that approaches equilibrium expectations. Unlike the moderate temperature range, the activity of the catalyst is not adversely affected by the

presence of CH_4, ethylene, and/or diethyl ether. As previously discussed, the rate of carbon deposition is dependent upon the relative rates of the carbon-depositing and carbon-consuming reactions, but loss in catalytic activity is not necessarily affected by the deposition of carbon. For example, encapsulating film deposits, which entirely coat the surface of the catalyst crystallites adversely affect the catalyst activity, while filamentous carbon, which grows with the catalyst crystallite at the exposed end of the filament, does not necessarily affect the activity of the catalyst [Bartholomew (2001)]. Filamentous carbon formation is favored for temperatures above 723 K, while encapsulating films are favored below 773 K [Bartholomew (2001)]. Therefore, increasing temperature above 750 K resulted in a reduction in the selectivity for the deposition of encapsulating film carbon and an increase in the selectivity for filamentous carbon deposits, which resulted in an increase in ethanol conversion with increasing temperature.

At temperatures above 750 K, the effect of the H_2O:EtOH feed ratio on the product distribution becomes very apparent. The product gas composition closely matches equilibrium expectations for the high water content feed mixture (H_2O:EtOH = 8.4:1). Deviation from the equilibrium-expected product composition for the sub- (1:1) and stoichiometric (3:1) feed mixtures is due to selectivity for the dehydration products. As ethylene and diethyl ether disappear with increasing temperature, the product compositions more closely approach equilibrium expectations. For the H_2O:EtOH feed ratios of 3 and 8.4, the acetaldehyde yield decreases with increasing temperature, approaching zero. However, the acetaldehyde yield for the 1:1 feed ratio remains constant at approximately 0.1 for reaction temperatures up to 923 K. Above 750 K, diethyl ether yield declines and approaches zero for all H_2O:EtOH feed ratios, while ethylene yield passes through a maximum. The location of the maximum shifts to higher temperatures for lower H_2O:EtOH feed ratios. The remaining products, H_2, CO, CH_4, and CO_2 approach equilibrium expectations and above 850 K, only C_1 products are detected in the product gas for the supra-stoichiometric feed ratio experiment. The role of the water-gas shift reaction, specifically the reverse water-gas shift

reaction, becomes apparent as the H_2 and CO_2 yields begin to decline with increasing temperature while the CO yield declines.

6.1.2 Acetaldehyde: Primary reaction intermediate and/or undesirable by-product?

Acetaldehyde steam reforming was investigated using a temperature programmed reaction technique to determine whether acetaldehyde was a primary reaction intermediate of the ethanol steam reforming reaction network or an undesirable by-product. The effect that the feed reactant, ethanol or acetaldehyde, had on the activity of the catalyst and the product distribution was determined by comparing the performance of acetaldehyde and ethanol steam reforming having the same H_2O:reactant feed ratio of 8.4:1. Similar to the previous section, the reaction temperature was ramped at a rate of 1 K min^{-1} from 523 K (250°C) to 923 K (650°C) and the liquid feed flow rate was adjusted to maintain the total GHSV. The GHSVs for the ethanol and acetaldehyde steam reforming experiments were 275700 and 278200 mL$_{Feed}$ h^{-1} g$_{cat}$$^{-1}$ respectively.

Figure 6.2(a-g) presents the effects of the starting reactant, acetaldehyde or ethanol, on the catalyst activity for steam reforming and product distribution as a function of temperature. Acetaldehyde conversion (Figure 6.2a), although less than ethanol conversion below 800 K, was found to follow a similar trend with increasing temperature. Ethanol conversion exceeds acetaldehyde conversion for temperatures at which acetaldehyde is found in the ethanol steam reforming product gas. Once acetaldehyde was no longer detected in the ethanol steam reforming product gas (Figure 6.2b), which occurred at approximately 800 K, the conversion of ethanol and acetaldehyde become the same. This suggests that ethanol conversion was greater than acetaldehyde conversion due to the higher activity of nickel for the ethanol dehydrogenation reaction (R.7) [Fatsikostas and Veykios (2004)]. The acetaldehyde yield for the ethanol steam reforming experiment and ethanol yield for the acetaldehyde steam reforming experiment are shown in Figure 6.2b. Ethanol is produced by the reverse dehydrogenation reaction (R.7); the hydrogenation of acetaldehyde. Low activity for the hydrogenation of acetaldehyde to ethanol is related to the absence of hydrogen;

128

however, as the temperature increases above 675 K and the concentration of hydrogen in the product gas increases, no ethanol is produced, suggesting that the reverse reaction is not favorable at higher reaction temperatures.

Acetaldehyde steam reforming, unlike ethanol steam reforming, does not produce hydrogen at temperatures below 600 K. This verifies that ethanol dehydrogenation (R.7) is responsible for hydrogen production below 600 K yielding approximately 1 mole of hydrogen per mole of ethanol consumed (Figure 6.2c). In this temperature range, CO_2 (Figure 6.2d), although thermodynamically favorable, is present only in small quantities. CO_2 can be produced by two reactions, water-gas shift (R.3) and CO disproportionation (R.6). It is difficult to decipher which pathway is contributing to CO_2 production because hydrogen, a water-gas shift reaction co-product, was not detected in the product gas. If the water-gas shift reaction (R.3) was responsible for the production of CO_2, the equimolecular amount of hydrogen in the product gas would be below the TC detector sensitivity of the gas chromatograph and therefore was not detected. The lack of H_2 might be interpreted as evidence for the CO disproportionation reaction (R.6), but the ethanol conversion and CO_2 yield were very low, making it impossible to distinguish which reaction leads to the CO_2.
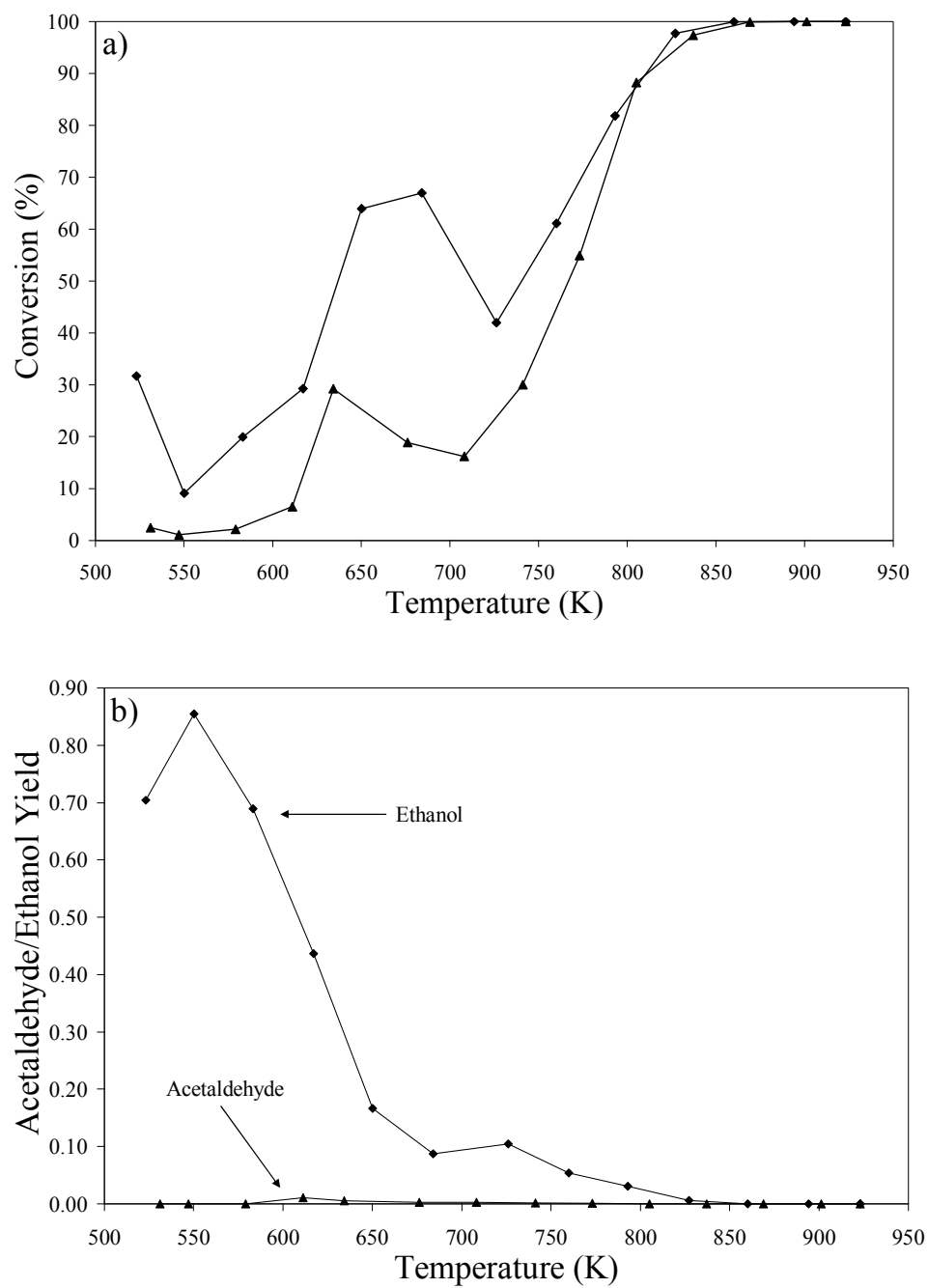
Figure 6.2 (a-b): Temperature programmed reaction for ethanol and acetaldehyde steam reforming. Ethanol (—◆—), Acetaldehyde (—▲—). H_2O:Reactant feed ratio was maintained at 8.4:1 for both ethanol and acetaldehyde.
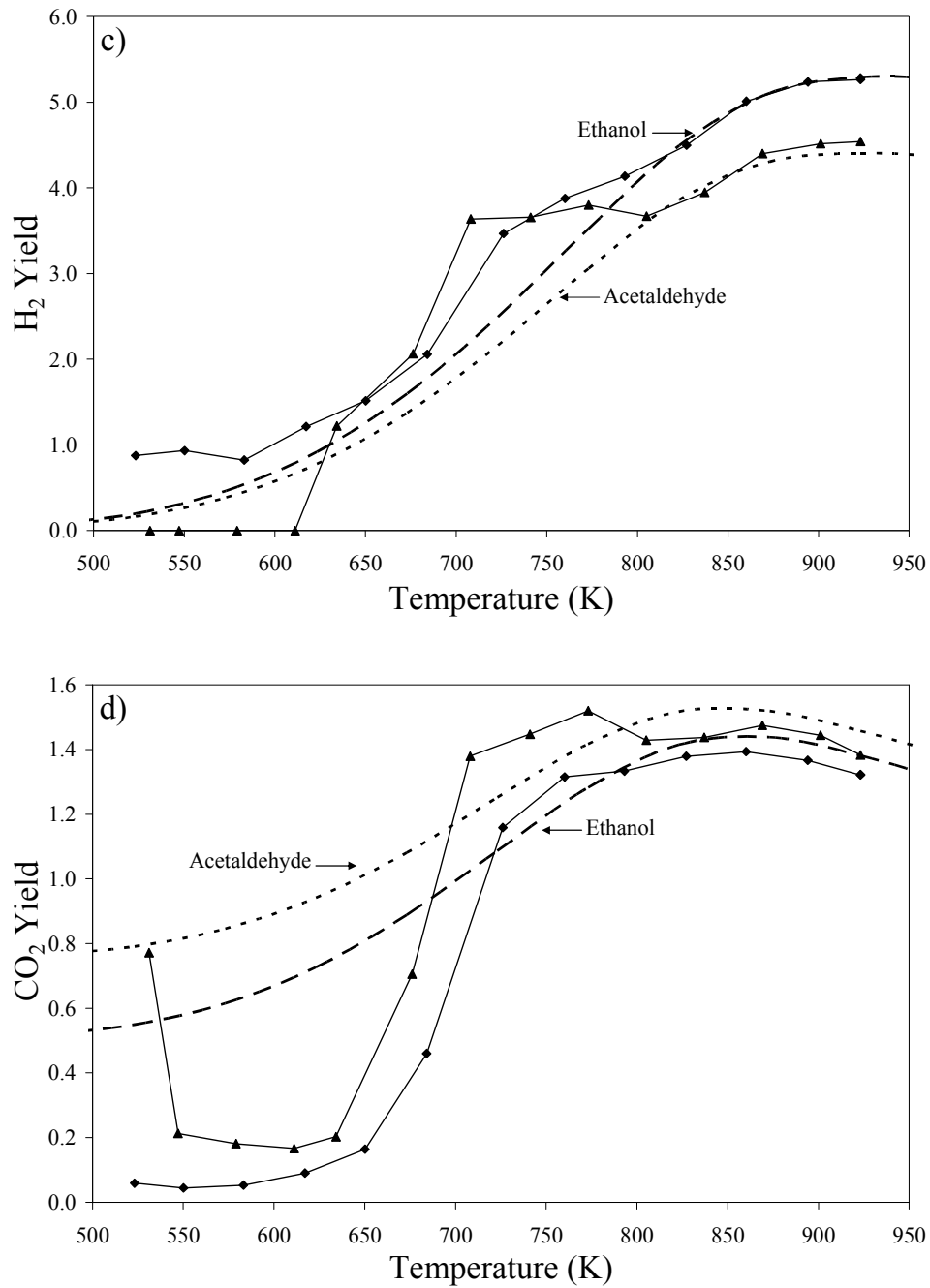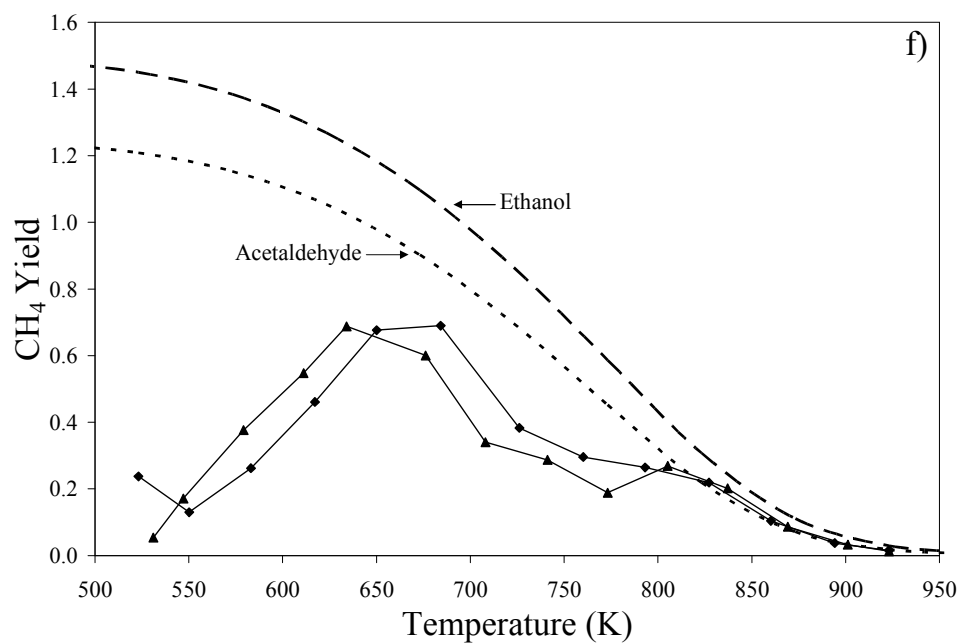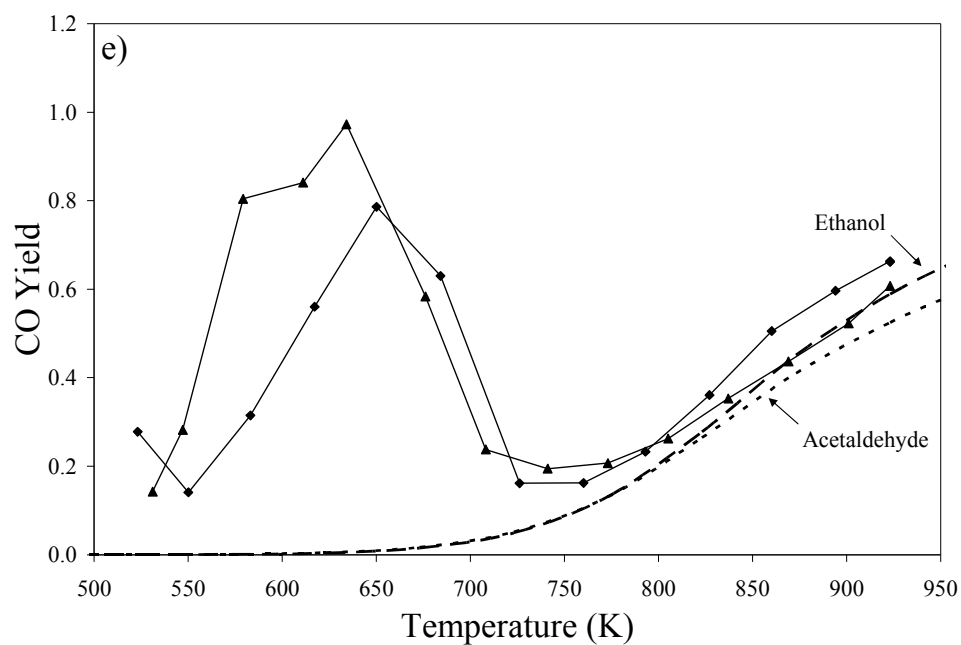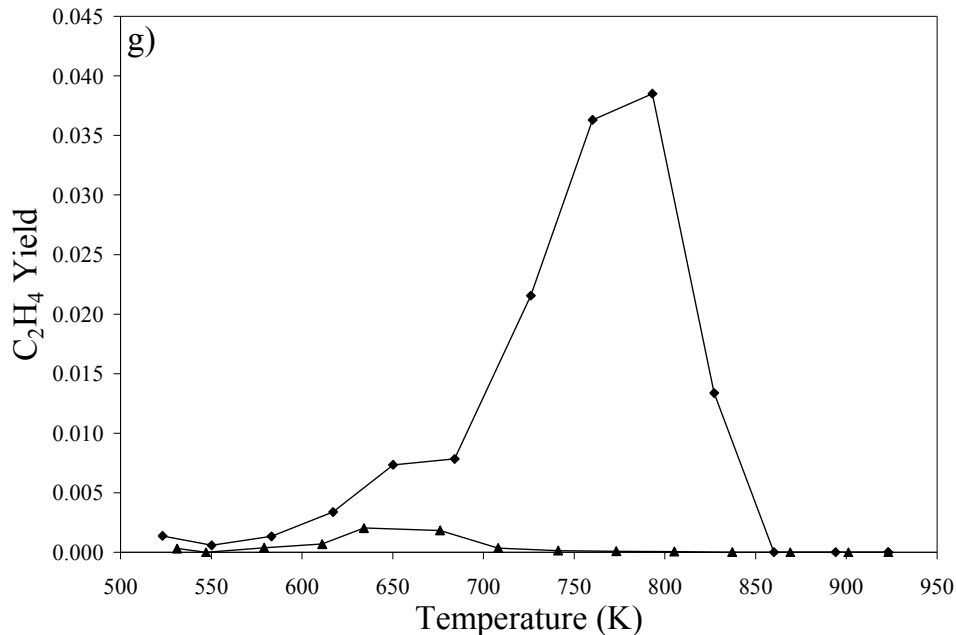
Figure 6.2 (c-d): Temperature programmed reaction for ethanol and acetaldehyde steam reforming. Ethanol (——◆——) and Acetaldehyde (——▲——). Equilibrium expectations are presented by dashed lines. H_2O:Reactant feed ratio was maintained at 8.4:1 for both ethanol and acetaldehyde.

Figure 6.2 (e-f): Temperature programmed reaction for ethanol and acetaldehyde steam reforming. Ethanol (——◆——) and Acetaldehyde (——▲——). Equilibrium expectations are presented by dashed lines. H$_2$O:Reactant feed ratio was maintained at 8.4:1 for both ethanol and acetaldehyde.

Figure 6.2(g): Temperature programmed reaction for ethanol and acetaldehyde steam reforming. Ethanol (—◆—) and acetaldehyde (—▲—). Equilibrium expectations are presented by dashed lines. H_2O:Reactant feed ratio was maintained at 8.4:1 for both ethanol and acetaldehyde.

The acetaldehyde temperature programmed reaction experiment experienced a similar maximum in conversion as the ethanol steam reforming reactions. The mechanism for the onset of deactivation in this moderate temperature range has been discussed in section 6.1.1.2, however, unlike the ethanol steam reforming experiments, very little ethylene (Figure 6.2g) was produced. Therefore, loss in catalytic activity must be directly associated with CH_3^* dehydrogenation (R.24) and CO disproportionation (R.6). Upon removing the catalysts from the reactor, carbon deposits were found on both spent catalysts. The presence of carbon on the spent acetaldehyde steam reforming catalyst indicates that ethylene is not the only reaction byproduct responsible for carbon deposition and that CH_3^* dehydration (R.24) and possibly CO disproportionation (R.6) contribute to the deposition of carbon. In retrospect, characterization of the carbonaceous deposits on these samples might have shed

much light on the roles of ethylene, CH_3^*, and CO in deactivation. However, the significance of ethylene in the deactivation of the ethanol steam reforming reactions becomes apparent when comparing the curves in Figure 6.2a and Figure 6.2g.

Comparison of the catalytic performance of Ni/Mg1Al2 for ethanol and acetaldehyde steam reforming shows that ethanol is more readily consumed than acetaldehyde (Figure 6.2a). The primary product of the ethanol steam reforming reaction at low temperatures is acetaldehyde, suggesting that ethanol dehydrogenation is the first step in the ethanol steam reforming reaction network at these temperatures. Starting from acetaldehyde or ethanol does not affect the product distribution regardless of the difference in the rate of consumption of the feed reactant. This relationship suggests that ethanol dehydrogenation (R.7) forming acetaldehyde and hydrogen occurs very quickly on the nickel supported catalyst (Ni/Mg1Al2) and that ethanol and acetaldehyde steam reforming share a common reaction intermediate that dictates the rate of the steam reforming reaction (rate determining step). Therefore, acetaldehyde is a primary reaction product on supported nickel catalyst and an undesirable byproduct.

### 6.1.3 Methane steam reforming: Importance of the methyl group (CH_3^*)

Methane steam reforming reaction experiments were performed to determine the role of the CH_3^* group in the ethanol steam reforming reaction network and to determine if ethanol steam reforming could essentially be regarded as a combination of methane steam reforming and additional water-gas shift. Since the ethanol/acetaldehyde steam reforming reaction network on nickel proceeds through an intermediate that decomposes to CH_3^*, CO^*, and H^* via reaction (R.18) [Gates et al. (1985) and Saleh et al. (1986)], the difference between CH_4 and CH_3^* steam reforming was investigated. Temperature programmed methane steam reforming experiments were performed under the same conditions as discussed above. The H_2O:CH_4 molar feed ratios was maintained at 8.4:1 as in the ethanol steam reforming experiments. Since one mole of CH_4 is produced via ethanol/acetaldehyde decomposition and therefore the molar ratio H_2O:CH_4 or H_2O:CH_3^* would remain constant.

The liquid feed flow rate was adjusted to ensure that the total GHSV was similar to the ethanol/acetaldehyde reactions (GHSV = 266700 mL_{Feed} h^{-1} g_{cat}^{-1}).

Increasing the temperature from 523 to 923 K at 1 K min^{-1} revealed that the catalyst was not active for the methane steam reforming reaction since no methane was consumed and no products were detected. The most likely explanation for this phenomenon is that the reduced nickel, Ni^0, catalyst had been oxidized to NiO by water [Xu and Froment (1989)] via reaction (R.25), especially at low temperatures below which methane would adsorb and react on the surface.

$$Ni^0 + H_2O \longrightarrow NiO + H_2 \quad\quad\quad\quad (R.25)$$

Several methane partial oxidation studies have shown that CH_4 reacts with NiO via an Eley-Rideal mechanism producing a reduced nickel site via reaction and is very slow in comparison to the interaction between CH_4 and reduced nickel sites [Hu and Ruckenstein (1998) and Coleman et al. (submitted)].

$$CH_4 + 2NiO \longrightarrow CO_2 + 2H_2 + 2Ni^0 \quad\quad\quad\quad (R.26)$$
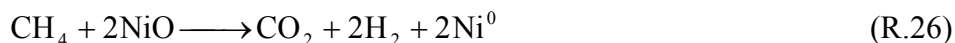
Therefore, at the reaction temperatures used in this study, the rate of oxidation of the in-situ reduced nickel sites by water was greater than the rate of CH_4 adsorption and reaction on the reduced nickel sites, resulting in no conversion of CH_4. This is in stark contrast to the ethanol and acetaldehyde steam reforming experiments. In both cases, the reactants were able to adsorb and react on the surface prior to nickel oxidation by water and produce steam reforming products, H_2, CO, and CO_2, in addition to CH_4.

To increase the likelihood of CH_4 adsorbing on the reduced nickel catalyst before it was oxidized by water, methane steam reforming experiments were performed stepwise at 723, 823, and 923 K. The reaction temperature was increased from 723 to 923 K at 100 K

intervals almost instantaneously every 8 h on stream. Methane conversion and product yields are presented as a function of time on stream and temperature in Figure 6.3a-d.

Immediately upon introduction of the reactants to the catalyst bed the reaction initiated. Methane was consumed and steam reforming products H_2, CO, and CO_2 were exclusively produced. Methane conversion (Figure 6.3a) increased with increasing temperature but more importantly, the deviation between the experimental and equilibrium expected conversion decreased from 47.3% at 723 K to 14.0% for 823 K, and to 1.7% at 923 K. In addition, the activity and selectivity were unaffected by time on stream suggesting that CH_4 dehydrogenation leading to carbonaceous deposits either did not occur or did not affect catalyst activity within the time evaluated.
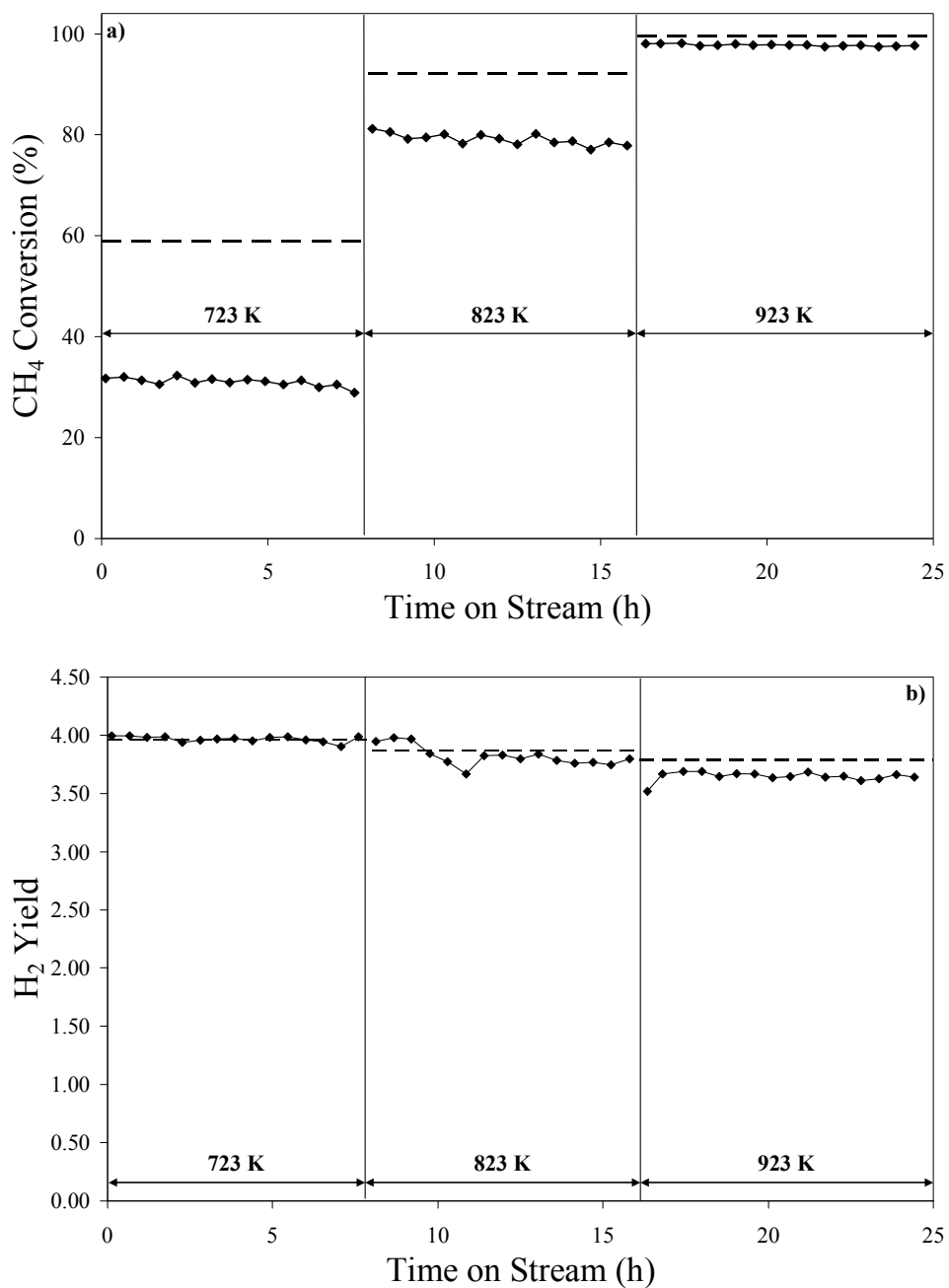
Figure 6.3 (a-b): Methane steam reforming over Ni/Mg1Al2 at 723, 823, and 923 K. $H_2O:CH_4$ = 8.4:1. GHSV = 266,655 mL_{Feed} h^{-1} g_{cat}^{-1}. Equilibrium expectations are presented by dashed lines.
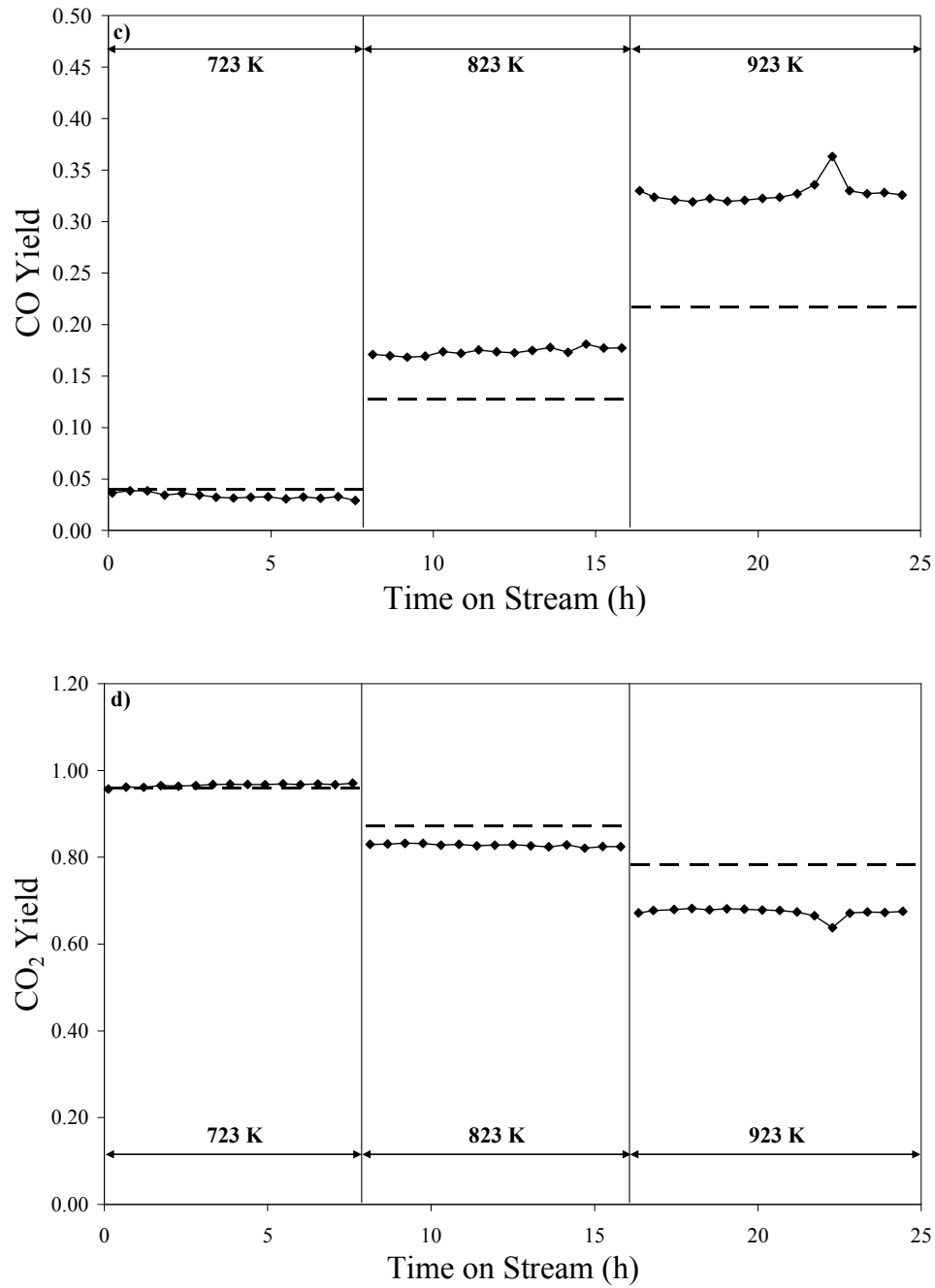
Figure 6.3 (c-d): Methane steam reforming over Ni/Mg1Al2 at 723, 823, and 923 K. $H_2O:CH_4 = 8.4:1$. GHSV $= 266,655$ mL$_{Feed}$ h^{-1} g$_{cat}^{-1}$. Equilibrium expectations are presented by dashed lines.

As mentioned, at 723 K, the product distribution (Figure 6.3b-d) closely matched the equilibrium expectations, however, increasing temperature increased the difference between experimental and equilibrium expectations. Hydrogen and CO_2 yields fell below while the CO yield exceeded equilibrium expectations suggesting that CO is a primary reaction product and that H_2 and CO_2 are produced via secondary reactions with CO. This relationship suggests that the methane steam reforming reaction network proceeds through reaction (R.5) producing H_2 and CO and continues via the water-gas shift reaction (R.3) to produce CO_2 and additional H_2.

$$CH_4 + H_2O \longrightarrow 3H_2 + CO \qquad\qquad (R.5)$$

$$CO + H_2O \longrightarrow H_2 + CO_2 \qquad\qquad (R.3)$$

Wei and Iglesia (2004), using a kinetic/isotopic experimental approach, revealed that methane steam reforming and methane decomposition are mechanistically equivalent. Their work verified the rate determining step to be C-H abstraction where CH_4 is sequentially dehydrogenated via reactions (R.20-R.23) and each C-H abstraction became successively easier. DFT calculations [Burghgraef et al. (1995)] revealed that the activation energy for the complete C-H abstraction of $CH_4(g)$ was 211 kJ mol^{-1}, the summation of the activation energies in reactions (R.27-30) compares well with reported activation energies for methane steam reforming [240.1 kJ mol^{-1} [Xu and Froment (1989)] and 209.2 kJ mol^{-1} [Hou and Hughes (2001)].

$$CH_4^{(g)} + 2^* \longrightarrow H_3C^* + H^* \qquad E_a = 142\,kJ\,mol^{-1} \quad (R.27)$$

$$H_3C^* + {}^* \longrightarrow H_2C^* + H^* \qquad E_a = 38\,kJ\,mol^{-1} \quad (R.28)$$

$$H_2C^* + {}^* \longrightarrow HC^* + H^* \qquad E_a = -61\,kJ\,mol^{-1} \quad (R.29)$$

$$HC^* + {}^* \longrightarrow C^* + H^* \qquad E_a = 92\,kJ\,mol^{-1} \quad (R.30)$$

The work by Wei and Iglesia (2004) coupled with the DFT calculations [Burghgraef et al. (1995)] suggest that once CH_4 is activated on the nickel surface (R.27) the subsequent dehydrogenation steps (R.28-30) are relatively fast leading to very low CH_x surface coverage and therefore all oxidizing reactions producing CO and CO_2 proceed through C^*. The product distribution becomes dependent upon the relative rates of the competing reactions. For example, the rate of CO desorption from the nickel surface (R.21) is highly affected by increasing temperature (E_a = 113 kJ mol^{-1} [Hei et al. (1998)], while the rate of CO_2 desorption, having an activation energy of 27.2 kJ mol^{-1} [Hei et al. (1998)]), is not as strongly affected.

Therefore, ethanol/acetaldehyde steam reforming cannot be regarded as pseudo methane steam reforming. Methane steam reforming is kinetically limited by the activation and C-H abstraction of CH_4 to CH_3^*. This rate-limiting step represents the essential difference between CH_4 steam reforming and reforming of the surface methyl group, CH_3^*, produced by ethanol/acetaldehyde decomposition.

6.1.4 Bidirectional temperature ramps: The effect of catalyst history

The effect of catalyst history on the performance of Ni/Mg1Al2 for ethanol steam reforming was evaluated using a bidirectional temperature programmed reaction technique. The reaction temperature was increased from 523 K to 923 K at 1 K min^{-1} and maintained for 0.5 h and reduced at 1 K min^{-1} to 523 K. Figure 4a-i presents the catalytic activity and product yields for the ramp up and ramp down experiments for the 8.4:1 ethanol steam reforming experiment previously discussed in section 6.1.1 (Figure 6.1). A comparison of the ramp up and ramp down results reveals several significant differences. Above 725 K, the ramp direction does not affect any of the catalyst evaluation parameters: conversion, water utilization, and product yields (Figure 6.4a-i). However, below 725 K, the catalyst activity and product selectivity are affected by the ramp direction. Ethanol conversion for the ramp down experiment, although always lower than the ramp up conversion, follows a more

kinetically expected relationship with temperature. The reduction in catalytic activity below 725 K suggests that the catalyst has been modified by the reaction environment. Loss in catalytic activity with decreasing temperature below 725 K coincided with an increase in water utilization, and hydrogen and CO_2 yields, while CO and CH_4 yields, strongly affected by temperature for the ramp up experiment, became relatively independent of the reaction temperature. For temperatures below 600 K, the hydrogen yield dropped to zero, or to such a small amount that the concentration was below the TC detector sensitivity of the gas chromatograph. Below 625 K, the acetaldehyde yield for the ramp down experiment falls well below the ramp up yield results.

The product composition during the ramp up and ramp down segments of the temperature programmed experiment suggest that a steam reforming reaction pathway is dominant during the ramp down portion of the experiment. For this to have occurred, the supported nickel catalyst was modified during the ramp up portion of the experiment resulting in a significant reduction in the activity of the catalyst below 725 K and a change in the dominant reaction pathway, from ethanol dehydration/decomposition to ethanol steam reforming.
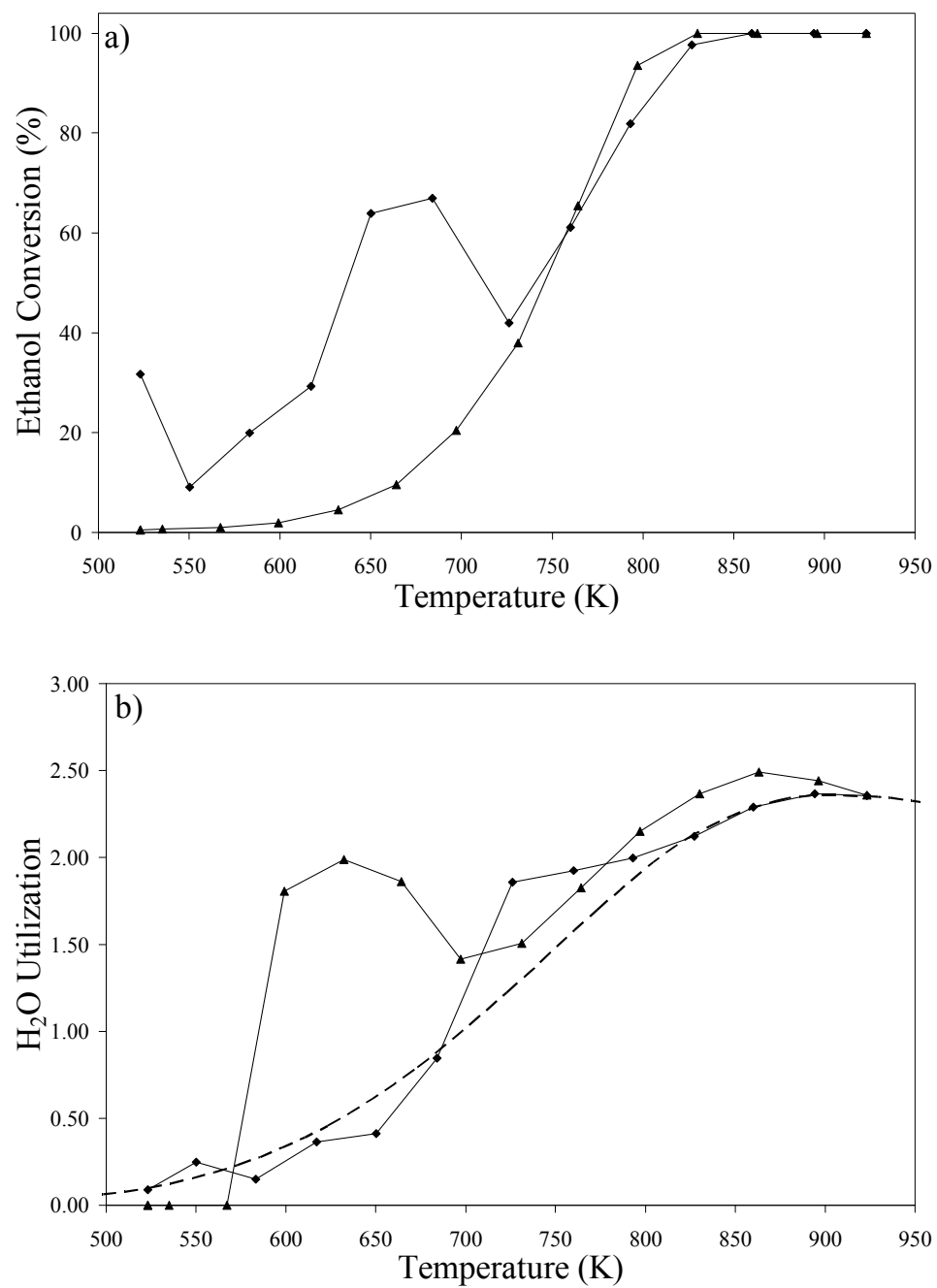
Figure 6.4 (a-b): Effect of reaction history on performance of Ni/Mg1Al2. H_2O:EtOH=8.4, GHSV = 275740 mL_{Feed} h^{-1} g_{cat}^{-1}.(—♦—)Ramp up,(—▲—) Ramp down. Equilibrium expectations are represented by dashed lines.
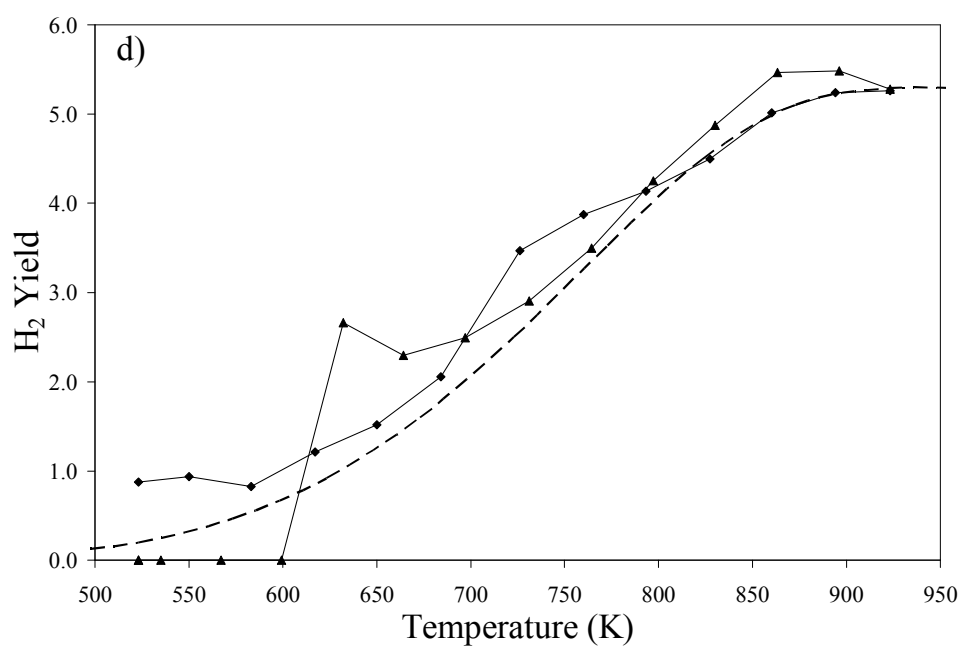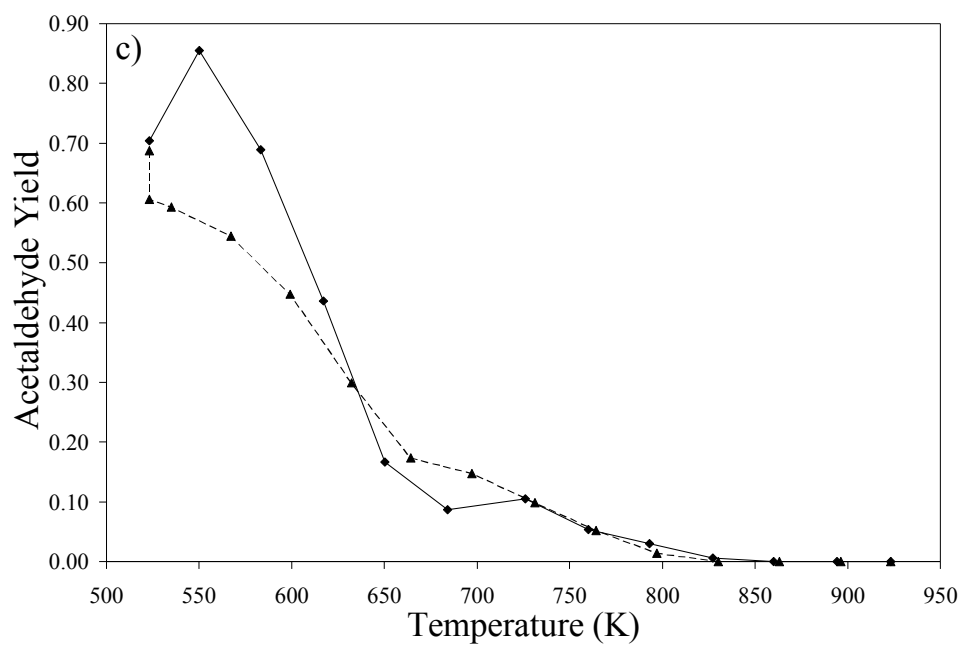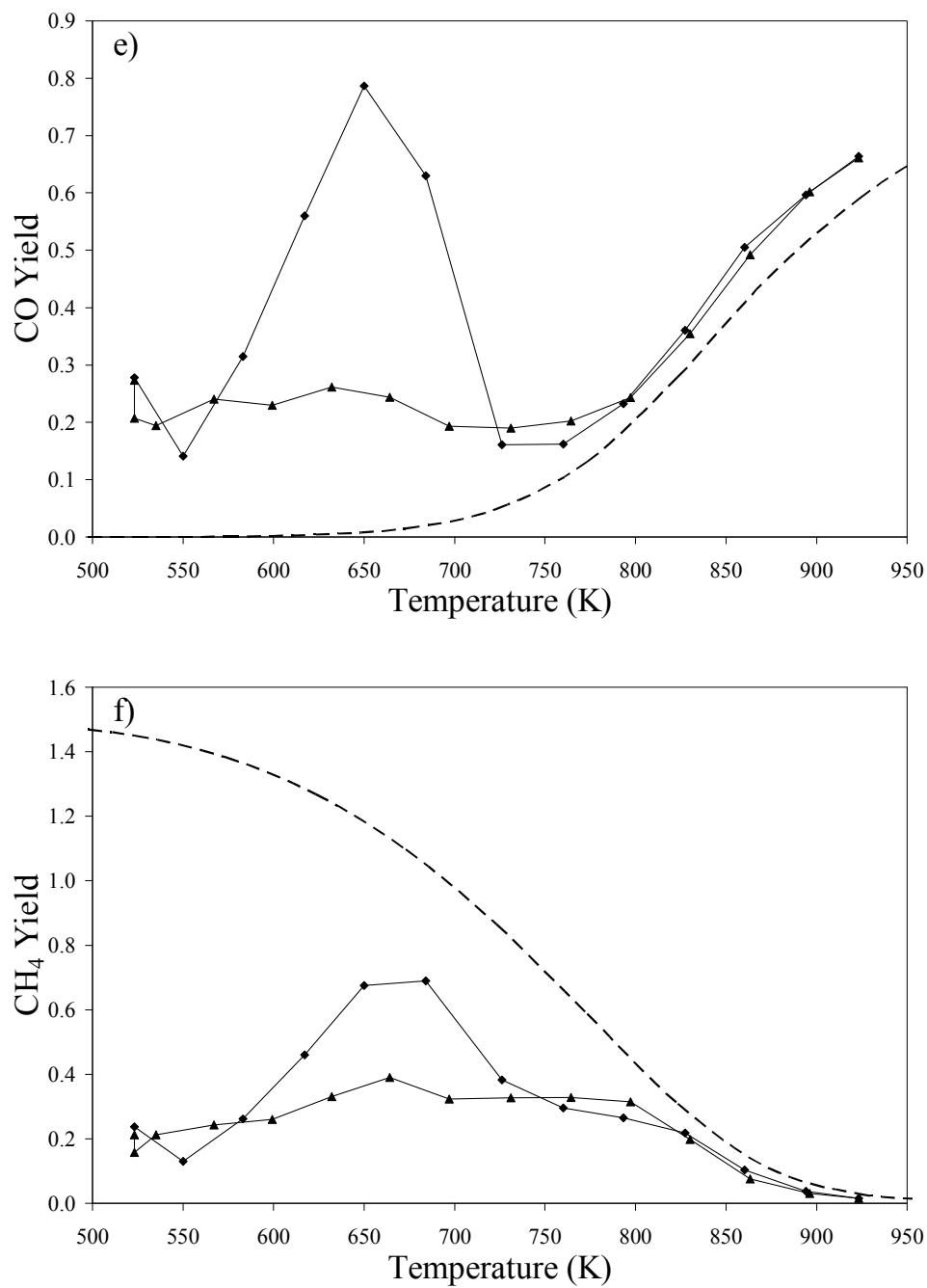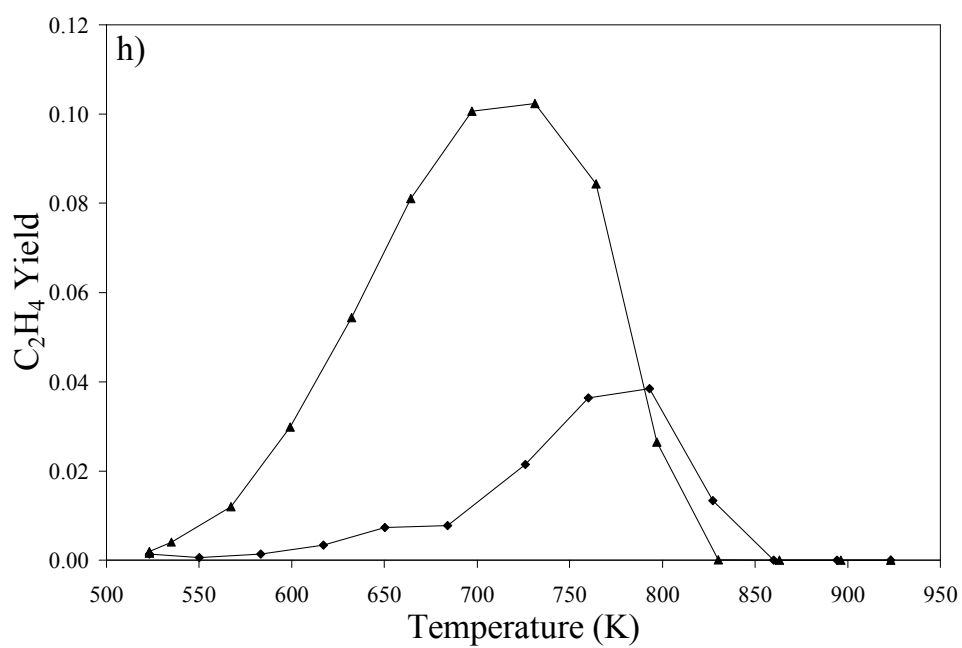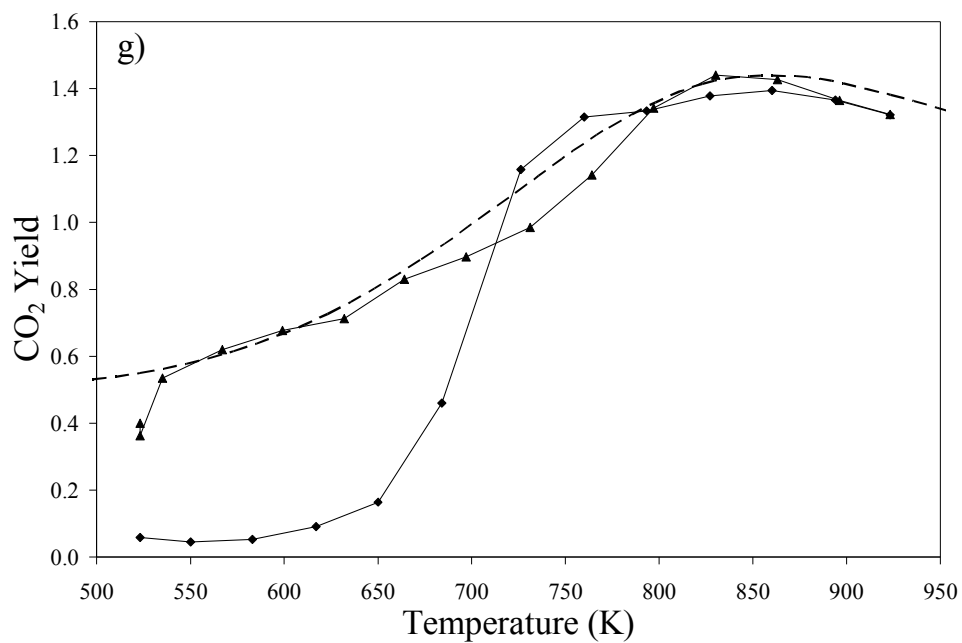
142

Figure 6.4 (c-d): Effect of reaction history on performance of Ni/Mg1Al2. H_2O:EtOH=8.4, GHSV = 275740 mL_{Feed} h^{-1} g_{cat}^{-1}.(——◆——)Ramp up(——▲——) Ramp down. Equilibrium expectations are represented by dashed lines.
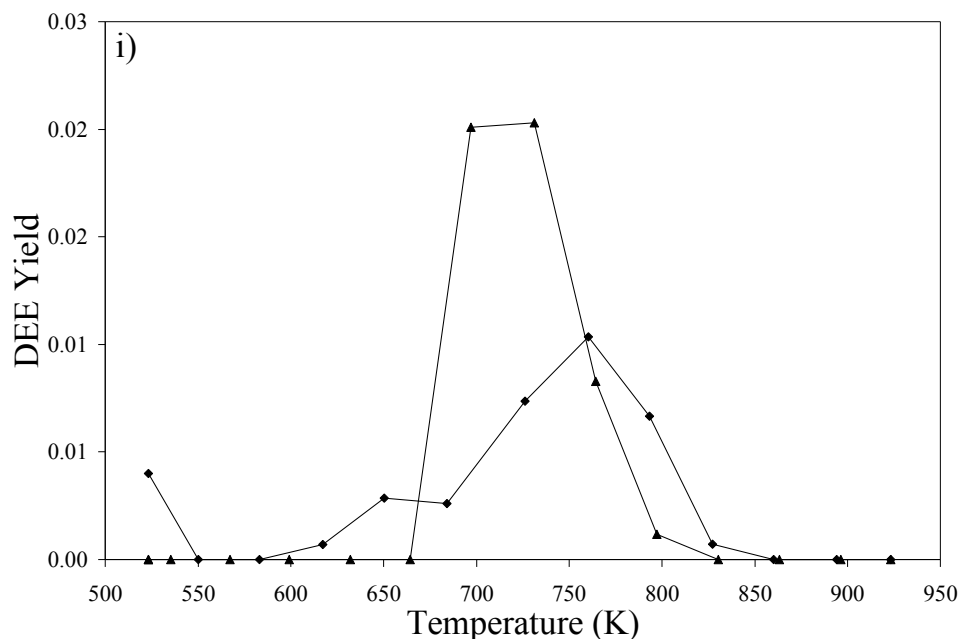
Figure 6.4 (e-f): Effect of reaction history on performance of Ni/Mg1Al2. H_2O:EtOH=8.4, GHSV = 275740 mL$_{Feed}$ h^{-1} g$_{cat}$$^{-1}$.(—◆—)Ramp up,(—▲—) Ramp down. Equilibrium expectations are represented by dashed lines.

144

Figure 6.4 (g-h): Effect of reaction history on performance of Ni/Mg1Al2. H_2O:EtOH=8.4, GHSV = 275740 mL_{Feed} h^{-1} g_{cat}^{-1}.($-\blacklozenge-$)Ramp up,($-\blacktriangle-$) Ramp down. Equilibrium expectations are represented by dashed lines.

Figure 6.4 (i): Effect of reaction history on performance of Ni/Mg1Al2. H_2O:EtOH=8.4, GHSV = 275740 mL_{Feed} h^{-1} g_{cat}^{-1}. (——◆——) Ramp up, (——▲——) Ramp down. Equilibrium expectations are represented by dashed lines.

The most probable explanation, from the results presented, is that the deposition of carbon on the catalyst resulted in modification to the support-nickel interaction or the active metal phase. Of the two types of carbon deposits expected, encapsulating film or filamentous, filamentous carbon is the more probable candidate. The effect of the heating direction on activity and product selectivity occurred at temperatures below 725 K, where the formation of filamentous carbon is not favored. Filamentous carbon formation is favorable at temperatures above 723 K [Bartholomew (2001)]. Therefore, during the second leg of the experiment (ramp down), decreasing the temperature below 723 K resulted in the presence of filamentous carbon deposits on the surface of the catalyst below a temperature that they would normally form. As discussed in the previous chapter, see Section 5.3 and Figure 5.19, filamentous carbon extracts the nickel crystallite from the surface of the catalyst and grows away from the support material. The extracted nickel crystallites are no longer affected by

146

metal-support interactions resulting in the gas phase having direct access to the nickel crystallite. Thus, selectivity for reactions catalyzed in entirety by nickel increased.

Regardless of the specific mechanism responsible for this substantial improvement in the selectivity for the steam reforming products, H_2, CO, and CO_2, be it the deactivation of undesirable sites or the activation of new desirable sites, the result is reduced CH_4 yield. The results presented up to this portion suggest that a low temperature direct ethanol steam reforming reaction mechanism is active over the Ni/Mg1Al2 catalyst in which CH_4 yields do not meet thermodynamic expectations.

6.2 Time on Stream Experiments

To further explore the transition of the dominant reaction pathway from ethanol/acetaldehyde decomposition producing high CH_4 yields to a direct steam reforming route and the role of catalyst deactivation on this transition, time-on-stream experiments were performed. Time on stream experiments, lasting approximately 20 h, were performed at several reaction temperatures spanning 648 to 923 K for a constant GHSV (Gas Hourly Space Velocity) of approximately 260,000 mL_{Feed} h^{-1} g_{cat}^{-1} and at several GHSVs ranging from 66300 (200 mg Ni/Mg1Al2) to 2547000 (5 mg Ni/Mg1Al2) mL_{Feed} h^{-1} g_{cat}^{-1} at a constant temperature of 823 K using the same reactor system and pretreatment procedure as discussed in previous sections. The H_2O:EtOH molar feed ratio used all experiments was maintained at 8.4:1.

6.2.1 Effect of temperature

The effect of temperature on ethanol conversion for a constant feed GHSV of approximately 260,000 mL_{Feed} h^{-1} g_{cat}^{-1} is presented in Figure 6.5a. Initially ethanol conversion was high for all temperatures investigated, with several temperatures achieving near complete ethanol conversion. As time on stream progressed, ethanol conversion decreased with the lowest temperature experiments experiencing the most severe and rapid

deactivation. However, regardless of the degree or rate of deactivation experienced, the catalysts performance stabilized while the time to reach steady state conversion increased with increasing temperature. Of significant importance is the improvement in catalyst stability upon increasing the temperature from 873 to 923 K. At 873 K, catalyst deactivation was apparent within the first hour of operation and ethanol conversion declined by approximately 25% within the first 20 h of operation, whereas at 923 K complete conversion was maintained for 20 h time on stream.

The onset of catalyst deactivation and incomplete ethanol conversion was accompanied by the appearance of ethylene (Figure 6.5b) in the product gas. For example, at 923 K, ethanol conversion remained complete for at least 20 h time on stream and ethylene was not detected in the product gas, whereas at 873 K, incomplete ethanol conversion coincided with the appearance of ethylene. The relationship between ethylene yield and catalyst deactivation was further strengthened by considering experiments performed at reaction temperatures above 723 K. Initially, ethylene is not detected in the product gas and ethanol conversion is complete. However, within the first hour of operation, ethanol conversion decreases and ethylene breaks through and is detected in the product gas. For reaction temperatures below 723 K, ethanol conversion is initially incomplete and ethylene is detected immediately in the product gas. These results indicate that catalyst deactivation under these test conditions is associated with ethylene. Ethylene is produced via the ethanol dehydration reaction (R.11) which is catalyzed by the acidic sites associated with the support (Mg1Al2).
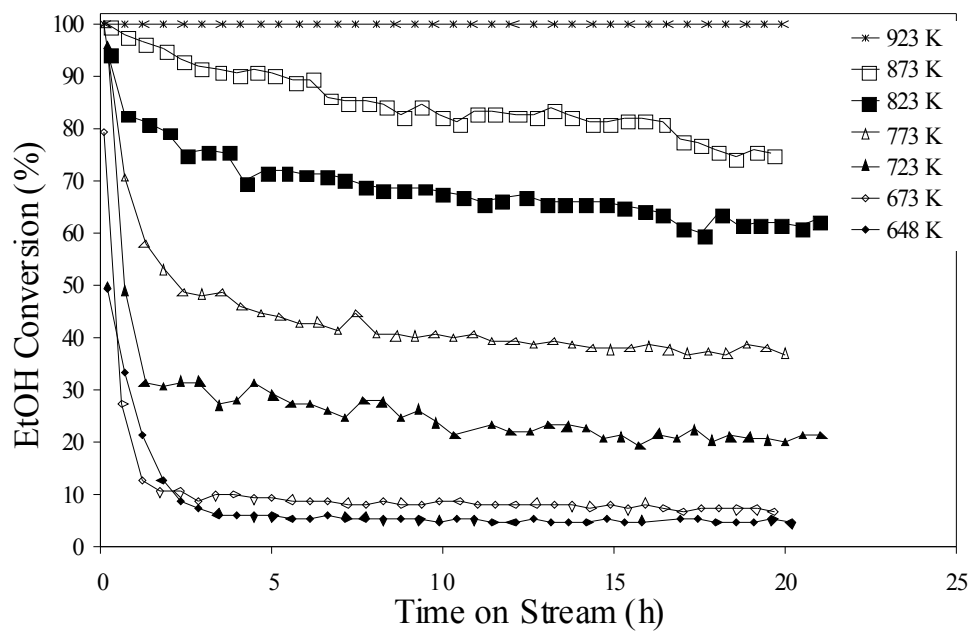
Figure 6.5a: Effect of temperature on ethanol conversion as a function time on stream.
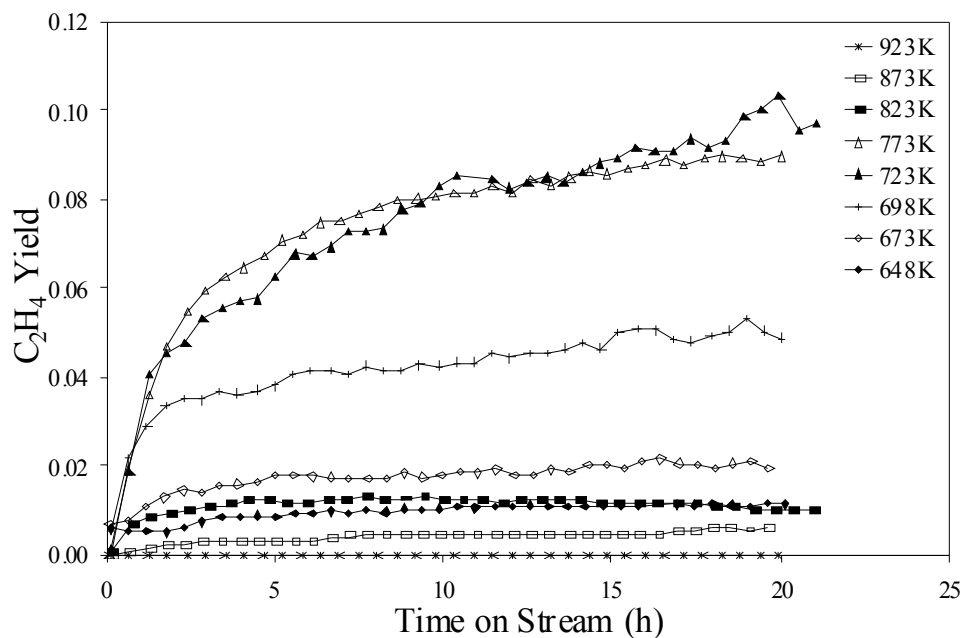

Figure 6.5b: Effect of temperature on C$_2$H$_4$ yield as a function of time on stream.
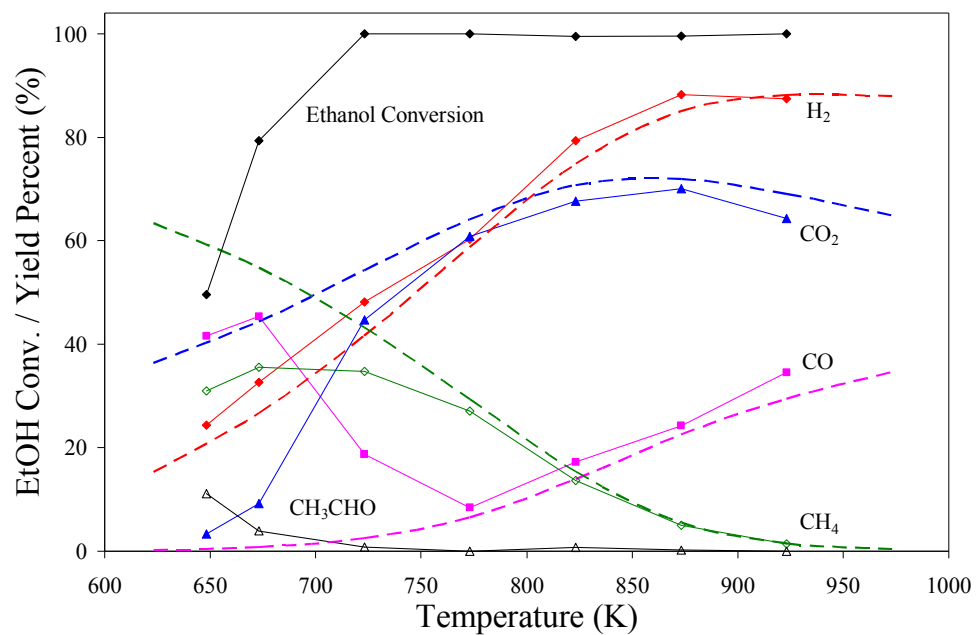
149

Figure 6.5c: Effect of temperature on product distribution at 0.15 h time on stream. Equilibrium expectations are represented by dashed lines.
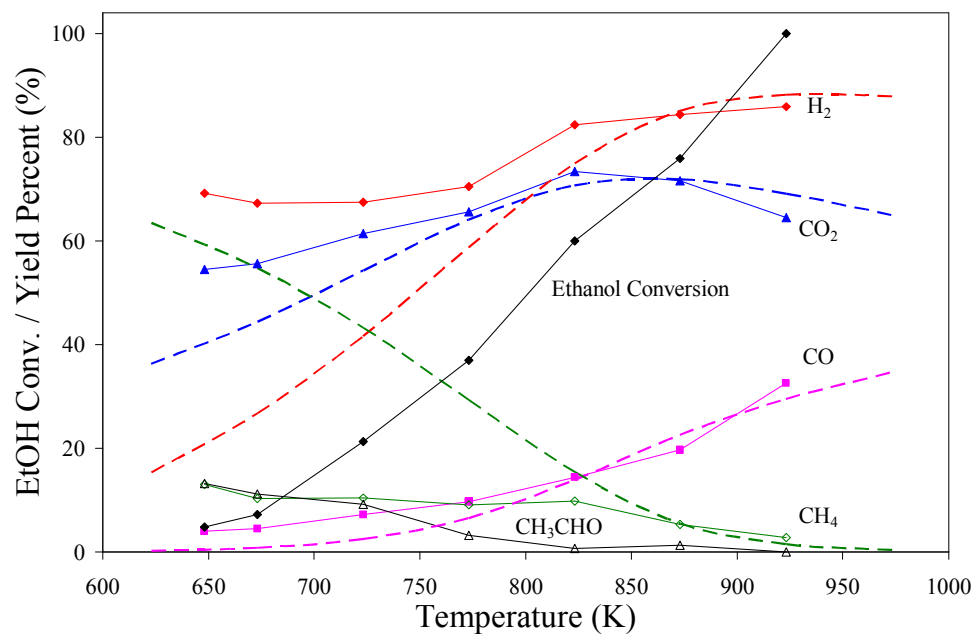

Figure 6.5d: Effect of temperature on product distribution at 20 h time on stream. Equilibrium expectations are represented by dashed lines.

$$CH_3CH_2OH \longrightarrow C_2H_4 + H_2O \qquad\qquad\qquad (R.11)$$

As previously discussed, ethylene is a known carbon deposition precursor and carbonaceous deposits were detected visually on all used samples, but have been verified by SEM micrographs given in Figure 5.19. Analytical techniques to characterize and quantify the amount of carbon deposited on the catalysts were not performed on these spent samples; therefore, it is not possible to comment on the relationship between ethylene yield and carbon deposition, or the effect of carbonaceous deposits on the rate and extent of deactivation. However, as discussed in the previous chapter, the relationship between carbon deposition and catalyst deactivation is not necessarily direct.

Considering the results presented in Figure 6.5a and Figure 6.5b, the rate and magnitude of deactivation increases with decreasing reaction temperature; however, ethylene yield passes through a maximum located around 723 or 773 K. This suggests that the deactivation mechanism is highly complex and that the rate of deactivation is controlled by the individual rates of competing reactions, for example, reactions leading to deactivation, ethanol dehydration (R.11), ethylene to carbon, and reactions minimizing the effects of deactivation such as ethylene steam reforming, and regeneration reactions such as carbon gasification.

The effect of catalyst deactivation on product selectivity can be seen by comparing the product distributions at the startup stage of the reaction, 0.15 h time on stream, (Figure 6.5c) to the pseudo-steady state stage, 20 h time on stream, (Figure 6.5d). Figure 6.5c and Figure 6.5d should be considered in light of the relationship between ethanol conversion and time on stream (Figure 6.5a), or in other words, in terms of catalyst deactivation. Recall that the initial catalyst activity was very high, giving near complete ethanol conversion for almost all temperatures studied. For reaction temperatures above 773 K, the distribution of products (H_2, CO_2, CO, and CH_4 yields), closely matched equilibrium expectations (Figure 6.5c) with no C_2-products, acetaldehyde and ethylene, detected in the product gas. For reaction

temperatures below 773 K, the product distribution deviated from equilibrium expectations and C_2-products were detected. The relationship between the divergence of the CO and CO_2 yields from their respective equilibrium expectations as previously discussed and can be explained by a reduction in activity for the water-gas shift (R.3) or CO disproportionation (R.6) reactions. The specific reaction responsible for this deviation, if not a combination effect, cannot be ascertained due primarily to the relationship between H_2 and CH_4. H_2 yield closely matched equilibrium expectations while CH_4 yield plateaued at approximately 35%. Assuming that the CO methanation reaction (R.5), does not occur or is very slow, CH_4 is produced solely by ethanol or acetaldehyde decomposition, therefore, CH_4 yield % can theoretically attain a maximum of 50%.

$$CO + H_2O \rightarrow H_2 + CO_2 \tag{R.3}$$
$$2CO \rightarrow C + CO_2 \tag{R.6}$$
$$CO + 3H_2 \rightarrow CH_4 + H_2O \tag{R.5}$$

Since the CH_4 yield falls below its equilibrium expectation and therefore the H_2 yield must consequently increase. The lower than expected CH_4 yields can be viewed as:

1) the CO methanation reaction (R.5) either does not occur or is very slow,
2) the hydrogenation of surface adsorbed CH_3^* to CH_4 and subsequent desorption from the surface is retarded, and/or
3) the rates of CH_4 consumption via either the decomposition or steam reforming reactions are increased.

Regardless of which mechanism is responsible for this behavior, the most important feature in this temperature range at 0.15 h time on stream is the deviation of the CO and CO_2 yields from their equilibrium expectations and that the ethanol/acetaldehyde decomposition products, H_2, CO and CH_4, dominate the product gas.

After 20 h time on stream, the dominant mechanism for reaction temperatures below 773 K changed from ethanol/acetaldehyde decomposition resulting in high CH_4 yields to a direct steam reforming reaction pathway, producing primarily H_2, CO, and CO_2 (Figure 6.5d). The transition in the dominant reaction pathway can be further demonstrated by considering the time on stream behavior of the H_2 (Figure 6.5e), CO_2 (Figure 6.5f), CO (Figure 6.5g), CH_4 (Figure 6.5h), and acetaldehyde (Figure 6.5i) yields for temperatures between 648 and 923 K. For temperatures of 823 K and above, the product gas composition remains independent of time on stream even though the catalysts experience deactivation as seen in Figure 6.5a. However, for temperatures below 823K, the product gas composition is strongly affected by time on stream, and more specifically, catalyst deactivation. H_2 and CO_2 yields increase and stabilize with time on stream while the yield of the decomposition products, CO and CH_4, decline and stabilize. Acetaldehyde yield for experiments performed below 773 K rapidly increases with time on stream, passes through a maximum, declines, and stabilizes. Interestingly, the location of the maximum in acetaldehyde yield coincides with the point of inflection in the ethanol conversion curve (Figure 6.5a). The incline portion of the acetaldehyde yield curve (Figure 6.5i) was accompanied by a decline in the CO (Figure 6.5g) and CH_4 (Figure 6.5h) yields which suggests that catalyst deactivation is adversely affecting the rate of the acetaldehyde decomposition reaction (R.8). However, as acetaldehyde yield passed through the maximum and dropped, selectivity for the decomposition products remained constant, while H_2 and CO_2 yields continued to increase. This behavior suggests that acetaldehyde, or a surface intermediate that leads to the formation of gaseous acetaldehyde, is being directly converted to H_2 and CO_2 without passing through gas phase CO and CH_4.
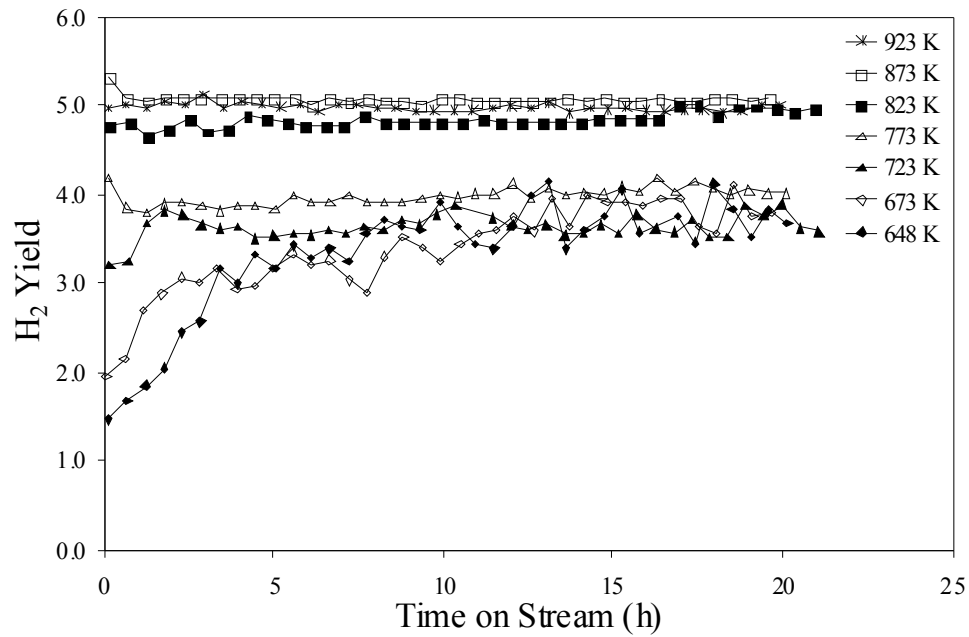
Figure 6.5e: Effect of temperature on H_2 yield as a function of time on stream.

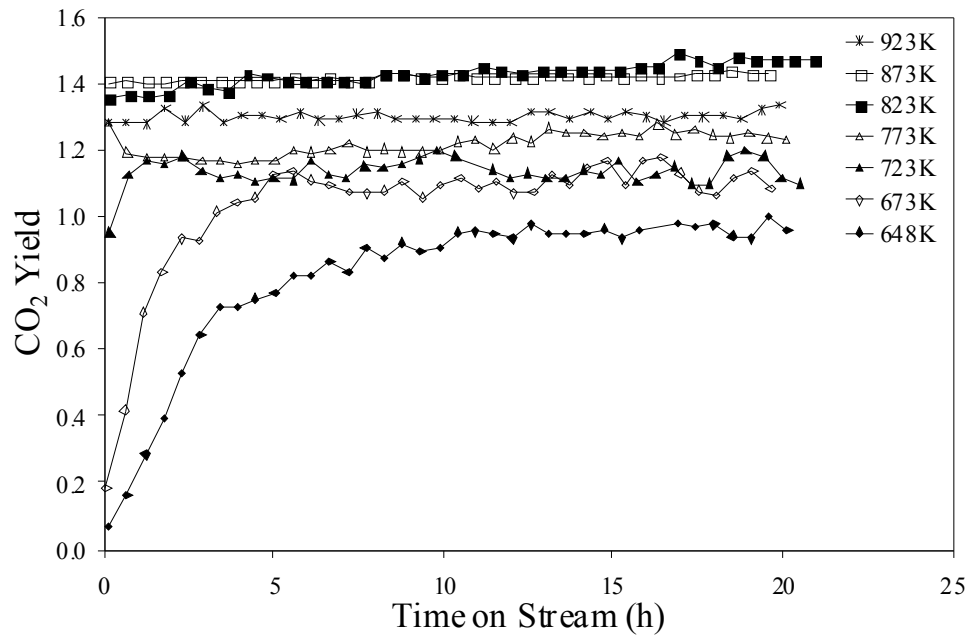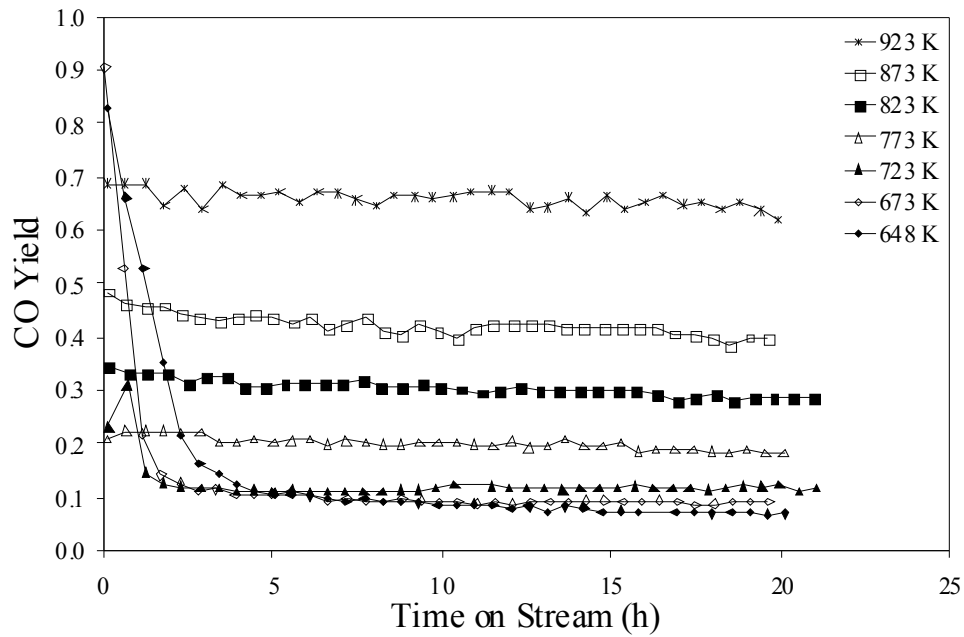**Figure 6.5f:** Effect of temperature on CO_2 yield as a function of time on stream.

154

Figure 6.5g: Effect of temperature on CO yield as a function of time on stream.

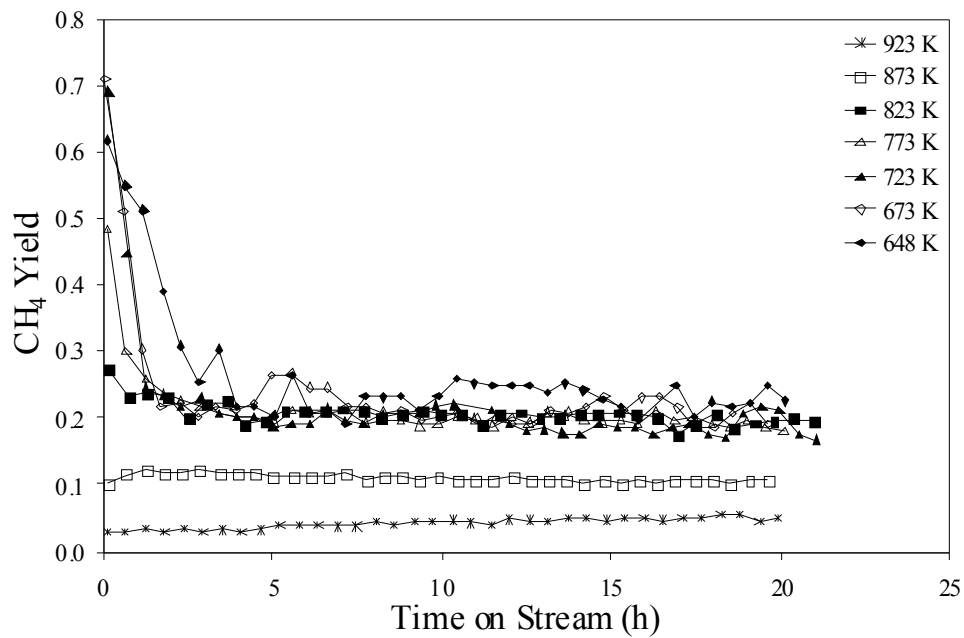**Figure 6.5h:** Effect of temperature on CH₄ yield as a function of time on stream.
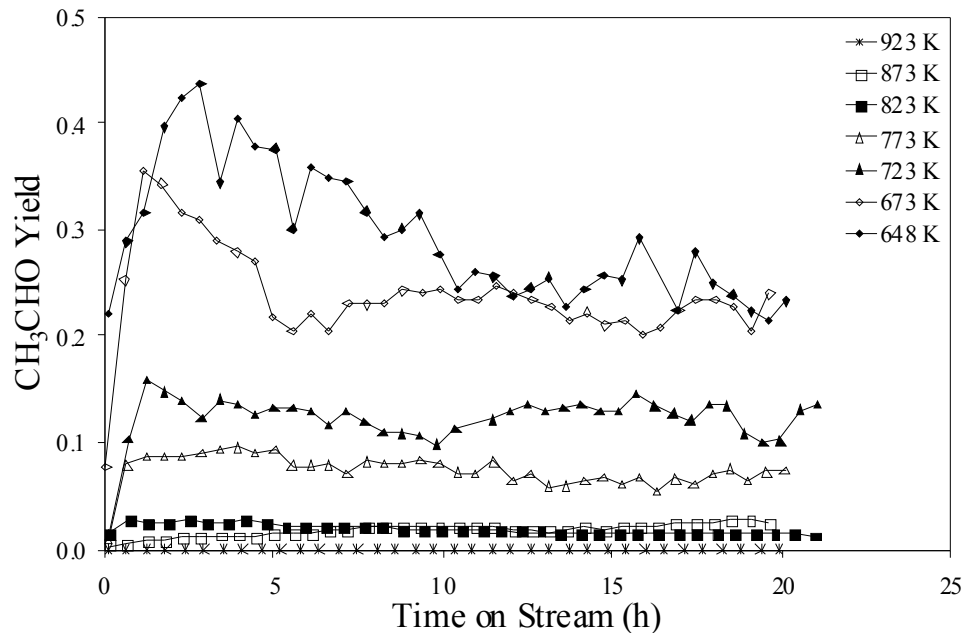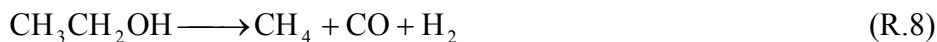
155

Figure 6.5i: Effect of temperature on acetaldehyde yield as a function of time on stream.

The evolution of the catalyst with time on stream can be classified into three stages: initial, transitional, and stable. The initial stage exhibits high ethanol conversion and therefore activity, suggesting that the catalyst initially has many active sites. The dominant products were H_2, CO, and CH_4 which originate from the decomposition of ethanol (R.9) and/or acetaldehyde (R.8).

$$CH_3CH_2OH \longrightarrow CH_4 + CO + H_2 \qquad\qquad (R.8)$$

$$CH_3CHO \longrightarrow CH_4 + CO \qquad\qquad (R.9)$$

As time on stream progressed into the transitional stage, the number of catalytically active sites declined, as exhibited by the reduction in ethanol conversion (Figure 6.5a), which resulted in an increase in the yield of the primary reaction intermediate, acetaldehyde. In addition, the reduction in the number of catalytic sites adversely affected the rate of the acetaldehyde decomposition reaction resulting in a decrease in the CO and CH_4 yields.

156

However, during this stage, H_2 and CO_2 yields continued to increase suggesting that they were produced on catalytic sites that were either not adversely affected by the deactivation mechanism, or more realistically that the sites producing H_2 and CO_2 directly from ethanol or acetaldehyde were activated or possibly created during the deactivation process. Acetaldehyde yield began to decrease and as previously discussed, H_2 and CO_2 yields continue to increase suggesting that acetaldehyde, or a surface intermediate that led to gas phase acetaldehyde, is being directly converted to H_2 and CO_2.

The time on stream to obtain stable operation of the catalyst increases with increasing reaction temperature; however, in surprising contrast, the product distribution stabilizes earlier for the higher temperature experiments. The obvious exception to this is the experiment performed at 923 K, which was capable of maintaining 100% ethanol conversion for over 20 h of operation. For reaction temperatures below 773 K, the product yields stabilize and are maintained even though they do not match the expected equilibrium. In fact, the H_2 yield for reaction temperatures of 648 to 773 K stabilize at approximately 3.75 moles of H_2 per mole of ethanol converted showing very little dependence upon temperature.

6.2.2 Effect of GHSV

The effect of gas hourly space velocity on ethanol conversion for a constant temperature of 823 K is presented in Figure 6.6a. The values in parenthesis refer to the mass of catalyst loaded for each respective experiment. Gas hourly space velocity (GHSV) is defined as the volume of gas delivered to a unit weight of catalyst per hour. In this study, varying the GHSV was achieved by loading different amounts of catalyst (10Ni/Mg1Al2) into the reactor which ensured that the mass- and heat-transfer characteristics, functions of the gas velocity through the bed, remained constant for all experiments. Ethanol conversion increased with decreasing GHSV (or increasing catalyst loading) as shown in Figure 6.6a. Initially, ethanol conversion was high for all GHSVs studied, but as time on stream progressed, conversion decreased. For catalyst loadings of 50 mg and less (GHSVs greater than 264,295 mL h^{-1} g_{cat}^{-1}), catalyst deactivation was immediately apparent. Increasing the

catalyst loading to 100 and 200 mg significantly improved the stability of the catalyst bed and time for ethanol breakthrough to occur. In fact, when the catalyst loading was increased to 200 mg, the onset of deactivation was not detected for over 110 h of operation. Similarly, a large improvement in catalyst stability is noted when increasing the catalyst loading from 50 to 100 mg. A doubling of the catalyst loading from 25 to 50 mg, and similarly from 12.5 to 25 mg resulted in an improvement in ethanol conversion but not in catalyst stability.
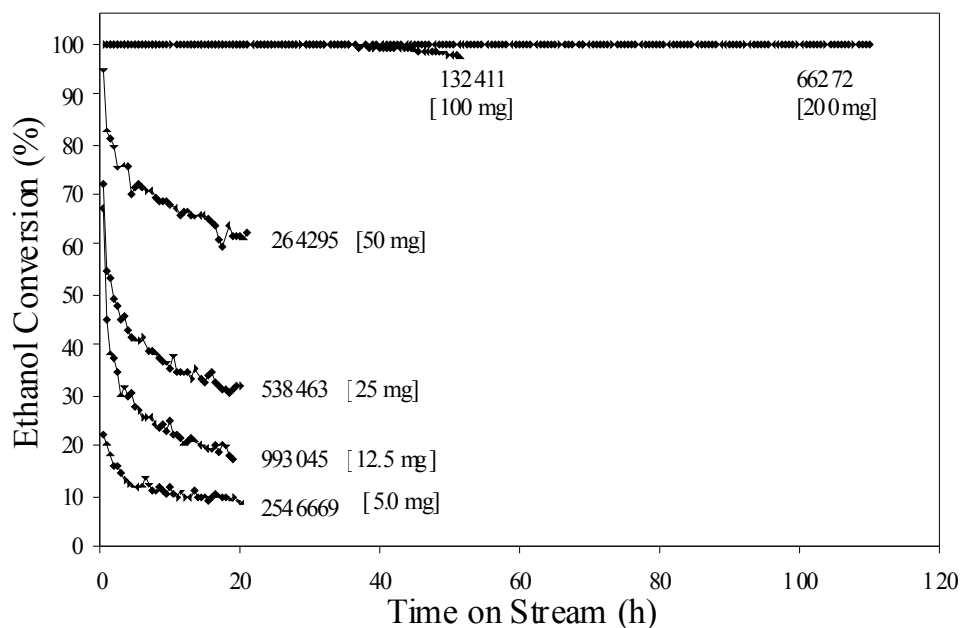

Figure 6.6a: Effect of GHSV on ethanol conversion as a function of time on stream at 823 K. GHSVs reported in the figure have units of mL_{Feed} h^{-1} g_{cat}^{-1}. Values in parenthesis refer to the amount of catalyst loaded in the reactor.
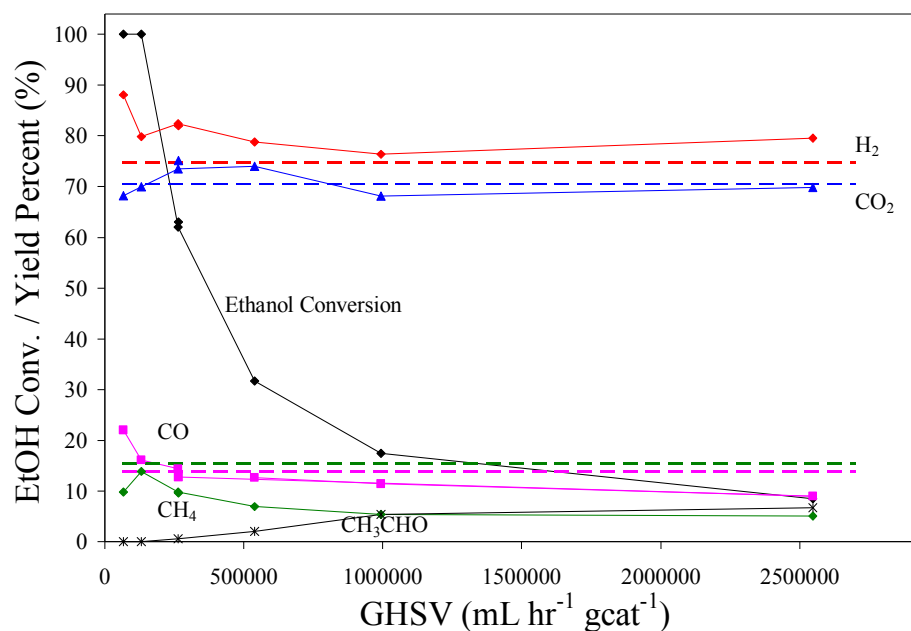
Figure 6.6b: Effect of GHSV on product distribution at 20 h time on stream ay 823 K. Equilibrium expectations are represented by dashed lines.

Ethanol conversion and product yield percent are presented in Figure 6.6b as a function of GHSV after 20 h time on stream. The thick dashed lines presented in Figure 6.6b represent the equilibrium yield percent expectations. At 823 K, ethanol conversion decreases with increasing GHSV while the product distribution is relatively unaffected. Acetaldehyde yield percent increases with increasing GHSV. At low GHSVs corresponding to 100% ethanol conversion, acetaldehyde yield percent is zero. Increasing the GHSV to the point of incomplete ethanol conversion resulted in the appearance of acetaldehyde in the product stream. Further increases in the GHSV lead to lower ethanol conversions and increased acetaldehyde yield. Considering that at the highest GHSV where ethanol conversion was very low (approximately 8%) acetaldehyde was only a minor component of the product gas and that decreasing GHSV resulted in increased ethanol conversion but a decrease in acetaldehyde yield. These points indicate that acetaldehyde is a reaction intermediate, but at this temperature and during the stable stage of operation, the dominant reaction pathway leading to H_2 and CO_2 does not proceed through gaseous acetaldehyde. To further strengthen

159

this argument, acetaldehyde yield decreased with decreasing GHSV and the yield of the decomposition products, CO and CH_4, increased, but H_2 and CO_2 yields remained relatively constant. The fact that the H_2 and CO_2 yields remained constant over the entire range of GHSVs studied, considering that ethanol conversion spanned $8 - 100\%$, suggests that H_2 and CO_2 are produced via an alternative reaction pathway independent of gaseous acetaldehyde and CH_4.

6.3 Effect of Pressure

Thermodynamic studies investigating the effect of pressure on ethanol steam reforming showed that increasing pressure had a negative effect on H_2 yield favoring CH_4 production [Garcia and Laborde (1991); Ionnides (2001)]. Experimentally, Aupretre et al. (2004), the only study reporting on the effect of pressure on ethanol steam reforming, showed that increasing the total pressure from atmospheric pressure to 11 bar at 973 K over a Rh/Ni-Mg/Al_2O_3 catalyst resulted in a reduction in the H_2 yield and a concomitant increase in the CH_4 yield, which closely matched thermodynamic expectations. In this study, thorough time on stream and bidirectional temperature ramped experiments identified an alternative direct ethanol steam reforming reaction pathway occurring over Ni/Mg1Al2 at temperatures below 823 K only after the catalyst had experienced significant deactivation and performance had stabilized. The transition to direct ethanol steam reforming was accompanied by substantial catalyst deactivation and H_2 and CO_2 yields exceeding equilibrium expectations at the expense of a reduced CH_4 yield. Hence, it is proposed that for temperatures below 823 K, the effect of pressure on ethanol steam reforming product distribution over Ni/Mg1Al2 during the stable portion of its operation should have very little effect on the product yields.

The effect of pressure was investigated at two temperatures, 673 and 823 K, at atmospheric pressure, 2 atm, 3 atm, and 5 atm using the same experimental apparatus as previously described. As in previous studies, the H_2O:EtOH molar feed ratio was maintained at 8.4:1 and the GHSV was maintained at approximately 265,000 mL_{Feed} h^{-1} g_{cat}^{-1}. The objective of this study was to determine the effect of total pressure on the activity and

product distribution for the steam reforming of ethanol over the Ni/Mg1Al2 catalyst after the catalyst performance had stabilized. Therefore, the water-ethanol feed mixture was delivered to the reactor for approximately 20 h at atmospheric pressure to stabilize performance, activate the direct ethanol steam reforming reaction pathway, and provide a baseline for comparison. The total pressure was elevated stepwise from atmospheric pressure to 2 atm, 2 atm to 3 atm, and so on. The rise in pressure occurred almost instantaneously. The product gas composition was monitored at the each pressure until performance stabilized, which occurred in less than 8 h for each change in pressure. After the experiment was completed, the pressure was reduced to atmospheric pressure to verify the effect of pressure on catalyst stability.

6.3.1 Effect of pressure at 823 K

At atmospheric pressure, ethanol conversion declined with time on stream as previously observed and discussed in section 6.2.1. Increasing the total pressure stepwise from atmospheric pressure to 2 atm resulted in increased ethanol conversion as shown in Figure 6.7a. This trend continued for subsequent increases in total pressure. Considering the thermodynamics of the ethanol steam reforming system, ethanol conversion is predicted to be complete and is essentially independent of pressure and temperature. Therefore, any effect of pressure on ethanol conversion was unexpected from a thermodynamic standpoint. However, ethanol conversion is incomplete because of insufficient catalyst loading indicating that ethanol conversion is a kinetically controlled process. The effect of increasing pressure on conversion is indicative of a kinetic system in which the rate of reaction is limited by the adsorption of reactant species. Increasing total pressure increases the rate of reactant adsorption on the catalyst surface resulting in increased conversion. Reducing the pressure from 5 atm to atmospheric pressure resulted in a decrease in ethanol conversion to similar levels as previously observed, showing no significant signs of enhanced rates of deactivation or regeneration.
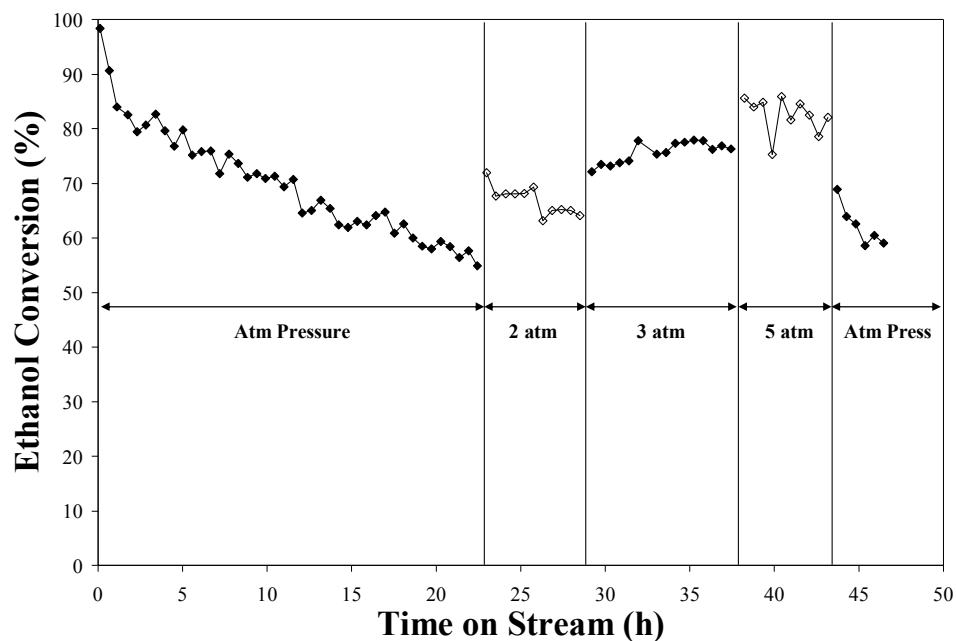
Figure 6.7a: Effect of pressure on ethanol conversion at 823 K over Ni/Mg1Al2. H_2O:EtOH = 8.4:1 and GHSV = 273903 mL_{Feed} h^{-1} g_{cat}^{-1}.

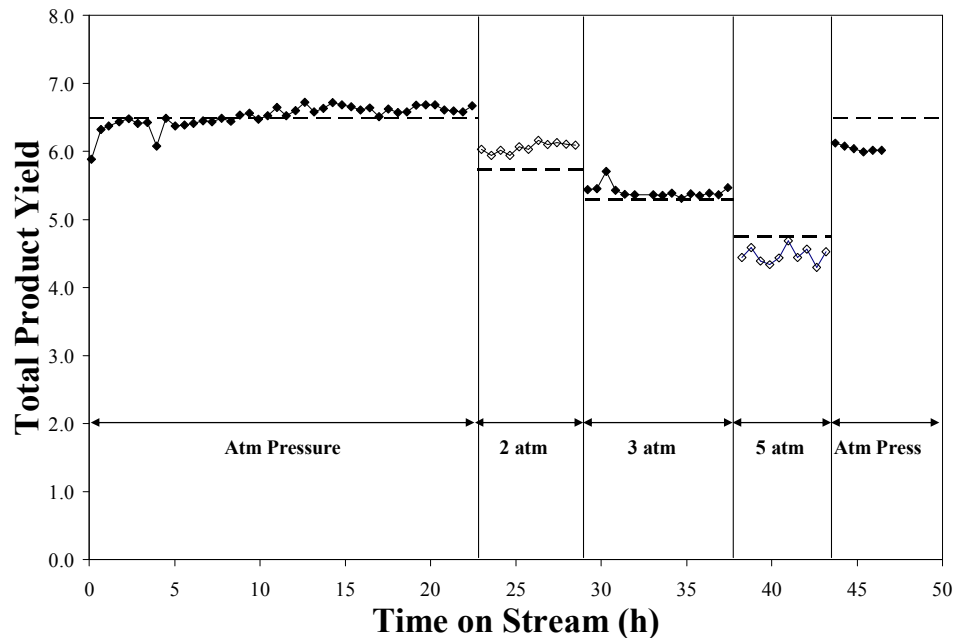**Figure 6.7b:** Effect of pressure on total product yield at 823 K over Ni/Mg1Al2. H_2O:EtOH = 8.4:1 and GHSV = 273903 mL_{Feed} h^{-1} g_{cat}^{-1}. Dashed lines represent equilibrium expectations.

The effect of total pressure on the total molar product yield is given in Figure 6.7b. The total molar yield decreased with increasing pressure even though ethanol conversion increased. This suggests that several reaction pathways for the conversion of ethanol to products are present and that the reaction pathways are thermodynamically limited favoring lower product molar yield pathways with increasing pressure.

The effect of total pressure on H_2, CO_2, CO, and CH_4 product yields at 823 K are shown in Figure 6.7c-f. The most important observation, as was observed for the total product yield (Figure 6.7b), is that the product yield for each species closely matches equilibrium expectations, usually within ~20%. Increasing the total pressure resulted in reduced yields for the steam reforming products, H_2, CO, and CO_2, while the yield of the decomposition product, CH_4, increased. The fact that the product distribution is equilibrium limited and ethanol conversion is kinetically limited indicates that the adsorption of ethanol or a surface species produced upon the interaction of ethanol and the active site is the rate limiting step at this temperature.

At 823 K, as expected, the ethanol steam reforming reaction system was highly thermodynamically limited, because as discussed in section 6.2.1, the presence of a direct ethanol steam reforming reaction pathway only becomes active at reaction temperatures below 823 K (823 K seems to be the transition temperature). Therefore, as predicted from thermodynamics, increasing the total pressure would favor the formation of species leading to lowest total molar number, i.e., CH_4.
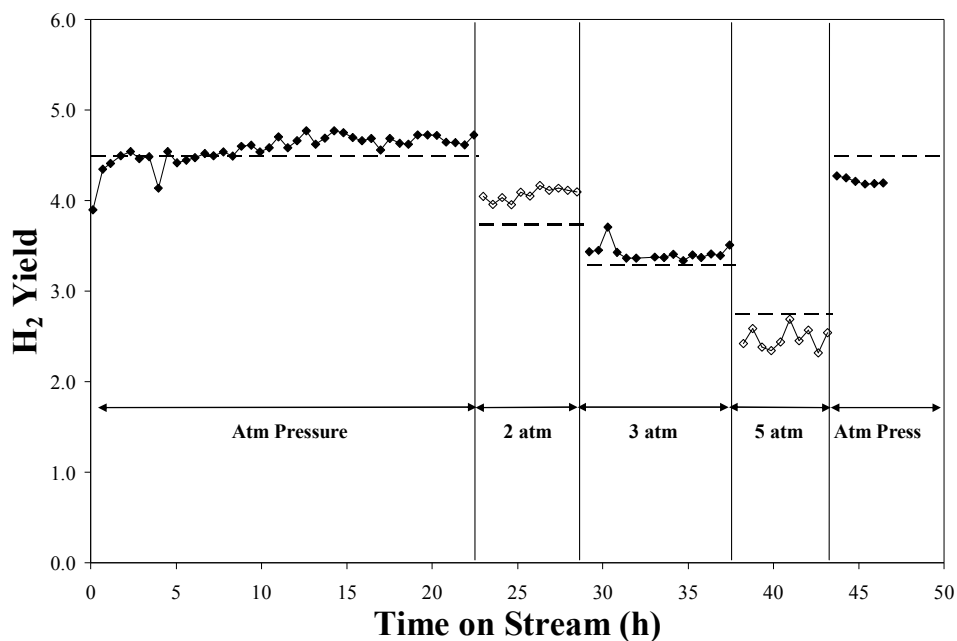
Figure 6.7c: Effect of pressure on H_2 yield at 823 K over Ni/Mg1Al2. H_2O:EtOH = 8.4:1 and GHSV = 273903 mL_{Feed} h^{-1} g_{cat}^{-1}. Dashed lines represent equilibrium expectations.

Figure 6.7d: Effect of pressure on CO_2 yield at 823 K over Ni/Mg1Al2. H_2O:EtOH = 8.4:1 and GHSV = 273903 mL_{Feed} h^{-1} g_{cat}^{-1}. Dashed lines represent equilibrium expectations.
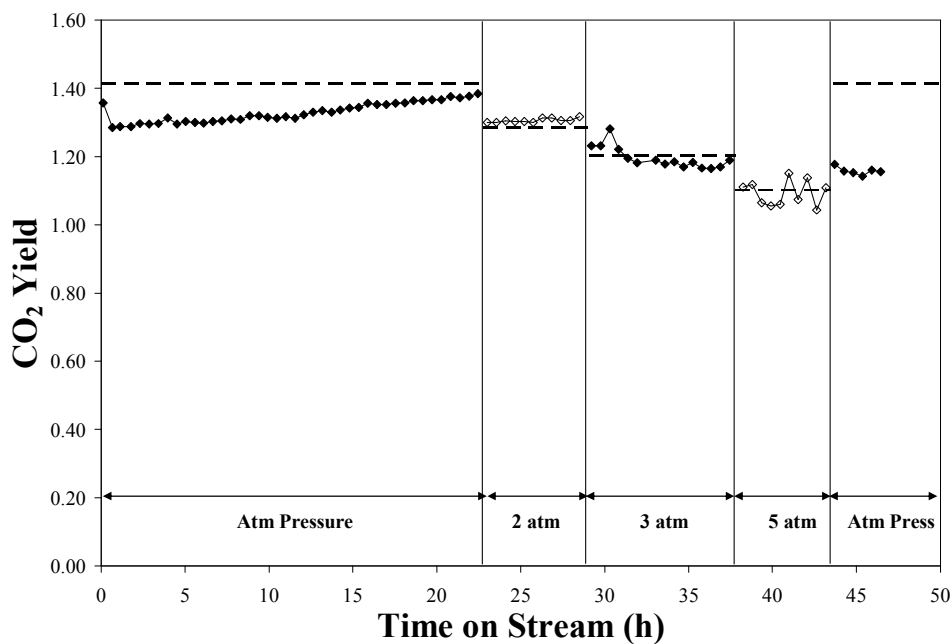
164

Figure 6.7e: Effect of pressure on CO yield at 823 K over Ni/Mg1Al2. H_2O:EtOH = 8.4:1 and GHSV = 273903 mL_{Feed} h^{-1} g_{cat}^{-1}. Dashed lines represent equilibrium expectations.

Figure 6.7f: Effect of pressure on CH_4 yield at 823 K over Ni/Mg1Al2. H_2O:EtOH = 8.4:1 and GHSV = 273903 mL_{Feed} h^{-1} g_{cat}^{-1}. Dashed lines represent equilibrium expectations.
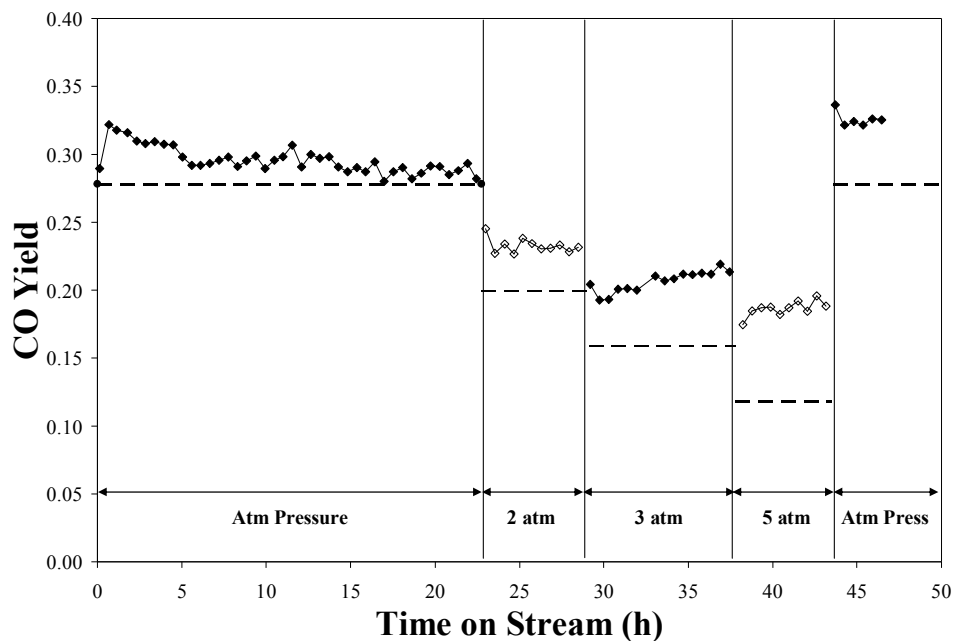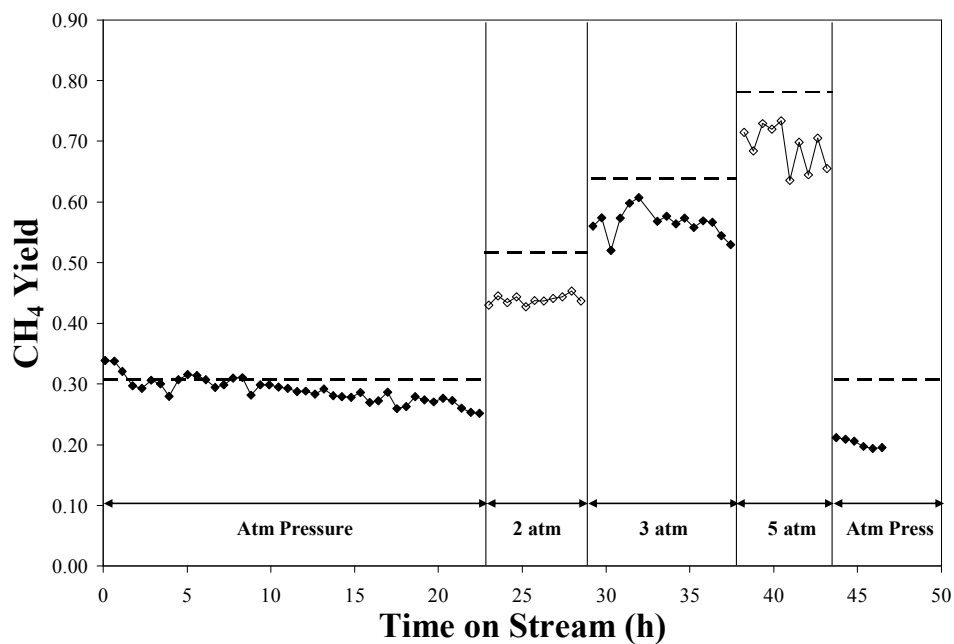
165

6.3.2 Effect of pressure at 673 K

The effect of total pressure on ethanol conversion at 673 K is given in Figure 6.8a. As observed in the time on stream study, Ni/Mg1Al2 experienced substantial deactivation at 673 K and atmospheric pressure, however, a stable activity was achieved. Increasing the pressure from atmospheric to 5 atm had no effect on ethanol conversion indicating that the steam reforming of ethanol over the stabilized-Ni/Mg1Al2 catalyst was not limited by the rate of ethanol adsorption as was the case at 823 K. Also, since an increase in pressure did not negatively affect the rate of ethanol conversion, it can be stated that the rate of reaction is not controlled by a product desorption process. Reducing the pressure from 5 atm to atmospheric pressure resulted in a small decrease in ethanol conversion. This small drop in ethanol conversion is not considered significant.

The effect of total pressure on the total product yield is given in Figure 6.8b. Initially at atmospheric pressure, the total product yield closely matches the thermodynamic equilibrium expectations, but as time on stream progresses, the product yield increases and stabilizes. As observed in section 6.2.1, the rise in product yield coincides with the decline in ethanol conversion. Unlike results obtained at 823 K, which was a thermodynamically limited reaction system, where the product yield closely matched the thermodynamic expectations, at 673 K the total product yield is marginally reduced by increasing pressure. Most important is that at 673 K, the total product yield consistently exceeds equilibrium expectations in stark contrast to experiments performed at 823 K.
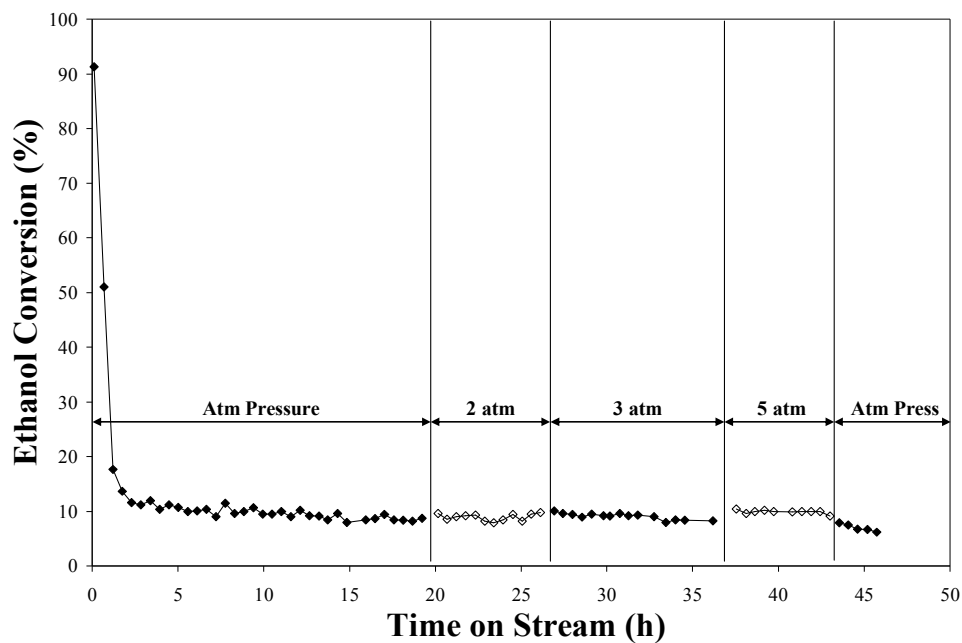
Figure 6.8a: Effect of pressure on ethanol conversion at 673 K over Ni/Mg1Al2. H_2O:EtOH = 8.4:1 and GHSV = 270783 mL_{Feed} h^{-1} g_{cat}^{-1}.

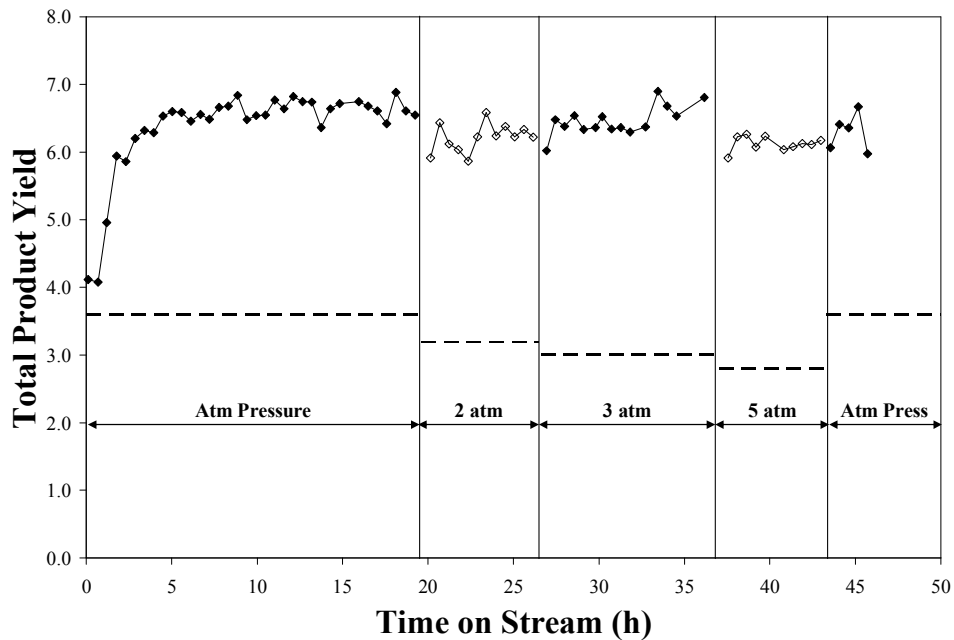**Figure 6.8b:** Effect of pressure on total product yield at 673 K over Ni/Mg1Al2. H_2O:EtOH = 8.4:1 and GHSV = 270,783 mL_{Feed} h^{-1} g_{cat}^{-1}. Dashed lines represent equilibrium expectations.
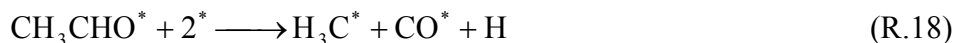
167

The fact that the initial product yield closely matched equilibrium expectations indicates that the ethanol steam reforming reaction network was modified during the deactivation process. The ethanol steam reforming reaction network was modified such that reactions leading to lower total product yields, which would be thermodynamically favorable at higher pressures, were no longer catalyzed by the modified catalyst.

Figure 6.8 (c-f) presents the effect of pressure on the distribution of products, H_2, CO_2, CO, and CH_4. CH_4 yield increased by approximately 0.2 moles per mole of ethanol converted over the 5 times increase in pressure, which closely matched the increase predicted thermodynamically for the same increase in pressure. However, the deviation between experimental and equilibrium expected CH_4 yields remained the same. The single most important observation is that the CH_4 yield remained substantially below the equilibrium expectation. The yield of the steam reforming products, H_2, CO, and CO_2, were not affected or only slightly affected by increasing the total pressure from atmospheric pressure to 5 atm. H_2 and CO yields decreased with increasing pressure while CO_2 rose slightly. The decline in the H_2 and CO yields does not match their respective thermodynamically predicted decrease. The relative independence of this catalytic system to increasing pressure suggests that although the system is thermodynamically limited, the catalyst is not active for, or only slight active for reactions that lead to the formation of CH_4. Instead, stabilized-Ni/Mg1Al2 seems to exhibit very little activity for CO methanation (R.5).

$$CO + 3H_2 \longrightarrow CH_4 + H_2O \tag{R.5}$$

Assuming that the CO methanation reaction is not active on Ni/Mg1Al2, the theoretical maximum yield for CH_4 would be 1.0, produced via ethanol (R.9) or acetaldehyde (R.8) decomposition. Considering that at 673 K, the CH_4 yield reaches a maximum of 0.4 moles per mole of ethanol converted at 5 atm, the Ni/Mg1Al2 catalyst shows very good activity for ensuring that CH_4 does not desorb from the surface. Instead of desorbing from the surface as CH_4, the CH_3^* group, produced by the decomposition of the surface adsorbed

ethoxy group (R.18), dehydrogenates to H_xC^* via (R.28-R.30). These species have been shown to be highly reactive in the presence of surface oxygen (O^*) produced from water via (R.31) [Xu and Froment (1989)], which has been extensively studied for the steam reforming or partial oxidation of methane to produce H^* and CO^* via (R.32) [Xu and Froment (1989); Deutschmann and Schmidt (1998); York et al. (2003)].

$$CH_3CHO^* + 2^* \longrightarrow H_3C^* + CO^* + H \qquad \text{(R.18)}$$

$$H_3C^* + {}^* \longrightarrow H_2C^* + H^* \qquad \text{(R.28)}$$

$$H_2C^* + {}^* \longrightarrow HC^* + H^* \qquad \text{(R.29)}$$

$$HC^* + {}^* \longrightarrow C^* + H^* \qquad \text{(R.30)}$$

$$H_2O + {}^* \longrightarrow H_2 + O^* \qquad \text{(R.31)}$$

$$H_xC^* + (x+1)O^* \longrightarrow xH^* + CO^* \qquad \text{(R.32)}$$

As indicated by the work of Wei and Iglesia (2004) and Burghgraef et al. (1995), the rates of the dehydrogenation steps (R.28-30) are relatively fast, which leads to very low CH_x surface coverage and therefore, essentially all CH_3^* produced during the decomposition of ethanol or acetaldehyde proceeds directly to C^*. A fine balance exists between the oxidation of H_xC^* and C^* via (R.32) and the inclusion of C^* into a carbonaceous deposit.

The fact that CH_4 yield does not respond to increasing pressure suggests that the hydrogenation of CH_3^* and subsequent desorption of CH_4 (R.27) from the catalyst surface is a relatively slow process compared to the dehydrogenation reactions (R.28-30) especially considering the high concentration of H_2. The small rise in CH_4 yield with increasing pressure from atmospheric pressure to 5 atm is proposed to be related to the increase in the rate of the hydrogenation reaction (R.27, page 139) due to the increase in the H_2 partial pressure.
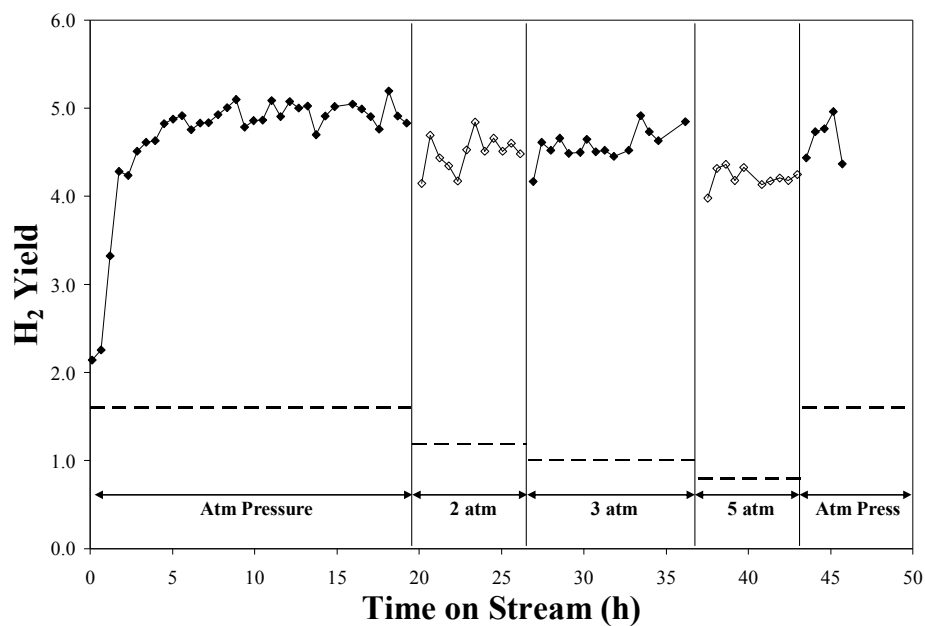
Figure 6.8c: Effect of pressure on H_2 yield at 673 K over Ni/Mg1Al2. H_2O:EtOH = 8.4:1 and GHSV = 270783 mL_{Feed} h^{-1} g_{cat}^{-1}. Dashed lines represent equilibrium expectations.

Figure 6.8d: Effect of pressure on CO_2 yield at 673 K over Ni/Mg1Al2. H_2O:EtOH = 8.4:1 and GHSV = 270783 mL_{Feed} h^{-1} g_{cat}^{-1}. Dashed lines represent equilibrium expectations.

170

Figure 6.8e: Effect of pressure on CO yield at 673 K over Ni/Mg1Al2. H_2O:EtOH = 8.4:1 and GHSV = 270783 mL_{Feed} h^{-1} g_{cat}^{-1}. Dashed lines represent equilibrium expectations.

Figure 6.8f: Effect of pressure on CH_4 yield at 673 K over Ni/Mg1Al2. H_2O:EtOH = 8.4:1 and GHSV = 270783 mL_{Feed} h^{-1} g_{cat}^{-1}. Dashed lines represent equilibrium expectations.

171

6.3.3 Comments on the effect of pressure

The effect of pressure on the product distribution for experiments performed at 673 K significantly deviates from equilibrium expectations. As has been discussed in previous sections, the key to exceeding equilibrium expectations for the steam reforming products, H_2, CO, and CO_2, especially at low temperatures, is improving the catalyst's ability to keep the CH_3^* intermediate surface species produced in (R.18) on the surface and reduce activity for hydrogenation and desorption of CH_4. In fact, this is most likely achieved by the rapid dehydrogenation of the surface methyl group to H_xC^* or C^* groups as suggested by Wei and Iglesia (2004) and Burghgraef et al. (1995). These species can then be steam reformed via reactions with O* (R.32) to produce H_2, CO, and CO_2 in the absence of CH_4. Since this ethanol steam reforming reaction pathway over stabilized-Ni/Mg1Al2 has very little selectivity for the formation of CH_4, the thermodynamic limitations of low H_2 yield at low temperatures can be circumvented.
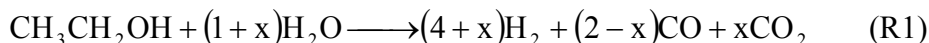
6.4 Summary

Temperature programmed reaction experiments revealed much about the reaction pathways forming the ethanol steam reforming reaction network. At low reaction temperatures, below 600 K, ethanol dehydrogenation (R.7) is the dominant reaction producing almost exclusively acetaldehyde and hydrogen. Between 600 and 675 K, the ethanol/acetaldehyde decomposition reactions (R.9 and R.8) activate, yielding a product gas composed primarily of H_2, CO, and CH_4. The support-catalyzed dehydration reactions (R11 and R.23) producing ethylene and diethyl ether contributed to deactivation of the supported-nickel catalyst. Further increases in temperature led to increased reforming of ethanol as exhibited by an increase in water utilization, and H_2 and CO_2 yields resulting in the decline and disappearance of the hydrocarbon species (CH_4, CH_3CHO, ethylene, and diethyl ether). At temperatures above 800 K, the product gas is comprised almost entirely of the steam reforming products, H_2, CO, and CO_2 in near equilibrium proportions even though ethanol conversion in not necessarily complete. In this temperature range, the water-gas shift reaction (R.3) significantly contributes to the product gas composition.

172

Temperature programmed acetaldehyde steam reforming reaction experiments revealed that ethanol and acetaldehyde are kinetically equivalent reactant species having very similar activities on Ni/Mg1Al2. In addition, the product distribution was essentially independent of the starting reactant suggesting that the ethanol steam reforming proceeds through an acetaldehyde intermediate and that ethanol and acetaldehyde share a similar rate limiting step. CH_4 steam reforming experiments revealed that gas phase CH_4 steam reforming functions differently than surface methyl groups, CH_3^*, produced via ethanol/acetaldehyde decomposition. The major difference being that CH_4 adsorption and the abstraction of the first hydrogen, which would yield a surface methyl group, is the rate limiting step in the CH_4 steam reforming reaction network. Although, the kinetic rates are different, the reaction mechanism, excluding the rate-limiting step, was determined to be the same.

During the steam reforming of ethanol, the supported nickel catalyst was modified such that upon reducing the reaction temperature below 725 K, the dominant reaction pathway changed from ethanol/acetaldehyde dehydrogenation/decomposition to steam reforming producing H_2 in excess of equilibrium expectations at the expense of reduced CH_4 yields. The most probable explanation for this phenomenon is that the carbon deposits or the process of forming these deposits modified the surface of the catalyst which resulted in a substantial change in the nickel crystallites ability to desorb CH_4.

Time on stream experiments investigating the effect of reaction temperature and GHSV on the activity and product selectivity of Ni/Mg1Al2 for the ethanol steam reforming reaction revealed that catalyst stability improved with reaction temperature, especially for reaction temperatures of 923 K and high catalyst loadings. At 923 K, Ni/Mg1Al2 exhibited very good stability maintaining 100% ethanol conversion and the product yields for over 20 hr time on stream. Long term stability experiments have indicated that Ni/Mg1Al2 can maintain complete ethanol conversion and product yields for over 110 h at 923 K.

For reaction temperatures of 823 K and above, the reaction pathway closely matched thermodynamic expectations throughout the entire time on stream. GHSV reaction experiments revealed that at 823 K, H_2 and CO_2 were primary reaction products or at least that the reaction pathways leading to H_2 and CO_2 were not rate-limiting steps. Below 823 K, Ni/Mg1Al2 experienced substantial deactivation resulting in reduced ethanol conversion but interestingly, the H_2 and CO_2 yields increased exceeding equilibrium expectations with time on stream while CH_4 yield decreased far below equilibrium expectations suggesting a direct ethanol steam reforming reaction pathway (R.1).

$$CH_3CH_2OH + (1+x)H_2O \longrightarrow (4+x)H_2 + (2-x)CO + xCO_2 \qquad (R1)$$

As discussed in section 6.1.3, methane steam reforming is kinetically more difficult than ethanol steam reforming, especially at low reaction temperatures. Therefore, in-situ production of methane is highly undesirable. Identification of a reaction pathway capable of producing steam reforming products, H_2, CO, and CO_2, without CH_4, a decomposition product, would be desirable. Over stabilized-Ni/Mg1Al2, direct ethanol steam reforming was activated by a reduction in the catalysts activity for the desorption of CH_4 from the surface. The production of steam reforming products at relatively low temperatures by exceeding thermodynamic expectations would ultimately result in substantial energy savings. For example, H_2 yield at 648 K is essentially the same as that predicted at 823 K by thermodynamics, representing a 180 K decrease in the operating temperature of the reactor.

The effect of pressure on the direct ethanol steam reforming reaction pathway over stabilized-Ni/Mg1Al2 was investigated at 673 and 823 K. At 823 K, increasing the total pressure resulted in a product distribution that closely matched the thermodynamic expectations. However, at 673 K, the product distribution deviated from thermodynamic expectations giving substantially greater yields for the steam reforming products, H_2, CO, and CO_2, while CH_4 yield was consistently less than equilibrium expectations.

174

Chapter 7

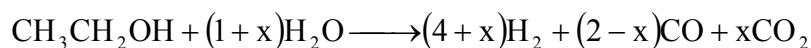# Conclusions and Recommendations

7.1 Conclusions

Mg-Al mixed oxide supported nickel catalysts gave superior activity, steam reforming product selectivity (H_2 and CO_x) then the pure oxide supported nickel catalyst at both temperatures investigated. Activity, product selectivity, and catalyst stability were dependent upon the Al and Mg content of the support. At 923 K, the Mg-Al mixed oxide supported nickel catalysts were the best performing catalysts exhibiting the highest steam reforming product yield (H_2 and CO_x) and were highly stable, showing no signs of deactivation after 20 h operation. The improved performance of the Mg-Al mixed oxide supported catalysts was related to the incorporation of the pure oxides, MgO and Al_2O_3, into $MgAl_2O_4$. The formation of $MgAl_2O_4$ reduced nickel incorporation with the support material since $MgAl_2O_4$ does not react with Ni; therefore, nickel was retained in its active form. In addition, incorporation of Mg and Al in to $MgAl_2O_4$, a slight basic material, modified the acid-base properties resulting in a catalyst that exhibited moderate acidic and basic site strength and density compared to the pure oxide supported catalysts. Moderation of the acid-base properties improved the activity, selectivity, and stability of the catalysts by reducing activity for by-product reactions producing ethylene and acetaldehyde.

The ethanol steam reforming reaction network was investigated using temperature programmed reaction techniques. The reaction network was found to be highly dependent upon the temperature and H_2O:EtOH molar feed ratio. At low reaction temperatures, below 600 K, ethanol dehydrogenation is the dominant reaction producing almost exclusively acetaldehyde and hydrogen. Between 600 and 675 K, the ethanol/acetaldehyde decomposition reactions activate yielding a product gas composed primarily of H_2, CO, and CH_4. At temperatures above 800 K, the product gas is comprised almost entirely of the steam

reforming products, H_2, CO, and CO_2 in near-equilibrium proportions even though ethanol conversion in not necessarily complete.

Investigating the effect of starting reactant, ethanol or acetaldehyde, it was verified that ethanol steam reforming over supported nickel catalyst proceeds through an acetaldehyde intermediate. The role of the ethanol/acetaldehyde decomposition product CH_3^* was evaluated for similarity with CH_4 steam reforming. It was found that the decomposition product differed from CH_4 in that the adsorption and the abstraction of the first hydrogen, which would yield a surface methyl group, is the rate limiting step in the CH_4 steam reforming reaction network. Although, the kinetic rates are different, the reaction mechanism, excluding the rate-limiting step, was determined to be the same.

At 923 K, the Mg-Al mixed oxide supported nickel catalysts gave excellent ethanol steam reforming performance being highly active, selective, and most importantly, stable. Mg-Al mixed oxide supported catalysts were able to maintain 100% ethanol conversion for over 20 h without change in the product yields. At lower reaction temperatures, below 823 K, Mg-Al mixed oxide supported nickel catalysts experienced substantial deactivation resulting in reduced ethanol conversion but interestingly, the H_2 and CO_2 yields increased exceeding equilibrium expectations with time on stream while CH_4 yield decreased far below equilibrium expectations suggesting a direct ethanol steam reforming reaction pathway.

$$CH_3CH_2OH + (1+x)H_2O \longrightarrow (4+x)H_2 + (2-x)CO + xCO_2$$

Over stabilized-Ni/Mg1Al2, direct ethanol steam reforming was activated by a reduction in the catalysts activity for the desorption of CH_4 from the surface. The production of steam reforming products at relatively low temperatures by exceeding thermodynamic expectations would ultimately result in substantial energy savings.

The effect of pressure on the direct ethanol steam reforming reaction pathway over stabilized-Ni/Mg1Al2 was investigated at 673 and 823 K. At 823 K, increasing the total pressure resulted in a product distribution that closely matched the thermodynamic expectations. However, at 673 K, the product distribution deviated from thermodynamic expectations giving substantially greater yields for the steam reforming products, H_2, CO, and CO_2, while CH_4 yield was consistently less than equilibrium expectations.

7.2 Scientific Contribution

The major contributions that this thesis made to the scientific literature were:

1. Mg-Al mixed oxide supported nickel catalysts are superior catalyst for the steam reforming of ethanol compared to the pure oxide supported nickel catalysts.
   - At high temperatures, Mg-Al mixed oxide supported nickel catalysts were highly active, selective, and stable for the steam reforming of ethanol.
   - Improved performance of the Mg-Al mixed oxide supported nickel catalysts was related to:
     - Moderate acid-base properties of the Mg-Al mixed oxides.
     - Inclusion of pure oxides into $MgAl_2O_4$ spinel phase.

2. Identification of a low temperature, direct ethanol steam reforming reaction pathway
   - The dominant mechanism was found to change with the deactivation of the catalyst.
   - The direct ethanol steam reforming reaction pathway favored the formation of H_2 and CO_2 yields, at low temperatures (623 to 823 K), which vastly exceed equilibrium expectations at the expense of CH_4 yield.

3. Potential for low temperature, moderate pressure H_2 production from ethanol.
   - Increasing pressure had very little effect on product distribution of the direct ethanol steam reforming reaction.

7.3 Recommendations

The effect of catalyst deactivation, although significantly affecting catalyst activity, modified the dominant reaction pathway favoring a direct ethanol steam reforming reaction mechanism. This study was able to show the benefits of a direct ethanol steam reforming reaction pathway by highlighting the significant reduction in temperature needed to obtain desirable H_2 yields and the reduced effect of increasing pressure on H_2 yield. However, the mechanism for the transition in reaction pathway was not sufficiently elucidated. Further understanding of the transition in mechanism and identification of the characteristics of the catalytic site responsible for this reaction mechanism could lead to alternative catalyst formulations and preparation techniques capable of producing a more active catalyst while maintaining the steam reforming product selectivity.

1. Employ state-of-the-art surface reaction characterization techniques to investigate the transition in the reaction mechanism to aid in the identification of the characteristics of the catalytic site responsible for the direct ethanol steam reforming reaction pathway. Suggested techniques:
   - Kinetic-isotope exchange
   - DRIFTS-MS
2. Investigate the use of carbon nanotubes (filamentous carbon structures) as a nickel catalyst support material for the steam reforming of ethanol.
   - The transition in mechanism to the direct ethanol steam reforming reaction pathways coincided with catalyst deactivation and the formation of carbonaceous deposits on the catalyst surface.
3. Evaluate the effect of ramping direction in temperature programmed reaction experiments.
   - In this study temperature programmed reactions were performed by ramping the temperature up then down. Performing the temperature ramp in the opposite direction might provide much more insight into the transition in the ethanol steam reforming reaction mechanism.

Chapter 8 References

Abbattista. F., Delmastro, S., Gozzelino, G., Mazza, D., Vallino, M., Busca, G., Lorenzelli, V., and G. Ramis (1989). Surface characterization of amorphous alumina and its crystallization products. *J. Catal.* **117** 42-51.

Aberuagba, F., Kumar, M., Gupta, J.K., Muralidhar, G., and L.D. Sharma (2002). Preparation and characterization of MgO/Al_2O_3 mixed oxides support for hydrotreating catalysts. *React. Kinet. Catal. Lett.* **75** 2 245-250.

Agrell, J., Lindström, B., Pettersson, L. J., and Järås, S. G., (2002). Catalytic Hydrogen Generation From Methanol. In: *Catalysis*, **vol. 16** pp. 67-132. Cambridge, UK: The Royal Society of Chemistry.

Akande, A., Aboudheir, A., Idem, R., and A. Dalai (2006). Kinetic modeling of hydrogen production by the catalytic reforming of crude ethanol over a co-precipitated $Ni-Al_2O_3$ catalyst in a packed bed tubular reactor. *Int. J. Hydrogen Energy* **31** 1707-1715.

Arena, F., Horrell, B.A., Cocke, D.L., and A. Parmaliana (1991). Magnesia-supported nickel catalysts. I. Factors affecting the structure and morphological properties. *J. Catal.* **132** 58-67.

Aupretre, F., Descorme, C., Duprez, D., Casanave, D., and D. Uzio (2005). Ethanol steam reforming over $Mg_xNi_{1-x}Al_2O_3$ spinel oxide-supported Rh catalysts. *J. Catal.* **233** 464-477.

Auroux, A. and A. Gervasini (1990). Microcalorimetric study of the acidity and basicity of metal oxide surfaces. *J. Phys. Chem.* **94** 16 6371-6379.

Basile, F., Fornasari, G., Poluzzi, E., and A. Vaccari (1998). Catalytic partial oxidation and CO_2-reforming on Rh- and Ni-based catalysts obtained from hydrotalcite-type precursors. *Appl. Clay Sci.* **13** 329–345.

Basile, F., Fornasari, G., Gazzano, M., Kiennemann, A., and A. Vaccari (2003). Preparation and characterization of a stable Rh catalyst for the partial oxidation of methane. *J. Catal.* **217** 245–252.

Bartholomew, C.H. (2001). Mechanisms of catalyst deactivation. *Appl. Catal. A:Gen* **212** 17-60.

Batista, M. S., Santos, R. K. S., Assaf, E. M., Assaf, J. M., and Ticianelli, E. A., (2003). Characterization of the activity and stability of supported cobalt catalysts for the steam reforming of ethanol. *J.Power Sources* **124** 99-103.

Benito. M., Sanz, J.L., Isabel, R., Padilla, R., Arjona, R., and L. Daza (2005). Bio-ethanol steam reforming: Insights on the mechanism for hydrogen production. *J. Power Sources* **151** 11-17.

Breen, J. P., Burch, R., and Coleman, H. M., (2002). Metal-catalysed steam reforming of ethanol in the production of hydrogen for fuel cell applications. *Applied Catalysis B: Environmental*, **39**, 65-74.

Burghgraef, H., Jansen, A.P.J., and R.A. van Santen (1995). Methane activation and dehydrogenation on nickel and cobalt: a computational study. *Surf. Sci.* **324** 345-356.

Cai, X., Ren, Z., Hu, T., and Y. Xie (2001). Structures of surface- and bulk-dispersion phases of NiO/Al_2O_3. *Surf. Interface Anal.* **32** 293–295.

Cardona Alzate, C.A. and O.J. Sanchez Toro (2006). Energy consumption analysis of integrated flowsheets for production of fuel ethanol from lignocellulosic biomass. *Energy* **31** 2447–2459.

Cavallaro, S., (2000). Ethanol steam reforming on Rh/Al_2O_3 catalysts. *Energy Fuels*, **14**, 1195-1199.

Cavallaro, S., Mondello, N., and Freni, S., (2001). Hydrogen produced from ethanol for internal reforming molten carbonate fuel cell. *J.Power Sources*, **102**, 198-204.

Cavallaro, S., Chiodo, V., Vita, A., and Freni, S., (2003a). Hydrogen production by auto-thermal reforming of ethanol on Rh/Al_2O_3 catalyst. *J.Power Sources*, **123**, 10-16.

Cavallaro, S., Chiodo, V., Freni, S., Mondello, N., and Frusteri, F., (2003b). Performance of Rh/Al_2O_3 catalyst in the steam reforming of ethanol: H_2 production for MCFC. *Applied Catalysis A: General*, **249**, 119-128.

Chang, F.-W., Kuo, M.-S., Tsay, M.-T., and M.-C. Hsieh (2004). Effect of calcination temperature on catalyst reducibility and hydrogenation reactivity in rice husk ash-alumina supported nickel systems. *J. Chem. Technol. Biotechnol.* **79** 691-699.

Chladek, P, Coleman, L.J.I., Croiset, E., and R.R. Hudgins (2007). Gas chromatography method for the characterization of ethanol steam reforming products. *J. Chrom. Sci.* **45** 153-157.

Coleman, L.J.I., Epling, W., Hudgins, R.R., Silveston, P.L., and E. Croiset (2007). Ethanol steam reforming over Mg-Al mixed-oxide catalysts. In Proceedings for Hydrogen and Fuel Cells 2007 International Conference and Trade Show held in Vancouver, Canada April 29th-May 2nd, 2007. 279-289. Vancouver: Westpoint Conference Services Ltd. 2007.

Coleman, L.J.I., Croiset, E., Epling, W., Fowler, M, and R.R. Hudgins (To be submitted to Fuels). Production of syngas via catalytic partial oxidation of methane over foam nickel.

Comas, J., Dieuzeide, M.L., Baronetti, G., Laborde, M., and N. Amadeo (2006). Methane steam reforming and ethanol steam reforming using a Ni(II)-Al(III) catalyst prepared from lamellar double hydroxides. *Chem. Eng. J.* 188 11-15.

Constantino, V.R.L. and T.J. Pinnavaia (1995). Basic properties of Mg-Al layered double hydroxide intercalated by carbonate, hydroxide, chloride, and sulfate anions. *Inorg. Chem.* **34** 883-892.

Demicheli., M.C., Duprez, D., Barbier, J., Ferretti, O.A., and E.N. Ponzi (1994). Deactivation of steam-reforming model catalysts by coke formation. II Promotion with potassium and effect of water. *J. Catal.* **145** 437-449.

Deluga, G. A., Salge, J. R., Schmidt, L. D., and Verykios, X. E., (2004). Renewable Hydrogen from Ethanol by Autothermal Reforming. *Science*, **303**, 993-997.

Deutschmann, O. and L.D. Schmidt (1998). Modeling the partial oxidation of methane in a short-contact-time reactor. *AIChE J.* **44** 11 2465-2477.

Diagne, C., Idriss, H., and Kiennemann, A., (2002). Hydrogen production by ethanol reforming over Rh/CeO$_2$–ZrO$_2$ catalysts. *Catalysis Communications*, **3**, 565-571.

Djaidja, A., Libs, S., Kiennemann, A., and A. Barama (2006). Characterization and activity in dry reforming of methane on NiMg/Al and Ni/MgO catalysts. *Catal. Today* **113** 194-200.

Di Cosimo J.I., Diez, V.K., Xu, M., Iglesia, E., and C.R. Apesteguia (1998). Structure and surface and catalytic properties of Mg-Al basic oxides. *J. Catal.* **178** 499-510.

Di Cosimo J.I., Apesteguia, C.R., Gines, M.J.L., and E. Iglesia (2000). Structural requirements and reaction pathways in condensation reaction of alcohols on Mg$_y$AlO$_x$ catalysts. J. *Catal.* **190** 261-275.

Diez, V.K., Apesteguia, C.R., and J.I. Di Cosimo (2003). Effect of the chemical composition on the catalytic performance of Mg_yAlO_x catalysts for alcohol elimination reactions. *J. Catal.* **215** 220-233.

Dybkjaer, I., (1995). Tubular reforming and autothermal reforming of natural gas - an overview of available processes. *Fuel Processing Technology*, **42**, 85-107.

Erdohelyi, A., Rasko, J., Kecskes, T., Toth, M., Domok, M., and K. Baan (2006). Hydrogen formation in ethanol reforming on supported noble metal catalysts. *Catal. Today* **116** 367-376.

Fatsikostas, A. N., Kondarides, D., and Verykios, X. E., (2002). Production of hydrogen for fuel cells by reformation of biomass-derived ethanol. *Catal.Today*, **75**, 145-155.

Fatsikostas, A.N. and X. Verykios (2004). Reaction Network of steam reforming of ethanol over Ni-based catalysts. *J. Catal*. **225** 439-452.

Fierro, V., Klouz, V., Akdim, O., and Mirodatos, C., (2002). Oxidative reforming of biomass derived ethanol for hydrogen production in fuel cell applications. *Catal.Today*, **75**, 141-144.

Fierro, V., Akdim, O., Provendier, H., and C. Mirodatos (2005). Ethanol oxidative steam reforming over Ni-based catalysts. *J. Power Sources* **145** 659-666.

Fishel, C.T., and R.J. Davis (1994). Characterization of Mg-Al mixed oxides by temperature-programmed reaction of 2-propanol. *Langmuir* **10** 159-165.

Fishtik, I., Alexander, A., Datta, R., and Geana, D., (2000). A thermodynamic analysis of hydrogen production by steam reforming of ethanol via response reactions. *Int.J.Hydrogen Energy*, **25**, 31-45.

Fogler, H.S. (1999). Elements of Chemical Reaction Engineering, 3rd Ed., Prentice Hall, Toronto, Upper Saddle River, NJ.

Forzatti, P. and L. Lietti (1999). Catalyst deactivation. *Catal. Today* **52** 165-181.

Freni, S., (2001). Rh based catalysts for indirect internal reforming ethanol applications in molten carbonate fuel cells. *J.Power Sources*, **94**, 14-19.

Freni, S., Cavallaro, S., Mondello, N., Spadaro, L., and Frusteri, F., (2002). Steam reforming of ethanol on Ni/MgO catalysts: H_2 production for MCFC. *J.Power Sources*, **108**, 53-57.

Freni, S., Cavallaro, S., Mondello, N., Spadaro, L., and Frusteri, F., (2003). Production of hydrogen for MC fuel cell by steam reforming of ethanol over MgO supported Ni and Co catalysts. *Catalysis Communications*, **4**, 259-268.

Froment G. F. and K.B. Bischoff (1980). Chemical Reactor Analysis and Design, John Wiley and Sons, Toronto.

Frusteri F., Freni, S., Chiodo, V., Spadaro, L., Di Blasi, O., Bonur, G., and S. Cavallaro (2004). Steam reforming of bio-ethanol on alkali-doped Ni/MgO catalysts: hydrogen production for MC fuel cell. *Appl. Cat A:Gen* **270** 1-7.

Garcia, E. Y. and Laborde, M. A., (1991). Hydrogen Production By The Steam Reforming of Ethanol: Thermodynamic Analysis. *Int.J.Hydrogen Energy*, **16**, 307-312.

Gates, S.M., Russell Jr., J.N., and J.T. Yates Jr. (1986). Bond activation sequence observed in the chemisorption and surface reaction of ethanol on Ni(111). *Surf. Sci.* **171** 111-134.

Geankopolis, C. (1993). Transport Processes and Unit Operations, 3rd ed., Prentice Hall, Englewood Cliffs, New Jersey.

Guo, J., Lou, H., Zhao, H., Chai, D., and X. Zheng (2004). Dry reforming of methane over nickel catalysts supported on magnesium aluminate spinels. *Appl. Catal. A: Gen.* **273** 75-82.

Haga, F., Nakajima, T., Yamashita, K., Mishima, S., and Suzuki, K., (1997a). *Nippon Kagaku Kaishi (J.Chem.Soc.Japan)*, **1**, 33.

Haga, F., Nakajima, T., Miya, H., and Mishima, S., (1997b). Catalytic properties of supported cobalt catalysts for steam reforming of ethanol. *Catal.Lett.*, **48**, 223-227.

Haryanto A., Fernando, S., Murali, N., and S. Adhikari (2005). Current status of hydrogen production techniques by steam reforming of ethanol: A review. *Energy and Fuels* **19** 2098-2106.

Hei, M.J., Chen, H.B., Yi., J., Lin, Y.J., Lin, Y.Z., Wei, G., and D.W. Liao (1998). CO_2-reforming of methane on transition metal surfaces. *Surf. Sci.* **417** 82-96.

Hill, J. (2007). Environmental costs and benefits of transportation biofuel production from food- and lignocellulose-based energy crops. A review. *Agronomy for sustainable development* **27** 1 1-12.

Hickmann, D.A. and L.D. Schmidt (1993). Steps in CH_4 oxidation on Pt and Rh surfaces: High-temperature reactor simulations. *AIChE J.* **39** 7 1164-1177.

Hou, K., and R. Hughes (2001). The kinetics of methane steam reforming over a Ni/α-Al$_2$O$_3$ catalyst. *Chem. Eng. J.* **82** 311-328.

Hou, Z. and T. Yashima (2004). Meso-porous Ni/Mg/Al catalysts for methane reforming with CO$_2$. *Appl. Catal. A: Gen.* **261** 205-209.

Hou, Z., Yokota, O., Tanaka, T., and T. Yashima (2003). Characterization of Ca-promoted Ni/γ-Al$_2$O$_3$ catalyst for CH$_4$ reforming with CO$_2$. *Appl. Catal. A: Gen.* **253** 381–387.

Hu, Y.H. and E. Ruckenstein (1998). Isotopic GCMS study of the mechanism of methane partial oxidation to synthesis gas. *J. Phys. Chem. A.* **102** 10568-10571.

Hudgins, R.R. (1968). A General Criterion for Absence of Diffusion Control in an Isothermal Catalyst Pellet, *Chem. Eng. Sci.* **23** 93-94.

Hudgins, R.R. (1972). General Criterion for Avoiding Film Diffusion Control in Heterogeneous Catalytic Reactions, *Can. J. Chem. Eng.* **50** 3 427.

Ioannides, T., (2001). Thermodynamic analysis of ethanol processors for fuel cell applications. *J.Power Sources*, **92**, 17-25.

Jacobs, G., Keogh, R.A., and B.H. Davis (2007). Steam reforming of ethanol over Pt/ceria with co-feed hydrogen. *J. Catal.* **245** 326-337.

Juan-Juan, J., Roman-Martınez, M.C., and M.J. Illan-Gomez (2004). Catalytic activity and characterization of Ni/Al$_2$O$_3$ and NiK/Al$_2$O$_3$ catalysts for CO$_2$ methane reforming. *Appl. Catal. A: Gen.* **264** 169–174.

Juan-Juan, J., Roman-Martinez, M.C., and M.J. Illan-Gomez (2006). Effect of potassium content in the activity of K-promoted Ni/Al$_2$O$_3$ catalysts for the dry reforming of methane. *Appl. Catal. A: Gen.* **301** 9-15.

Kim, P., Kim, Y., Kim, H., Song, I.K., and J, Yi (2004). Synthesis and characterization of mesoporous alumina with nickel incorporated for use in the partial oxidation of methane into synthesis gas. *Appl. Catal. A: Gen.* **272** 157–166.

Klouz, V., Fierro, V., Denton, P., Katz, H., Lisse, J. P., Bouvot-Mauduit, S., and Mirodatos, C., (2002). Ethanol reforming for hydrogen production in a hybrid electric vehicle: process optimisation. *J.Power Sources*, **105**, 26-34.

Lan, K. and J.W. Jorgenson (2001). A hybrid of exponential and gaussian functions as a simple model of asymmetric chromatographic peaks. *J. Chrom. A* **915** 1 1-13.

Lee, K.M. and W.Y. Lee (2002). Partial oxidation of methane to syngas over calcined Ni-Mg/Al layered double hydroxides. *Catal. Lett.* **83** 1-2 65-70.

Li, G., Hu, L., and J.M. Hill (2006). Comparison of reducibility and stability of alumina-supported Ni catalysts prepared by impregnation and co-precipitation. *Appl. Catal. A: Gen.* **301** 16–24.

Liguras, D. K., Kondarides, D. I., and Verykios, X. E., (2003). Production of hydrogen for fuel cells by steam reforming of ethanol over supported noble metal catalysts. *Applied Catalysis B: Environmental*, **43**, 345-354.

Lif, J., Skoglundh, M., and L. Löwendahl (2004). Stabilizing alumina supported nickel particles against sintering in ammonia/hydrogen atmosphere. *Appl. Catal. A: Gen.* **274** 61–69.

Llorca, J., Homs, N., Sales, J., and de la Piscina, P. R., (2002). Efficient Production of Hydrogen over Supported Cobalt Catalysts from Ethanol Steam Reforming. *J.Catal.*, **209**, 306-317.

Llorca, J., de la Piscina, P. R., Dalmon, J. A., Sales, J., and Homs, N., (2003). CO-free hydrogen from steam-reforming of bioethanol over ZnO-supported cobalt catalysts. *Applied Catalysis B: Environmental*, **43**, 355-369.

Mariño, F. J., Cerrella, E. G., Duhalde, S., Jobbagy, M., and Laborde, M. A., (1998). Hydrogen from steam reforming of ethanol. Characterization and performance of copper-nickel supported catalysts. *Int.J.Hydrogen Energy*, **23**, 1095-1101.

Mariño, F., Boveri, M., Baronetti, G., and Laborde, M., (2001). Hydrogen production from steam reforming of bioethanol using Cu/Ni/K/γ-Al$_2$O$_3$ catalysts. Effect of Ni. *Int.J.Hydrogen Energy*, **26**, 665-668.

Marino, F., Boveri, M., Baronetti, G., and M. Laborde (2004). Hydrogen production via catalytic gasification of ethanol. A mechanism proposal over copper-nickel catalysts. *Int. J. Hydrogen Energy* **29** 1 67-71.

McKenzie A.L., Fishel, C.T., and R.J. Davis (1992). Investigation of the surface structure and basic properties of calcined hydrotalcites. *J. Catal* **138** 547-561.

Mears, D.E. (1971). Tests for Transport Limitations in Experimental Catalytic Reactors, *Ind. Eng. Chem. Process Des. Develop.* **10** 4 541-547.

Mears, D.E. (1973). On the Relative Important of Intraparticle and Interphase Transport Effects in Gas-Solid Catalysis, *J. Catal*. **20** 283-287.

Ohi, T., Miyata. T., Li, D., Shishido, T., Kawabata, T., Sano, T., and K. Takehira (2006). Sustainability of Ni loaded Mg-Al mixed oxide catalyst in daily startup and shutdown operation of CH_4 steam reforming. *Appl. Catal. A: Gen* **308** 194-203.

Parmaliana A., Arena, F., Frusteri, F., and N. Giodano (1990). Temperature-programmed reduction study of NiO-MgO interactions in Magnesia-supported Ni catalysts and Ni-MgO physical mixtures. *J. Chem. Soc. Faraday Trans*. **86** 14 2663-2669.

Pechimuthu, N.A., Pant, K.K., Dhingra, S., and R. Bhalla (2006). Characterization and Activity of K, CeO_2, and Mn Promoted Ni/Al_2O_3 Catalysts for Carbon Dioxide Reforming of Methane. *Ind. Eng. Chem. Res*. **45** 7435-7443.

Perry, R.H. and D.W. Green (1997). Perry's Chemical Engineers' Handbook, 7th ed., McGraw-Hill, Toronto.

Prescott, H.A., Z.-J. Li, E. Kemnitz, A. Trunschke, J. Deutsch, H. Lieske, and A. Auroux (2005). Application of calcined Mg-Al hydrotalcites for Michael additions: an investigation of catalytic activity and acid-base properties. *J. Catal* **234** 119-130.

Prinetto, F., Ghiotti, G., Durand, R., and D. Tichit (2000). Investigation of acid-base properties of catalysts obtained from layered double hydroxides. *J. Phys. Chem. B* **104** 11117-11126.

Rajamthi, M., Thomas, G.S., and P.V. Kamath (2001). The many ways of making anionic clays. *Proc. Indian Acad. Sci, (Chem. Sci.)* **113** 5&6 671-680.

Rasko, J., Hancz, A., and A. Erdohelyi (2004). Surface species and gas phase products in steam reforming of ethanol on TiO_2 and Rh/TiO_2. *Appl. Catal. A: Gen.* **269** 13–25.

Rasko, J., Domok, M., Baan, K., and A. Erdohelyi (2006). FTIR and mass spectrometric study of the interaction of ethanol and ethanol-water with oxide-supported platinum catalysts. *Appl. Catal. A: Gen.* **299** 202-211.

Rass-Hansen, J. Christensen, C.H., Sehested, J., Helveg, S., Rostrup-Nielsen, J.R., and S. Dahl. Renewable hydrogen: carbon formation on Ni and Ru catalysts during ethanol steam reforming. *Green Chemistry* **9** (2007) 1016-1021.
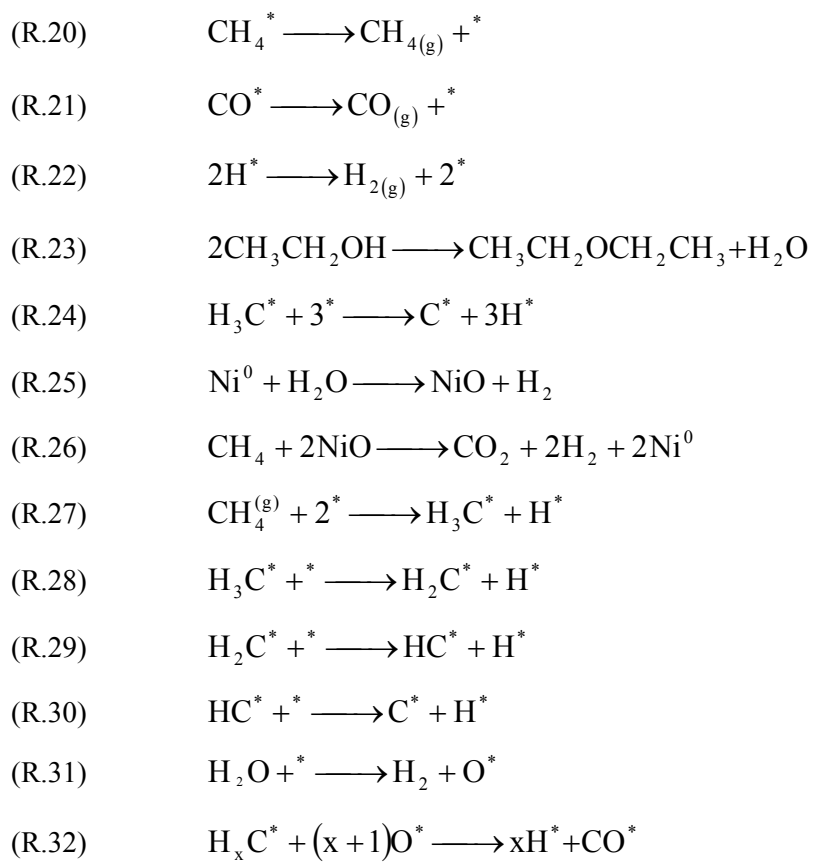
Reid R.C. and T.K Sherwood (1966). The Properties of Gases and Liquids, 2nd ed., McGraw-Hill, Toronto.

Resini, C., Cavallaro, S., Frusteri, F., Freni, S., and G. Busca (2007). Initial steps in the production of H_2 from ethanol: A FT-IR study of adsorbed species on Ni/MgO catalyst surface. *React. Kinet. Catal. Lett.* **90** 1 117-126.

Roh H.-S., Wang. Y., King, D.L., Platon, A., and Y.-H. Chin (2006a). Low temperature and H2 selective catalysts for ethanol steam reforming. *Catal. Lett.* **108** 1-2 15-19.

Roh H.-S., Platon, A., Wang. Y., and D.L.King (2006b). Catalyst deactivation and regeneration in low temperature ethanol steam reforming with Rh/CeO_2-ZrO_2 catalysts. . *Catal. Lett.* **110** 1-2 1-6.

Rossi, P.F., Busca, G., Lorenzelli, V., Waqif, M., Saur, O., and J.-C. Lavalley (1991). Surface basicity of mixed oxides: Magnesium and zinc aluminates. *Langmuir* **7** 2677-2681.

Rostrup-Nielsen, J.R. (2001). Conversion of hydrocarbons and alcohols for fuel cells. *Phys. Chem. Chem. Phys.* **3** 283-288.

Sahoo, D.R., Vajpai, S., Patel, S., and K.K. Pant (2007). Kinetic modeling of steam reforming of ethanol for the production of hydrogen over Co/Al_2O_3 catalyst. *Chem Eng J.* **125** 139-147.

Saleh, J.M, ad S.M. Hussain (1986). Adsorption, desorption and surface decomposition of formaldehyde and acetaldehnyde on metal films of nickel, palladium, and aluminum. *J. Chem. Soc., Faraday Trans. I*., **82** 2221-2234.

Satterfield, C.N. (1970). Mass Transfer in Heterogeneous Catalysis, MIT Press, Cambridge, Mass.

Schaper H., Berg-Slot, J.J., and W.H.J. Stork (1989). Stabilized magnesia: a novel catalyst (support) material. *Appl. Catal.* **54** 79-90.

Schlapbach, L. and A. Zuttel (2001). Hydrogen-storage materials for mobile applications. *Nature* **414** 353-358.

Sehested, J., J.A.P. Gelten, Remediakis, I.N., Bengaard, H., and J. K. Norskov (2004). Sintering of nickel steam reforming catalysts: Effects of temperature and steam and hysrogen pressures. J. *Catal* **223** 432-443.

Sehested, J., J.A.P. Gelten, and S. Helveg (2006). Sintering of nickel catalysts: Effects of time, atmosphere, temperature, nickel-carrier, and dopants. *Appl. Catal. A: Gen* **309** 237-246.

Shen, J., Tu, M., and C. Hu (1998). Structural and surface acid/base properties of hydrotalcite-derived MgAlO oxides calcined at varying temperatures. *J. Solid State Chem* **137** 295-301.

Shen, J., Cortright, R.D., Chen, Y., and J.A. Dumesic (1994). Microcalorimetric and infrared spectroscopic studies of γ-Al_2O_3 modified by basic metal oxides. *J. Phys. Chem.* **98** 8067-8073.

Sloczynski. J., Ziolkowski, J., Grzybowska, B., Grabowski, R., Jachewicz, D., Wcislo, K., and L. Gengembre (1999). Oxidative dehydrogenation of propane on $Ni_xMg_{1-x}Al_2O_4$ and $NiCr_2O_4$ spinels. *J. Catal.* **187** 410-418.

Song, C. (2002). Fuel processing for low-temperature and high-temperature fuel cells. Challenges and opportunities for sustainable development if the 21st century. *Catal. Today* **77** 17-49.

Srinivas, D., Satyanarayana, C. V. V., Potdar, H. S., and Ratnasamy, P., (2003). Structural studies on NiO-CeO_2-ZrO_2 catalysts for steam reforming of ethanol. *Applied Catalysis A: General*, **246**, 323-334.

Stobbe, D.E., van Buren, F.R., Groenendijk, P.E., van Dillen, A.J., and J.W. Geus (1991). Magnesium oxide as a support material for dehydrogenation catalysts. *J. Mater. Chem.* **1** 539-543.

Sun J., Qui, X.-P., Wu, F., and W.-T.Zhu (2005). H_2 from steam reforming of ethanol at low temperature over Ni/Y_2O_3, Ni/La_2O_3, and Ni/Al_2O_3 catalysts for fuel-cell applications. *Int. J. Hydrogen Energy* **30** 437-445

Takehira, K., Shishido, T., Wang, P., Kosaka, T., and K. Takaki (2004). Autopthermal reforming of CH4 over supported Ni catalysts prepared from Mg-Al hydrotalcite-like anionic clays. *J. Catal.* **221** 43-54.

Treybal, R.E. (1980). Mass-Transfer Operations, 3rd ed., McGraw-Hill chemical engineering series, New York.

Vaidya, P.D. and A.E. Rodrigues (2006). Insight into steam reforming of ethanol to produce hydrogen for fuel cells. *Chem. Eng. J.* **117** (2006) 39-49.

Vasudeva, K., Mitra, N., Umasankar, P., and Dhingra, S. C., (1996). Steam reforming of ethanol for hydrogen production: thermodynamic analysis. *Int.J.Hydrogen Energy*, **21**, 13-18.

Vaccari, A. (1998). Preparation and catalytic properties of cationic and anionic clays. *Catal. Today* **41** 53-71.

Vaccari, A. (1999). Clays and catalysts: a promising future. *Appl. Clay Sci.* **14** 161-198.

Velu, S., Suzuki, K., Okazaki, M., Kapoor, M. P., Osaki, T., and Ohashi, F., (2000). Oxidative Steam Reforming of Methanol over CuZnAl(Zr)-Oxide Catalysts for the Selective Production of Hydrogen for Fuel Cells: Catalyst Characterization and Performance Evaluation. *J.Catal.*, **194**, 373-384.

Velu, S., Suzuki, K., Kapoor, M. P., Ohashi, F., and Osaki, T., (2001). Selective production of hydrogen for fuel cells via oxidative steam reforming of methanol over CuZnAl(Zr)-oxide catalysts. *Applied Catalysis A: General*, **213**, 47-63.

Velu, S., Satoh, N., Gopinath, C. S., and Suzuki, K., (2002). Oxidative Reforming of Bio-Ethanol Over CuNiZnAl Mixed Oxide Catalysts for Hydrogen Production. *Catal.Lett.*, **82**, 145-152.

Villa, R., Cristiani, C., Groppi, G., Lietti, L., Forzatti, P., Cornaro, U., and S. Rossini (2003). Ni based mixed oxide materials for CH_4 oxidation under redox cycle conditions. *J. Mol. Catal. A: Chem.* **204-205** 637-646.

Wang, J.A., Novaro, O., Bokhimi, X., Lopez, T., Gomez, R., Navarrete, J., Llanos, M.E., and E. Lopez-Salinas (1997). Structural defects and acidic and basic sites in sol-gel MgO. *J. Phys. Chem. B.* **101** 7448-7451.

Wei , J., and E. Iglesia (2004). Isotopic and kinetic assessment of the mechanism of reactions of CH_4 with CO_2 or H_2O to form synthesis gas and carbon on nickel catalysts. *J. Catal.* **224** 370-383.

Wu. M., Y. Wu, and M. Wang (2006). Energy and Emission Benefits of Alternative Transportation Liquid Fuels Derived from Switchgrass: A Fuel Life Cycle Assessment. *Biotechnol. Prog.* **22** 1012-1024.

Xu., J., and G.F. Froment (1989). Methane steam reforming, methanation and water-gas shift: 1. Intrinsic kinetics. *AIChE J.* **35** 88-96.

Yang, Y., Ma, J., and F. Wu (2006). Production of hydrogen by steam reforming of ethanol over a Ni/ZnO catalyst. *Int. J. Hydrogen Energy* **31** 877-882.

York, A.P.E., Xiao, T, amd M.L.H. Green (2003). Brief overview of the partial oxidation of methane to synthesis gas. Topics in Catal. 22 3-4 345-358

Zuhr, R.A., and J.B. Hudson (1977). The adsorption and decomposition of ethylene on Ni(110). *Surf. Sci.* **66** 405-422.

Appendix A: List of Reactions

(R.1) $CH_3CH_2OH + (1 + x)H_2O \longrightarrow (4 + x)H_2 + (2 - x)CO + xCO_2$

(R.2) $CH_3CH_2OH + H_2O \longrightarrow 4H_2 + 2CO$

(R.3) $CO + H_2O \longrightarrow H_2 + CO_2$

(R.4) $CH_3CH_2OH \longrightarrow \dfrac{3}{2}CH_4 + \dfrac{1}{2}CO_2$

(R.5) $CH_4 + (1 + y)H_2O \longrightarrow (3 + y)H_2 + (1 - y)CO + yCO_2$

(R.6) $2CO \longrightarrow CO_2 + C$

(R.7) $CH_3CH_2OH \longrightarrow CH_3CHO + H_2$

(R.8) $CH_3CHO \longrightarrow CH_4 + CO$

(R.9) $CH_3CH_2OH \longrightarrow CH_4 + CO + H_2$

(R.10) $CH_3CHO + H_2O \longrightarrow 3H_2 + 2CO$

(R.11) $CH_3CH_2OH \longrightarrow C_2H_4 + H_2O$

(R.12) $C_2H_4 \longrightarrow$ olefins $\longrightarrow$ polymers $\longrightarrow$ coke

(R.13) $CH_4 \longrightarrow C + 2H_2$

(R.14) $CO + \dfrac{1}{2}O_2 \longrightarrow CO_2$

(R.15) $CH_3CH_2OH_{(g)} + 2^* \longrightarrow CH_3CH_2O^* + H^*$

(R.16) $CH_3CH_2O^* + {}^* \longrightarrow CH_3CHO^* + H^*$

(R.17) $CH_3CHO^* \longrightarrow CH_3CHO_{(g)} + {}^*$

(R.18) $CH_3CHO^* + 2^* \longrightarrow H_3C^* + CO^* + H^*$

(R.19) $H_3C^* + H^* \longrightarrow CH_4{}^* + {}^*$

191

(R.20) $\quad$ $CH_4^* \longrightarrow CH_{4(g)} + {}^*$

(R.21) $\quad$ $CO^* \longrightarrow CO_{(g)} + {}^*$

(R.22) $\quad$ $2H^* \longrightarrow H_{2(g)} + 2^*$

(R.23) $\quad$ $2CH_3CH_2OH \longrightarrow CH_3CH_2OCH_2CH_3 + H_2O$

(R.24) $\quad$ $H_3C^* + 3^* \longrightarrow C^* + 3H^*$

(R.25) $\quad$ $Ni^0 + H_2O \longrightarrow NiO + H_2$

(R.26) $\quad$ $CH_4 + 2NiO \longrightarrow CO_2 + 2H_2 + 2Ni^0$

(R.27) $\quad$ $CH_4^{(g)} + 2^* \longrightarrow H_3C^* + H^*$

(R.28) $\quad$ $H_3C^* + {}^* \longrightarrow H_2C^* + H^*$

(R.29) $\quad$ $H_2C^* + {}^* \longrightarrow HC^* + H^*$

(R.30) $\quad$ $HC^* + {}^* \longrightarrow C^* + H^*$

(R.31) $\quad$ $H_2O + {}^* \longrightarrow H_2 + O^*$

(R.32) $\quad$ $H_xC^* + (x+1)O^* \longrightarrow xH^* + CO^*$

Appendix B: Gas chromatography method for the characterization of ethanol steam reforming products

Gas Chromatography Method for the Characterization of Ethanol Steam Reforming Products

Petr Chladek , Luke J.I. Coleman*, E. Croiset, and Robert R. Hudgins

Department of Chemical Engineering, University of Waterloo, Waterloo, ON, N2L 3G1,

Canada

*Corresponding author: E-mail: ljicolem@uwaterloo.ca

Abstract

Ethanol steam reforming is a promising reaction for producing fuel cell hydrogen. Depending on catalyst and reaction conditions, mixtures of condensable hydrocarbons and organic and inorganic gases are produced. This paper proposes an economic and effective solution for separating and detecting these compounds employing a GC equipped with two columns, two 6-way valves and two detectors.

Introduction

The production of hydrogen from bio-ethanol has received much research attention in the last few years. Ethanol derived from cellulosic materials is considered an eco-friendly hydrogen source because it is renewable, non-toxic, and could significantly reduce greenhouse gas emissions, making it a good candidate for hydrogen production. Ethanol steam reforming is the most commonly studied ethanol conversion process due to its high hydrogen and potentially low carbon monoxide yields. For hydrogen production, the overall ethanol steam reforming reaction is given in equation 1.

$$CH_3CH_2OH_{(g)} + 3H_2O_{(g)} \xleftrightarrow{\text{Catalyst}} 6H_{2(g)} + 2CO_{2(g)} \qquad (1)$$
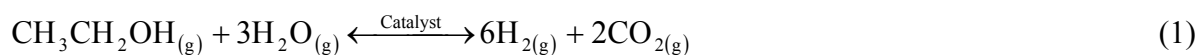
The ethanol steam reforming reaction, given in equation 1, is an endothermic equilibrium limited reaction that is not favoured in the forward direction for reaction temperatures below 330°C.

The overall ethanol steam reforming reaction above is an idealized reaction. In real applications, depending on the catalyst and the operating conditions, a wide variety of reaction products could be expected such as H_2, H_2O, CO, CO_2, methane, ethylene, ethane, propylene, acetaldehyde, ethanol, acetone, acetic acid, diethyl ether, ethyl acetate, crotonaldehyde, butanol, and deposited amorphous carbon. In general, ethanol steam reforming is conducted in continuous fixed-bed reactors at temperatures ranging from 300 to 850°C on a variety of catalysts. The analysis of such a wide range of species by conventional gas chromatography is not trivial, especially on-line.

Throughout the ethanol steam reforming literature, the product gas streams have been analyzed by several techniques. A commonly used approach requires the partitioning of the sample by condensation, in which the incondensable species are detected and quantified in an on-line manner, and the liquid sample periodically collected and analyzed [1-4]. This analytical approach generally requires multiple GCs, which can be prohibitively expensive; however, method development and column selection are relatively easy tasks. A major drawback of this analytical approach is the determination of the species and overall material balances due to inaccurate measurement of the liquid flow rate, which is generally quite low. In addition, unlike the discrete gas sampling, the collected liquid sample represents a time-averaged sample, which leads to inaccurate determination of species distribution and does not allow for accurate determination of kinetics, especially when the studied system is inherently dynamic. Finally, the volatility of species in the collected liquid sample can be a problem and must be considered.

Another common analytical approach employs a single or multiple GC(s) with multiple columns, multiple detectors, and multiple sample injections [5-14]. This approach requires the entire product sample to remain in the gas phase and the sample is separated into multiple injections and each injection is analyzed for specific species. This requires more thorough method development and column selection. The columns are usually selected such that the

sample is divided into separable and inseparable fractions on each column/detector arrangement and all separable species are quantified. This technique has been successful in accurately determining the composition of the detectable species in the product stream, but the quantification of the amount of the undetectable species, especially water, is difficult because there are numerous undetectable species for each column/detector arrangement. The result is a lack of confidence for the quantity of water in the product stream, which is a major concern because water typically accounts for up to 50 volume % of the total injected sample, and consequently a lack of confidence in the species and overall material balances.

The single GC, multi-column, multi-detector, single injection approach described here was developed to overcome the limitations mentioned above. On the one hand the product stream is analyzed in its entirety without necessitating any phase separation. On the other hand in this method all species are detected in one injection (no undetectable species) and the concentration of water can be determined with confidence by subtraction. This approach exploits differences in column selectivity and species affinity in addition to temperature programming and column order switching to separate and detect the entire injected sample.

Separation and Quantification Strategy

Figure 1 presents a schematic diagram of the GC's column, valve, and detector arrangement. The product stream exiting the reactor is continuously fed to the sample injection valve that is maintained at the same temperature as the product stream. A block diagram of the initial column/detector arrangement is given in Figure 2a. The entire sample is injected and the sample enters the first column, which is capable of separating condensable (heavy fraction) species. The initial GC oven temperature is selected such that the condensable species adsorb in the heavy fraction column, and the non-condensable (light fraction) species continue to a second, light fraction, column. Once the light fraction species elute from the heavy fraction column, the decision valve, shown in Figure 1, switches to position 2. As shown in Figure 2b, the column/detector arrangement changes, so that the carrier gas is fed directly to the light fraction column. The carrier gas enters the light fraction column, passes through a flow-through, preferably non-destructive, detector (e.g. thermal conductivity detector (TCD)), and

continues to the heavy fraction column. A temperature program is applied and species elute from their respective columns. The first detector (e.g. TCD) whose effluent becomes the carrier gas for the column separating the heavy fraction detects the light fraction species initially. The heavy fraction column effluent, which contains the heavy and light fraction species, is sent to a second detector (e.g. flame ionization detector (FID)) for analysis. This arrangement allows for double detection of the combustible light fraction components, such as methane. The temperature program must be developed such that the light fraction species do not adsorb on the heavy fraction column, but are retained by the light fraction column and the species eluting from the light fraction column do not interfere, or co-elute, with the species from the heavy fraction column.

Experimental
Instrument
The gas chromatograph (GC) used in this study was a Varian CP-3800 (Varian Inc., Palo Alto, CA) equipped with a 1041 splitless on-column injector, TCD, FID, two 6-way valves (VICI, Houston, TX) enclosed in a dual valve heating oven, and electronic flow controllers (EFCs) controlling all gas flow rates. The GC was controlled and automated by the Star GC Workstation (ver. 5.50) software package (Varian Inc.).

Ultra-high purity helium, 99.999%, (Praxair Inc., Danbury, CT), which was further purified by passing through a helium purifier (Supelco, Inc., Bellefonte, PA), was used as the carrier and TCD reference gas. Hydrogen, 99.995%, (Praxair Inc.) and in-house produced zero-gas air were used to generate the FID flame. A 15' x 1/8" stainless steel column containing 60/80 mesh Carboxen-1000 (Supelco Inc.) was used for separation of the light fraction species. For separation of the heavy fraction species, a 6' x 1/8" stainless steel column containing 50/80 mesh Porapak Q was used. The carrier gas flow rate was set at 55 mL/min. The valve heating oven, injector, and detectors were set at 250°C. The sample loop volume was 500 μL.

Chemicals

For species identification and calibration, two custom certified calibration gas mixtures (Praxair Inc.) whose compositions are given in Table I, were used in addition to pure H_2, N_2, CH_4, C_2H_4, propylene, acetaldehyde, acetone, diethyl ether, ethyl acetate, crotonaldehyde, 1-butanol, and anhydrous ethanol (Commercial Alcohols Inc., Toronto, ON). All gases were minimum 99.995% grade and supplied by Praxair Inc. and all liquids were ACS grade and supplied by Sigma-Aldrich Co., unless otherwise stated.

Results and Discussion

The first step of method development was the characterization of the light and heavy fractions and identification of suitable light and heavy fraction columns. The Carboxen-1000 column was identified from literature [15] as a good candidate for separating the light fraction, permanent gases and light (C1-C2) hydrocarbons. The heavy fraction column was identified on a trial-and-error basis, because the constraints for selection of this column were more stringent. The heavy fraction column must adequately separate the heavy fraction species, have no activity for the separation of the light fraction species, and its integrity cannot be hindered by any of the species in the injected sample. Porapak Q, a high surface area, cross-linked polymer packing without a stationary phase coating, typically used for separating small chain, slightly polar species, was selected as the heavy fraction column.

The next step was the identification of the light fraction, and determination of its retention time in the heavy fraction column. This was achieved by connecting the Porapak Q (heavy fraction) column directly to the TCD and injecting a prepared mixture of the two certified calibration gases with the column oven at 35°C. The permanent gases (H_2, N_2, CO, CH_4, and CO_2) co-eluted in less than 4 minutes while the C2-species from calibration gas #2 were adequately separated and eluted after 4 minutes. The 4-minute mark was selected as the time to actuate the decision valve to position 2.

The column, detector, and valve arrangement given in Figure 1 was then implemented. The temperature program suggested by Supelco Application Note 112 [15] for separation of permanent gases and C2 hydrocarbons using the Carboxen-1000 column was selected as the

starting point for temperature program development. The proposed temperature program consisted of a temperature hold at 35°C for 4 minutes and an aggressive temperature ramp rate of 20°C min^{-1} to 225°C. Mixtures containing the two custom calibration gases and condensable species (e.g. water, ethanol, acetaldehyde, etc.) were used to "tailor" the temperature program. Analysis of the simulated product stream resulted in good separation and quantification of the permanent gas species, C2 hydrocarbons (acetylene, ethylene, and ethane), but resulted in co-elution, or peak shouldering of acetaldehyde and methane from the heavy fraction column and poor separation of the remaining hydrocarbons. The temperature ramp rate was reduced to 5°C min^{-1} from 155°C to 225°C to allow for better separation of these species. The resulting temperature program is given in Table II.

The separation strategy can be described with the aid of the schematic diagram (Figure 1), the column/detector arrangements (Figures 2a and 2b), and the resulting TCD and FID chromatograms given in Figures 3 and 4, respectively. The product gas stream exiting the reactor was injected into the GC. The sample passed through the decision valve and entered the Porapak Q column that was held at 35°C. The heavy condensable species adsorbed on to the column while the light gaseous species continued, unresolved, to the Carboxen-1000 column. Hydrogen, being the least retained species, was detected by the TCD (Figure 3) at minute 2 and was subsequently burned by the FID (no detection). After 4 minutes, the decision valve was switched to position 2 and at minute 5 the column oven temperature was ramped at a rate of 20°C min^{-1} to 155°C. During this temperature ramp ethylene, acetylene, ethane, and propylene eluted from the Porapak Q column and were detected by the FID (Figure 4). In addition, nitrogen and carbon monoxide eluted from the light fraction column, were detected by the TCD, and then fed to the heavy fraction, Porapak Q column, as a pseudo-carrier gas. These species were not detected by the FID and did not interfere with the quantification of species eluting from the Porapak Q column. The temperature oven was then increased to 225°C at a reduced ramp rate of 5°C min^{-1} to give better separation of the more strongly adsorbed species. At minute 10.5, the FID sensitivity was reduced from attenuation level 12 to 11, because the concentrations of acetaldehyde, methane, and ethanol were

expected to be high, and would therefore create very large, potentially detector saturated peaks. Acetaldehyde was the next species to desorb from the heavy fraction column, while shortly afterwards, methane eluted from the light fraction column. Methane was detected by the TCD and then eluted from the heavy fraction column and was detected by the FID. Ethanol desorbs from the heavy fraction column at minute 12.75 followed by CO_2 from the light fraction column. Again, when CO_2 eluted from the light fraction column it passed through the TCD, where it was detected, then passed through the heavy fraction column and the FID, but being non-combustible was not detected by the FID. The elution of acetone and diethyl ether from the heavy fraction column occurred at minutes 15.6 and 16.0, respectively. At minute 18, the FID sensitivity was increased from attenuation 11 to 12 to allow for detection of trace amounts of the remaining species. The remaining hydrocarbon species, ethyl acetate, crotonaldehyde, and butanol eluted from the heavy fraction column and were detected by the FID. The method ended at minute 25 at which point the decision valve was returned to position 1 and the column oven cooled to its initial temperature.

Once the separation method was developed a calibration of each species was obtained using combinations of the two custom calibration gases, pure gases (H_2, N_2, CH_4, and C_2H_4), water and liquid organics. The results of the calibration are given in Table III. The calibrated range for hydrogen is quite broad (3.0-99.0%), but the flow rate of the carrier gas, helium, was very large, resulting in a hydrogen concentration seen by the detector below 5%. The polarity of the hydrogen peak was positive for the entire range (no peak inversion), however, the relationship between hydrogen concentration and peak area was quadratic, not linear. The resulting concave-upward quadratic model accounts for the nonlinearity in the thermal conductivity of mixture of hydrogen and helium [16].

Conclusions

The composition of the stream resulting from ethanol steam reforming varies with the catalyst employed, reaction conditions (temperature, reactant feed concentration, feed gas flow rate, and time on-stream (catalyst deactivation)). The analysis of such a complex and varying gas composition is no trivial task. The described analytical method provides a

versatile and inexpensive tool for separating and detecting samples containing both gaseous and condensable species. By adjusting the time of the decision valve actuation, temperature program and detector sensitivity, the method can be fitted to obtain a desirable degree of separation and detection for different species produced in various reactions all in one GC. The authors believe that by simply employing appropriate column selections, temperature programming, and detector type and sensitivity, a broader range of applications can be achieved.

References
1. F. Auprêtre, C. Descorme, and D. Duprez. Bio-ethanol catalytic steam reforming over supported metal catalysts. Catal. Comm. 3: 263-267 (2002).
2. A.J. Akande, R.O. Idem, and A.K. Dalai. Synthesis, characterization and performance evaluation of Ni/Al2O3 catalysts for reforming of crude ethanol for hydrogen production. Appl. Catal. A: Gen. 287: 159-175 (2005).
3. A. Aboudheir, A. Akande, R. Idem, and A. Dalai. Experimental studies and comprehensive reactor modeling of hydrogen production by the catalytic reforming of crude ethanol in a packed bed tubular reactor over a Ni/Al2O3 catalyst. Int. J. Hydrogen Energy 31: 752-761 (2006).
4. H.S. Roh, Y. Wang, D.L. King, A. Platon, and Y.H. Chin. Low temperature and H2 selective catalysts for ethanol steam reforming. Catal. Lett. 108(1–2): 15-19 (2006).
5. M.S. Batista, R.K.S. Santos, E.M. Assaf, J.M. Assaf, and E.A. Ticianelli. Characterization of the activity and stability of supported cobalt catalysts for the steam reforming of ethanol. J. Power Sources 124: 99-103 (2003).
6. S. Cavallaro, V. Chiodo, A. Vita, and S. Freni. Hydrogen production by auto-thermal reforming of ethanol on Rh/Al$_2$O$_3$ catalyst. J. Power Sources 123: 10-16 (2003).
7. C. Diagne, H. Idriss, and A. Kiennemann. Hydrogen production by ethanol reforming over Rh/CeO$_2$–ZrO$_2$ catalysts. Catal. Comm. 3: 565-571 (2002).
8. A.N. Fatsikostas, D. Kondarides, and X.E. Verykios. Production of hydrogen for fuel cells by reformation of biomass-derived ethanol. Catal.Today 75: 145-155 (2002).
9. S. Freni. Rh based catalysts for indirect internal reforming ethanol applications in molten carbonate fuel cells. J .Power Sources 94: 14-19 (2001).
10. V.V Galvita, G.L. Semin, V.D. Belyaev, V.A. Semikolenov, P. Tsiakaras, and V.A. Sobyanin. Synthesis gas production by steam reforming of ethanol. Appl Catal A: Gen 220: 123-127 (2001).
11. V. Klouz, V. Fierro, P. Denton, H. Katz, J.P. Lisse, S. Bouvot-Mauduit, and C. Mirodatos. Ethanol reforming for hydrogen production in a hybrid electric vehicle: process optimisation. J.Power Sources 105: 26-34 (2002).

12. D.K. Liguras, D.I. Kondarides, and X,E, Verykios. Production of hydrogen for fuel cells by steam reforming of ethanol over supported noble metal catalysts. Appl Catal B: Enviro 43: 345-354 (2003).
13. J. Llorca, P.R. de la Piscina, J.A. Dalmon, J. Sales, and N. Homs. CO-free hydrogen from steam-reforming of bioethanol over ZnO-supported cobalt catalysts. Appl Catal B: Enviro 43: 355-369 (2003).
14. S. Velu, N. Satoh, C.S. Gopinath, and K. Suzuki. Oxidative reforming of bioethanol over CuNiZnAl mixed oxide catalysts for hydrogen production. Catal. Lett. 82: 145-152 (2002).
15. Application Note 112 "Analysis of Permanent Gases, Light Hydrocarbons, and Light Polar Compounds, Using Packed Column GC". Supelco, Inc. (1996).
16. B.J. Gudzinowicz. The Practice of Gas Chromatography. L.S. Ettre and A. Zlatkis, Eds. John Wiley and Sons, New York, NY, 1967, p. 246.

List of Figures
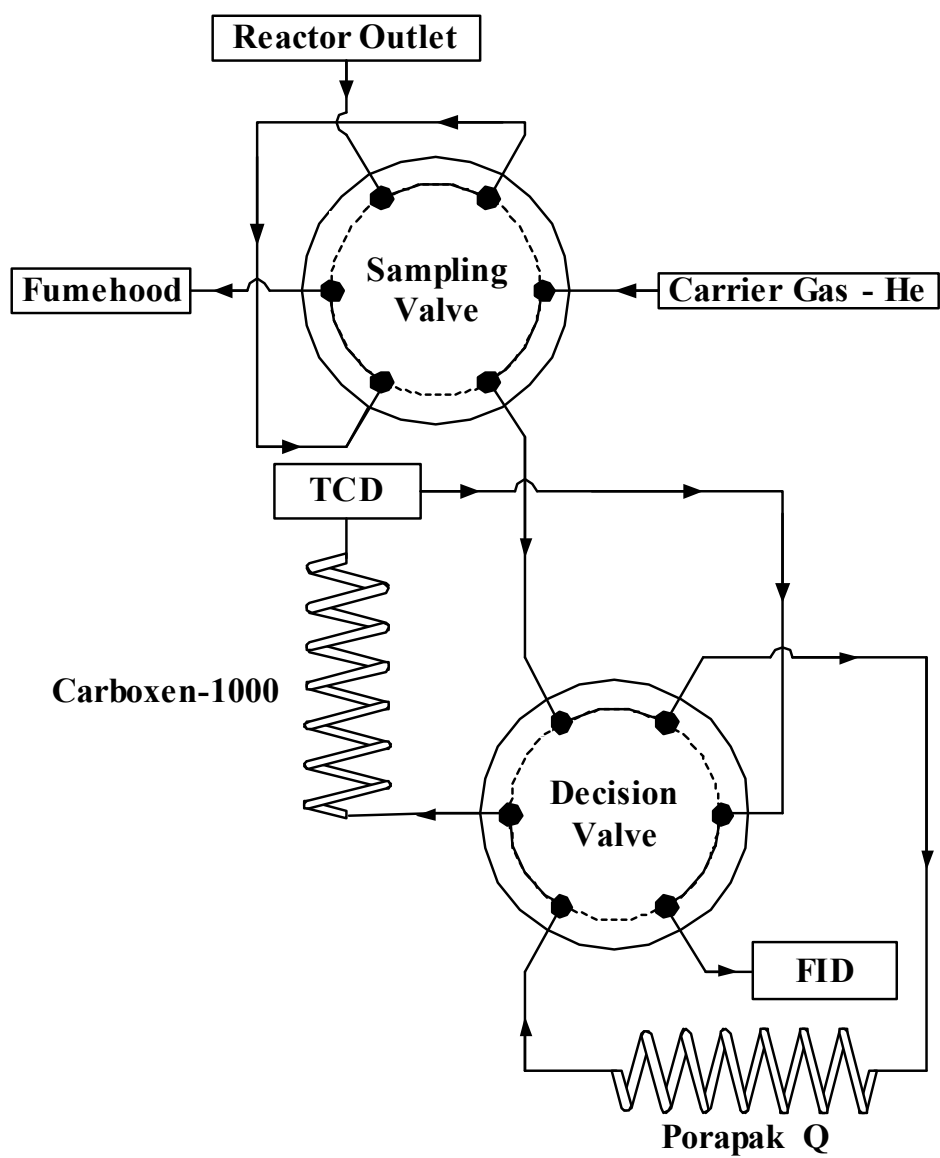
Figure 1
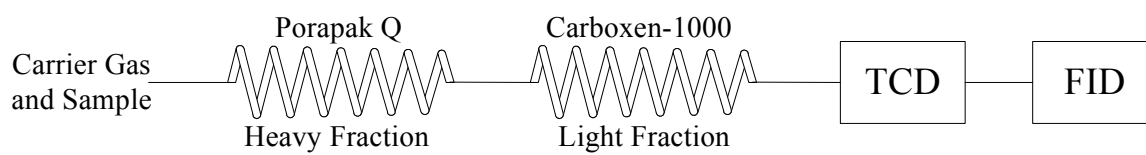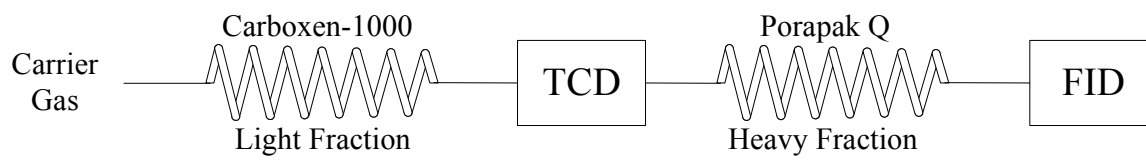
Figure 2a

Figure 2b

Figure 3

Figure 4

206
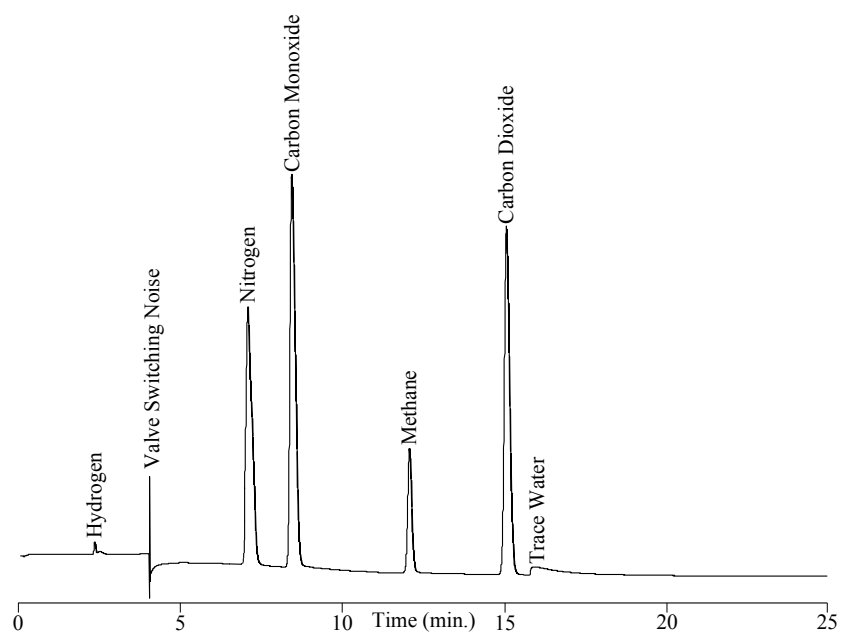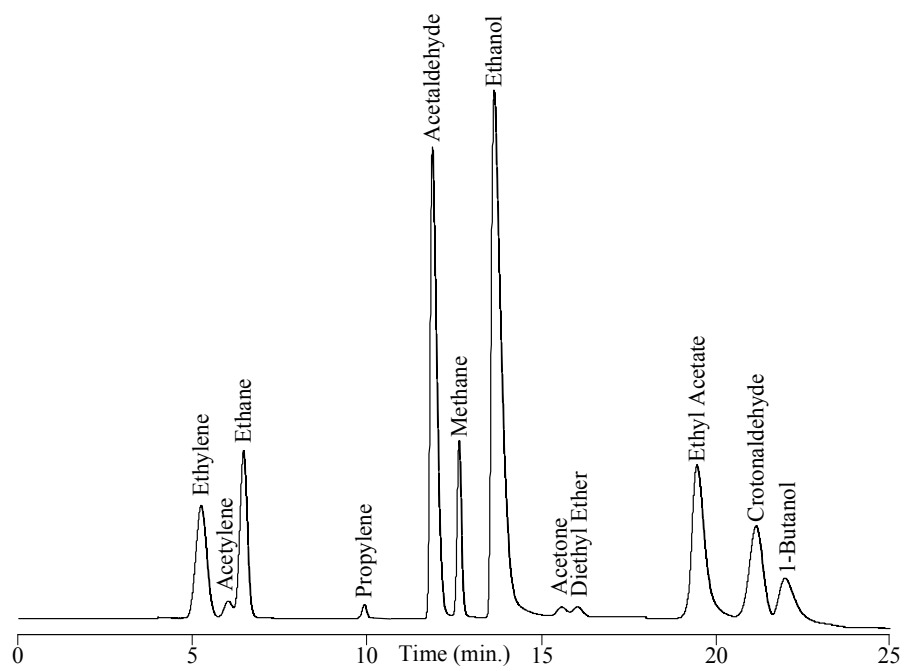
Table I: Composition of custom certified calibration gases

Calibration Gas #1		Calibration Gas #2	
Species	Concentration (vol%)	Species	Concentration (vol%)
H_2	30.03	C_2H_2	0.499
O_2	3.0	C_2H_4	3.09
Ar	9.0	C_2H_6	3.00
CO	30.0	N_2	93.0
CH_4	7.97	Trace Hydrocarbon	Balance
CO_2	20.0	Mixture	

Table II: GC oven temperature program

Temperature(°C)	Rate (°C min^{-1})	Hold (min)	Total Time (min)
35	0.0	5.0	5.0
155	20.0	0.0	11.0
225	5.0	0.0	25.0

Table III: GC calibration results

Species	Range (%mol)	Detector	Model	R^2	# of data points*
Hydrogen	3.0 - 99.0	TCD	Quadratic	0.9996	17
Nitrogen	1.0 - 99.3	TCD	Linear	0.9991	33
Carbon Monoxide	3.0 - 30.0	TCD	Linear	0.9991	6
Methane	0.8 - 20.0	TCD	Linear	0.9991	10
		FID	Linear	0.9990	10
Carbon Dioxide	2.0 - 20.0	TCD	Linear	0.9995	6
Acetylene	0.05 - 0.499	FID	Linear	0.9977	6
Ethylene	0.031 - 30.0	FID	Linear	0.9951	14
Ethane	0.30 - 3.0	FID	Linear	0.9973	6
Propylene	0.01 - 0.1	FID	Linear	0.9989	6
Acetaldehyde	0.44 – 18.0	FID	Linear	0.9987	7
Ethanol	0.30 – 84.0	FID	Linear	0.9991	12
Acetone	0.01 - 0.17	FID	Linear	0.9999	3
Diethyl Ether	0.01 - 0.1	FID	Linear	0.9975	3
Ethyl Acetate	0.01 - 0.16	FID	Linear	0.9996	3
Crotonaldehyde	0.01 - 0.1	FID	Linear	0.9829	3
1-Butanol	0.01 - 0.09	FID	Linear	0.897	3

* Each data point represents an average of a minimum of five replicate injections.

Appendix C: Gas Chromatograph Calibration
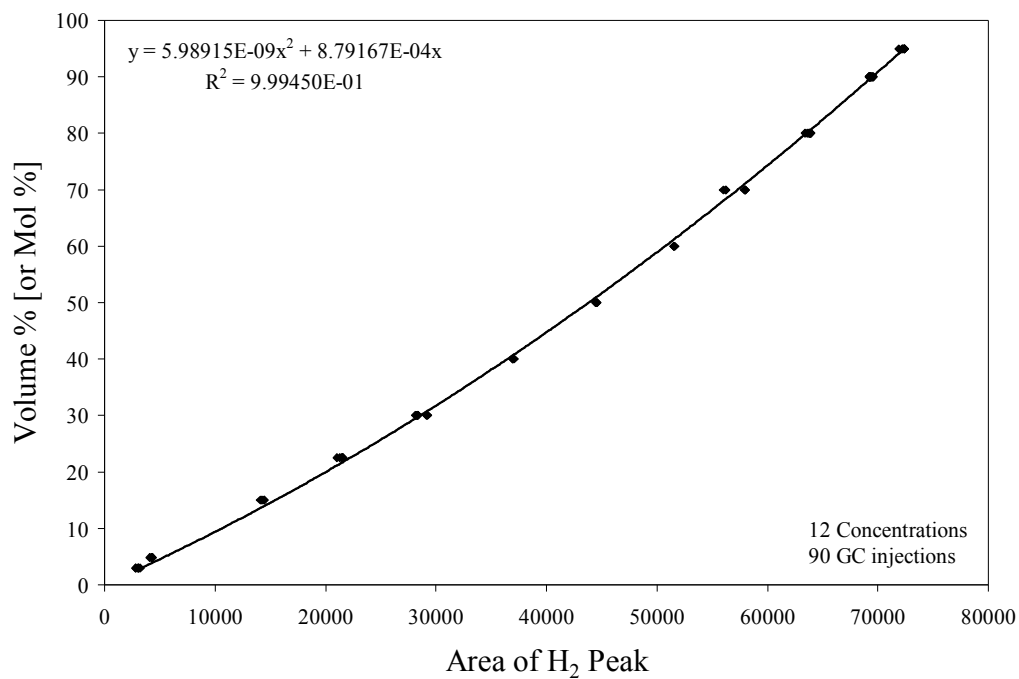
Figure C.1: TCD response calibration for H_2
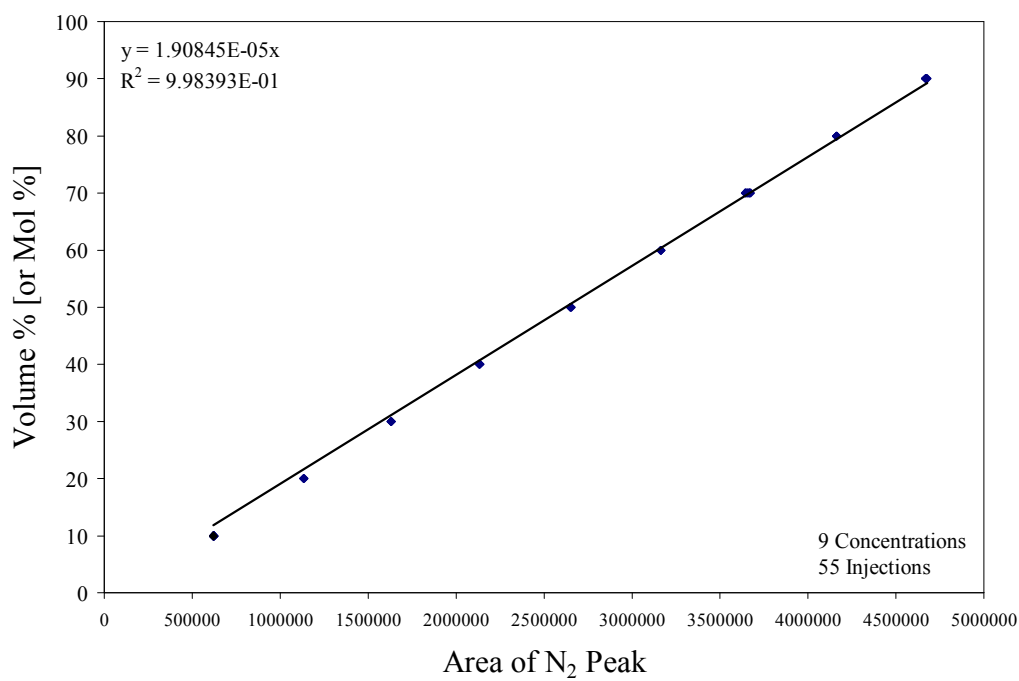
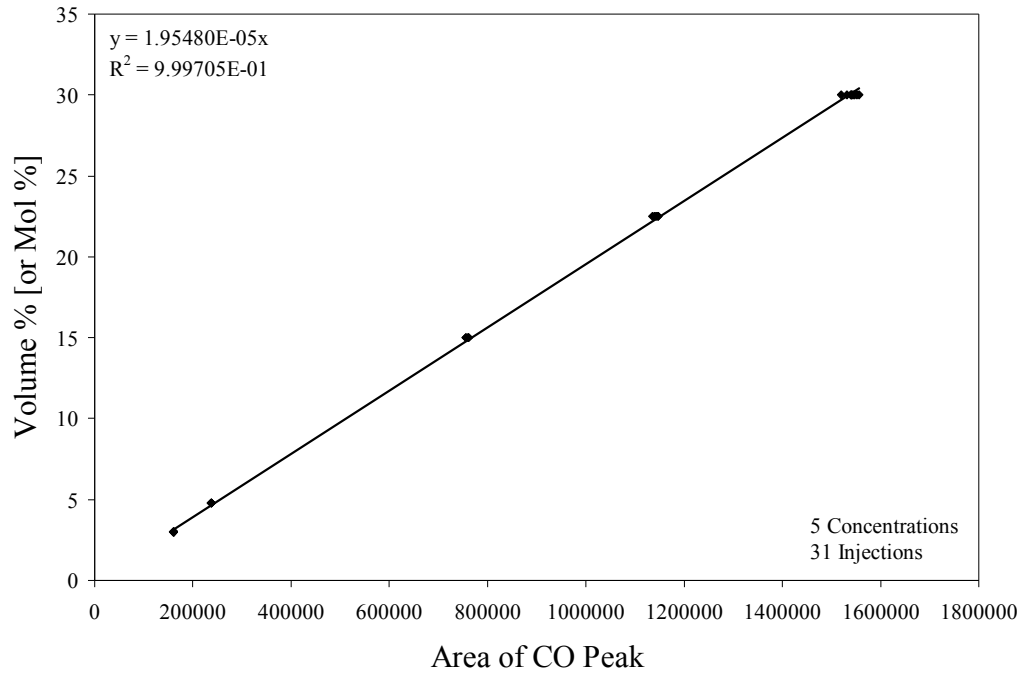**Figure C.2:** TCD response calibration results for N_2

210

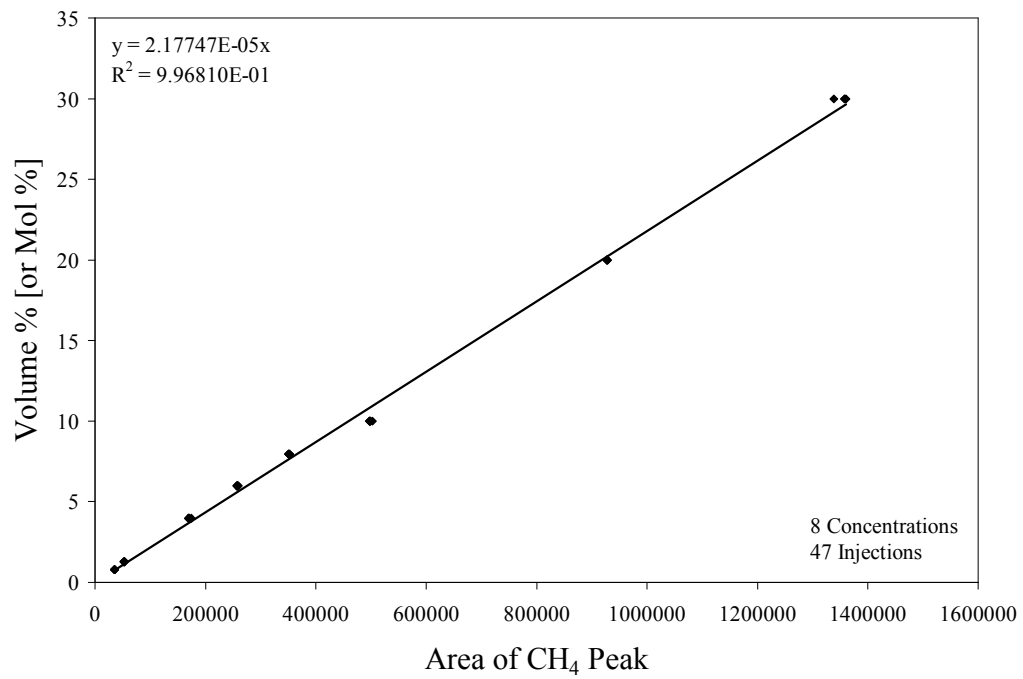**Figure C.3:** TCD response calibration for CO
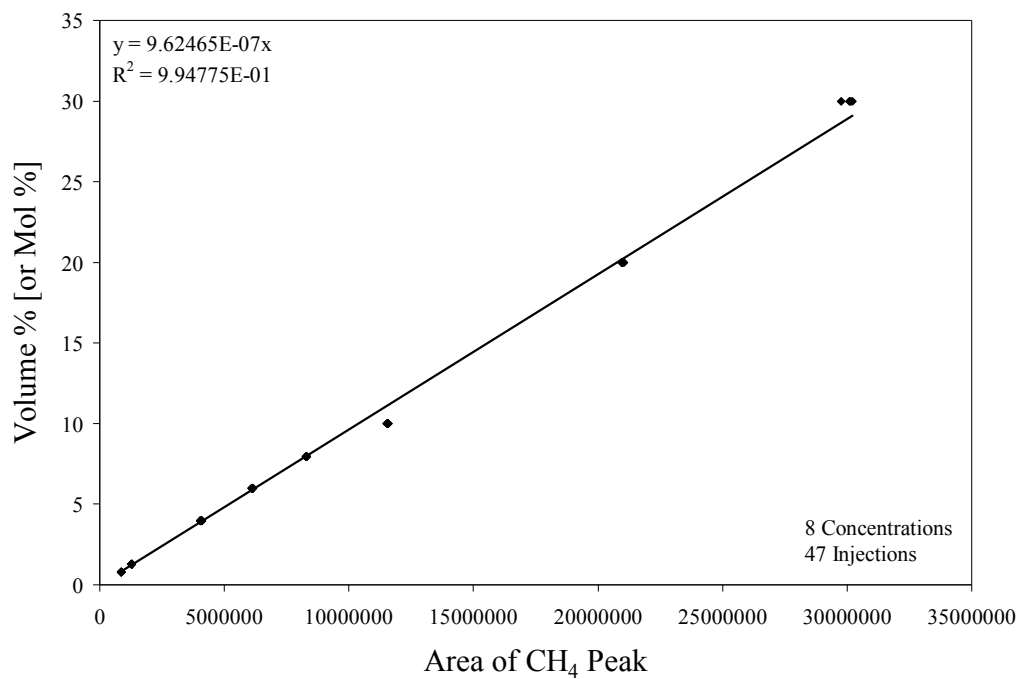

Figure C.4: TCD response calibration for CH$_4$

211

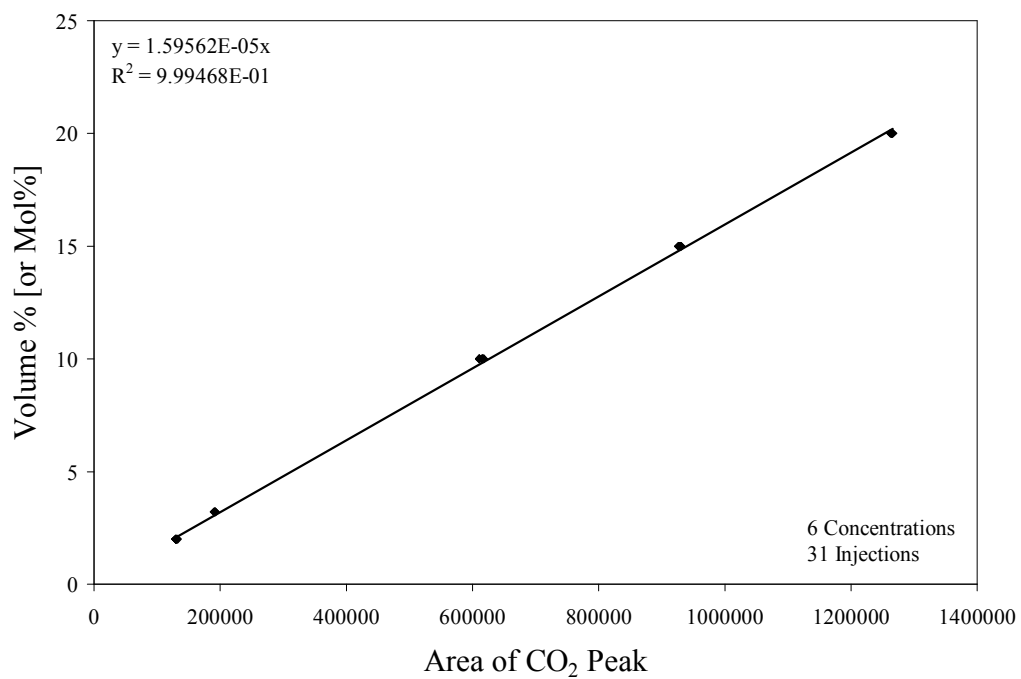**Figure C.5:** FID response calibration for CH_4
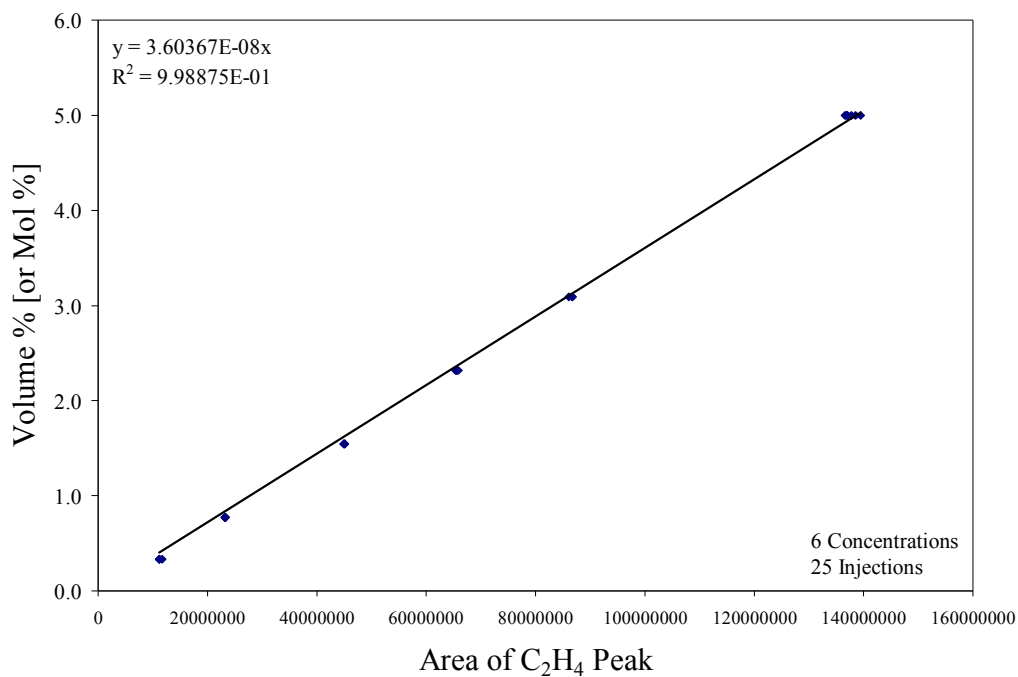

Figure C.6: TCD response calibration for CO_2
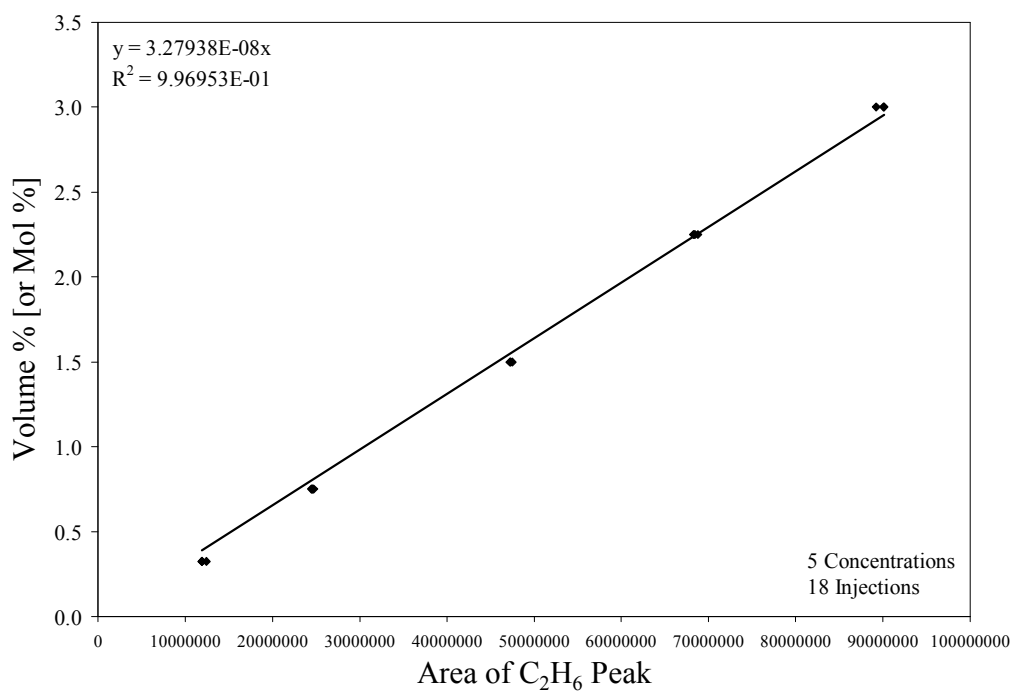
Figure C.7: FID response calibration for C_2H_4
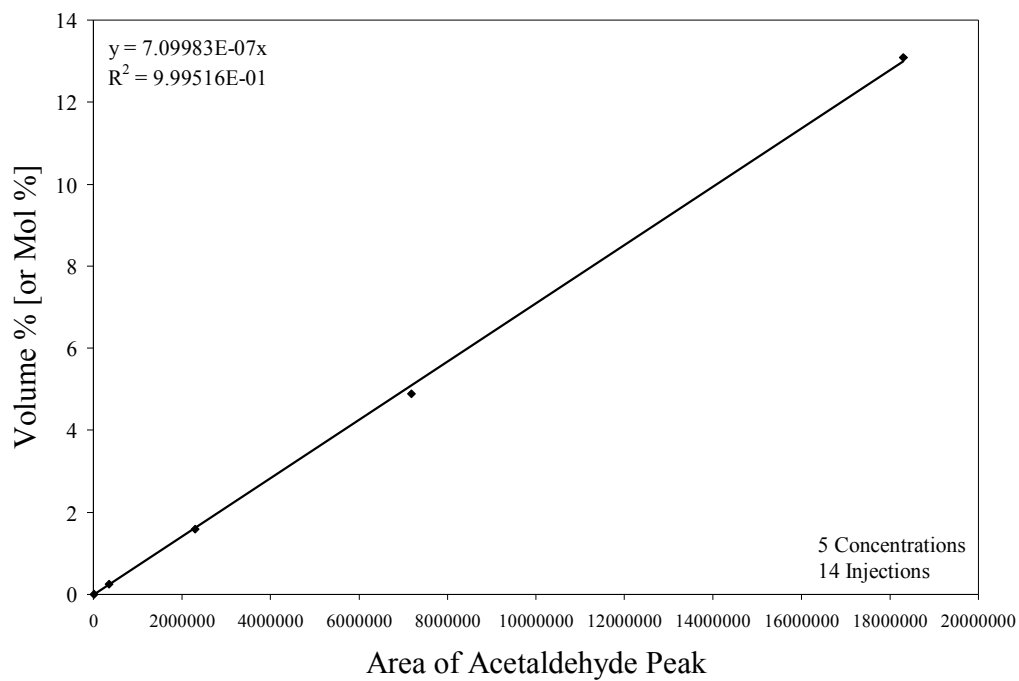

Figure C.8: FID response calibration for C_2H_6

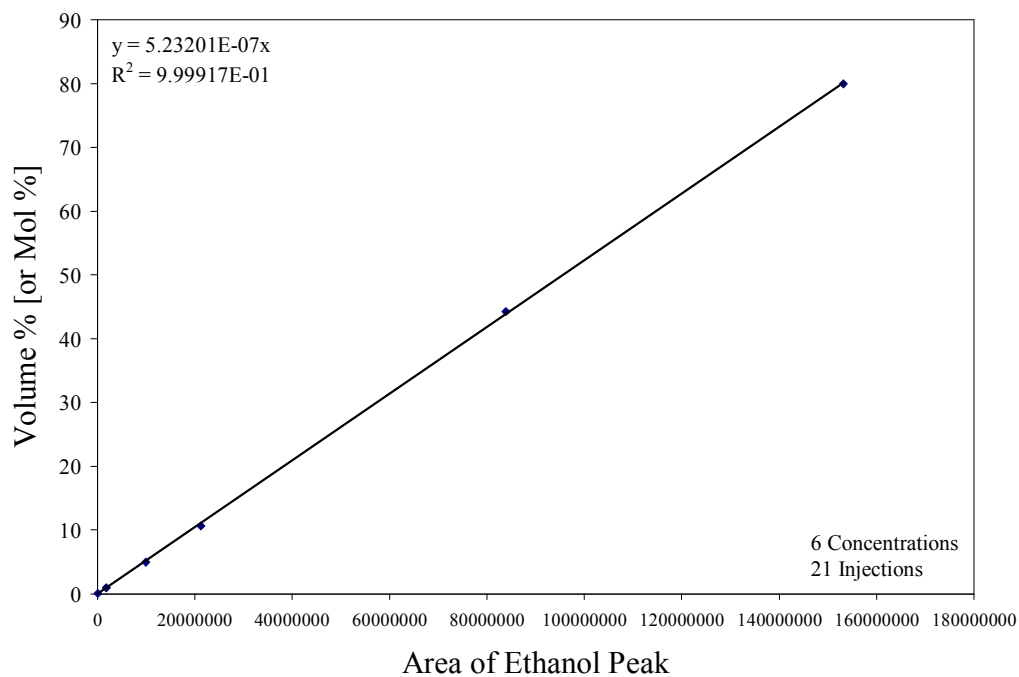**Figure C.9:** FID response calibration for Acetaldehyde

Figure C.10: FID response calibration for Ethanol

214

y = 2.48509E-08x
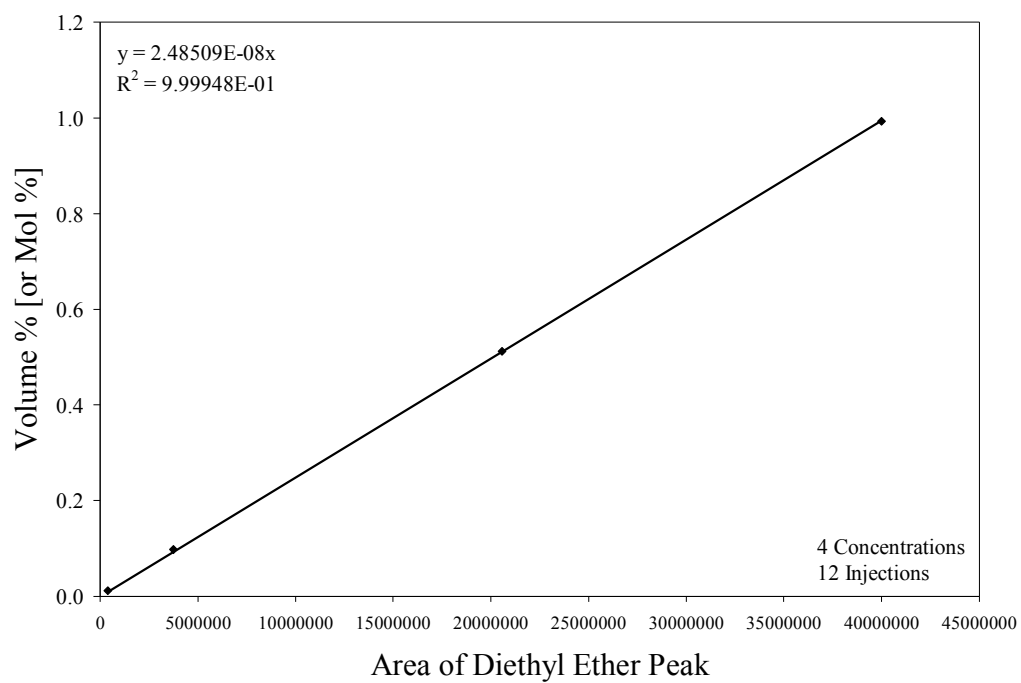R^2 = 9.99948E-01

4 Concentrations
12 Injections

Figure C.11: FID response calibration for Diethyl ether

Appendix D: Sample calculations for the determination of catalyst evaluation parameters

---

Ethanol Conversion

H$_2$O Utilization

Product Yield

Carbon Balance

Sample calculations are provided for a typical ethanol steam reforming experiment. The specific experiment being detailed was selected from the ethanol steam reforming temperature programmed reaction experiment. Experimental conditions:

GHSV: ~260 000 mL$_{Feed}$ h^{-1} gcat^{-1}

Pressure: atmospheric

H$_2$O:EtOH: 8.4:1 molar feed ratio

Temperature: ~764 K at time of injection (injection 18)

The TCD and FID chromatograms shown in Figures D.1 and D.2 are the specific chromatograms obtained for injection 18 of the experiment detailed above. The results are provided as representations of typical chromatograms.
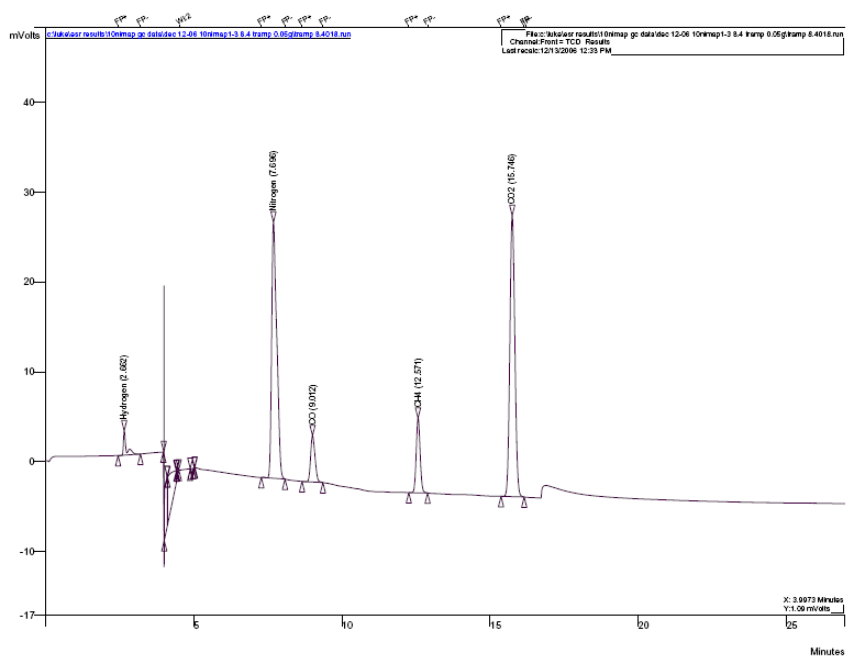
Figure D.1: TCD chromatogram for a typical ethanol steam reforming experiment. Data taken from the 8.4:1 temperature programmed reaction experiment injection 18.
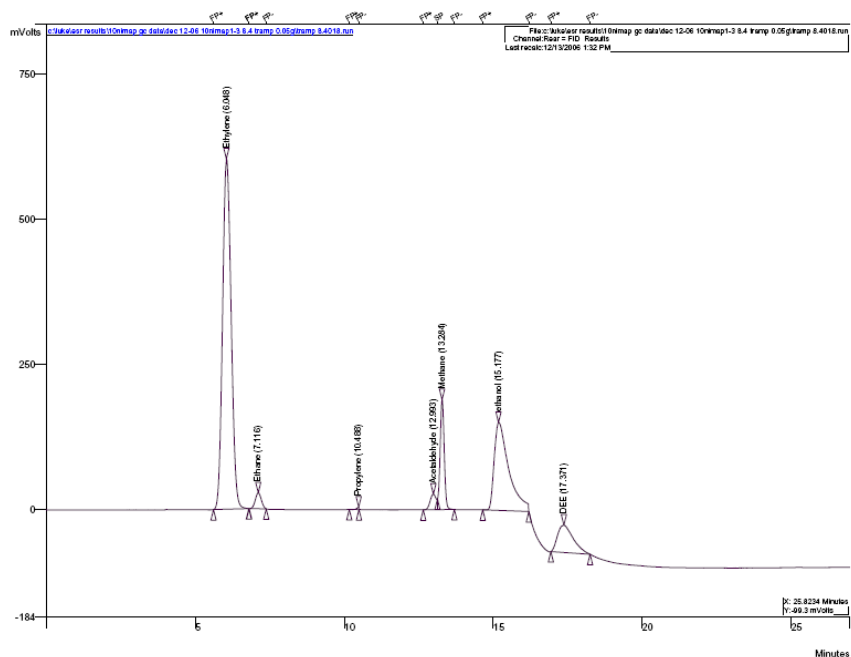

Figure D.2: FID chromatogram for a typical ethanol steam reforming experiment. Data taken from the 8.4:1 temperature programmed reaction experiment, injection 18**.**

217

Integration of the TCD and FID chromatograms was achieved by using the peak integration utility of the Varian Star 5.1 chromatograph analysis software. The resulting peak areas from the above chromatograms are given in Table D.1

Table D.1: Peak areas for the above chromatograms

TCD		FID	
Species	**Peak Area**	**Species**	**Peak Area**
H_2	19 663	C_2H_4	12 991 168
N_2	314 309	C_2H_6	412 854
CO	57 367	AcHO	408 489
CH_4	82 283	CH_4	1 931 876
CO_2	397 310	EtOH	5 553 912
		DEE	1 853 530

The composition of the product gas exiting the reactor was determined by applying the calibration curves, relating peak area for each species to a volume %, and which are present in Tables D.2 and D.3.

Table D.2: TCD Calibration curves

Species	Calibration Curve (Peak Area →Vol%)
H_2	$5.98915 \cdot 10^{-9} \cdot PA_{H_2}^{2} + 8.79167 \cdot 10^{-4} \cdot PA_{H_2}$
N_2	$1.90845 \cdot 10^{-5} \cdot PA_{N_2}$
CO	$1.95480 \cdot 10^{-5} \cdot PA_{CO}$
CH_4	$2.17747 \cdot 10^{-5} \cdot PA_{CH_4}$
CO_2	$1.59562 \cdot 10^{-5} \cdot PA_{CO_2}$

Table D.3: FID calibration curves

Species	Calibration Curve (Peak Area →Vol%)
C_2H_4	$3.60367 \cdot 10^{-8} \cdot PA_{C_2H_4}$
C_2H_6	$3.27938 \cdot 10^{-8} \cdot PA_{C_2H_6}$
AcHO	$7.09983 \cdot 10^{-7} \cdot PA_{AcHO}$
CH_4	$9.62465 \cdot 10^{-7} \cdot PA_{CH_4}$
EtOH	$5.23201 \cdot 10^{-7} \cdot PA_{EtOH}$
DEE	$2.48509 \cdot 10^{-7} \cdot PA_{DEE}$

Table D.4: Product gas composition exiting the reactor

TCD		FID	
Species	**Volume %**	**Species**	**Volume %**
H_2	19.60	C_2H_4	0.468
N_2	5.59	C_2H_6	0.014
CO	1.12	AcHO	0.290
CH_4	1.79	CH_4	1.86
CO_2	6.34	EtOH	2.91
		DEE	0.046

The remaining volume is assigned to $H_2O = 61.79\ \%$.

The total volumetric flow rate of the product gas exiting the reactor was determined by the use of a trace gas. N_2 was co-feed with the $EtOH$-H_2O feed mixture at a rate of 15 mL min^{-1}. Knowing the concentration of N_2 in the product gas it is possible to evaluate the total volumetric flow rate:

$$F_T = \frac{F_{N_2}}{y_{N_2}} = \frac{15\dfrac{mL}{min}}{0.0559} = 268.4\frac{mL}{min}$$

The total molar flow rate can be determined by application of the Ideal gas law:

$$n_T = \frac{PF_T}{RT} = \frac{1\ atm \cdot 0.2684\ \dfrac{L}{min}}{0.08206\dfrac{L\cdot atm}{mol\cdot K}\cdot (20+273.15)K} = 1.115\cdot 10^{-2}\frac{mol}{min}$$

The $EtOH$-H_2O steam reforming feed has a molar composition of 8.4 moles of H_2O per mole of ethanol (8.4:1). Below details how the volumetric composition of the liquid feed was determined.

Volume of 1 mol of Ethanol

$$1\ mol_{EtOH}\cdot 46\ \frac{g}{mol}\cdot \frac{1}{0.787}\cdot \frac{mL}{g} = 58.45\ mL$$

Volume of 8.4 moles of H_2O

$$8.4\ mol_{H_2O}\cdot 18\ \frac{g}{mol}\cdot \frac{1}{0.997}\frac{mL}{g} = 151.65\ mL$$

Volumetric Composition (% EtOH)

$$EtOH(vol\%) = \frac{58.45\ mL}{(151.65+58.45)\ mL}\cdot 100\% = 27.82\%$$

The liquid feed mixture (8.4:1 molar) was delivered to the reactor at a rate of 0.2 mL min^{-1}. The molar feed flow rate of ethanol and H_2O were determined as follows:

Ethanol molar flow rate

$$n_{EtOH}^{in} = 0.2\frac{mL}{min} \cdot 0.2782\frac{mL}{mL} \cdot 0.787\frac{g}{mL} \cdot \frac{1}{46}\frac{mol}{g} = 9.52 \cdot 10^{-4}\frac{mol}{min}$$

H_2O molar flow rate

$$n_{H_2O}^{in} = 0.2\frac{mL}{min} \cdot 0.7218\frac{mL}{mL} \cdot 0.997\frac{g}{mL} \cdot \frac{1}{18}\frac{mol}{g} = 8.00 \cdot 10^{-3}\frac{mol}{min}$$

N_2 molar flow rate

$$n_{N_2}^{in} = \frac{PF_{N_2}}{RT} = \frac{1\,atm \cdot 15 \cdot 10^{-3}\frac{L}{min}}{0.08206\frac{atm \cdot L}{mol \cdot K} \cdot (20 + 273.15)K} = 6.24 \cdot 10^{-4}\frac{mol}{min}$$

Table D.5: Species molar flow rate exiting the reactor

Species (i)	Molar flow rate, n_i^{out} [mol min^{-1}]
H_2	2.186·10^{-3}
N_2	6.235·10^{-4}
CO	1.250·10^{-4}
CH_4	2.073·10^{-4}
CO_2	7.068·10^{-4}
C_2H_4	5.220·10^{-5}
C_2H_6	1.510·10^{-6}
AcHO	3.234·10^{-5}
EtOH	3.240·10^{-4}
DEE	5.136·10^{-6}
H_2O	6.890·10^{-3}

Catalyst performance evaluation parameters

The performance of the catalyst was evaluated using the parameters defined in Table 3.3: Ethanol steam reforming evaluation parameters.

Ethanol conversion:

$$X_{EtOH} = \frac{n_{EtOH}^{in} - n_{EtOH}^{out}}{n_{EtOH}^{in}} \cdot 100\% = \frac{9.52 \cdot 10^{-4} - 3.240 \cdot 10^{-4}}{9.52 \cdot 10^{-4}} \cdot 100\% = 65.97\%$$

Water conversion:

$$X_{H_2O} = \frac{n_{H_2O}^{in} - n_{H_2O}^{out}}{n_{H_2O}^{in}} \cdot 100\% = \frac{8.00 \cdot 10^{-3} - 6.89 \cdot 10^{-3}}{8.00 \cdot 10^{-3}} \cdot 100\% = 13.88\%$$

Water utilization:

$$\eta_{H_2O} = \frac{n_{H_2O}^{in} \cdot X_{H_2O}}{n_{H_2O}^{in} \cdot X_{EtOH}} = \frac{8.00 \cdot 10^{-3} \frac{mol}{min} \cdot 0.1388}{9.52 \cdot 10^{-4} \frac{mol}{min} \cdot 0.6597} = 1.77 \frac{mol_{H_2O}}{mol_{EtOH}}$$

H_2 yield:

$$Y_{H_2} = \frac{n_{H_2}^{out}}{n_{EtOH}^{in} \cdot X_{EtOH}} = \frac{2.186 \cdot 10^{-3} \frac{mol_{H_2}}{min}}{9.52 \cdot 10^{-4} \frac{mol_{EtOH}}{min} \cdot 0.6597} = 3.48 \frac{mol_{H_2}}{mol_{EtOH}}$$

Table D.6: Product yields

Species (i)	Product Yield, Y_i [mol/mol$_{EtOH}$ converted]
H_2	3.48
CO	0.200
CH_4	0.330
CO_2	1.13
C_2H_4	0.083
C_2H_6	0.002
AcHO	0.051
DEE	0.008

Carbon balance:

$$CBal = \frac{\sum \chi_i n_i^{out}}{2n_{EtOH}^{in}}$$

$$\sum \chi_i n_i^{out} = 1 \cdot n_{CO}^{out} + 1 \cdot n_{CH_4}^{out} + 1 \cdot n_{CO_2}^{out} + 2 \cdot n_{C_2H_4}^{out} + 2 \cdot n_{C_2H_6}^{out} + 2 \cdot n_{AcHO}^{out} + 2 \cdot n_{EtOH}^{out} + 4 \cdot n_{DEE}^{out}$$

$$\sum \chi_i n_i^{out} = 1 \cdot 1.250 \cdot 10^{-4} + 1 \cdot 2.073 \cdot 10^{-4} + 1 \cdot 7.068 \cdot 10^{-4} + 2 \cdot 5.220 \cdot 10^{-5} + 2 \cdot 1.510 \cdot 10^{-5}$$
$$+ 2 \cdot 3.234 \cdot 10^{-5} + 2 \cdot 3.240 \cdot 10^{-4} + 4 \cdot 5.136 \cdot 10^{-6}$$

$$\sum \chi_i n_i^{out} = 1.880 \cdot 10^{-3} \, mol_{Carbon}$$

$$CBal = \frac{\sum \chi_i n_i^{out}}{2n_{EtOH}^{in}} = \frac{1.880 \cdot 10^{-3} \, mol_{Carbon}^{out}}{2 \cdot 9.52 \cdot 10^{-3} \, mol_{Carbon}^{in}} = 98.74\%$$

Appendix E: Propagation of Error Analysis

In this experimental study many calculations were performed to evaluate the performance of the prepared catalysts. In this study the performance of prepared catalysts were evaluated based on ethanol conversion, water utilization, and product yields and to validate the quality and utility of the collected data, a carbon balance was performed.

In experimental work, the compounding or propagation of error can become substantial and in fact may render the experimental findings, statistical anomalies. Since every measurement made in this study, as in all studies, had an associated error or uncertainty and each performance evaluation parameter used a multitude of measurements, the uncertainty in the calculated performance evaluation parameters needed to be evaluated to access the level of uncertainty in the evaluation parameters. In the following sections, the propagation of error throughout the calculation procedure detailed in Appendix D is provided.

The propagation of error, or uncertainty, u( ), in calculated values was determined using the following rules.

1. $u(A + B) = u(A - B) = \sqrt{[u(A)]^2 + [u(B)]^2}$ Summation

2. $u(A \cdot B) = A \cdot B \sqrt{\left[\dfrac{u(A)}{A}\right]^2 + \left[\dfrac{u(B)}{B}\right]^2}$ Multiplication

3. $u\left(\dfrac{A}{B}\right) = \dfrac{A}{B} \sqrt{\left[\dfrac{u(A)}{A}\right]^2 + \left[\dfrac{u(B)}{B}\right]^2}$ Division

4. $u(k \cdot A) = k \cdot u(A)$ Multiplication by Constant

5. $u(A^n) = n \cdot A^{n-1} \cdot u(A)$ Power

where A and B represent measured values and u(A) and u(B) the uncertainty in the measurement.

Sample calculations for the propagation of error are provided for a typical ethanol steam reforming experiment. The specific experiment being detailed was selected from the ethanol steam reforming

temperature programmed reaction experiment. This is the same experiment as detailed in Appendix D.

Experimental conditions:

GHSV: $\sim$260 000 mL$_{Feed}$ h^{-1} gcat^{-1}

Pressure: Atmospheric

H$_2$O:EtOH: 8.4:1 molar feed ratio

Temperature: $\sim$764 K at time of injection (injection 18)

Uncertainty in Ethanol-Water feed mixture composition

Ethanol-water mixtures were prepared to have 27.8 vol% ethanol (8.4 moles of H$_2$O to 1 mole of ethanol). Feed solutions were prepared in 1.00 L. The volume of ethanol and water in the feed mixture are provided in the Table E.1 with the associated uncertainty.

Table E.1: Volume of ethanol and water used to make the feed mixture

Volume	Measurement
Ethanol	278 ± 2.5 mL
Water	722 ± 2.5 mL

The total volume of the solution is:

$$V_T = V_{EtOH} + V_{H_2O}$$
$$V_T = 278 \text{ mL} + 772 \text{ mL} = 1000 \text{ mL}$$

The error associated with the total volume is calculates using "Propagation Rule #1":

$$u(V_T) = u(V_{EtOH} + V_{H_2O})$$

$$u(V_T) = \sqrt{[u(V_{EtOH})]^2 + [u(V_{EtOH})]^2}$$
$$u(V_T) = \sqrt{[2.5 \text{ mL}]^2 + [2.5 \text{ mL}]^2}$$
$$u(V_T) = 3.5 \text{ mL}$$

Therefore the total volume of the solution is: **1000 ± 3.5 mL**

The ethanol composition of the ethanol-water feed mixture can be determined by:

$$v_{EtOH} = \frac{V_{EtOH}}{V_T} = \frac{278 \text{ mL}}{1000 \text{ mL}} = 0.278$$

The ethanol composition of the ethanol-water feed mixture has an uncertainty of:
(use "Propagation Rule #3)

$$u(v_{EtOH}) = u\left(\frac{V_{EtOH}}{V_T}\right) = \frac{V_{EtOH}}{V_T}\sqrt{\left[\frac{u(V_{EtOH})}{V_{EtOH}}\right]^2 + \left[\frac{u(V_T)}{V_T}\right]^2}$$

$$u(v_{EtOH}) = \frac{278 \text{ mL}}{1000 \text{ mL}}\sqrt{\left[\frac{2.5 \text{ mL}}{278 \text{ mL}}\right]^2 + \left[\frac{3.5 \text{ mL}}{1000 \text{ mL}}\right]^2}$$

$$u(V_T) = 0.0027$$

Therefore ethanol composition of the feed solution is: **0.278 ± 0.0027**

Uncertainty in ethanol molar feed flow rate

As detailed in the Appendix D, the ethanol molar flow rate is determined by:

$$n_{EtOH}^{in} = F_{pump} \cdot \frac{\rho_{EtOH}}{MW_{EtOH}} \cdot v_{EtOH}$$

The pump flow rate (F_{pump}) was set at 0.2 mL min^{-1}. The manufacturer (Eldex) reported the reproducibility of the pump to be ± 0.3% of the full scale. The full scale flow rate for the pump is 3.00 mL min^{-1} which represents an uncertainty in the volumetric flow rate of 0.009 mL min^{-1}. The ethanol molar flow rate was determined assuming that the density and molecular weight of ethanol were perfectly known and had no error associated with their values.

$$n_{EtOH}^{in} = 0.2 \frac{\text{mL}}{\text{min}} \cdot \frac{0.787 \frac{\text{g}}{\text{mL}}}{46 \frac{\text{g}}{\text{mol}}} \cdot 0.278 = 9.52 \cdot 10^{-4} \frac{\text{mol}}{\text{min}}$$

The uncertainty associated with the ethanol molar feed flow rate can be determined by:

$$u(n_{EtOH}^{in}) = \frac{\rho_{EtOH}}{MW_{EtOH}} \cdot u(F_{pump} \cdot v_{EtOH})$$

$$u(n_{EtOH}^{in}) = \frac{\rho_{EtOH}}{MW_{EtOH}} F_{pump} \cdot v_{EtOH}\sqrt{\left[\frac{u(F_{pump})}{F_{pump}}\right]^2 + \left[\frac{u(v_{EtOH})}{v_{EtOH}}\right]^2}$$

$$u\left(n_{EtOH}^{in}\right) = \frac{0.787 \frac{g}{mL}}{46 \frac{g}{mol}} 0.2 \frac{mL}{min} \cdot 0.278 \sqrt{\left[\frac{0.009}{0.2}\right]^2 + \left[\frac{0.0027}{0.278}\right]^2}$$

$$u\left(n_{EtOH}^{in}\right) = 4.38 \cdot 10^{-5} \frac{mol}{min}$$

Therefore the ethanol molar feed flow rate was found to be $(9.52 \pm 0.438) \cdot 10^{-4}$ **mol min**$^{-1}$.

Uncertainty in the total product flow rate and GC determined concentrations

The volumetric flow rate of the product gas exiting the reactor (F_T) was determined using an inert tracer technique. N_2, an inert in this reaction system, was mixed with the ethanol-water feed mixture at a set rate of 15 mL min^{-1}. Determination of the volumetric flow rate of the product gas was achieved by measurement of the N_2 concentration in the product gas. The volumetric flow rate of the product gas was calculated by:

$$F_T = \frac{F_{N_2,Feed}}{y_{N_2}}$$

The uncertainty associated with the volumetric flow rate of the product gas was determined by:

$$u\left(F_T\right) = u\left(\frac{F_{N_2}}{y_{N_2}}\right) = \frac{F_{N_2}}{y_{N_2}} \sqrt{\left[\frac{u\left(F_{N_2}\right)}{F_{N_2}}\right]^2 + \left[\frac{u\left(y_{N_2}\right)}{y_{N_2}}\right]^2}$$

However, the uncertainty in the measured values was initially unclear. The discussion below will describe the rationale behind the assigned uncertainty values.

The gas mass flow controller (Unit 1100) was reported by the manufacturer to have an accuracy of ±1% of the full scale. For this specific flow controller, the full scale flow range was 200 mL min^{-1}. Using the reported accuracy as the uncertainty in the flow rate, the set reading would have an error of approximately 27%. That is 15 ± 2 mL min^{-1}, meaning that the flow rate could range between 13 and 17 mL min^{-1}. However, the accuracy of a flow meter does not refer to the uncertainty or reproducibility of the set flow rate, but instead describes the accuracy of the factory set calibration. That is the flow meter has an input of 0-5 VDC corresponding to a flow rate range of 0-200 mL min^{-1}. If the operator desired a flow rate of 100 mL min^{-1}, the required voltage would be 2.5 VDC. Using this relationship, the accuracy of the flow rate would be ±1% of the full scale. In our lab, all flow

controllers are calibrated with their respective gases using a BIOS automated gas flow meter calibration unit and verified with a 100 mL bubble-film calibration unit. Therefore a high degree of confidence in the set flow rate was achieved. Aside from the flow controller accuracy, the manufacturer reported a repeatability of 0.25% of the rate. This value was used as the uncertainty associated with the N_2 flow rate.

In addition to the uncertainty in the N_2 tracer gas flow rate, the uncertainty associated with the determination of the gas composition using a gas chromatographic technique must be addressed. The approach chosen to address this issue was to consider the data collected during calibration of the GC to represent the uncertainty associated with the gas composition. Assuming that the composition of the calibration mixtures were perfectly known, the uncertainty assigned to the concentration of the species would be related directly to the uncertainty of the respective detectors. Analyzing the calibration data, the determination of H_2 on the TCD detector was found have the highest relative deviation in peak area. This is an expected result because TCDs are less sensitive than the FIDs and H_2 has the lowest response factor for TCDs using a helium reference gas. This combination would compound to make H_2 the most susceptible species to error. Analysis of the H_2 calibration data revealed that the largest variation in peak area for a known concentration of H_2 represented an uncertainty of approximately 2.0% of the measured peak area. To simplify the analysis, all species measured on the TCD were assigned the same uncertainty of 2.0% while all species measured on the FID were assigned an uncertainty of 0.5% because the FID detector is much more sensitive than the TCD.

Using a 2.0% uncertainty in peak area for the TCD species and 0.05% uncertainty for FID species the uncertainty in the determined concentrations can be made from the calibration curves. Since all species, except H_2, have linear relationships between peak area and concentration, the error in peak area will translate directly into error in the concentration. That is a 2.0% uncertainty in peak area results in a 2.0% uncertainty in concentration (Rule #4). However, since the relationship between peak area and concentration for H_2 is quadratic,

$$y_{H_2} = 5.99 \cdot 10^{-9} \left[PA(H_2) \right]^2 + 8.79 \cdot 10^{-4} \left[PA(H_2) \right]$$

The propagation of error can be determined by,

$$u(y_{H_2}) = u(k_1 \cdot PA(H_2)^2 + k_2 \cdot PA(H_2))$$
$$u(y_{H_2}) = u(2 \cdot k_1 \cdot PA(H_2) + k_2 \cdot PA(H_2))$$
$$u(y_{H_2}) = \sqrt{[2 \cdot k_1 \cdot PA(H_2)]^2 + [k_2 \cdot PA(H_2)]^2}$$

The volumetric flow rate of the product gas exiting the reactor was found to be (Appendix D):

$$F_T = \frac{F_{N_2}}{y_{N_2}} = \frac{15 \frac{mL}{min}}{0.0559} = 268.38 \frac{mL}{min}$$

The uncertainty in the N_2 volumetric flow rate and N_2 composition in the product gas as described above is:

$$u(F_{N_2}) = 0.0025 \cdot 15 \frac{mL}{min} = 0.0375 \frac{mL}{min} \qquad u(y_{N_2}) = 0.02 \cdot 0.0559 = 0.00112$$

Therefore the uncertainty associated with the volumetric flow rate of the product gas flow rate exiting the reactor is:

$$u(F_T) = u\left(\frac{F_{N_2}}{y_{N_2}}\right) = \frac{F_{N_2}}{y_{N_2}} \sqrt{\left[\frac{u(F_{N_2})}{F_{N_2}}\right]^2 + \left[\frac{u(y_{N_2})}{y_{N_2}}\right]^2}$$

$$u(F_T) = \frac{15 \frac{mL}{min}}{0.0559} \sqrt{\left[\frac{0.0375}{15}\right]^2 + \left[\frac{0.00112}{0.0559}\right]^2} = 5.41 \frac{mL}{min}$$

Therefore the total volumetric flow rate was found to be **268.38 ± 5.41 mL min⁻¹**, which represents about 2% error.

Converting the volumetric flow rate to a molar flow rate was achieved by application of the Ideal gas law. The total molar flow rate of the product gas exiting the reactor was found by:

$$n_T = \frac{PF_T}{RT} = \frac{1\ atm \cdot 0.2684 \frac{L}{min}}{0.08206 \frac{L \cdot atm}{mol \cdot K} \cdot (20 + 273.15)K} = 1.115 \cdot 10^{-2} \frac{mol}{min}$$

It was assumed that the pressure and temperature were very well known. Considering that the GC injector was enclosed in a heated valve box and the temperature was closely controlled and monitored. In addition, since temperature in the Ideal gas law is in K, the variation of a few °C (K)

would result in very little uncertainty in the molar flow rate. Therefore P, R, and T can be considered as constants and therefore the uncertainty in the molar flow rate can be determined by,

$$u\left(\frac{PF_T}{RT}\right) = u\left(\frac{P}{RT} \cdot F_T\right) = \frac{P}{RT} \cdot u(F_T) = 0.04157 \frac{mol}{L} \cdot 0.00541 \frac{L}{min} = 2.25 \cdot 10^{-4} \frac{mol}{min}$$

The total molar flow was **(1.115±0.0225)·10^{-2} mol min^{-1}**.

<u>Uncertainty in the individual molar flow rates</u>

The molar flow rate of each species (i) in the product gas was determined by

$$n_i^{out} = y_i \cdot n_T$$

For example, the H_2 product molar flow rate is calculated by

$$n_{H_2}^{out} = y_{H_2} \cdot n_T = 0.1960 \cdot 1.115 \cdot 10^{-2} \frac{mol}{min} = 2.186 \cdot 10^{-2} \frac{mol}{min}$$

Propagation of error in the product molar flow rates was related to uncertainty in the total molar flow rate exiting the reactor and the composition of the respective species in the product gas. The uncertainty associated with the product molar flow rates is calculated by:

$$u\left(n_{H_2}^{out}\right) = u\left(y_{H_2} \cdot n_T\right) = y_i \cdot n_T \sqrt{\left[\frac{u(y_i)}{y_i}\right]^2 + \left[\frac{u(n_T)}{n_T}\right]^2}$$

$$u\left(n_{H_2}^{out}\right) = 0.1960 \cdot 1.115 \cdot 10^{-2} \frac{mol}{min} \sqrt{\left[\frac{0.00346}{0.1960}\right]^2 + \left[\frac{2.25 \cdot 10^{-4}}{1.115 \cdot 10^{-2}}\right]^2}$$

$$u\left(n_{H_2}^{out}\right) = 5.86 \cdot 10^{-4} \frac{mol}{min}$$

The H_2 molar flow rate exiting the reactor was **(2.186 ± 0.0586)·10^{-3} mol min^{-1}**.

Table E.2 reports the product molar flow rates for each species as reported in Table D.5 in Appendix D with their respective calculated uncertainties.

Table E.2: Species molar flow rate exiting the reactor

Species (i)	Molar flow rate, n_i^{out} [mol min^{-1}]	
H_2	2.186 ± 0.0586	$\cdot 10^{-3}$
N_2	6.235 ± 0.177	$\cdot 10^{-4}$
CO	1.250 ± 0.0355	$\cdot 10^{-4}$
CH_4	2.073 ± 0.0431	$\cdot 10^{-4}$
CO_2	7.068 ± 0.201	$\cdot 10^{-4}$
C_2H_4	5.220 ± 0.108	$\cdot 10^{-5}$
C_2H_6	1.510 ± 0.033	$\cdot 10^{-6}$
$AcHO$	3.234 ± 0.0671	$\cdot 10^{-5}$
$EtOH$	3.240 ± 0.0673	$\cdot 10^{-4}$
DEE	5.136 ± 0.107	$\cdot 10^{-6}$
H_2O	6.890 ± 0.281	$\cdot 10^{-3}$

Uncertainty in the performance evaluation parameters

The performance evaluation parameters were determined using the calculated feed and product molar flow rates. The procedure for calculating the uncertainty in the performance parameters is given below.

Ethanol Conversion

$$X_{EtOH} = \frac{n_{EtOH}^{in} - n_{EtOH}^{out}}{n_{EtOH}^{in}} \cdot 100\% = \frac{9.52 \cdot 10^{-4} - 3.240 \cdot 10^{-4}}{9.52 \cdot 10^{-4}} \cdot 100\% = 65.97\%$$

Uncertainty in ethanol conversion

$$u(X_{EtOH}) = u\left(\frac{n_{EtOH}^{in} - n_{EtOH}^{out}}{n_{EtOH}^{in}} \right) \cdot 100\%$$

$$u(n_{EtOH}^{in} - n_{EtOH}^{out}) = \sqrt{[u(n_{EtOH}^{in})]^2 + [u(n_{EtOH}^{out})]^2} = \sqrt{[4.38 \cdot 10^{-5}]^2 + [6.73 \cdot 10^{-6}]^2}$$

$$u(n_{EtOH}^{in} - n_{EtOH}^{out}) = 4.43 \cdot 10^{-5}$$

$$u\left(\frac{n_{EtOH}^{in} - n_{EtOH}^{out}}{n_{EtOH}^{in}} \right) = \frac{n_{EtOH}^{in} - n_{EtOH}^{out}}{n_{EtOH}^{in}} \sqrt{\left[\frac{u(n_{EtOH}^{in} - n_{EtOH}^{out})}{n_{EtOH}^{in} - n_{EtOH}^{out}} \right]^2 + \left[\frac{u(n_{EtOH}^{in})}{n_{EtOH}^{in}} \right]^2}$$

$$u\left(\frac{n_{EtOH}^{in} - n_{EtOH}^{out}}{n_{EtOH}^{in}} \right) = \frac{6.27 \cdot 10^{-4}}{9.52 \cdot 10^{-4}} \sqrt{\left[\frac{4.43 \cdot 10^{-5}}{6.27 \cdot 10^{-4}} \right]^2 + \left[\frac{4.38 \cdot 10^{-5}}{9.52 \cdot 10^{-4}} \right]^2}$$

$$u(X_{EtOH}) = u\left(\frac{n_{EtOH}^{in} - n_{EtOH}^{out}}{n_{EtOH}^{in}} \right) \cdot 100\% = 0.0556 \cdot 100\% = 5.56\%$$

Ethanol conversion can be reported as: **65.97 ± 5.56%**

Product yield is calculated using the following procedure. For example, the H_2 yield

$$Y_{H_2} = \frac{n_{H_2}^{out}}{n_{EtOH}^{in} - n_{EtOH}^{out}} = \frac{2.186 \cdot 10^{-3}}{6.27 \cdot 10^{-4}} = 3.48 \frac{mol \; H_2}{mol \; of \; EtOH \; converted}$$

The uncertainty in the product yield is determined by.

$$u(Y_{H_2}) = u\left(\frac{n_{H_2}^{out}}{n_{EtOH}^{in} - n_{EtOH}^{out}}\right) = \frac{2.186 \cdot 10^{-3}}{6.27 \cdot 10^{-4}} \sqrt{\left[\frac{5.86 \cdot 10^{-5}}{2.186 \cdot 10^{-3}}\right]^2 + \left[\frac{4.43 \cdot 10^{-5}}{6.27 \cdot 10^{-4}}\right]^2}$$

$$u(Y_{H_2}) = 0.263$$

Therefore the H_2 yield can be reported as: **3.489 ± 0.263** moles H_2 per mole of EtOH converted. The product yields and uncertainties for the experiment detailed in Appendix D are given in Table E.3.

Table E.3: Product yields and uncertainties

Species (i)	Product Yield, Y_i [mol/mol$_{EtOH}$ converted]
H_2	3.48 ± 0.263
CO	0.200 ± 0.0151
CH_4	0.330 ± 0.0241
CO_2	1.13 ± 0.0851
C_2H_4	0.083 ± 0.0061
C_2H_6	0.002 ± 0.00018
AcHO	0.051 ± 0.0038
DEE	0.008 ± 0.0006

Uncertainty in the carbon balance

The carbon balance was determined to validate the quality and utility of the data. In almost all cases the carbon balance exceeded 98% and was below 102% indicating that the analytical system was highly accurate and reproducible. The calculations presented below details how the uncertainty in the carbon balance was evaluated

The carbon balance was defined as the ratio of the molar flow rates of atomic carbon exiting the reactor to the atomic carbon entering the reactor.

$$\text{CBal} = \frac{\sum \chi_i n_i^{out}}{2n_{EtOH}^{in}} = \frac{n_T \sum \chi_i y_i}{2n_{EtOH}^{in}}$$

The uncertainty in the carbon balance can be expressed as

$$u(\text{CBal}) = u\left(\frac{n_T \sum \chi_i y_i}{2n_{EtOH}^{in}}\right)$$

This is a highly complex term wit many sources of uncertainty that contribute to the overall uncertainty in the carbon balance. To simplify, uncertainty will be determined in subsections. Therefore,

$$u\left(\sum \chi_i y_i\right) = \sqrt{\begin{array}{l} 1^2 \cdot u\left(y_{CO}\right)^2 + 1^2 \cdot u\left(y_{CH_4}\right)^2 + 1^2 \cdot u\left(y_{CO_2}\right)^2 + 2^2 \cdot u\left(y_{C_2H_4}\right)^2 + \\ 2^2 \cdot u\left(y_{C_2H_6}\right)^2 + 2^2 \cdot u\left(y_{AcHO}\right)^2 + 2^2 \cdot u\left(y_{EtOH}\right)^2 + 4^2 \cdot u\left(y_{DEE}\right)^2 \end{array}}$$

The uncertainties in the species measured by the thermal conductivity detector are,

$$u\left(y_{CO}\right) = 0.02 \cdot 0.0112 = 2.24 \cdot 10^{-4}$$
$$u\left(y_{CO_2}\right) = 0.02 \cdot 0634 = 1.27 \cdot 10^{-3}$$

The uncertainties in the species measured by the flame ionization detector are,

$$u\left(y_{CH_4}\right) = 0.005 \cdot 0.0186 = 9.3 \cdot 10^{-5}$$
$$u\left(y_{C_2H_4}\right) = 0.005 \cdot 00468 = 2.34 \cdot 10^{-5}$$
$$u\left(y_{C_2H_6}\right) = 0.005 \cdot 00014 = 7.00 \cdot 10^{-7}$$
$$u\left(y_{AcHO}\right) = 0.005 \cdot 0029 = 1.45 \cdot 10^{-5}$$
$$u\left(y_{EtOH}\right) = 0.005 \cdot 0291 = 1.45 \cdot 10^{-4}$$
$$u\left(y_{DEE}\right) = 0.005 \cdot 00046 = 2.3 \cdot 10^{-6}$$

The error associated with the amount of atomic carbon in the product gas is:

$$\sum \chi_i y_i = 0.1686$$

$$u\left(\sum \chi_i y_i\right) = 0.001324$$

The molar flow rate of carbon exiting the reactor in the product gas

$$n_T \sum \chi_i y_i = 1.115 \cdot 10^{-2} \frac{\text{mol}}{\text{min}} \cdot 0.1686 = 1.880 \cdot 10^{-3} \frac{\text{mol}}{\text{min}}$$

$$u(n_T \sum \chi_i y_i) = 1.115 \cdot 10^{-2} \frac{mol}{min} \cdot 0.1686 \sqrt{\left[\frac{0.0225 \cdot 10^{-2}}{1.115 \cdot 10^{-2}}\right]^2 + \left[\frac{0.001324}{0.1686}\right]^2}$$

$$u(n_T \sum \chi_i y_i) = 4.076 \cdot 10^{-5} \frac{mol}{min}$$

The molar flow rate of atomic carbon exiting the reactor can be expressed as:

1.880 ± 0.04076·10⁻³ mol min⁻¹

The uncertainty in the carbon balance is determined by:

Recall: ethanol molar feed flow rate was found to be **(9.52 ± 0.438)·10-4 mol min⁻¹**.

$$u(CBal) = u\left(\frac{n_T \sum \chi_i y_i}{2n_{EtOH}^{in}}\right) = \frac{1.880 \cdot 10^{-3} \frac{mol_{Carbon}^{out}}{min}}{1.904 \cdot 10^{-3} \frac{mol_{Carbon}^{in}}{min}} \sqrt{\left[\frac{4.074 \cdot 10^{-5}}{1.880 \cdot 10^{-3}}\right]^2 + \left[\frac{8.76 \cdot 10^{-5}}{1.904 \cdot 10^{-3}}\right]^2}$$

$$u(CBal) = 0.0506$$

The carbon balance can be expressed as: **98.74 ± 5.06 %**

<u>Uncertainty in the performance parameters for an ethanol steam reforming</u>

To illustrate the uncertainty in the performance evaluation parameters, the results from the 8.4:1 ethanol steam reforming temperature programmed reaction experiment are presented. This experiment was selected as a representative experiment since the ethanol conversion and all product yields spanned their respective ranges. The high degree of accuracy and reproducibility of the fixed-bed reactor and analytical system is exhibited by the results presented in the following figures (E.1 to E.8).
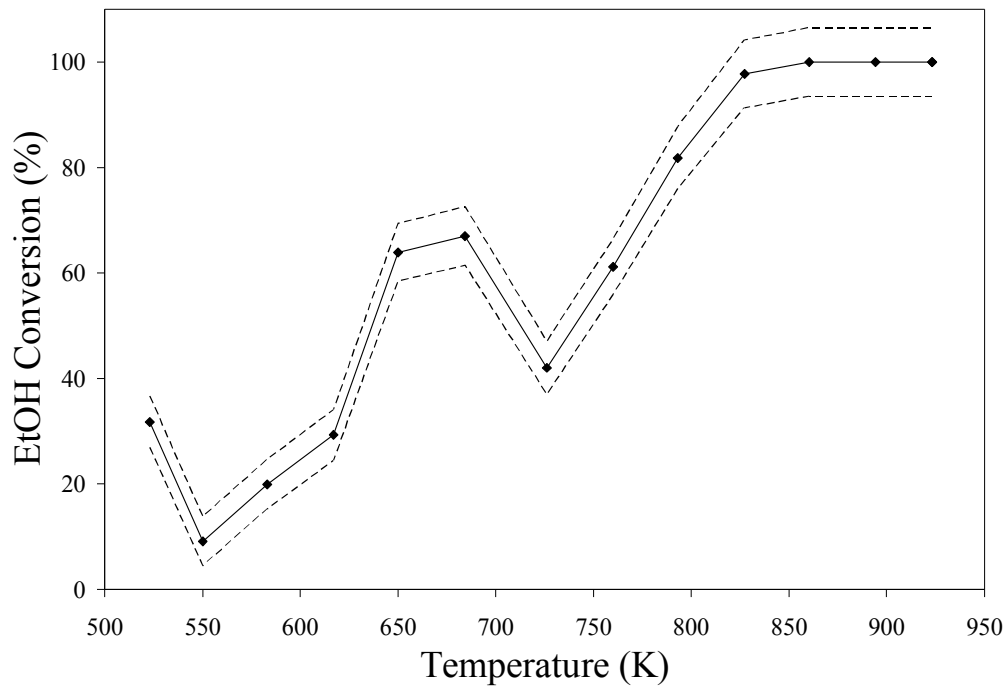
Figure E.1: Ethanol conversion with upper and lower uncertainty bounds.
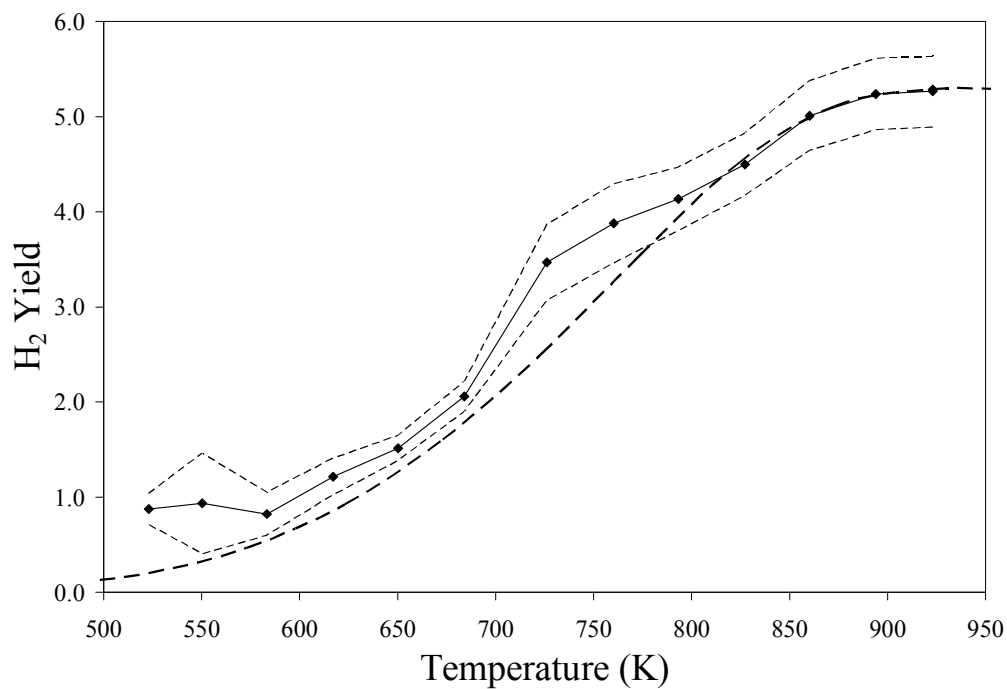

Figure E.2: H$_2$ Yield with upper and lower uncertainty bounds.

234

Figure E.3: CO_2 yield with upper and lower uncertainty bounds.
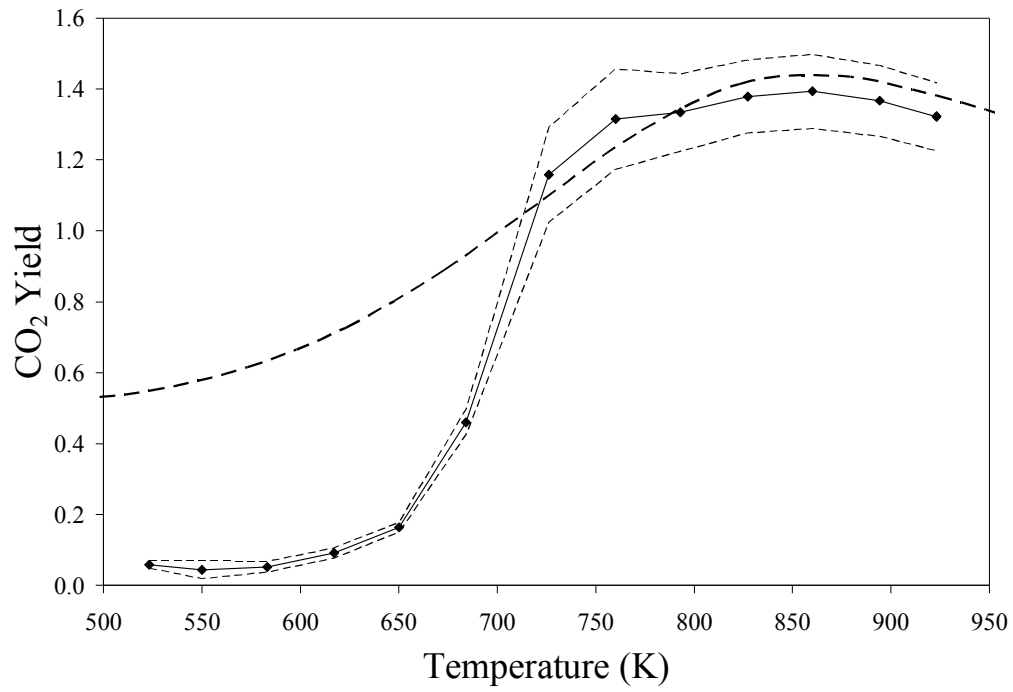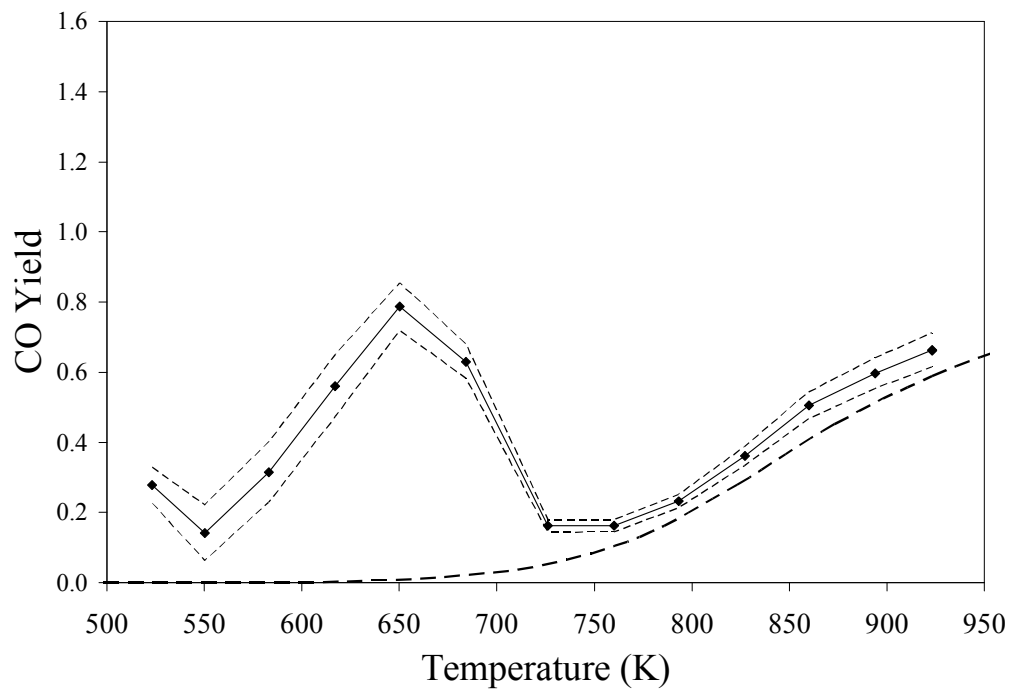

Figure E.4: CO yield with upper and lower uncertainty bounds.

Figure E.5: CH₄ yield with upper and lower uncertainty bounds.
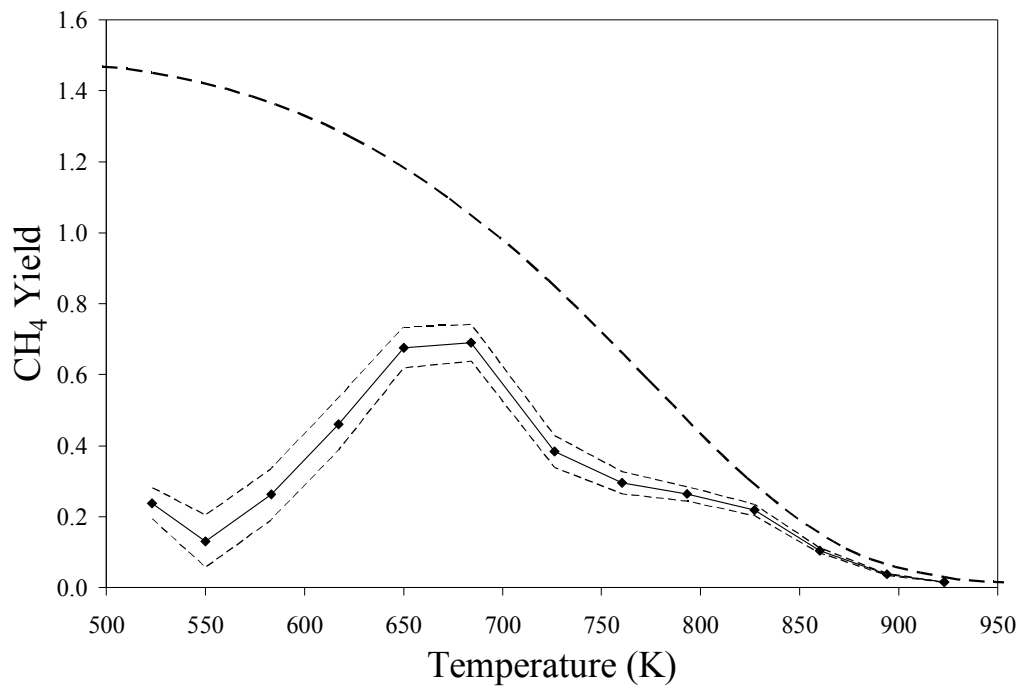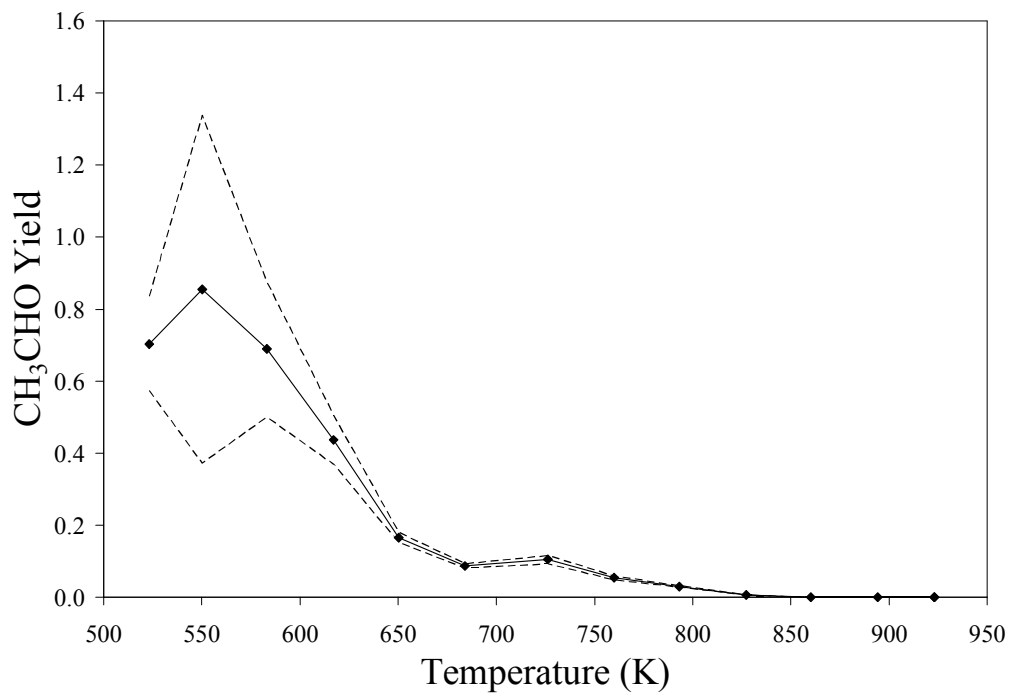

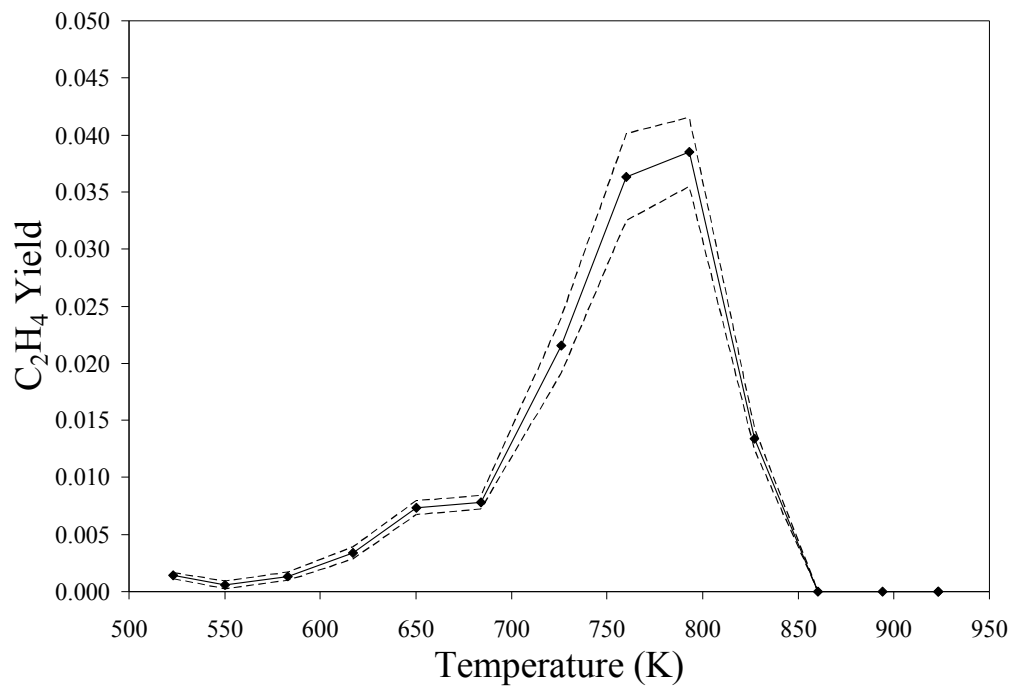**Figure E.6:** Acetaldehyde yield with upper and lower uncertainty bounds.

236

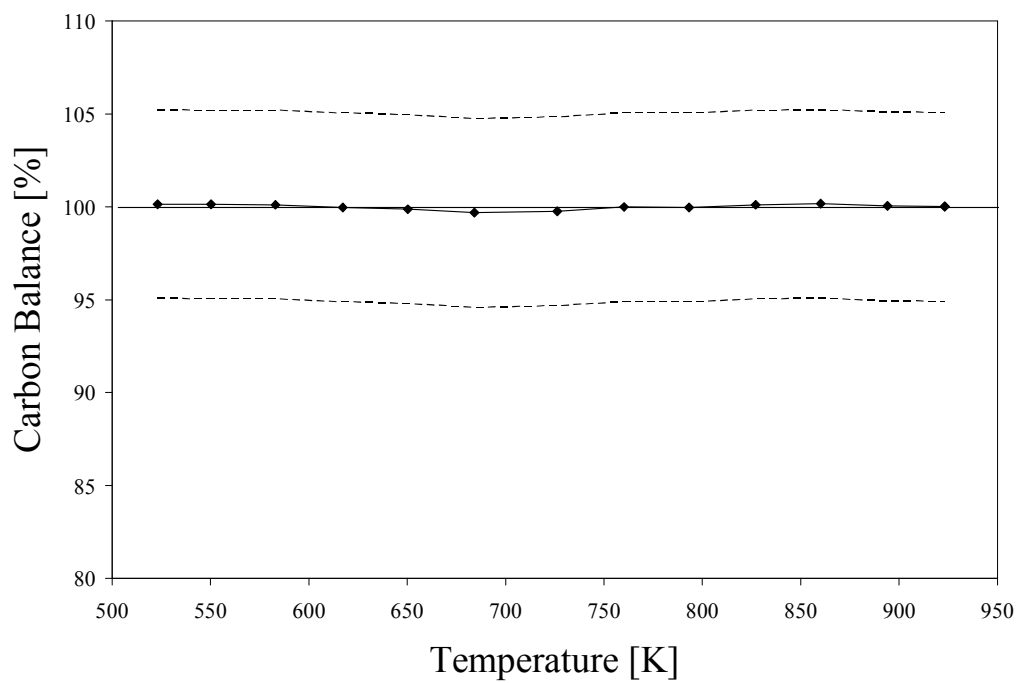**Figure E.7:** C_2H_4 yield with upper and lower uncertainty bounds.

Figure E.8: Carbon balance with upper and lower uncertainty bounds.

237

Appendix F: Reproducibility between repeat experiments and catalyst batches

To ensure that the data produced from any single experiment is truly representative of the mean result, reproducibility experiments must be performed. In this study, reproducibility experiments were performed to understand the variability in the catalyst performance parameters between experiments with:

- Same catalyst batch performed at set reaction conditions, and
- Different catalyst batches having the same composition performed at set reaction conditions

The results from these reproducibility experiments will be given below.

Reproducibility of results obtained for the same catalyst batch

The reproducibility of the catalyst performance parameters was studied at the experimental conditions given below for four experiments for different lengths of time on stream, 16, 8, 4, and 2 h. The results presented in Figures F.1 to F.4 indicate that the variability in the catalyst performance parameters is quite small and show that a high degree of confidence can be placed on the generated data.

Experimental conditions:

GHSV[mL h^{-1} g$_{cat}^{-1}$]:   1062100(16 h) 1055200(8 h) 1069300(4 h) 10652000(2h)

Pressure: Atmospheric

Temperature: 923 K

Feed: 8.4:1 molar

Catalyst: Ni/Mg1Al2

Figure F.1: Reproducibility of the ethanol conversion and carbon balance for the same catalyst batch at set reaction conditions.
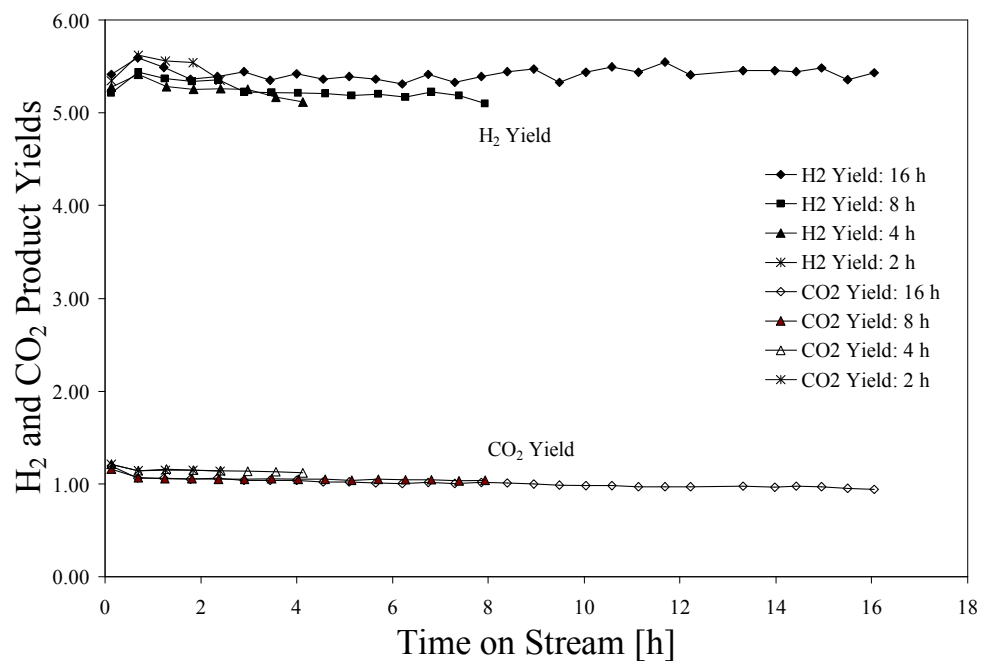
Figure F.2: Reproducibility of the H_2 and CO_2 product yields for the same catalyst batch at set reaction conditions.
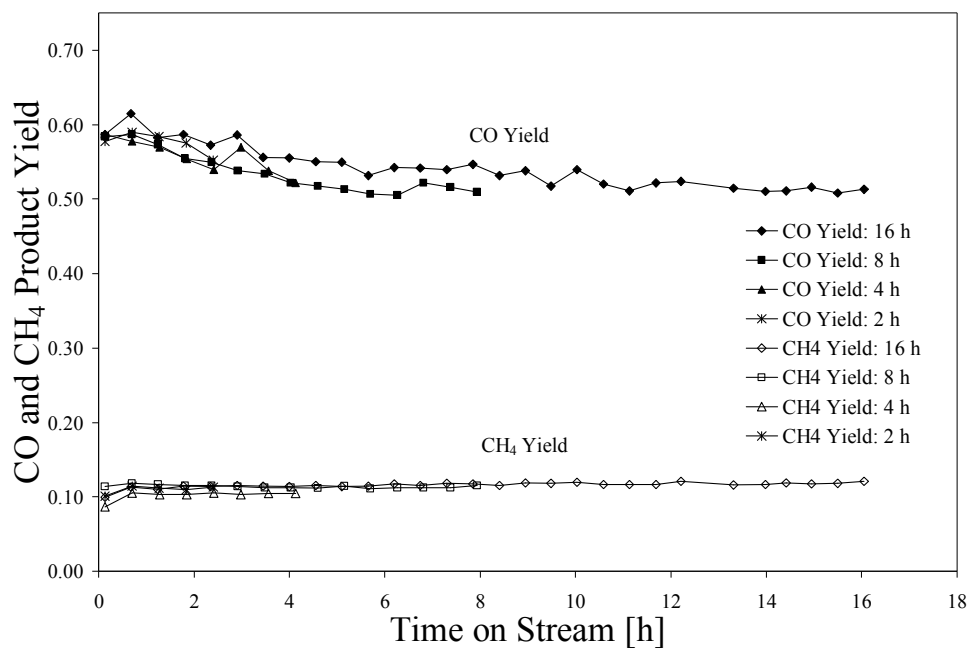
Figure F.3: Reproducibility of the CO and CH_4 product yields for the same catalyst batch at set reaction conditions.

Figure F.4: Reproducibility of the acetaldehyde and ethylene product yields for the same catalyst batch at set reaction conditions.

Reproducibility of results obtained for different catalyst batches with the same composition

In this study two batches of the Ni/Mg1Al2 catalyst were prepared for evaluation. Before using the second batch of catalyst, reproducibility experiments were conducted to validate that the second batch performed the same as the first. This allowed for evaluation of the reproducibility of the catalyst performance parameters between catalyst batches. The performance of the two catalyst batches were compared at the experimental conditions given below.

Experimental conditions:

GHSV[mL h^{-1} g$_{cat}^{-1}$]:   264300 (Batch #1) 268000 (Batch #2)

Pressure: Atmospheric

Temperature: 823 K

Feed: 8.4:1 molar

The results presented in Figures F.5 to F.8 indicate that the reproducibility of the catalyst performance parameters between catalyst batches is quite high as all evaluation parameters were found to closely match.
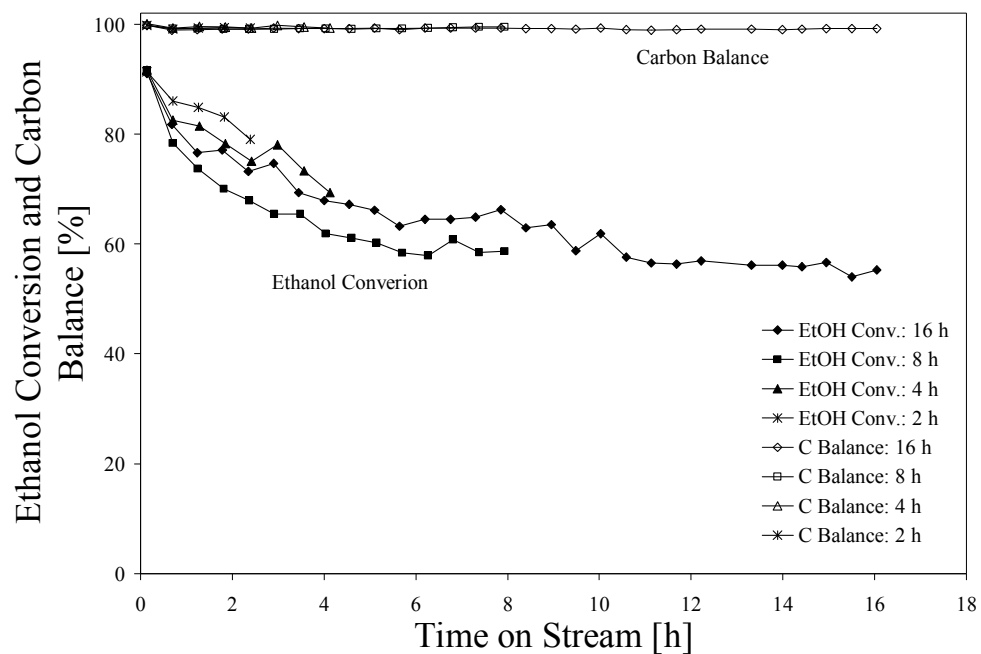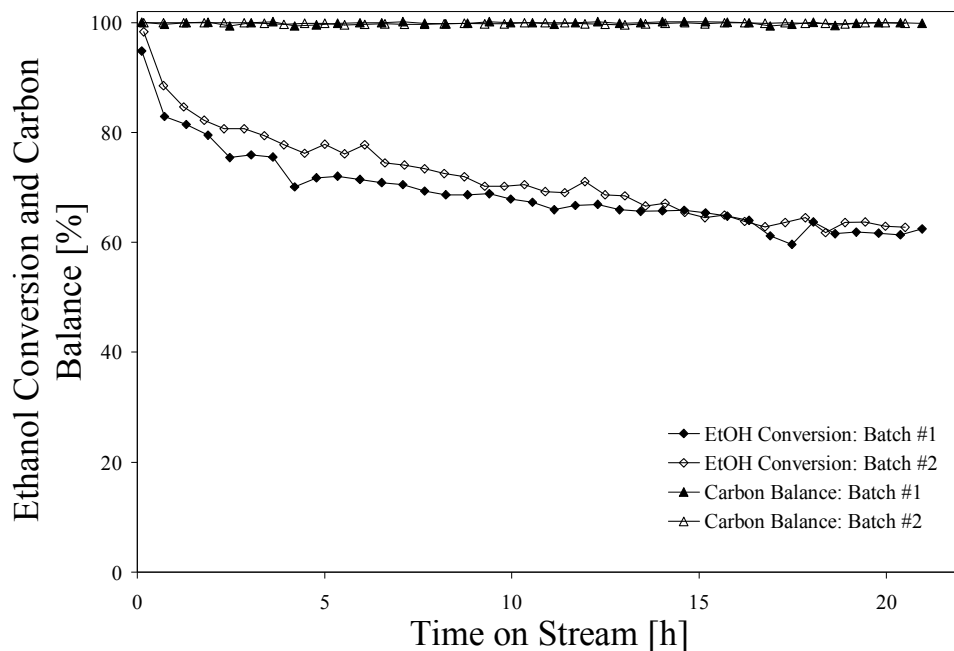

Figure F.5: Reproducibility of the ethanol conversion and carbon balance between catalyst batches at the same reaction conditions.
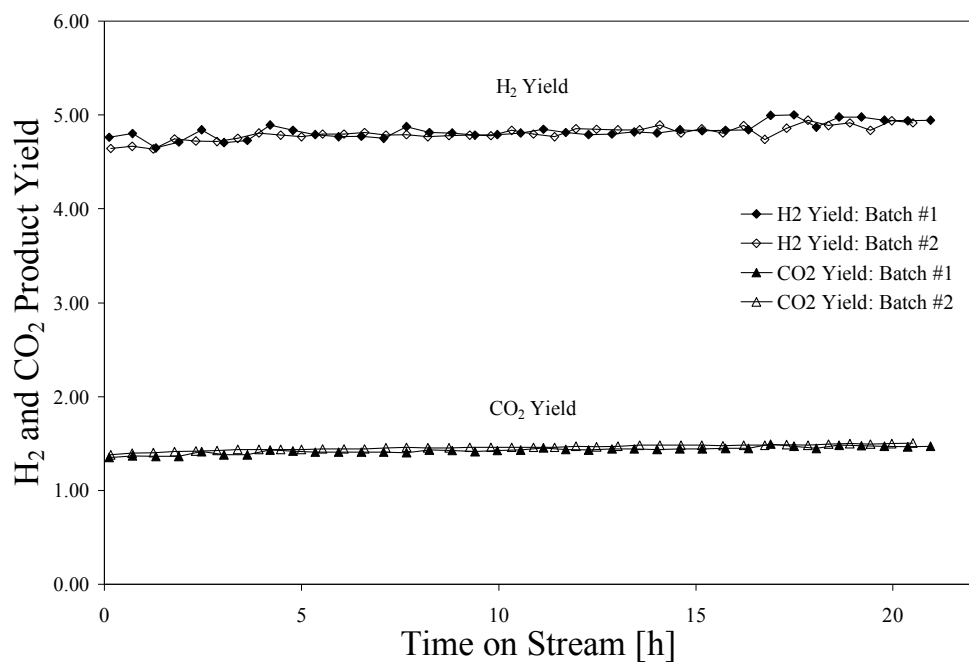
Figure F.6: Reproducibility of the H_2 and CO_2 product yields between catalyst batches at the same reaction conditions.
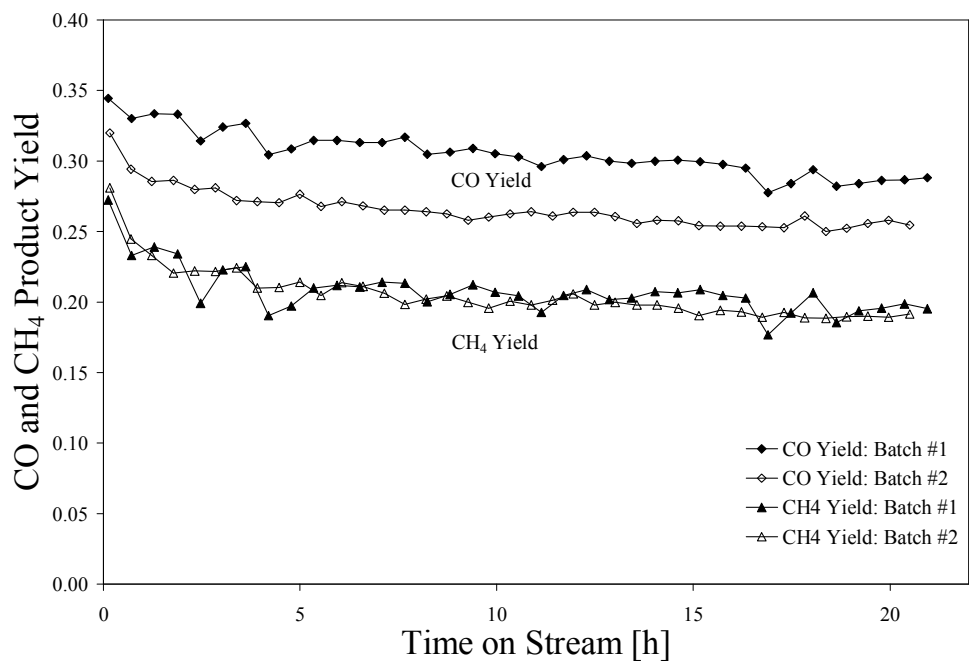
Figure F.7: Reproducibility of the CO and CH_4 product yields between catalyst batches at the same reaction conditions.
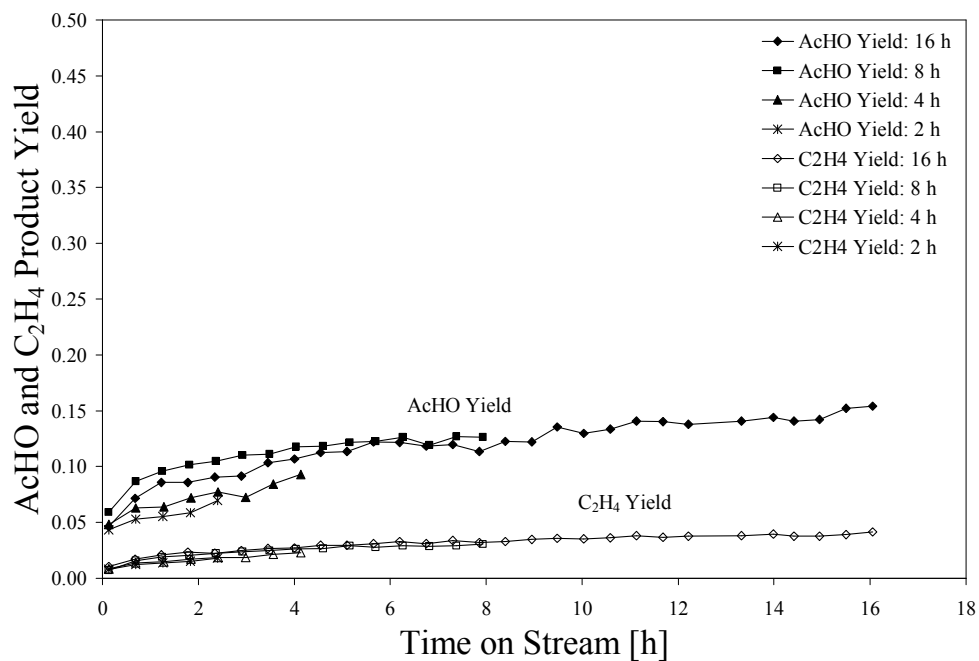
242
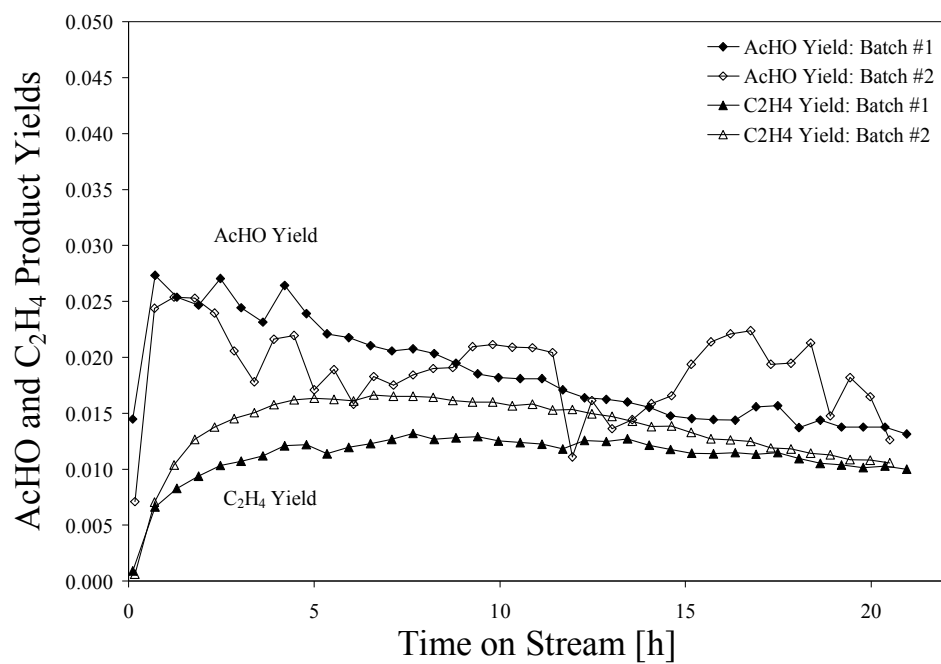
Figure F.8: Reproducibility of the acetaldehyde and ethylene product yields between catalyst batches at the same reaction conditions.

Appendix G: Calculations for the evaluation of transport limitations

---

Nomenclature

A	: cross section area of reactor [m^2]
b	: dilution ratio, volumetric [$m_{dil}^3\ m_{cat}^{-3}$]
C_A^0	: ethanol feed concentration [mol m^{-3}]
$C_{P,i}$	: heat capacity [J $kg^{-1}\ K^{-1}$]
D_{AB}	: binary diffusion coefficient for species A in B [$m^2\ s^{-1}$]
D_e	: effective diffusivity [$m^2\ s^{-1}$]
d_P	: catalyst particle diameter [m]
E_a	: activation energy [J mol^{-1}]
F_A^0	: molar flow rate of A [mol s^{-1}]
$\left(-\Delta H\right)$	: heat of reaction [J mol^{-1}]
h	: gas-solid heat transfer coefficient [J $m^{-2}\ s^{-1}\ K^{-1}$]
j_D	: mass transfer dimensionless group [-]
j_H	: heat transfer dimensionless group [-]
k_C	: gas-solid mass transfer coefficient [m s^{-1}]
k_i	: thermal conductivity [J $m^{-1}\ s^{-1}\ K^{-1}$]
L	: length of catalyst bed [m]
MW	: molecular weight [kg $kmol^{-1}$]
P	: pressure [Pa]
Pe_a	: Peclet number [-]
Pr	: Prandtl number [-]
r_{AB}	: molecular separation at collision [nm]
$\left(-r_A\right)_{obs}$	: observed reaction rate [mol $m_{cat}^{-3}\ s^{-1}$]

$-r_A\left(C_A^0\right)$: reaction rate as a function of the concentration

$-r_A'\left(C_A^0\right)$: 1st derivative of $-r_A\left(C_A^0\right)$

Re   : Reynolds number [-]

r_P : catalyst particle radius [m]

r_R : reactor internal radius [m]

R   : gas constant [J mol^{-1} K^{-1}] or [m^3 Pa mol^{-1} K^{-1}]

Sc   : Schmidt number [-]

Sh   : Sherwood number [-]

T   : temperature [K]

T_B : bulk gas phase temperature [K]

T_S : catalyst surface temperature [K]

u   : superficial velocity [m s^{-1}]

$\dot{V}$: volumetric flow rate [m^3 s^{-1}]

W_{Cat} : catalyst weight [kg]

X   : ethanol conversion [-]

y_i : mole fraction [mol$_i$ mol$_{total}^{-1}$]

ε : catalyst bed porosity [-]

ε_{AB} : energy of molecular attraction

κ : Boltzmann's constant

λ : thermal conductivity of the catalyst particle [J m^{-2} s^{-1} K^{-1}]

μ_i : viscosity [kg m^{-1} s^{-1}]

ρ_C : catalyst bulk density [kg m^{-3}]

ρ_i : density [kg m^{-3}]

Binary diffusion coefficient

Wilke-Lee modification to the Hirshfelder-Bird-Spotz method (Treybal (1980) p.31)

$$D_{AB} = \frac{1e^{-4}\left(1.084 - 0.249\sqrt{\frac{1}{MW_A} + \frac{1}{MW_B}}\right)T^{\frac{3}{2}}\sqrt{\frac{1}{MW_A} + \frac{1}{MW_B}}}{P\ r_{AB}^2\ f\left(\frac{\kappa T}{\varepsilon_{AB}}\right)}$$

$f\left(\dfrac{\kappa T}{\varepsilon_{AB}}\right)$: collision function determined graphically (Treybal, p.32)

$$r_{AB} = \frac{r_A + r_B}{2} = \frac{0.46nm + 0.2641nm}{2} = 0.36205nm$$

$$\frac{\varepsilon_{AB}}{\kappa} = \sqrt{\frac{\varepsilon_A}{\kappa}\frac{\varepsilon_B}{\kappa}} = \sqrt{425K \cdot 809.1K} = 586.40K$$

At 673 K, $f\left(\dfrac{\kappa T}{\varepsilon_{AB}}\right) = 0.7$ (Treybal, p.32)

Diffusivity of Ethanol in Steam at 673 K

$$D_{AB}(673.15\,K) = \frac{1e^{-4}\left(1.084 - 0.249\sqrt{\frac{1}{46} + \frac{1}{18}}\right)673.15^{\frac{3}{2}}\sqrt{\frac{1}{46} + \frac{1}{18}}}{101325 \cdot 0.36205^2 \cdot 0.7}$$

$$D_{AB}(673.15\,K) = 5.30 \cdot 10^{-5}\,m^2 s^{-1}$$

Determination of viscosity

Ethanol

Data taken from Figure 2-32 in Perry and Green (1997).

$$\mu_{EtOH}(673.15\,\text{K}) = 1.90 \cdot 10^{-5} \ \text{kg}\,\text{m}^{-1}\,\text{s}^{-1}$$

Steam

Data taken from Table A.2-12 in Geankopolis (1993).

$$\mu_{H_2O}(673.15\,\text{K}) = 2.42 \cdot 10^{-5} \ \text{kg}\,\text{m}^{-1}\,\text{s}^{-1}$$

Viscosity of the mixture at 673K was determined by

$$\mu_{AB} = \frac{y_{EtOH}\mu_{EtOH}\sqrt{MW_{EtOH}} + y_{H_2O}\mu_{H_2O}\sqrt{MW_{H_2O}}}{y_{EtOH}\sqrt{MW_{EtOH}} + y_{H_2O}\sqrt{MW_{H_2O}}}$$

$$\mu_{AB} = \frac{\left(\dfrac{1}{9.4}\right)\cdot 1.90 \cdot 10^{-5} \cdot \sqrt{46} + \left(\dfrac{1}{9.4}\right)\cdot 2.42 \cdot 10^{-5} \cdot \sqrt{18}}{\left(\dfrac{1}{9.4}\right)\sqrt{46} + \left(\dfrac{1}{9.4}\right)\sqrt{18}}$$

$$\mu_{AB} = 2.34 \cdot 10^{-5} \ \text{kg}\,\text{m}^{-1}\text{s}^{-1}$$

Determination of density

Density of the mixture was determined from the ideal gas law

$$\rho_{AB} = \frac{n}{V}\cdot MW_{AB} = \frac{P}{RT}MW_{AB} = \frac{101325 \ \text{Pa}}{8.314\text{m}^3 \ \text{Pa} \ \text{mol}^{-1} \ \text{K}^{-1} \ 673.15\text{K}} \cdot 20.98\,\text{g}\,\text{mol}^{-1}$$

$$\rho_{EtOH} = 379.8 \ \text{g}\,\text{m}^{-3} = 0.3798 \ \text{kg}\,\text{m}^{-3}$$

Determination of heat capacity

Perry and Green (1997)

$$C_P \left[J\ kmol^{-1} \cdot K^{-1} \right] = C_1 + C_2 \left[\frac{C_3}{T} \bigg/ \sinh\left(\frac{C_3}{T}\right) \right]^2 + C_4 \left[\frac{C_5}{T} \bigg/ \cosh\left(\frac{C_5}{T}\right) \right]^2$$

Species	C_1	C_2	C_3	C_4	C_5
Ethanol	4.92E+04	1.46E+05	1.66E+03	9.39E+04	7.45E+02
Steam	3.34E+04	2.68E+04	2.61E+03	8.90E+03	1.17E+03

Ethanol

$$C_{P,EtOH}\,(673.15\,K) = 4.92 \cdot 10^4 + 1.46 \cdot 10^5 \left[\frac{1.66 \cdot 10^3}{673.15} \bigg/ \sinh\left(\frac{1.66 \cdot 10^3}{673.15}\right) \right]^2$$

$$+ 9.39 \cdot 10^4 \left[\frac{7.45 \cdot 10^2}{673.15} \bigg/ \cosh\left(\frac{7.45 \cdot 10^2}{673.15}\right) \right]^2$$

$$C_{P,EtOH}\,(673.15\,K) = 115.88\ kJ\,kmol^{-1}\,K^{-1}$$

Steam: following the same procedure above

$$C_{P,H_2O}\,(673.15K) = 37.18\ kJ\,kmol^{-1}\,K^{-1}$$

Heat capacity of the feed mixture at 673 K

$$C_{P,AB} = \frac{y_{EtOH} C_{P,EtOH} \sqrt{MW_{EtOH}} + y_{H_2O} C_{P,H_2O} \sqrt{MW_{H_2O}}}{y_{EtOH} \sqrt{MW_{EtOH}} + y_{H_2O} \sqrt{MW_{H_2O}}}$$

$$C_{P,AB} = \frac{\left(\dfrac{1}{9.4}\right) \cdot 115.88 \cdot \sqrt{46} + \left(\dfrac{1}{9.4}\right) \cdot 37.18 \cdot \sqrt{18}}{\left(\dfrac{1}{9.4}\right) \sqrt{46} + \left(\dfrac{1}{9.4}\right) \sqrt{18}}$$

$$C_{P,AB} = 49.77 \ \text{kJ kmol}^{-1} \text{K}^{-1}$$

$$C_{P,AB} = 49.77 \ \text{kJ kmol}^{-1} \text{K}^{-1} \cdot \frac{1}{20.98} \ \text{kmol kg}^{-1} = 2372.26 \ \text{J kg}^{-1} \text{K}^{-1}$$

Determination of thermal conductivity

Ethanol

Taken from Reid and Sherwood (1966).

$$k_{EtOH}(673.15 \, \text{K}) = 0.05169 \ \text{J m}^{-1} \text{s}^{-1} \text{K}^{-1}$$

Steam

Perry and Green (1997)

$$k_{H_2O}(673.15 \, \text{K}) = 0.05264 \ \text{J m}^{-1} \text{s}^{-1} \text{K}^{-1}$$

Thermal conductivity of the feed mixture at 673 K

$$k_{AB} = \frac{\sum_i y_i k_i \sqrt{MW_i}}{\sum_i y_i \sqrt{MW_i}}$$

$$k_{AB} = \frac{y_{EtOH} k_{EtOH} \sqrt{MW_{EtOH}} + y_{H_2O} k_{H_2O} \sqrt{MW_{H_2O}}}{y_{EtOH} \sqrt{MW_{EtOH}} + y_{H_2O} \sqrt{MW_{H_2O}}}$$

$$k_{AB} = \frac{\left(\dfrac{1}{9.4}\right) 0.05169 \sqrt{46} + \left(\dfrac{1}{9.4}\right) 0.05264 \sqrt{18}}{\left(\dfrac{1}{9.4}\right) \sqrt{46} + \left(\dfrac{1}{9.4}\right) \sqrt{18}}$$

$$k_{AB} = 0.05249 \text{ J m}^{-1} \text{s}^{-1} \text{K}^{-1}$$

Determination of the mass transfer coefficient, k_C

$$j_D = 1.66 \, Re^{-0.51} \quad \text{Froment and Bischoff (1980)}$$

$$Re = \frac{\rho d_p u}{\mu}$$

$$u = \frac{\dot{V}}{A}, \quad A = \frac{\pi}{4} d_R^2 = \frac{\pi}{4} (0.01 \text{ m})^2 = 7.854 \cdot 10^{-5} \text{ m}^2$$

$$\dot{V} = \dot{V}_{N_2} + \dot{V}_{Reactants}$$

$$\dot{V}_{Reactants} = \frac{\left(\dfrac{\dot{V}_L \rho_L}{MW_{AB}}\right) RT}{P}$$

$$\dot{V}_{Reactants} = \frac{\left(\dfrac{0.2 \text{ mL min}^{-1} \cdot 0.938 \text{ g mL}^{-1}}{20.98 \text{ g mol}^{-1}}\right) \cdot 8.314 \text{ m}^3 \text{ Pa mol}^{-1} \text{ K}^{-1} \cdot 673.15 \text{ K}}{101325 \text{ Pa}}$$

$$\dot{V}_{Reactants} = 4.939 \cdot 10^{-4} \text{ m}^3 \text{ min}^{-1}$$

$$\dot{V} = \left(1.5 \cdot 10^{-5} \text{ m}^3 \text{ min}^{-1} + 4.939 \cdot 10^{-4} \text{ m}^3 \text{ min}^{-1}\right) \cdot \frac{1}{60} \text{ min s}^{-1} = 8.482 \cdot 10^{-6} \text{ m}^3 \text{ s}^{-1}$$

$$u(673.15 \text{K}) = \frac{8.482 \cdot 10^{-6} \text{ m}^3 \text{ s}^{-1}}{7.845 \cdot 10^{-5} \text{ m}^2} = 1.08 \cdot 10^{-1} \text{ m s}^{-1}$$

$$Sc = \frac{\mu}{\rho D_{AB}} = \frac{2.34 \cdot 10^{-5} \ kg \, m^{-1} \, s^{-1}}{0.3798 \ kg \, m^{-3} \cdot 5.30 \cdot 10^{-5} \, m^2 s^{-1}} = 1.163$$

$$Re = \frac{\rho d_P u}{\mu} = \frac{0.3798 \ kg \, m^{-3} \cdot 4.25 \cdot 10^{-4} \ m \cdot 1.08 \cdot 10^{-1} \ m s^{-1}}{2.34 \cdot 10^{-5} \ kg \, m^{-1} s^{-1}} = 0.745$$

$$j_D = 1.66 \, Re^{-0.51} = 1.66 (0.745)^{-0.51} = 1.93$$

$$k_C = \frac{j_D RT \rho_{AB} u}{y_i \ P \ MW_{AB} \ Sc^{\frac{2}{3}}}$$

$$k_C = \frac{1.93 \cdot 8.314 \ m^3 \, Pa \, mol^{-1} \, K^{-1} \cdot 673.15 \, K \cdot 0.3798 \ kg \, m^{-3} \cdot 0.108 \ m s^{-1}}{\dfrac{1}{9.4} \cdot 101325 \ Pa \cdot 20.98 \ g \, mol^{-1} \cdot \dfrac{1}{1000} \ kg \, g^{-1} \cdot 1.163^{\frac{2}{3}}}$$

$$k_C = 1.77 \ m s^{-1}$$

Check that the minimum Sherwood number of 2 is attained,

$$Sh = \frac{k_C d_P}{D_{AB}} = \frac{1.77 \ m s^{-1} \cdot 4.25 \cdot 10^{-4} \ m}{5.30 \cdot 10^{-5} \ m^2 \, s^{-1}} = 14.20$$

Concentration of ethanol on the feed

$$C_A^0 = \frac{y_{EtOH} P}{RT} = \frac{\dfrac{1}{9.4} \cdot 101325 \ Pa}{8.314 \ m^3 \, Pa \, mol^{-1} \, K^{-1} \cdot 673.15 \, K} = 1.93 \, mol \, m^{-3}$$

Ethanol molar feed flow rate

$$F_A^0 = \dot{V}_{Reac \tan ts} C_A^0 = 4.939 \cdot 10^{-4} \ mol \, min^{-1} \cdot 1.93 \ mol \, m^{-3} \cdot \frac{1}{60} \ min \, s^{-1} = 1.585 \cdot 10^{-5} \ mol \, s^{-1}$$

Observed reaction rate

$$r_A = \frac{F_A^0 X \rho_C}{W_{Cat}} = \frac{1.585 \cdot 10^{-5}\ \text{mol}\,\text{s}^{-1} \cdot \dfrac{7.2}{100} \cdot 1200\ \text{kg}_{Cat}\ \text{m}_{Cat}^{-3}}{5.0 \cdot 10^{-5}\ \text{kg}_{Cat}} = 27.40\ \text{mol}\,\text{m}_{Cat}^{-3}\,\text{s}^{-1}$$

Criterion for external mass transfer limitations, Hudgins (1972)

$$\frac{r_A d_P}{k_C C_A^0} < 0.3$$

$$\frac{r_A d_P}{k_C C_A^0} = \frac{27.40\ \text{mol}\,\text{m}_{Cat}^{-3}\,\text{s}^{-1} \cdot 4.25 \cdot 10^{-4}\ \text{m}}{1.77\ \text{m}\,\text{s}^{-1} \cdot 1.93\ \text{mol}\,\text{m}^{-3}} = 0.003$$

Effective diffusivity can be estimated by [Froment and Bischoff (1980)]

$$D_{e,AB} = \frac{D_{AB}}{10} = \frac{5.30 \cdot 10^{-5}\ \text{m}^2\,\text{s}^{-1}}{10} = 5.30 \cdot 10^{-6}\ \text{m}^2\,\text{s}^{-1}$$

Criterion for internal diffusion limitations, Hudgins (1968)

$$\frac{r_A r_P^2}{D_{e,AB} C_A^0} < 1$$

$$\frac{r_A r_P^2}{D_{e,AB} C_A^0} = \frac{27.40\ \text{mol}\,\text{m}_{Cat}^{-3}\,\text{s}^{-1} \cdot \left(\dfrac{4.25 \cdot 10^{-4}}{2}\ \text{m}\right)^2}{5.30 \cdot 10^{-6}\ \text{m}_2\,\text{s}^{-1} \cdot 1.93\ \text{mol}\,\text{m}^{-3}} = 0.12$$

Heat transfer coefficient, h

$$j_H = j_D = 1.93$$

$$Pr = \frac{C_{P,AB} \mu_{AB}}{k_{AB}} = \frac{2372.26\ \text{J}\,\text{kg}^{-1}\,\text{K}^{-1} \cdot 2.34 \cdot 10^{-5}\ \text{kg}\,\text{m}^{-1}\text{s}^{-1}}{0.05249\ \text{J}\,\text{m}^{-1}\text{s}^{-1}\text{K}^{-1}} = 1.058$$

$$h = \frac{j_H C_{P,AB} u \rho_{AB}}{Sc^{2/3}}$$

$$h = \frac{1.93 \cdot 2372.26 \ \text{J kg}^{-1} \ \text{K}^{-1} \cdot 1.08 \cdot 10^{-1} \ \text{m s}^{-1} \cdot 0.3798 \ \text{kg m}^{-3}}{(1.058)^{2/3}} = 180.87 \ \text{J m}^{-2} \ \text{s}^{-1} \ \text{K}^{-1}$$

Criterion of external heat transfer limitations, Mears (1971)

$$\left| \frac{(-\Delta H)(-r_A)_{obs} d_P E_a}{hRT_B^2} \right| < 0.3$$

$$\left| \frac{(-\Delta H)(-r_A)_{obs} d_P E_a}{hRT_B^2} \right| = \left| \frac{\left(177000 \ \text{J mol}^{-1} \cdot 27.40 \ \text{mol m}_{Cat}^{-3} \ \text{s}^{-1} \cdot 4.25 \cdot 10^{-4} \ \text{m} \cdot 80000 \ \text{J mol}^{-1} \right)}{180.87 \ \text{J m}^{-2} \ \text{s}^{-1} \ \text{K}^{-1} \cdot 8.314 \ \text{m}^3 \ \text{Pa mol}^{-1} \ \text{K}^{-1} \cdot (673.15 \ \text{K})^2} \right|$$

$$\left| \frac{(-\Delta H)(-r_A)_{obs} d_P E_a}{hRT_B^2} \right| = 0.24$$

Effective thermal conductivity can be estimated by [Satterfield (1970)]

$$\lambda = 10 k_{AB} = 10 \cdot 0.05249 \ \text{J m}^{-1} \text{s}^{-1} \text{K}^{-1} = 0.5249 \ \text{J m}^{-1} \text{s}^{-1} \text{K}^{-1}$$

Criterion for internal heat conduction limitations, Mears (1971)

$$\left| \frac{(-\Delta H)(-r_A)_{obs} r_P^2 E_a}{\lambda RT_B^2} \right| < 1$$

$$\left| \frac{(-\Delta H)(-r_A)_{obs} r_P^2 E_a}{\lambda RT_B^2} \right| = \left| \frac{\left(177000 \ \text{J mol}^{-1} \cdot 27.40 \ \text{mol m}_{Cat}^{-3} \ \text{s}^{-1} \cdot \left(\frac{4.25 \cdot 10^{-4}}{2} \ \text{m} \right)^2 \cdot 80000 \ \text{J mol}^{-1} \right)}{0.5249 \ \text{J m}^{-1} \text{s}^{-1} \text{K}^{-1} \cdot 8.314 \ \text{m}^3 \ \text{Pa mol}^{-1} \ \text{K}^{-1} \cdot (673.15 \ \text{K})^2} \right|$$

$$\left| \frac{(-\Delta H)(-r_A)_{obs} r_P^2 E_a}{\lambda RT_B^2} \right| = 0.009$$

Relative contribution of interphase and interparticle transport limitations, Mears (1971)

$$\frac{1-\varepsilon}{1+b}\frac{hd_P}{\lambda}\frac{r_R}{r_P} < 5.3$$

$$\frac{1-\varepsilon}{1+b}\frac{hd_P}{\lambda}\frac{r_R}{r} = \frac{1-0.4}{1+6.23}\frac{180.87\ \mathrm{J\,m^{-2}\,s^{-1}\,K^{-1}} \cdot 4.25 \cdot 10^{-4}\ \mathrm{m}}{0.5249\ \mathrm{J\,m^{-1}s^{-1}K^{-1}}}\frac{0.005\ \mathrm{m}}{\dfrac{4.25 \cdot 10^{-4}}{2}\ \mathrm{m}} = 0.285$$

Criterion for axial dispersion

$$\mathrm{Pe}_a \approx 1 \text{ from Levenspiel (1999) page 311, Figure 13.17}$$

$$\frac{20}{\mathrm{Pe}_a}\frac{d_P}{L}\ln\frac{1}{1-x} < 1$$

$$\frac{20}{\mathrm{Pe}_a}\frac{d_P}{L}\ln\frac{1}{1-x} = \frac{20}{1}\frac{4.25 \cdot 10^{-4}\ \mathrm{m}}{0.01\ \mathrm{m}}\ln\frac{1}{1-0.072} = 0.064$$

254

Appendix H: Ethanol steam reforming over Mg-Al mixed oxide catalysts

Published in:

Conference Proceedings, Hydrogen and Fuel Cells 2007 International Conference and Trade Show

Ethanol Steam Reforming over Mg-Al Mixed-Oxide Catalysts

L.J.I. Coleman*, W. Epling, R.R. Hudgins, P.L. Silveston, and E. Croiset

Department of Chemical Engineering, University of Waterloo, Waterloo, ON N2L 3G1, Canada
* ljicolem@uwaterloo.ca

Abstract

The motivation for this study was to identify a Mg-Al mixed oxide that would support nickel for the production of hydrogen via ethanol steam reforming. A set of eight Mg-Al mixed oxides and two pure oxide catalysts, MgO and Al_2O_3, were prepared by calcination of co-precipitated hydrotalcite-like precursors. XRD revealed that the co-precipitation resulted in intimate contact of Mg and Al in the form of Mg-Al layered double oxides (LDO) and $MgAl_2O_4$. The pure oxides, MgO and Al_2O_3, were never simultaneously detected in the samples suggesting that Mg and Al are chemically coupled in the mixed oxide catalysts and not merely mechanical mixtures. The effect of the Mg and Al content on the conversion of ethanol and product selectivity in the presence of steam at 773 and 923 K was evaluated. All catalysts performed poorly for the ethanol steam reforming reaction (listed as reaction 3 below) giving low production rates for H_2, CO, and CO_2. Catalysts having the $MgAl_2O_4$ spinel crystal structure gave the best performance at both reaction temperatures. Carbon deposits were found on all catalysts for reactions performed at 923 K. The Mg-Al catalyst with a Mg:Al ratio of 1:2, having a $MgAl_2O_4$ spinel crystal structure, had the least amount of carbon deposited on the catalyst surface.

Introduction

The production of hydrogen or syngas from renewable, biologically derived feedstocks, such as ethanol, can lessen the demand for, and reliance upon non-renewable fuels and reduce greenhouse gas emissions. A prime candidate is biologically derived ethanol since it is produced by the fermentation of a wide variety of carbohydrate sources that can be obtained from dedicated agricultural products or agricultural and forestry by-products. Ethanol has a high hydrogen content (H/C = 3) and is partially

oxidized making it a good hydrogen source. Conversion of ethanol to hydrogen can be achieved by reacting it with water via steam reforming.

$$CH_3CH_2OH + H_2O \rightarrow 4H_2 + 2CO \qquad (1)$$

$$CO + H_2O \rightarrow H_2 + CO_2 \qquad (2)$$

$$CH_3CH_2OH + (1+x)H_2O \rightarrow (4+x)H_2 + (2-x)CO + xCO_2 \qquad (3)$$
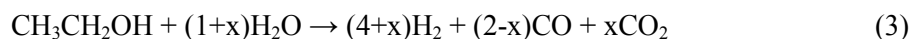
Ethanol steam reforming (3) is a combination of reactions (1) and (2) and takes into account the contribution of the equilibrium limited water-gas shift reaction. The value of x in reaction (3) is dependent upon temperature and water concentration in the feed and describes the extent of the water-gas shift reaction. Ethanol steam reforming produces a product gas having a high hydrogen content but the reaction is highly endothermic. The thermodynamic expectations of the effect of temperature on the dry product gas composition for the ethanol steam reforming chemical system are shown in Figure 1. Thermodynamics predict a mixture of H_2, CO_2, CO, and CH_4 below 950 K at which point the ethanol steam reforming reaction (3) adequately describes the system. In a real system, the reaction pathway is much more complex than proposed by reaction (3). In addition to H_2, CO_2, CO, and CH_4 in the product gas stream, C_2 species such as acetaldehyde and ethylene are commonly found as well as deposited carbon on catalytic surfaces.
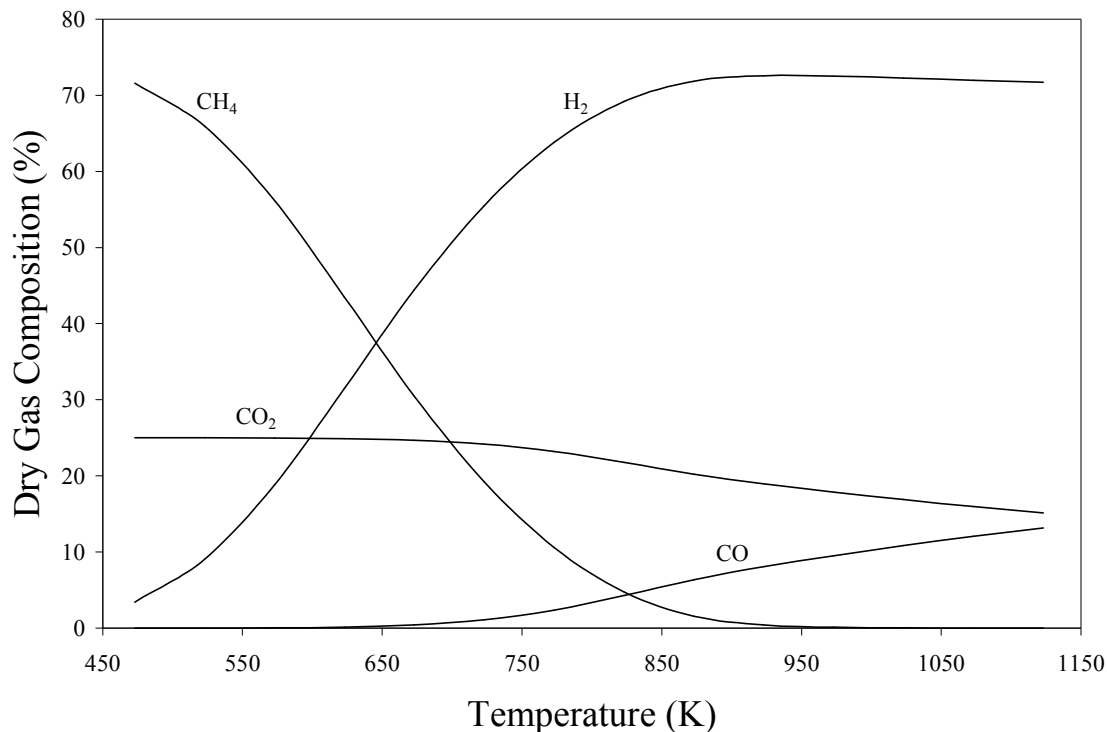
Figure 1: Thermodynamic equilibrium predicted effect of temperature on the dry product gas composition for ethanol steam reforming. H_2O:EtOH = 8.4:1. Equilibrium values obtained using the Gibbs' equilibrium reactor utility in Aspen Plus™ 12.1.

Steam reforming of ethanol has been investigated over a wide variety of supported metal catalysts and several reviews on the subject have recently been published [1,2]. Support nickel catalysts are the most commonly studied catalyst because they are good steam reforming catalysts and are relatively inexpensive compared to noble metal catalysts. Supported nickel catalysts have shown good activity and high product selectivity (H_2 and CO_x) from ethanol under steam reforming conditions, but have been found to deactivate by coking, sintering, and phase transformations [3]. The support properties have been found to contribute to the activity, selectivity, and stability of the supported nickel catalysts [4]. Nickel supported on γ-Al_2O_3 rapidly cokes and deactivates because γ-Al_2O_3 is active for the acid-site catalyzed ethanol dehydration reaction producing ethylene, a known coking precursor [4,5,6]. To minimize ethylene production and potentially coking, basic supports have been investigated. Ni supported on MgO has shown good activity for the ethanol steam reforming, however, coking still occurred but at a much-reduced rate compared to γ-Al_2O_3 supported catalysts [4]. In addition,

Ni/MgO catalysts were found to deactivated by nickel crystallite sintering [6,7]. In addition, MgO can rehydrate to the parent hydroxide, $Mg(OH)_2$ at temperatures below 673 K resulting in a loss of surface area [8] and significant shrinkage of the pore diameter [9].

Mg-Al mixed oxides derived from hydrotalcite–like precursors have been found to have high surface area and exhibit moderate acidic and basic properties compared to the pure oxides, MgO and γ-Al_2O_3, [10-13]. They also demonstrate improved stability in the presence of steam compared to MgO [8]. This study reports on the activity and product selectivity of Mg-Al mixed oxides under ethanol steam reforming reaction conditions to identify a better support for nickel catalysts.

Experimental

Catalyst preparation

Mg-Al mixed oxide precursors were prepared by co-precipitation of an aqueous solution of $Mg(NO_3)_2 \cdot 6H_2O$ (ACS, Sigma-Aldrich) and $Al(NO_3)_3 \cdot 9H_2O$ (ACS, Sigma- Aldrich) at 298 K and a constant pH of 10. 750 mL of the Mg-Al nitrate solution having a total metal ion concentration of 1.00 M was added drop-wise into 750 mL of 0.5 M Na_2CO_3 over a period of 2 h with vigorous stirring. The pH was maintained at 10.0 ± 0.1 by the addition of 3.0 M NaOH. The resulting precipitate was aged at 338 K for 12 h. The precipitant was filtered and washed in 2 L hot distilled deionized water and this process was repeated 4 times to remove residual Na^+ then dried at 373 K for 24 hours. The Mg-Al mixed oxide precursors were crushed into 35-80 mesh particles and calcined at 1123 K in air for 5 h to irreversibly decompose the precursor and give a mixed oxide. γ-Al_2O_3 and MgO were prepared following the same procedure. Some properties of the Mg-Al mixed oxide catalysts are presented in Table 1.

Catalyst characterization

The Mg and Al composition of the mixed oxide catalysts were determined by inductively coupled plasma atomic emission spectroscopy (ICP-AES). The catalyst samples were digested using a standard nitric acid digestion technique. The specific surface area was measured using a 5-point BET method on a Micromeritics Gemini 3 2375. Samples were outgassed at 573 K for 1 h in N_2 prior to measurement. Powder X-ray diffraction (XRD) patterns were measured on a Bruker AXS D8 Advance using standard Bragg-Brentano geometry with Ni-filtered Cu Ka radiation (λ_1=1.5406 Å,

λ_2=1.5444 Å). The spectra were collected for a 2θ range of 15 to 70° using a step size of 0.05° and a count time of 1 s.

Catalyst evaluation

Catalyst evaluation reactions were performed at 773 and 923 K at atmospheric pressure in a fixed-bed quartz tube reactor. The feed mixture having a H_2O:EtOH molar ratio of 8.4:1 was fed by a liquid pump (Eldex) at a rate of 0.2 mL min^{-1} to the vaporizer which was maintained at 435 K. N_2 was mixed with the vaporized reactant feed at a set rate of 15 mL min^{-1} as an internal standard to aid in analysis of the product stream and determination of the total product flow rate. The feed mixture passed through the preheater section that was maintained at 473 K to prevent condensation. The reactor was constructed from a quartz tube having an inner diameter of 10 mm containing a highly porous quartz frit upon which 500 mg (35-80 mesh) of catalyst was loaded. The temperature of the catalyst bed was measured and controlled by a quartz sheathed micro thermocouple located in the middle of the catalyst bed. The product stream exiting the reactor passed through a series of post-heater sections maintained at 473 K to ensure the product remained gaseous. A Varian CP3800 GC was used for composition analysis. The composition of the product stream was determined in its entirety using a single GC, multi-column, multi-detector approach described in [14].

Catalytic performance was evaluated using the following parameters:

Ethanol Conversion:

$$X_{EtOH} = \frac{n_{EtOH}^{in} - n_{EtOH}^{out}}{n_{EtOH}^{in}} \cdot 100$$

where n_{EtOH}^{in} and n_{EtOH}^{out} are the molar flow rates of ethanol into and out of the reactor, respectively.

Rate of ethanol consumption:

$$-r_{EtOH} \left[\frac{mol}{min \cdot m^2} \right] = \frac{n_{EtOH}^{in} - n_{EtOH}^{out}}{SSA \cdot W}$$

where SAA is the specific area [m^2 g^{-1}] and W is the mass of catalyst [g].

Rate of formation of species i:

$$r_i \left[\frac{\text{mol}}{\text{min} \cdot \text{m}^2} \right] = \frac{n_i^{\text{out}}}{\text{SSA} \cdot \text{W}}$$

where n_i^{out} the molar flow rate of species i exiting the reactor.

Product yield:

$$Y_i = \frac{n_i^{\text{out}}}{n_{\text{EtOH}}^{\text{in}} X_{\text{EtOH}}}$$

is defined as the ratio of the moles of species i produced to the amount of ethanol converted.

Carbonaceous species selectivity:

$$S_i = \frac{\chi_i n_i^{\text{out}}}{\sum \chi_i n_i^{\text{out}}} \cdot 100$$

where selectivity is relative to the carbonaceous product species only, excluding ethanol, and χ_i represents the number of carbons comprising species i.

Results and Discussion

Characterization of the physical properties

A total of ten catalyst precursors were prepared by a constant pH technique, eight Mg-Al mixed oxides and two pure oxides, MgO and Al_2O_3. The chemical composition, BET surface area, and observed crystalline phases for the calcined catalysts are reported in Table 1. Compositional analysis reveals good agreement between the desired and measured Al/(Al+Mg) atomic ratios for all catalysts confirming that the precipitation conditions (T = 298 K and pH = 10) were adequate to ensure complete precipitation of the Mg-Al salt solutions. The surface area of the precipitated catalyst precursors span a wide range (15-340 $m^2 g^{-1}$) and generally increase with increasing Al content. Calcination of the precursor resulted in a significant reduction in surface area for the catalysts having an Al/(Al+Mg) atomic ratio greater than 0.66. The extent of surface area loss upon calcination increases with increasing Al content. For the remaining catalysts, calcination increased the surface area. The extent of improvement increased with decreasing Al content. The result of calcination was a series of high surface area catalysts and the trend in surface area had no dependence upon composition.

261

Table 1: Composition, surface area, and observed crystalline phases for the Mg-Al mixed oxide calcined catalysts.

Catalyst	Al/(Al+Mg)[*]		Surface Area ($m^2 \ g^{-1}$)		Crystalline Phases
	Desired	Measured	Precursor	Calcined	
Mg1Al0 (MgO)	0.00	0.00	43.59	101.05	MgO
Mg9Al1	0.10	0.12	15.12	25.98	MgO, Mg-Al LDO
Mg4Al1	0.20	0.24	78.51	168.31	MgO, Mg-Al LDO
Mg3Al1	0.25	0.28	83.88	166.53	MgO, Mg-Al LDO
Mg2Al1	0.33	0.35	97.56	178.77	MgO, Mg-Al LDO, $MgAl_2O_4$
Mg1Al1	0.5	0.51	136.37	141.64	MgO, Mg-Al LDO, $MgAl_2O_4$
Mg1Al2	0.66	0.68	110.00	96.35	Mg-Al LDO, $MgAl_2O_4$
Mg1Al3	0.75	0.77	148.79	128.05	Al_2O_3 – with Mg incorporation
Mg1Al9	0.90	0.91	275.51	173.06	Al_2O_3 – with Mg incorporation
Mg0Al1 (Al_2O_3)	1.00	1.00	341.74	176.30	Al_2O_3

[*] Atomic ratio determined by ICP.

The X-ray diffraction patterns for the catalysts are shown in Figure 1 and the detected crystalline phases are given in Table 1. Four crystalline species were detected: MgO periclase, $MgAl_2O_4$ spinel, quasi-amorphous γ-Al_2O_3 defect spinel, and Mg-Al layered double oxide (LDO). The pure oxide catalysts exhibit only a single pure crystalline phase with their peak locations matching well with expected values. The pure oxides, MgO and Al_2O_3, were not simultaneously detected in the samples suggesting that Mg and Al are chemically coupled in the mixed oxide catalysts and not merely mechanical mixtures. Chemically coupled Mg and Al exist in two forms, Mg-Al LDO and $MgAl_2O_4$. The Mg-Al LDO phase was detected in the catalysts having an Al/(Al+Mg) atomic ratio spanning 0.12 to 0.66 while the $MgAl_2O_4$ spinel phase was present for Al/(Al+Mg) = 0.35. An incomplete $MgAl_2O_4$ spinel phase was present in the catalysts having an Al/(Al+Mg) > 0.66. Incorporation of Mg^{2+} into the Al_2O_3 defect spinel structure is observed. Increasing the Mg content of the catalysts from Al/(Al+Mg) = 1.0 to 0.66 led to a shift in the defect Al_2O_3 spinel peaks to lower than expected 2θ angles. This is caused by Mg incorporation into the defect spinel structure which increases the lattice parameters since the ionic radius of Mg^{2+} is greater than Al^{3+}, thereby resulting in a lowering of the Bragg angle. The interplanar lattice parameter increased from 7.911 Å (Mg0Al1) [7.981 Å (Mg1Al9), 8.046 Å (Mg1Al3)] to 8.070 Å (Mg1Al2) with increasing Mg content. Increasing the Mg

content (or decreasing Al content) increased crystallite size in the $MgAl_2O_4$ and MgO as seen by a narrowing of the peaks.
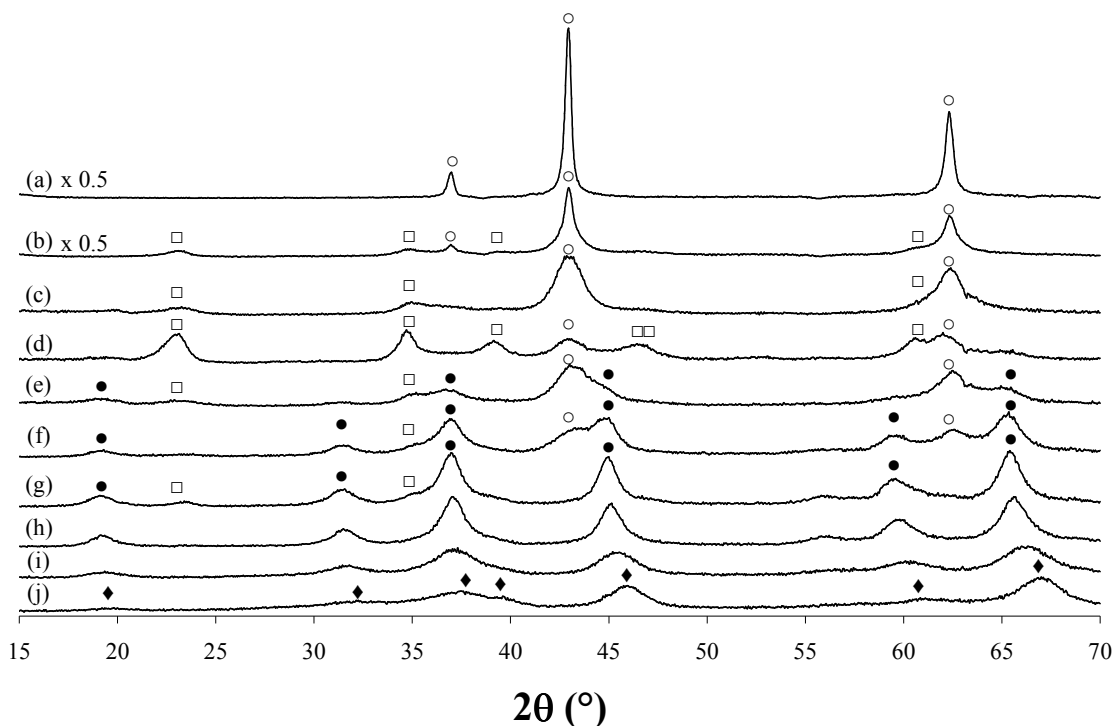
Figure 2: XRD patterns for the Mg-Al mixed oxide catalysts. (a) Mg1Al0 (MgO); (b) Mg9Al1; (c) Mg4Al1; (d) Mg3Al1; (e) Mg2Al1; (f) Mg1Al1; (g) Mg1Al2; (h) Mg1Al3; (i) Mg1Al9; (j) Mg0Al1 (Al_2O_3). (♦) Al_2O_3 defect spinel, (●) $MgAl_2O_4$ spinel, (□) Mg-Al Layered Double Oxide (LDO), (○) MgO periclase.

Catalyst evaluation

The Mg-Al mixed oxide and pure MgO and Al_2O_3 catalysts were evaluated at 773 K for activity and product selectivity in the presence of ethanol and water (H_2O:EtOH = 8.4:1). The rate of ethanol consumption and product formation are reported in Table 2. The rates presented in Table 2 are average rates and these were used because the catalysts showed no signs of deactivation (loss or change in rate) during the 8 h experiment. Rates were normalized to the specific area of the catalyst assuming that the catalysts had the same site density (sites m^{-2}) which therefore allows for evaluation of the activity and selectivity of the catalytic sites. Under steam reforming conditions at 773 K ethanol was converted to acetaldehyde (4), ethylene (5), diethyl ether (6), CO, CH_4, CO_2, and H_2.

Hydrogenation

$$CH_3CH_2OH \rightarrow CH_3CHO + H_2 \qquad\qquad (4)$$

Dehydration

$$CH_3CH_2OH \rightarrow CH_2CH_2 + H_2O \qquad\qquad (5)$$

Coupling and Dehydration

$$2CH_3CH_2OH \rightarrow CH_3CH_2OCH_2CH_3 + H_2O \qquad\qquad (6)$$

The reaction pathways for the production of H_2, CO, CH_4, and CO_2 are numerous and complex. For example, ethanol, acetaldehyde, ethylene, and diethyl ether can decompose and/or be steam reformed to produce mixtures of H_2, CO, CH_4, and CO_2 making it difficult to deconvolute their origin.

All catalysts performed poorly for the ethanol steam reforming reaction (3) giving low production rates for H_2, CO, and CO_2. The rate of ethanol consumption and product selectivity, however, were affected by the catalyst composition. MgO (Mg1Al0) was active for the production of acetaldehyde and ethylene giving the highest rate of production for acetaldehyde of the catalysts studied. Acetaldehyde formation via reaction (4) is catalyzed by a Lewis acid - strong Lewis base site pairing which are commonly found on alkaline earth oxides such as MgO. This acid-base site arrangement can also dehydrate ethanol to ethylene via reaction (5) but at a slower rate than reaction (4) [10]. The rates of formation for acetaldehyde and ethylene on MgO confirm this. Al_2O_3 (Mg0Al1) was the second least activity catalyst, however, it gave the second highest rate of ethylene formation making it the most selective catalyst for ethylene. The increased rate of ethylene formation on Al_2O_3 compared to MgO, especially considering the reduction in the rate of ethanol consumption, indicates that ethanol dehydration is catalyzed by a different site type than found on the MgO catalyst. In addition to the acid-base site arrangement mentioned above, ethylene can be formed on more acidic surfaces having strong Lewis acid - weak Lewis base site pairings following an E_2 elimination mechanism [10].

For Mg-Al mixed oxides, the rate of ethanol consumption passed through a maximum centered at Mg1Al2 [Al/(Al+Mg) = 0.67]. The Mg and Al content of the mixed oxide catalysts also affected the dominant reaction pathway. Acetaldehyde formation generally decreased with increasing Al content

264

while diethyl ether and C_2H_4 formation passed through maxima located at Mg1Al3 [Al/(Al+Mg) = 0.75] and Mg1Al2 [Al/(Al+Mg) = 0.67] respectively. The Mg1Al2 catalyst also gave the highest rates of production for H_2, CO, CH_4, and CO_2. The activity and dominant reaction pathway were affected by the composition of the catalyst with Mg2Al1, Mg1Al1, and Mg1Al2 being the most active in terms of ethanol conversion and H_2 and CO_2 productivity. The common property that these catalysts shared was a fully formed $MgAl_2O_4$ spinel crystal structure. To ensure the crystal structure and the resulting chemical properties were responsible for the improvement in performance, an equimolar mechanical mixture of the pure oxides was evaluated. The equimolar mechanical mixture was prepared to have a chemical composition of $MgO-Al_2O_3$, which is similar to $MgAl_2O_4$. The mechanical mixture denoted Mg0Al1:Mg1Al0 in Table 2 did not perform like the co-precipitated catalyst having the same chemical composition (Mg1Al2).

Table 2: Catalytic performance of Mg-Al mixed oxide catalyst under ethanol steam reforming conditions at 773 K.

Catalyst	Rate of EtOH consumption (μmol h^{-1} m^{-2})	Rate of production (μmol h^{-1} m^{-2})						
		H_2	CO	CH_4	CO_2	C_2H_4	AcHO	DEE
Mg1Al0 (MgO)	277.99	263.9	0.12	10.93	15.6	57.3	188.7	2.65
Mg9Al1	269.18	247.9	0.00	5.82	12.9	61.6	182.8	5.39
Mg4Al1	184.37	154.4	0.15	6.30	12.4	48.5	106.4	5.46
Mg3Al1	220.11	212.0	1.10	12.48	32.4	34.6	120.7	10.4
Mg2Al1	198.66	201.8	1.72	8.15	41.3	43.5	77.2	19.1
Mg1Al1	274.44	474.7	2.91	15.50	111.3	60.2	55.1	39.4
Mg1Al2	619.54	1129.2	14.1	24.77	298.3	57.1	22.6	172.6
Mg1Al3	352.10	144.5	0.08	3.10	12.1	222.4	70.2	23.2
Mg1Al9	96.78	53.7	0.00	5.60	7.4	30.3	57.0	0.79
Mg0Al1 (Al_2O_3)	153.05	87.4	0.05	2.36	1.7	75.8	67.5	3.21
Mg0Al1:Mg1Al0[*]	193.77	135.23	0.08	5.63	5.37	86.53	89.14	4.63

H_2O:EtOH molar (8.4:1), W_{cat} = 500 mg, GHSV = 26,000 mL$_{Feed}$ h^{-1} g$_{cat}$$^{-1}$
AcHO = Acetaldehyde; DEE = Diethyl ether.
[*]Mechanical mixture of having a 1:1 molar ratio of Al_2O_3 and MgO to approximate $MgAl_2O_4$

The pure and mixed oxide catalysts were also evaluated at 923 K and the results are reported in Table 3. The results are presented as ethanol conversion and product yield instead of rate because rate

information is useless for comparing catalytic performance when the catalysts achieve 100 % conversion. All catalysts experienced some form of deactivation at 923 K revealed by a loss in ethanol conversion, a change in product selectivity, or the presence of deposited carbon on the catalyst surface. Catalysts with high Al content (Al/(Al+Mg) = 0.75) were completely black and shiny when removed from the reactor, whereas the catalysts with high Mg content (Al/(Al+Mg) = 0.5) were also completely black but dull or matte in appearance. The sheen of the deposited carbon is indicative of the type of carbon on the surface. Shiny is believed to be graphitic while the dull or matte is a more amorphous, less dehydrogenated carbonaceous species. An anomaly to this was the Mg1Al2 catalyst, which experienced the least amount of carbon deposition. The catalyst was predominantly white with black flecks.

Similar to the finding at 773 K, catalysts with the $MgAl_2O_4$ crystal structure gave better performance in terms of ethanol conversion and H_2 and CO_2 yield. The performance of the catalysts with the Mg-AL LDO structure and low crystalline MgO (Mg3Al1 and Mg4Al1) was greatly improved by increasing the temperature 150 K suggesting that these mixed oxides might be of interest at higher reaction temperatures.

Table 3: Catalytic performance of Mg-Al mixed oxide catalyst under ethanol steam reforming conditions at 923 K.

Catalyst	EtOH conversion (%)	Yield						
		H$_2$	CO	CH$_4$	CO$_2$	C$_2$H$_4$	AcHO	DEE
Mg1Al0 (MgO)	97.01	1.08	0.08	0.15	0.31	0.34	0.06	0.13
Mg9Al1	55.92	0.75	0.15	0.19	0.07	0.30	0.51	0.01
Mg4Al1	100.00	1.11	0.06	0.20	0.38	0.32	0.03	0.13
Mg3Al1	100.00	1.21	0.05	0.13	0.37	0.30	0.02	0.17
Mg2Al1	100.00	1.24	0.03	0.16	0.43	0.29	0.03	0.17
Mg1Al1	100.00	1.29	0.04	0.23	0.46	0.28	0.02	0.16
Mg1Al2	100.00	1.37	0.07	0.79	0.74	0.16	0.01	0.00
Mg1Al3	88.65	0.43	0.10	0.12	0.04	0.47	0.27	0.01
Mg1Al9	64.22	1.05	0.18	0.20	0.12	0.24	0.45	0.03
Mg0Al1 (Al$_2$O$_3$)	73.62	0.63	0.13	0.14	0.03	0.34	0.38	0.01

H$_2$O:EtOH molar (8.4:1), W$_{cat}$ = 500 mg, GHSV = 26,000 mL$_{Feed}$ h^{-1} g$_{cat}^{-1}$

AcHO = Acetaldehyde; DEE = Diethyl ether.

Conclusions

Mg-Al mixed oxides were prepared by calcination of co-precipitated precursors. The surface area of the mixed oxides was found to be independent of the Mg-Al composition. Co-precipitation resulted in the intimate contact of Mg and Al in the form of Mg-Al LDO and MgAl$_2$O$_4$. The pure oxides, MgO and Al$_2$O$_3$, were not simultaneously detected in the samples suggesting that Mg and Al are chemically coupled in the mixed oxide catalysts and not merely mechanical mixtures.

The activity and selectivity of Mg-Al mixed oxides for the steam reforming of ethanol were evaluated at 773 and 923 K. All catalysts performed poorly for the ethanol steam reforming reaction (3) giving low production rates for H$_2$, CO, and CO$_2$. Catalysts having the MgAl$_2$O$_4$ spinel crystal structure gave the best performance at both reaction temperatures. Carbon deposits were found on all catalysts for reactions performed at 923 K. The Mg1Al2 catalyst, having a MgAl$_2$O$_4$ spinel crystal structure, had the least amount of carbon deposited on the catalyst surface.

The motivation for this study was to identify a Mg-Al mixed oxide for supporting nickel for the production of hydrogen via ethanol steam reforming. The Mg-Al mixed oxide having the Al/(Al+Mg) atomic ratio of 0.66 (Mg1Al2) was found to be the most active catalyst and gave the highest rate of production for H_2 and CO_2 and was less selective for ethylene production than Al_2O_3.

References

1. Haryanto A., Fernando, S., Murali, N., and S. Adhikari. Current status of hydrogen production techniques by steam reforming of ethanol: A review.

2. Vaidya, P.D. and A.E. Rodrigues. Insight into steam reforming of ethanol to produce hydrogen for fuel cells. Chem. Eng. J. 117 (2006) 39-49.

3. Sun J., Qui, X.-P., Wu, F., and W.-T.Zhu. H_2 from steam reforming of ethanol at low temperature over Ni/Y_2O_3, Ni/La_2O_3, and Ni/Al_2O_3 catalysts for fuel-cell applications. Int. J. Hydrogen Energy 30 (2005) 437-445.

4. Fatsikostas, A.N., Kondarides, D.I., and X. Verykios. Production of hydrogen for fuel cells by reformation of biomass-derived ethanol. Catal. Today 75 (2002) 145-155.

5. Freni, S., Cavallaro, S., Mondello, N., Spadaro, L., and F. Frusteri. Production of hydrogen for MC fuel cell by steam reforming of ethanol over MgO supported Ni and Co catalysts. Catal. Comm. 4 (2003) 259-268.

6. Freni, S., Cavallaro, S., Mondello, N., Spadaro, L., and F. Frusteri. Steam reforming of ethanol on Ni/MgO catalysts: H_2 production for MCFC. J. Power Sources 108 (2002) 53-57.

7. Frusteri F., Freni, S., Chiodo, V., Spadaro, L., Di Blasi, O., Bonur, G., and S. Cavallaro. Steam reforming of bio-ethanol on alkali-doped Ni/MgO catalysts: hydrogen production for MC fuel cell. Appl. Catal A:Gen 270 (2004) 1-7.

8. Schaper H., Berg-Slot, J.J., and W.H.J. Stork. Stabilized magnesia: a novel catalyst (support) material. Appl. Catal. 54 (1989) 79-90.

9. Stobbe, D.E., van Buren, F.R., Groenendijk, P.E., van Dillen, A.J., and J.W. Geus. Magnesium oxide as a support material for dehydrogenation catalysts. J. Mater. Chem. 1 (1991) 539-543.

10. Di Cosimo J.I., Diez, V.K., Xu, M., Iglesia, E., and C.R. Apesteguia. Structure and surface and catalytic properties of Mg-Al basic oxides. J. Catal. 178 (1998) 499-510.

11. Di Cosimo J.I., Apesteguia, C.R., Gines, M.J.L., and E. Iglesia. Structural requirements and reaction pathways in condensation reaction of alcohols on Mg_yAlO_x catalysts. J. Catal. 190 (2000) 261-275.

12. Diez, V.K., Apesteguia, C.R., and J.I. Di Cosimo. Effect of the chemical composition on the catalytic performance of Mg_yAlO_x catalysts for alcohol elimination reactions. J. Catal. 215 (2003) 220-233.

13. McKenzie A.L., Fishel, C.T., and R.J. Davis. Investigation of the surface structure and basic properties of calcined hydrotalcites.

14. Chladek, P, Coleman, L.J.I., Croiset, E., and R.R. Hudgins. Gas chromatography method for the characterization of ethanol steam reforming products. J. Chrom. Sci. 45 (2007) 153-157.